Photochemical Strategies for the Synthesis of Advanced Materials

Paul S. Billone

Thesis submitted to the Faculty of Graduate & Postdoctoral Studies
University of Ottawa
in partial fulfillment of the requirements for the
Ph. D. degree in the
Ottawa-Carleton Chemistry Institute

Candidate

Supervisor

Paul S. Billone

J.C. Scaiano

Table of Contents

Abstract

This thesis describes the study of a variety of nanoscale materials and the development of novel synthetic strategies for their production. While the focus and bulk of this study have been directed specifically at subwavelength lithography, a significant portion of this thesis research involves nanoparticle synthesis, characterization, and functionalization.

Put in very simple terms, optical lithography is a process where a beam of light, focused in a specific pattern, is used to generate a physical pattern on a solid substrate. This technology forms the basis for almost all microchip production in the world at the present time. As demand for faster and more powerful chips increases, the need to further miniaturize the patterns while minimizing cost has become very important.

Multiple photochemical systems were developed in the search for non-reciprocal photochemistry at 193 nm to increase the resolution of lithographic processes at that wavelength. One approach, based on anthracene sensitization of sulfonium salts for acid generation, used photochemically reversible 4+4 aromatic cycloaddition reactions to introduce the non-linear photochemistry. A second approach took advantage of the photochemistry of N-methylphenothiazine and provided the first true example of a lithographically-relevant multi-photon acid generating process.

Since all of the systems we studied used sulfonium salts as the acid generating species, we also looked at the photochemistry of the salts themselves. We evaluated the structural effects of the salts on their direct photochemistry and the implications for sensitized multi-photon photochemistry. We found that the identity of the anion plays a significant role in both processes and propose a new photochemical mechanism for acid generation that involves a charge transfer excitation process.

We also describe the synthesis and characterization of novel fluorescent silver nanoparticles, both in solution and polymer films. We show that the fluorescent images can be patterned easily and preliminary results show that photolithography based on nanoparticle formation may be possible. This latter approach could provide a facile route to nanoparticle-embedded functional materials. This work with nanoparticles was inspired partly by earlier work, also presented herein, on semiconductor nanoparticles and their interactions with disulfide ligands.

Acknowledgements

Incomparable educators have enabled all of my accomplishments.

First and foremost, my mom: She has been my biggest supporter and inspiration. Her love and guidance, and belief in my abilities, have lifted me to where I am now. From her I have learned so much, I can't even begin to explain. My Nonna and Nonno are not far behind, full of selfless love and unwavering support; I can't imagine any better grandparents. The rest of my family, particularly Aunt Jennie and Uncle John, have instilled in me the importance of family, balance, and confidence. I also need to thank my new family, the Blakes and the Findlays, for being so welcoming and loving.

Three great men have shaped my formal academic education. Tito has been an amazing supervisor. His support and belief in me have gotten me here today. He truly is a great man and a great teacher: I have always felt that no matter the question, whether personal or scientific, he would tell me exactly what I needed to hear. I never would have ended up with Tito in Ottawa without the guidance of Willie Leigh, my undergraduate research supervisor. I feel that my initial laboratory training was second to none thanks almost completely to him. Today I feel lucky to be able to call him a friend. Finally, Keith Ingold has been such an inspiration to me over the last few years. He has taught me so much, both scientifically and personally, and his confidence in me has given me a great deal of strength.

Anyone who has worked in a research group knows that the other students and post-docs around you are integral to your learning. I thank the entire Scaiano and Leigh research groups, both past and present, for all of their support and making the lab both a scientifically stimulating and fun place to be (too many to mention, but you know who you are). I would especially like to acknowledge Lawrence Huck and Mathieu Frenette for all of their help and support, Vincent Maurel for his exceptional guidance, Alexis Aspee for always making science fun, and Michel Grenier for a little bit of everything. I'd also like to thank Julie Park all of her hard work on some of the topics presented here.

Learning doesn't stop in the lab and having great friends around helps to establish a good mindset. Matty, Adam, Dave, Jimmy, and many, many more have always ensured that time outside of the lab is spent in good company.

Finally, to my best friend and wife-to-be Jessie, I owe so much to you. You've made me smile at least once every day for the last five years. You're always there for me, to talk about science or anything else, and I dedicate this work to you.

List of Figures

an increase in reflectance intensity is qualitatively indicative of dissolution. A) Unexposed film containing both I-2959 and AgOTf; B) Exposed film containing both I-2959 and AgOTf; C) Exposed film containing only I-2959; D) Unexposed film containing only I-2959. Films A) and B) were cast from TER-70 solution containing 0.25 M I-2959 and 0.05 M AgOTf; Films C) and D) case from TER-70 solution containing only 0.25 M I-2959. All films were spin-coated at 2000 rpm for 30 s followed by 1 min PAB @ 105°C. Films B) and C) were exposed to 30 min irradiation (UVB, 6 lamps) and *all* films were then baked again for 1 min 105°C.

List of Schemes

List of Tables

Abbreviations

$^1O_2$ – Singlet Oxygen

AgFNP – Silver Fluorescent Nanoparticle

BEOL – Back End Of Line

BET – Back Electron Transfer

C6 – Coumarin-6

CAR – Chemically Amplified Resist

CV – Cyclic Voltammetry

DE – Double Exposure

DFT – Density Functional Theory

DMB – *para*-dimethoxybenzene

DNQ – Diazonaphthoquinone

DUV – Deep Ultraviolet

EDS – Energy Dispersive Spectroscopy

EPR – Electron Paramagnetic Resonance

EUV – Extreme Ultraviolet

FEOL – Front End Of Line

GPC – Gel Permeation Chromatography

HDA – Hexadecylamine

IC – Integrated Circuit

ISC – Intersystem Crossing

LED – Light Emitting Diode

LFP – Laser Flash Photolysis

LLE – Litho Litho Etch

NA – Numerical Aperture

NP – Nanoparticle

PAB – Post-Application Bake

PAG – Photoacid Generator

PBOCS - poly(*t*-butoxycarbonyloxystyrene)

PD – Pitch Division

PEB – Post-Exposure Bake

PHS - poly(*p*-hydroxystyrene)

PMMA – polymethylmethacrylate

QD – Quantum Dot

rCEL – Reversible Contrast Enhancement Layer

RET – Resolution Enhancement Technology

SPB – Surface Plasmon Band

SV – Stern-Volmer

TD-DFT – Time-dependent Density Functional Theory

TEMPO - 2,2,6,6-tetramethylpiperidine oxide

TES – Triethylsulfonium

TMAH – Tetramethylammonium Hydroxide

TOP - Trioctylphosphine

TOPO – Trioctylphosphine oxide

TPS – Triphenylsulfonium

XPS – X-Ray Photoelectron Spectroscopy

ε - Absorption Coefficient

η - Refractive Index

Φ – Quantum Yield

Structure and Structural Abbreviation Glossary

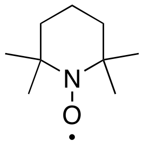

TEMPO

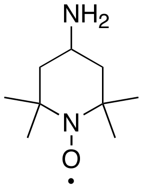

4aT

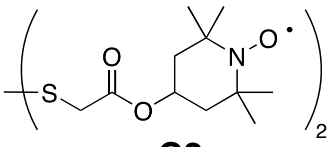

C2

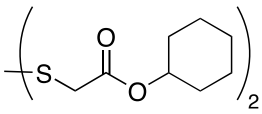

C2-cyclohexyl

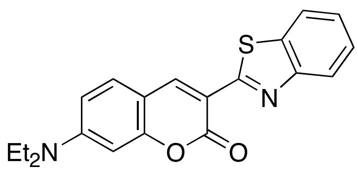

C6

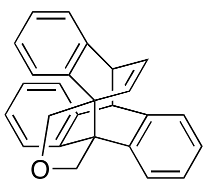

cNAME

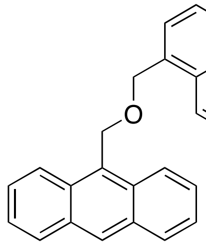

NAME

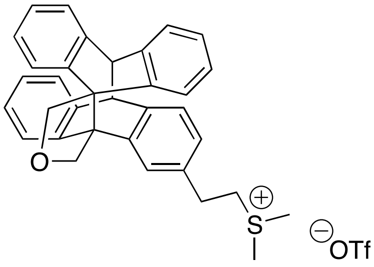

cDAME-PAG

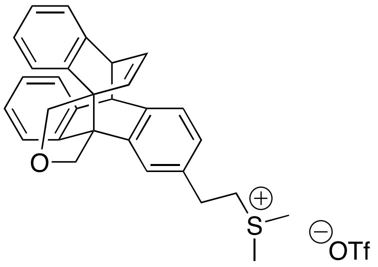

cNAME-PAG

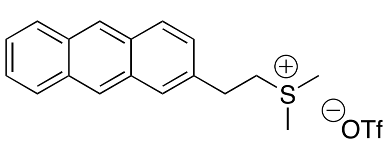

Anth-PAG

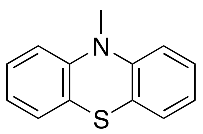

mPT

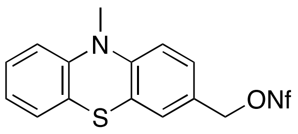

mPT-ONf

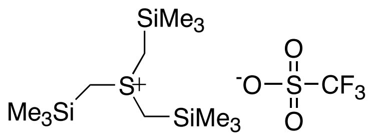

Si3PAG-2

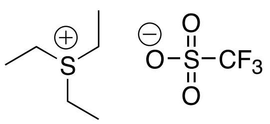

TES-2

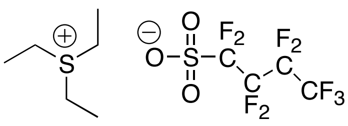

TES-3

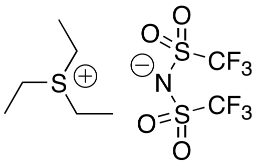

TES-6

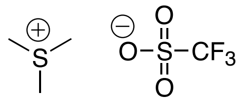

mPAG-2

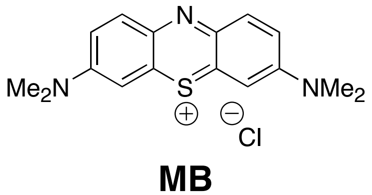

MB

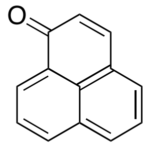

PH

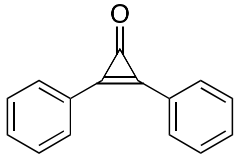

DPCP

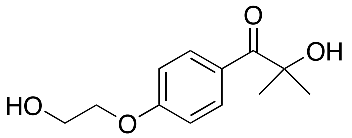

I-2959

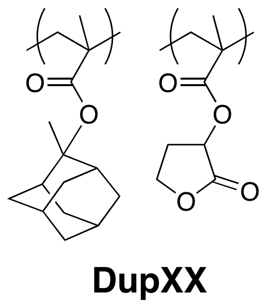

DupXX

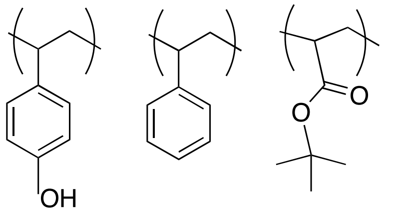

TER-70

1. Lithography: Past, Present, and Future

Table of Contents

1.1 Lithographic Technology and Industry Trends

The original meaning of the term lithography in modern usage refers to a process of printing based on hydrophilicity: A non-polar ink applied to a hydrophilic master plate patterned with a hydrophobic image.[1] The term has adapted and now applies to the general concept of using a master pattern to print an image on a substrate. While lithography has an exceptionally broad range of modern uses, arguably the most pervasive application has been in the semiconductor industry for the production of integrated circuits (ICs).[2] ICs are miniaturized arrays of transistors assembled and connected on a single semiconductor substrate that form the basis of modern microelectronic devices.

In the case of semiconductor lithography for modern IC production, the lithographic step involves writing a pattern in a polymer (the resist) on a silicon wafer. This process is currently done using UV light irradiation and referred to as photolithography. During the photolithographic process, the photoresist is exposed in a certain pattern through a mask and the incident irradiation induces some physical change in the material, typically a change in solubility.[3] In a positive-tone photoresist, the exposed area becomes more soluble in the developing media and can be subsequently removed; in a negative-tone photoresist, the exposed area is less soluble in the developing media (Figure 1.1). The resulting pattern is then used as an etch mask for the subsequent pattern transfer steps. To build the complex circuits required in modern microchips, the lithography and etch pattern transfer steps are typically repeated 25 to 40 times per circuit.

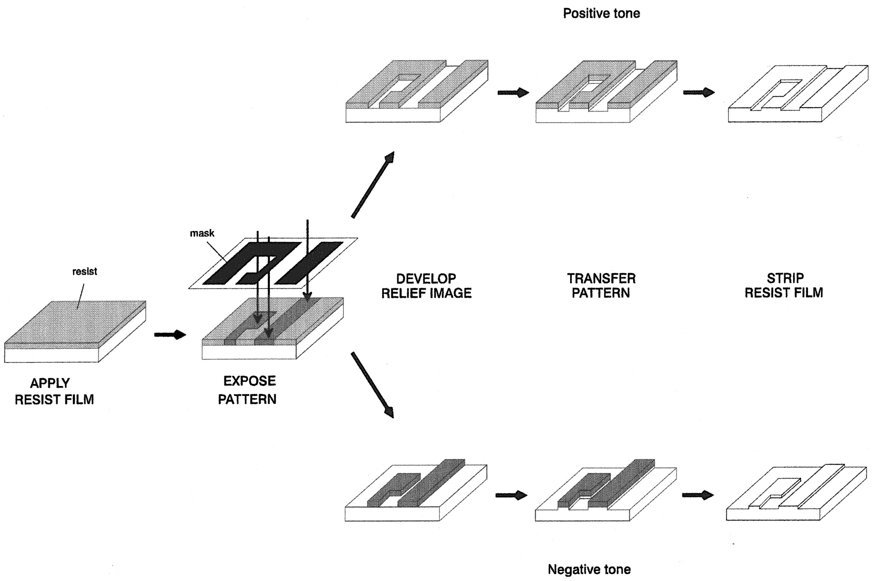

Figure 1.1 Schematic diagram of the photolithographic process for a positive-tone photoresist (top) and a negative-tone photoresist (bottom). Modified from Ref. 1.

Because of the large number of lithographic steps required for each circuit, lithography can account for about 30% of the entire cost of manufacturing an IC chip. In addition, the lithographic process, or more correctly the development of new lithographic processes, is typically the main technical limiter for the improvement of chip performance.[2] As such, lithographic process development is one of the main bottlenecks in the consumer-motivated computer industry: Consumers expect increasingly sophisticated electronics at progressively lower prices while semiconductor companies expect continually increasing profits. In 1977 Bob Noyce, a cofounder of Intel, stated that “future miniaturization is less likely to be limited by the laws of physics than by the laws of economics.”[4]

While the previous statement certainly held some merit in 1977, the rate of IC development has always been defined by a combination of both technical and economic limits. Surprisingly in 1965, Noyce’s colleague Gordon Moore, also a cofounder of Intel, famously analyzed the trends in the evolution of semiconductor technology and predicted that the number of electrical components per IC chip would double every year.[5] In 1975 he revisited his initial prediction and modified his expected growth rate to doubling every two years.[6] In his extrapolation, now referred to as Moore’s law, Moore considered economic and technical limitations that he saw in future development. Figure 1.2 illustrates one of the graphical manifestations of Moore’s law, showing the increase in the number of transistors per computer chip versus year. While Moore’s law was originally proposed as an empirical extrapolation, it has become part of the industry standard for chip development, one that semiconductor companies adhere to quite rigidly. In fact, Moore’s law has become so accepted that in 1994, the Semiconductor Industry Association drafted the *National Technology Roadmap for Semiconductors* (NTRS)[7] as the industry-standard Moore’s Law; the roadmap has seen many updates and is now known as the *International Technology Roadmap for Semiconductors* (ITRS).

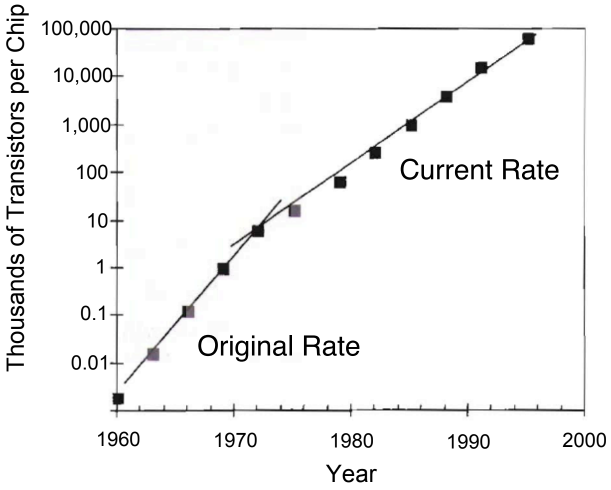

Figure 1.2 Plot of Moore's law showing an increase in the number of transistors per computer chip as a function of year on a semi-log scale. The change in the development rate, as predicted by Moore's 1975 document, is clearly defined but the rate has stayed consistent since then. More recent plots are available but generally do not show the original rate of development, thus the reason this plot is included. Modified from Ref. 2.

The resolution of a photolithographic feature, which is defined by the smallest feature which can be printed with adequate control,[2] can be described by the Rayleigh equation (Equation 1.1).[3]

$$R = k_1 \frac{\lambda_0}{n \cdot \sin\theta} \qquad (1.1)$$

where R is the resolution, k_1 is the Rayleigh coefficient of resolution, λ_0 is the wavelength of irradiation, n is the refractive index of the medium between the mask and the optics, and θ is the angular aperture of the lens. As is evident from Equation 1.1, the resolution is directly proportional to the wavelength of irradiation. Thus the most fundamental limiter in terms of lithographic resolution for IC development is the wavelength of irradiation. Indeed for most of the development in Figure 1.2, the main change has been to modify the irradiation source to shorter wavelengths. Figure 1.3 shows the progression of resolution as a function of the parameters in Equation 1.1.

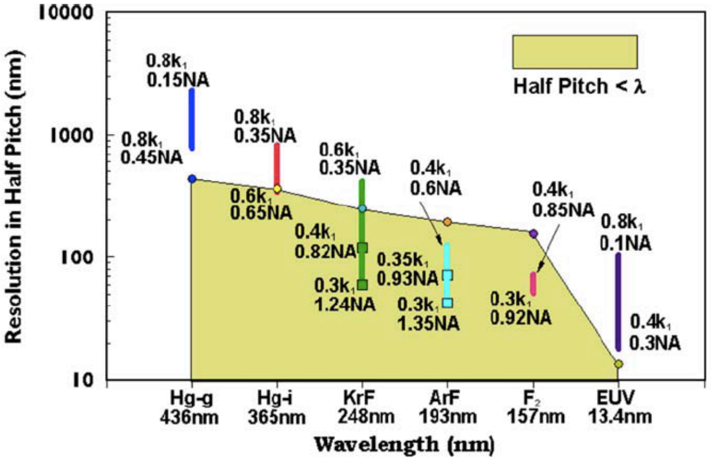

Figure 1.3 The evolution of resolution in optical projection lithography as a function of irradiation source and additional exposure/processing parameters according to Equation 1.1. The function outlined in yellow represents the conventional diffraction limit expected at each wavelength; half pitch (d) is half of the diffraction-limited periodicity of an image produced with the corresponding lithographic wavelength. Modified from Ref. 12.

The curve that defines the yellow area boundary in Figure 1.3 represents the conventional diffraction limit of each lithographic wavelength and therefore their expected resolution limits. It was these presumed limitations that has caused industry pundits to repeatedly, and incorrectly, predict the death of optical lithography.[2] However continuous modifications of lithographic parameters other than wavelength have enabled sub-wavelength lithography with optical sources.

The vertical coloured bars in Figure 1.3 represent the range of actual resolution obtained in the semiconductor industry using the indicated lithographic wavelengths. Immersion lithography effectively uses some high-refractive index media, namely water, to increase the numerical aperture (NA, $n \cdot \sin\theta$) of the process thus increasing the resolution according to Equation 1.1.[8] Research and system modifications that increase resolution based on factors other than the lithographic wavelength or NA are referred to as resolution enhancement technologies (RETs); these technologies are largely process-dependent factors that are meant to lower the k_1 value in Equation 1.1. It has been the aggressive use of these RETs, combined with the move to immersion lithography, that have enabled sub-wavelength lithography for many lithographic generations. Lithographic generations are represented by the points in Figure 1.2 (adhering to Moore's Law) and are generally defined by the minimum feature size attainable;[9] these generations are also referred to as "nodes". While immersion lithography has pushed NA values high above 1.0, the semiconductor industry is constrained to working with k_1 values above 0.25.

Consider a mask pattern which consists solely of a grating with a periodicity (pitch) of $2d$. As the periodicity approaches the resolution limit, the image transmitted through the mask is a cosine function with the same periodicity as the mask pattern

(Figure 1.4a).[10] The optical contrast between exposed and unexposed regions is defined as

$$C = \frac{I_{\max} - I_{\min}}{I_{\max} + I_{\min}} \qquad (1.2)$$

where $I_{\max}$ and $I_{\min}$ are the minimum and maximum light intensities incident on the surface in the exposed and unexposed regions, respectively. The normalized spatial frequency of an image through a mask is given by

$$\text{normalized spatial frequency} = \frac{\lambda}{2d \cdot NA} \qquad (1.3)$$

Figure 1.4b shows contrast as a function of the normalized spatial frequency and in the case of incoherent light, contrast becomes 0 when Equation 1.3 is equal to 2. This means that there is no contrast when the half pitch is 0.25λ/NA or smaller. Since the image pitch is equivalent to resolution (Equation 1.1), k_1 is limited to be greater than or equal to 0.25 for any single-stage optical lithographic process.

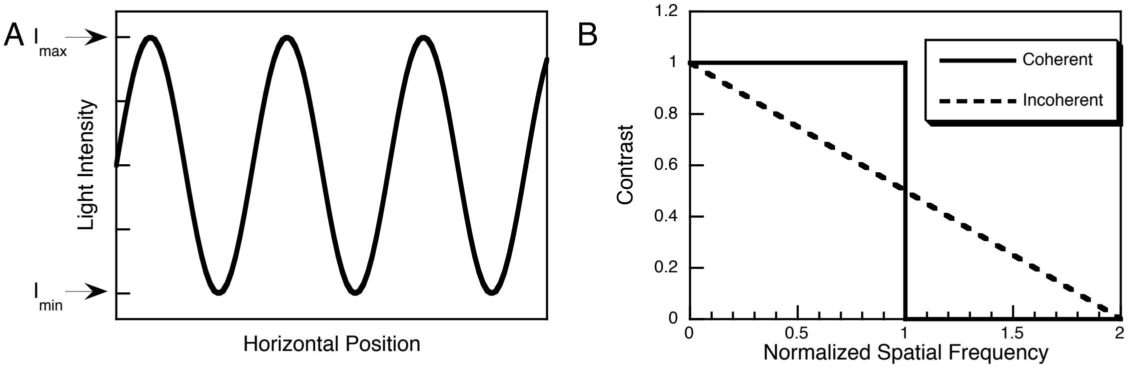

Figure 1.4 A) Projection of light intensity as a function of position on an exposed substrate for a grating pattern near the diffraction limit; B) The contrast of a diffraction-limited lens, as defined by Equation 1.2, as a function of the normalized

spatial frequency according to the modulation transfer function (see Ref. 10 for additional details) for coherent and incoherent light sources. While chip manufacturing processes generally use coherent sources, the imaging beam incident on the surface is only partially coherent and has the same contrast limitations as incoherent sources (see text above).

The most obvious way to circumvent the physics-imposed limits on 193 nm optical lithography would be for industry to adopt a new photolithographic standard source. The next logical lithographic wavelength is 157 nm, corresponding to the emission of a F_2 excimer laser, but the technical failures of that line are well documented.[10] Extreme ultraviolet (EUV), e.g., 8 or 13 nm, appears to be the best option for extending optical lithography for future generations[11-15] and if adopted, it will be the first time since the early stages of 248 nm technology that optical lithography returns to operating above the conventional diffraction limit (see Figure 1.3). However the materials and instruments required for EUV lithography are not developed to the point required for industry use and therefore it is unlikely to take over as the standard lithographic technology for the upcoming generation of chip design. X-ray lithography has been considered as an optical lithographic technology since the early 1980s but it suffers from even more severe technical limitations.[2, 16] Outside of optical lithography, multi-e-beam maskless lithography and nanoimprint lithography have been proposed and explored as potential options,[11, 12] but their prohibitive cost and low-throughput have limited their development. While all of these technologies have demonstrated the ability to meet the resolution requirements for next-generation devices with resolution to spare, optical lithography is unsurpassed in terms of cost per pixel[17] and as Moore's law has both economic and technical limitations associated with it, optical lithography seems poised to continue driving the IC industry for the near future.[2]

The most promising proposals for extending 193 nm lithography to the 22 nm node, only possible if either a higher NA system is found or a lower k_1 process is developed, have been double-patterning technologies. As the name implies, these methods involve two subsequent exposure steps, though many different combinations of intermediary steps have been explored.[18-20] However, there are significant limitations to all proposals thus far.[21] One of the approaches that shows the most potential for achieving pitch division (PD) is the double-exposure (DE) method, also referred to as litho-litho-etch (LLE) technology.[22] The DE technique would be able to extend 193 nm lithography to the next technology node by decreasing k_1 to half of the theoretical 0.25 limit. Figure 1.5 illustrates how DE is able to achieve PD, effectively doubling the resolution of conventional immersion 193 nm lithography. The technical requirements of LLE are minimal since DE does not require the wafer to be removed from the chuck[23] between exposures; it only requires translation of the stage or mask. Therefore the most significant set-back in the development of LLE is the availability of necessary materials; the photoresist material must possess a strong non-reciprocal photoresponse. The work in Chapters

3 and 4 of this thesis outlines the development and photochemical study of two potential non-reciprocal chemical systems for DE applications.

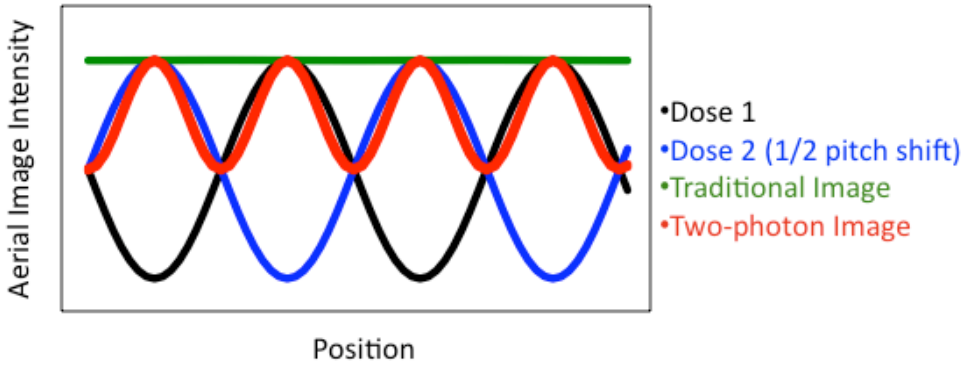

Figure 1.5 The theoretical contrast curves for two interspersed pitch-limit aerial images, Dose 1 (black) and Dose 2 (blue), for a traditional, single-photon photoresist (green) and for a two-photon, DE photoresist (red).

1.2 Photoresist Technology and Chemically Amplified Resists (CARs)

While the preceding section described lithography from a technological standpoint, no details were given on *how* optical lithography works to produce a solubility change that allows for the development of an exposure pattern (Figure 1.1). As mentioned, this is the role of the photoresist itself and is generally comprised of two distinct steps: An initial photochemical transformation followed by a thermal reaction that causes the solubility switch. All optical lithography in the semiconductor industry until 1995, which was based on high-pressure mercury arc lamp irradiation wavelengths, used diazonaphthoquinone (DNQ)-based photoresist technology.[24] Scheme 1.1 shows the mechanism of the solubility switch and some typical structures of the photoresist components. The most important point to be made about this resist technology is that despite its high contrast and desirable resist properties, it was insensitive to shorter lithographic wavelengths (specifically 248 nm) and was too inefficient at the next generation wavelengths since each photon absorbed resulted in only one deprotection.

Scheme 1.1 Photochemical solubility switch for DNQ-based photoresist. The polyhydroxystyrene resist (left) is cast with a high loading of the DNQ-based solubility inhibitor, comprised of a ballast group (typical examples of which are shown to the right of the scheme) and one or more tethered DNQ groups. Upon photolysis, the DNQ groups decompose *via* photochemical Wolff rearrangement into hydrophilic indenecarboxylic acids, rendering the exposed resist areas soluble in basic developing solutions.

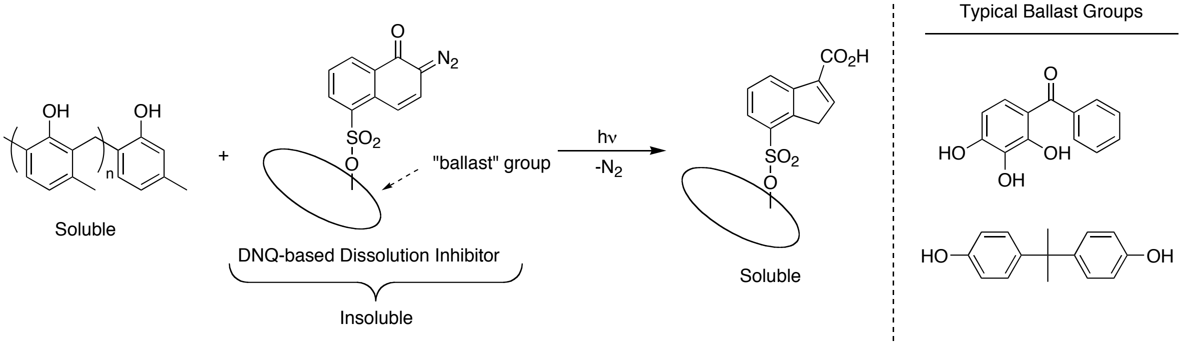

Early DUV (deep ultraviolet) lithographic sources, including mercury-xenon arc lamps, had low light output relative to the Hg g- and i-lines used in the previous generations and therefore required a resist technology that was far more sensitive to incident light than the DNQ-based 1:1 systems. This need resulted in the invention of chemically amplified resist (CAR) technology. A general scheme for a CAR deprotection mechanism is given in Figure 1.6. From the mechanism, it is evident that the process is acid-catalyzed and therefore one molecule of acid can deprotect many protecting group units. The removal of a protecting group results in a solubility change, generally from hydrophobic to hydrophilic, and thus the developing step proceeds in the same manner as in previous generations (Figure 1.1).[10] When the initial molecule of acid is generated photochemically, the CAR technology has the potential to exhibit effective quantum yields much greater than one, thus increasing the efficiency to the level required for DUV lithography.

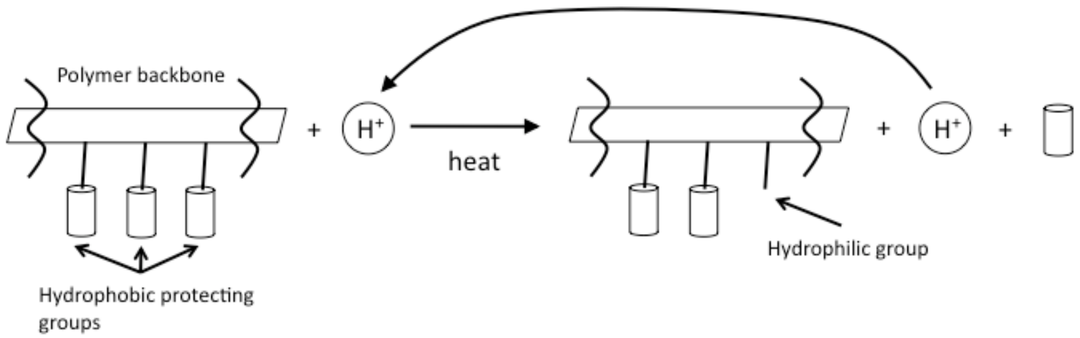

Figure 1.6 General mechanism of action for an acid-catalyzed CAR.

Unlike all previous developments in lithographic technology, it has been stated that the introduction of CARs was a revolutionary, not evolutionary, step.[25, 26] In addition to requiring modifications to the exposure and development tools, polymers had to be designed that would react in a manner outlined in Figure 1.6 and appropriate photoactive molecules had to be made that would generate acid efficiently with DUV irradiation. The initial polymers designed as CARs were composed mainly of poly(*t*-butoxycarbonyloxystyrene) (PBOCS) and relied on the acid-catalyzed cleavage of the labile *t*-BOC groups to form poly(*p*-hydroxystyrene) (PHS).[27] Scheme 1.2A shows the deprotection reaction of PBOCS. The PBOCS photoresist was an ideal candidate for lithography at 248 nm due to its low absorbance at that wavelength and its high sensitivity. The *t*-BOC protecting group was chosen due to the high activation energy required for the reaction in Scheme 1.2A to proceed; while other acid-labile protecting groups with lower activation energies have been used for CAR lithography, high activation resists are more readily controlled and thus generally produce more uniform feature sizes.[2]

Modern 193 nm resists could not be based on PBOCS/PHS polymers due to their opacity at the lithographic wavelength. In contrast, aliphatic methacrylate polymers are nearly transparent at 193 nm and have been developed as the predominant resist technology at 193 nm. They generally rely on acidolysis of their ester groups to affect a solubility change (see Scheme 1.2B); esters are also high activation energy blocking groups and thus they maintain the advantages of *t*-BOC mentioned above.[2] Most of the polymers used in this thesis will be methacrylate-based, though not all will contain an acid labile group. Due to the mechanism of cleavage (Scheme 1.2), the protecting group must form a relatively stable carbocation or the activation energy will be *too* high for cleavage to occur.

Scheme 1.2 A) The acid-catalyzed deprotection of PBOCS; B) The acid-catalyzed deprotection of poly(adamantylmethacrylate).

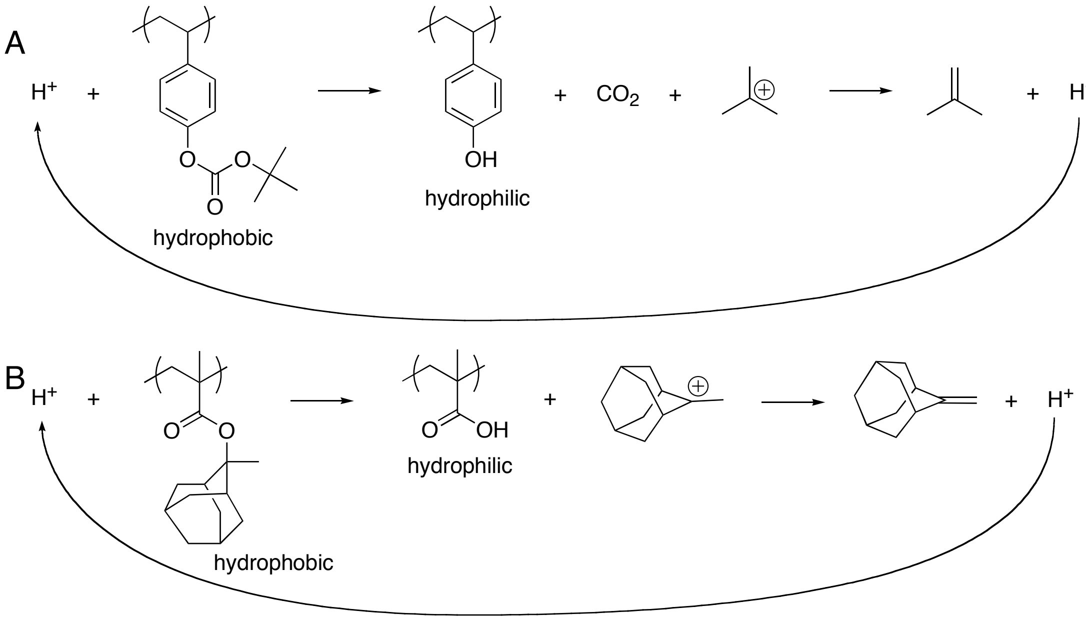

Since almost all of the industrially relevant CARs rely on acid-catalyzed deprotection steps, the development of appropriate photoacid generators (PAGs) was also required. While great care was taken to ensure that the resists themselves were transparent at the lithographic wavelengths used, the PAGs had to absorb the light and efficiently generate strong acid. There are many other considerations that must be taken into account for the synthesis of PAGs[25] and onium salts such as triarylsulfonium and diaryliodonium hexafluoroarsenates and antimonates satisfied most of them. Thus, despite being originally developed for photocuring epoxy resins, they were adopted for use in the very first CAR systems.[27] Eventually the metal-containing anions were replaced by sulfonates, such as trifluoromethanesulfonate (triflate, OTf), and triphenylsulfonium triflate remains the most widely-used PAG for lithographic applications.[28] One of the advantages of ionic PAGs like the onium salts are that they can easily be synthesized by metathesis reactions and thus the anion can be varied to change the pK_a, volatility, and size of the photogenerated acid.[1] The identity of the anion has always been an important factor in photolithography because it provides a means to limit diffusion distance. The larger the anion of an acid, the shorter the distance the acid molecule can diffuse throughout the polymer film after generation.[2] Limiting diffusion becomes particularly critical as the minimum feature size continues to decrease. If the industry is fabricating devices with 22 nm features, radial diffusion distances of just 4 nm would blur the patterned aerial image to 30 nm. Therefore significant effort has been dedicated towards tailoring the size of photogenerated acid to limit diffusion but little attention has been paid to whether changing the anion between model systems and the actual molecules used for patterning changes the photochemical or electrochemical properties of the PAG molecules themselves. Chapter 5 of this thesis explores a variety of potential PAGs for use in 193 nm DE lithography, with particular emphasis on the role of the anion in the overall photochemistry and acid-generating processes.

1.3 Additional Lithographic Patterning Applications

While the preceding sections were concerned primarily with lithography for IC development in the semiconductor industry, the applications of micro- and nano-lithography are by no means limited to that realm. The role of the resist in the above technology is one of brief (but essential) importance: The functionality of the final device does not rely on the resist used at all. Conversely the polymer itself, which has undergone some physicochemical change in the "developed" areas, can be considered a useful, functional structure.[29] The application that has garnered the most attention with respect to this type of organic semiconductor lithography has been the formation of organic electronics such as light emitting diodes (LEDs).[30] For these types of devices, pushing the resolution limit is not necessarily the goal, as it is for inorganic semiconductor IC production. Rather, emphasis is put on throughput and area coverage (the size of the macroscopic device, not the micro- or nano-scopic features, defines the device generation).[30] While a great deal of work has been dedicated to nano-patterning techniques, both in ground-up development and making them generally more high-throughput,[31-33] photolithography remains unrivalled in its cost-per-unit-area and potential throughput.

The main draw-back to photolithography for the production of large scale micro- or nano-organic devices is the cost of the photomask required. While projection lithography would allow for a small mask to pattern a large device area,[34] it becomes more costly and inefficient to operate at those scales. Thus the advantages of photolithography for organic patterning are best realized for creating complex micro- or nano-scopic patterns with high-resolution and high-throughput on smaller scale substrates.

One field of particular interest is that of nanoparticle polymer composites.[35] Such materials can be tuned to have desirable mechanical, physical, or chemical properties that are not possible in the parent materials themselves. As photolithography has been used to make complex organic structures, it could be reasoned that incorporation of metallic nanomaterials into these structures could dramatically increase their applicability.[36] Chapter 6 of this thesis will introduce the synthesis and characterization of a class of photochemically-generated metallic nanoparticles and demonstrate the ability to synthesize the same materials within a polymer matrix. Chapter 7 will present preliminary results on photoresist lithography combined with nanoparticle lithography for lithographically patterned polymer nanoparticle composite materials. While these materials may not increase resolution or throughput compared to modern materials, the novel functionality that they could potentially introduce to polymer films is very exciting nonetheless.

1.4 Semiconductor Quantum Dots and Nitroxides

While the main story of this thesis is concerned with the development and investigation of technologies for lithography, the first project I completed during my Ph.D. work involved studying the interaction of disulfide ligands with CdSe quantum dots (QDs). During my tenure as an undergraduate researcher in the Scaiano lab, I worked on the quenching of QD fluorescence by nitroxide free radicals.[37, 38] When I returned for my graduate studies, my initial idea was to continue using this quenching method to better understand the binding of other types of ligands to QD surfaces. As the biological applications of QDs were being rapidly developed,[39, 40] I felt that studying the binding of disulfide ligands was particularly relevant. The results of our brief study on these interactions are presented in Chapter 2.

While the work presented in Chapter 2 does not fit with the theme of lithography, it gave me important experience in working with nanoparticles. This project gave me the background that was necessary to develop the nanoparticle-based lithographic systems discussed in Chapters 6 and 7 of this thesis and introduced me to many of the advanced spectroscopic tools I would use in my subsequent studies.

1.5 Techniques and Methodologies Developed

This section will outline new instrumental set-ups, techniques, and methodologies developed specifically for this project. Only techniques that are used throughout multiple chapters will be included here; those that were developed for specific experiments are outlined in their respective chapters.

1.5.1 Dose-dependent Screening for Multi-photon Processes with Coumarin-6 Dye

The research performed in Chapters 3 and 4 of this thesis was primarily concerned with the evaluation of photochemical systems as potential non-linear acid-generators. Thus an easy and effective method to determine whether the acid-generating photochemistry that was occurring in the polymer films was multiphoton had to be developed. Coumarin-6 (C6) fluorescent dye had been previously used by members of the Scaiano group to quantify acid generation in thin polymer films[41] and we decided to use a method based on their protocol for screening multi-photon acid generation.

To use the C6 system to observe multiphoton acid generating behaviour, several identical quartz discs were spin-coated with the same polymer solution containing all components of the system under investigation. The absorbance of each film was checked to ensure that both the absorbance of C6 (see Figure 1.7a) and the absorbance at 193 nm were the same. Each film was then exposed to the same dose of 193 nm irradiation but the energy per shot and number of shots was varied for each film. Figure 1.7b illustrates the process for three films using a general total dose of 160 mJ/cm^2 irradiation energy. Following irradiation, the absorbance spectrum of each film was re-measured and the amount of protonated C6 (referred to as C6-H$^+$ in Figure 1.7a) was compared for each sample. In a single-photon acid generating process the yield of C6-H$^+$ would be the same for all films but for a multi-photon process the film with the highest energy per shot would have more C6-H$^+$.

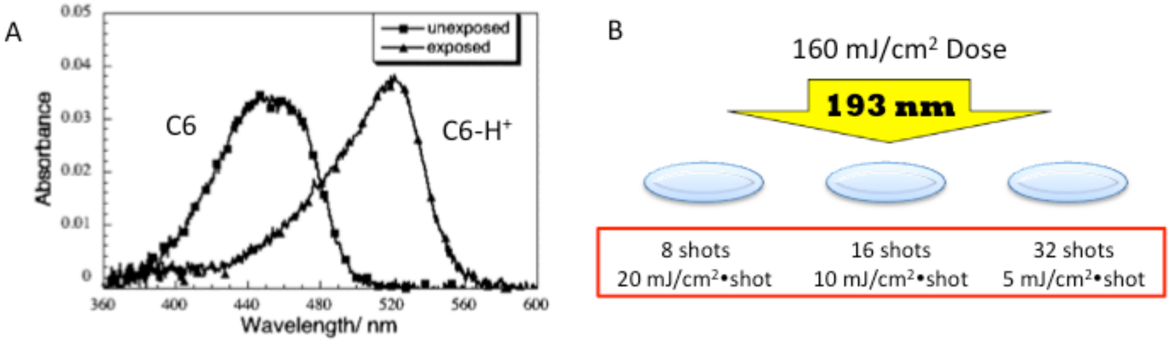

Figure 1.7 A) The absorbance spectrum of C6 and C6-H$^+$; modified from Ref. 37; B) A general cartoon illustration of the exposure conditions used to monitor for multi-photon acid-generation. The particular example shown uses a total dose of 160 mJ/cm^2 on three identical films, each exposed to a different energy per shot.

In the above experiment, low quality quartz pieces were used as neutral density filters, each cutting the transmitted 193 nm energy by approximately 50 %. For the experiments to be useful, careful power measurements were required to test the power dependence of this system and therefore we needed to verify that power measurements were linear over the range of energies used in the experiments. To do this, the energy of the transmitted beam through the quartz neutral density filters used in the power dependence experiments were measured using the power meter both individually and the same three filters together. The measurements and calculations are shown below.

E(0 filters) = 7.56 +/- 0.57 mJ/cm2
E(filter 1) = 4.05 +/- 0.14 mJ/cm2
E(filter 2) = 4.00 +/- 0.36 mJ/cm2
E(filter 3) = 3.79 +/- 0.34 mJ/cm2

E(filters 1 + 2 + 3) = 1.11 +/- 0.01 mJ/cm2

% T (filter 1) = 54 +/- 4.5
% T (filter 2) = 53 +/- 6.2
% T (filter 3) = 50 +/- 5.9
% T (average) = 14 +/- 2.6

% T (filter 1 + 2 + 3) = 15 +/- 1.1

The transmittance as measured is the same, within experimental error, for the three filters together as the average of the three filters measured individually. This confirms the linearity of our power measurements.

1.5.2 Thin-Film Laser Flash Photolysis (LFP)

The systems explored in Chapters 3 and 4 of this thesis were interesting from an application point of view but I was concerned with understanding some of the mechanistic aspects of the photochemical processes occurring in the films upon irradiation. The Scaiano group has played a strong role in developing laser flash photolysis for the study of reaction intermediates in solution[42] and in opaque solids.[43] Thin polymer film LFP had previously been described[44] but was not optimized for monitoring irreversible reactions. A schematic diagram of the system we designed[45] for measuring transient phenomenon in films is shown in Figure 1.8.

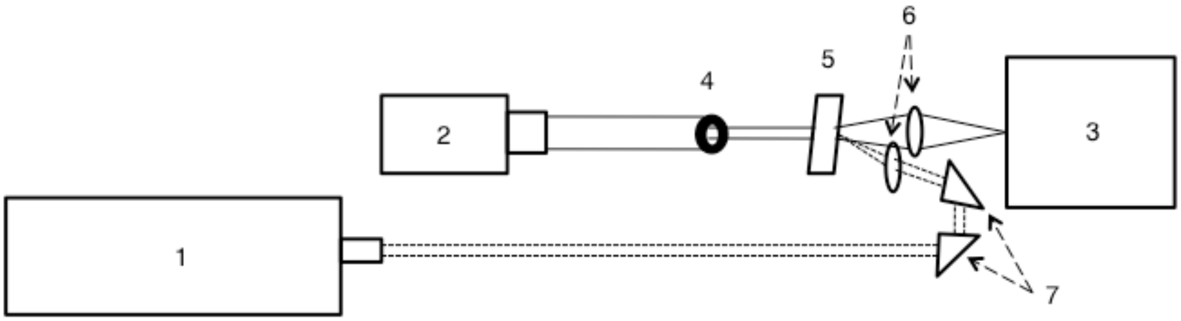

Figure 1.8 Schematic illustration of the set-up used to measure transient signals in thin polymer films. 1 – 193 nm laser, 2 – Xe Lamp, 3 – Monochromator and Photomultiplier Tube (PMT), 4 – Iris, 5 – Polymer sample coated on quartz microscope slide and mounted on traverser system (see text), 6 – Condenser lenses, 7 – Fused silica prisms.

The operation of the system in Figure 1.8 is nearly identical to that for traditional LFP and computer control of the acquisition has been explained elsewhere.[46] A few notes should be made about the set-up. First, we found it easier to use an iris (component 4 in Figure 1.8) rather than a lens due largely to geometry requirements and the fact that a lens with an appropriate focal length was not on-hand. The iris was placed in very close proximity to the sample to ensure that the smallest monitoring beam possible was used. In addition, the sample was a polymer film coated onto a quartz microscope slide. While glass slides could technically be used since the slide does not strictly *need* to transmit 193 nm light, they a) prohibit UV-Vis analysis of the sample before the experiment and b) have strong emission across the visible and UV range when hit with 193 nm light.

Most of the photochemistry explored in films is irreversible and thus following laser exposure, the starting materials are depleted in the exposed area. Thus the system was designed to expose a fresh area of the film with each laser pulse by using a traversing stepper motor mounted on a translational stage. Figure 1.9a shows a schematic diagram of the traverser set-up, including sample, and Figure 1.9b shows a picture of the entire set-up. The sample is always mounted with the film side facing the incident laser beam to minimize any emission that could result from exciting through the quartz. Care was taken that the energy of the laser beam is not high enough that it will ablate the polymer film during exposure. When the laser fires, it triggers the stepper motor to move the sample down a pre-defined number of steps[47] before the next laser shot. Once the sample has been moved to its maximum limit (when the laser is near the top edge of the sample), the sample is returned to its original vertical position and the traverser is manually moved horizontally along the translational stage. The sequence is repeated until the entire film has been exposed or sufficient data has been collected.

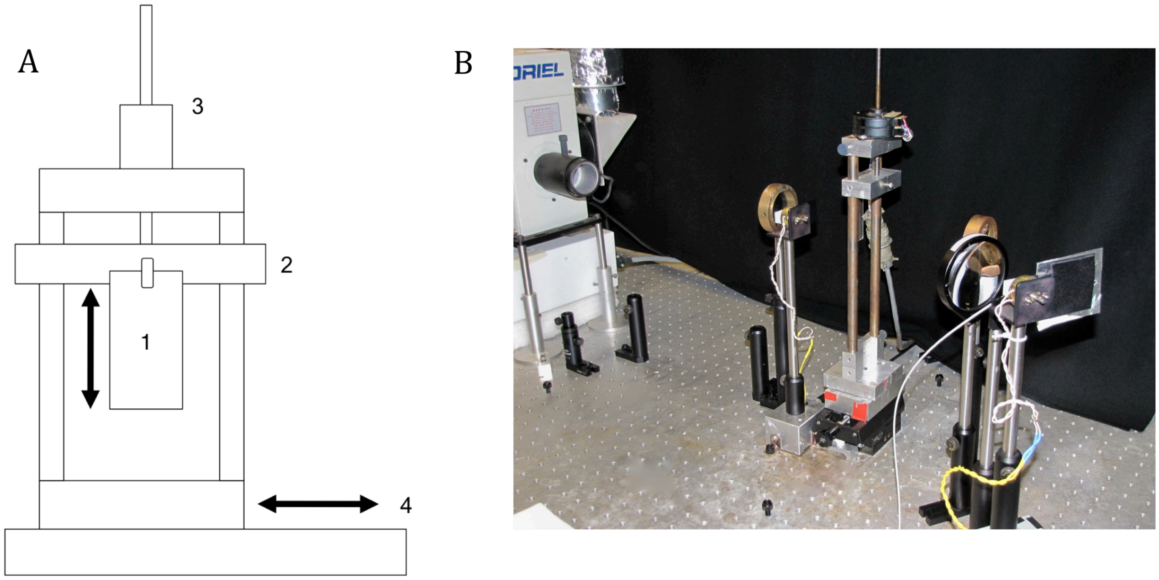

Figure 1.9 A) Schematic illustration of the traverser set-up used for thin-film LFP. 1 – Sample film on quartz microscope slide, 2 – Movable stage, with friction clip to attach sample slide, attached to stepper motor by vertical screw, 3 – Stepper motor, 4 – Horizontal translational stage; B) Picture of traverser set-up and some of the optics outlined in Figure 1.8.

1.6 Nature of Collaborative Work

As many of the projects described herein were collaborations with various other researchers, it is important to clarify the roles of the collaborators in the work presented. Unless otherwise specified, all experiments presented were designed and performed by myself.

In Chapter 2, Dr. Luca Maretti (post-doctoral fellow) synthesized the C2 disulfide and Dr. Vincent Maurel (post-doctoral fellow) provided technical assistance with EPR measurements. Chapter 3 presents a part of a larger collaborative project with Intel Corporation, Sigma-Aldrich, and Prof. Nick Turro's group at Columbia University; while some of the points used in the discussion section were taken from the work of these collaborators, all experiments and results presented, with the exception of those in Figure 3.1, were mine. All non-commercial compounds used were synthesized by collaborator Dr. Edward Jackson at Sigma-Aldrich. The projects in Chapters 4 and 5 were developed as part of the collaboration with Intel Corp. but were entirely performed in our labs. Si3PAG-2, TES-2, TES-3, and mPT-ONf were synthesized by Dr. Edward Jackson at Sigma-Aldrich; mPAG-2 was a generous gift from Prof. C. Grant Willson's group at University of Texas at Austin. In Chapter 6, initial experiments were performed by Dr. Luca Maretti (post-doctoral fellow) but experimental design was developed together. The majority of the experiments were performed by the two of us together, though all experiments performed in polymer films were designed and performed by myself.

1.7 Summary

Optical lithography has had a colossal impact on modern technology and even economics through its role in IC production. While it seems like it is simply a matter of time before next-generation lithographic technologies displace optical lithography in driving the semiconductor industry, it is still economically and logistically favourable to continue pushing the capabilities of DUV optical lithography. Double patterning lithography is one technique which holds promise in driving 193 nm lithography to the 22 nm technology node.[7] While the systems developed and explored in Chapters 3 and 4 of this thesis likely will never see industrial applications, they are important steps towards functional systems. The work on PAGs presented in Chapter 5 will remain relevant to the semiconductor industry as long as photoresists rely on acid-catalyzed amplification.

Device development and lithography is not only about pushing the resolution limit of ICs to the minimum but also about creating functional, high-density materials. Metallic nanoparticles will almost undoubtedly play a role in creating next-generation materials and thus the photochemical synthesis of nanoparticle-polymer composites, such as those described in Chapter 6 of this thesis, could potentially open the door to entirely new classes of functional materials. This photochemical method has all the advantages of optical lithography and thus holds real promise for future applications. The preliminary results and proposed future work in Chapter 7 outline some of the many potential ways in which this general method could be developed.

Chapter 2 presents some of the early non-lithographic work I did with nanoparticles that proved to be extremely helpful when moving on the future projects.

1.8 References

1. Wallraff, G. M.; Hinsberg, W. D., Lithographic Imaging Techniques For The Formation Of Nanoscopic Features. *Chem Rev* **1999,** *99* (7), 1801-1821.

2. Mack, C., *Fundamental Principles of Optical Lithography*. John Wiley & Sonds Ltd.: Mississauga, 2007.

3. Sanders, D. P., Advances in Patterning Materials for 193 nm Immersion Lithography. *Chem Rev* **2010,** *110* (1), 321-360.

4. Noyce, R., Microelectronics. *Scientific American* **1977,** *237*, 63-69.

5. Moore, G. E., Cramming More Components Onto Integrated Circuits. *Electronics* **1965,** *38* (8), 114-117.

6. Moore, G., Progress in Digital Integrated Electronics. *IEDM Technical Digest* **1975,** *21*, 11-13.

7. Association, S. I., The National Technology Roadmap for Semiconductors. San Jose, CA, 1994.

8. Zimmerman, P.; Byers, J.; Rice, B.; Ober, C.; Giannelis, E.; Rodriguez, R.; Wang, D.; O'connor, N.; Lei, X.; Turro, N.; Liberman, V.; Palmacci, S.; Rothschild, M.; Lafferty, N.; Smith, B., Development and Evaluation of 193 nm Immersion Generation-three Fluid Candidates. . *Proc SPIE* **2008,** (6923), 69230/A1-10.

9. The current generation of chips being produced are 35 nm while the next generation, as dictated by Moore's Law, will be 22 nm.

10. Levinson, H. J., *Principles of Lithography*. 2nd ed.; SPIE Press: Bellingham, 2005.

11. Lin, B. J., Successors of ArF Water-Immersion Lithography: EUV Lithography, Multi-E-Beam Maskless Lithography, or Nanoimprint? *J Micro-Nanolith Mem* **2008,** *7* (4), 040101.

12. Lin, B. J., New Prospect of Successors to ArF Water-Immersion Lithography. *J Micro-Nanolith Mem* **2010,** *9* (2), 020101.

13. Lin, B. J., The Ending Of Optical Lithography And The Prospects Of Its Successors. *Microelectron Eng* **2006,** *83* (4-9), 604-613.

14. Wua, B.; Kumar, A., Extreme Ultraviolet Lithography: A Review. *J Vac Sci Technol B* **2007,** *25* (6), 1743-1761.

15. Levinson, H. J., Extreme Ultraviolet Lithography's Path To Manufacturing. *J Micro-Nanolith Mem* **2009,** *8* (4), 041501.

16. Lyman, J., Optical Lithography Refuses To Die. *Electronics* **1985,** *58*, 36-38.

17. Defined as one square unit of minimum resolution.

18. Smayling, M.; Axelrad, V., 32nm and below Logic Patterning using Optimized Illumination and Double Patterning. *Proc SPIE* **2009,** *7274*, 72740K.

19. Tarutani, S.; Tsubaki, H.; Kanna, S., Development Of Materials And Processes For Double Patterning Toward 32 nm Node ArF Immersion Lithography. *J Photopolym Sci Tec* **2008,** *21* (5), 685-690.

20. Abdallah, D. J.; Alemy, E.; Chakrapani, S.; Padmanaban, M.; Dammel, R. R., A novel resist freeze process for double imaging. *J Photopolym Sci Tec* **2008,** *21* (5), 655-663.

21. Zimmerman, P. A., Extension Options for 193nm Immersion Lithography. *J Photopolym Sci Tec* **2009,** *22* (5), 625-634.

22. Bristol, R.; Shykind, D.; Kim, S.; Borodovsky, Y.; Schwartz, E.; Turner, C.; Masson, G.; Min, K.; Esswein, K.; Blackwell, J. M.; Suetin, N., Double-Exposure Materials for Pitch Division with 193nm Lithography: Requirements, Results. *Proc SPIE* **2009,** *7273*, 727307/1-12.

23. The holding device in the lithographic tool.

24. Moon, S.; Kim, J., Chemistry of Photolithographic Imaging Materials Based on the Chemical Amplification Concept. *J Photochem Photobio C* **2007,** *8*, 157-173.

25. Ito, H., Chemical Amplification Resists For Microlithography. *Adv Polym Sci* **2005,** *172*, 37-245.

26. Ito, H., Chemical Amplification Resists: Inception, Implementation In Device Manufacture, And New Developments. *J Polym Sci Pol Chem* **2003,** *41* (24), 3863-3870.

27. Ito, H.; Willson, C. G.; Frechet, J. M. J. Positive- And Negative-Working Resist Compositions With Acid Generating Photoinitiator And Polymer With Acid Labile Groups Pendant From Polymer Backbone. U.S. Patent #4,491,628, 1985.

28. Crivello, J. V., Design And Synthesis Of Photoacid Generating Systems. *J Photopolym Sci Tec* **2008,** *21* (4), 493-497.

29. Vekselman, A. M.; Zhang, C. H.; Darling, G. D., Functional Imaging With Chemically Amplified Resists And Organic Molecules. *Chem Mater* **1997,** *9* (9), 1942-1948.

30. Menard, E.; Meitl, M. A.; Sun, Y.; Park, J.; Shir, D. J.; Nam, Y.; Jeon, S.; Rogers, J. A., Micro- And Nanopatterning Techniques For Organic Electronic And Optoelectronic Systems. *Chem Rev* **2007,** *107* (4), 1117-1160.

31. Huo, F.; Zheng, Z.; Zheng, G.; Giam, L. R.; Zhang, H.; Mirkin, C. A., Polymer Pen Lithography. *Science* **2008,** *321* (5896), 1658-1660.

32. Cavallini, M.; Albonetti, C.; Biscarini, F., Nanopatterning Soluble Multifunctional Materials by Unconventional Wet Lithography. *Adv Mater* **2009,** *21* (10-11), 1043-1053.

33. Duan, X.; Zhao, Y.; Berenschot, E.; Tas, N. R.; Reinhoudt, D. N.; Huskens, J., Large-Area Nanoscale Patterning of Functional Materials by Nanomolding in Capillaries. *Adv Funct Mater* **2010,** *20* (15), 2519-2526.

34. Gates, B. D.; Xu, Q. B.; Stewart, M.; Ryan, D.; Willson, C. G.; Whitesides, G. M., New Approaches To Nanofabrication: Molding, Printing, And Other Techniques. *Chem Rev* **2005,** *105* (4), 1171-1196.

35. Balazs, A. C.; Emrick, T.; Russell, T. P., Nanoparticle Polymer Composites: Where Two Small Worlds Meet. *Science* **2006,** *314* (5802), 1107-1110.

36. Leong, T. G.; Zarafshar, A. M.; Gracias, D. H., Three-Dimensional Fabrication at Small Size Scales. *Small* **2010,** *6* (7), 792-806.

37. Maurel, V.; Laferriere, M.; Billone, P.; Godin, R.; Scaiano, J. C., Free Radical Sensor Based On Cdse Quantum Dots With Added 4-Amino-2,2,6,6-Tetramethylpiperidine Oxide Functionality. *J Phys Chem B* **2006,** *110* (33), 16353-16358.

38. Scaiano, J. C.; Laferriere, M.; Galian, R. E.; Maurel, V.; Billone, P., Non-Linear Effects In The Quenching Of Fluorescent Semiconductor Nanoparticles By Paramagnetic Species. *Phys Stat Sol A* **2006,** *203* (6), 1337-1343.

39. Bruchez Jr., M., Moronne, M., Gin, P., Weiss, S., Alivisatos, A.P., Semiconductor Nanocrystals as Fluorescent Biological Labels. *Science* **1998,** *281*, 2013-2016.

40. Heuff, R. F.; Swift, J. L.; Cramb, D. T., Fluorescence Correlation Spectroscopy Using Quantum Dots: Advances, Challenges And Opportunities. *Phys Chem Chem Phys* **2007,** *9*, 1870-1880.

41. Scaiano, J. C.; Laferriere, M.; Ivan, M. G.; Taylor, G. N., A Protocol for the Verification of Acid Generation in 157 nm Lithography. *Macromolecules* **2003,** *36*, 6692-6694.

42. See for example Scaiano, J. C., Solvent Effects in the Photochemistry of Xanthone. *J Am Chem Soc* **1980,** *102* (26), 7747-7753.

43. Scaiano, J. C.; Garcia, H., Intrazeolite Photochemistry: Toward Supramolecular Control Of Molecular Photochemistry. *Acc Chem Res* **1999,** *32* (9), 783-793.

44. Arnold, B. R.; Scaiano, J. C., Laser Ablation Of Doped Polymers - Transient Phenomena As The Ablation Threshold Is Approached. *Macromolecules* **1992,** *25* (5), 1582-1587.

45. I had a great deal of help from Michel Grenier with the technical aspects of building this system.

46. Scaiano, J. C., Laser Flash-Photolysis Studies of the Reactions of Some 1,4-Biradicals. *Acc Chem Res* **1982,** *15* (8), 252-258.

47. Controlled by a LabVIEW 8.5 software program, written by Michel Grenier, interfaced to the analog stepper motor control box.

2. Disulfide Binding to CdSe Quantum Dots

Table of Contents

Graphical Abstract

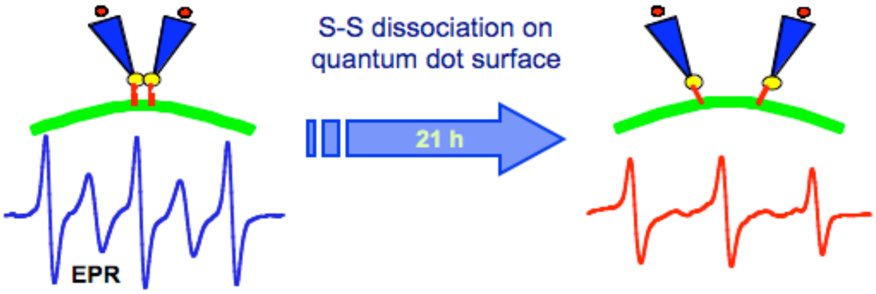

2.1 Introduction

As applications for semiconductor nanoparticle quantum dots (QDs) continue to expand in fields such as biology, imaging and sensors,[1-3] it is paramount to have a fundamental understanding of their chemical and electronic interactions with surrounding organic molecules. Thiol-stabilized QDs have received considerable attention because they suffer from fewer fluctuations in their properties, and in certain cases their photoluminescence quantum yields show an improvement over trioctylphosphine oxide (TOPO)-capped QDs.[4-8] Further, from the perspective of QDs biological applications the interaction of RS-H and RS-SR bonds with the surface is of the utmost importance.

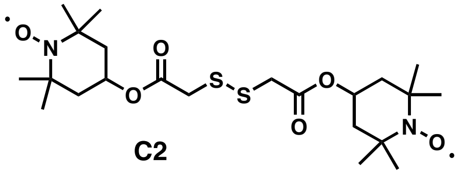

C2

Our study of the interactions between QDs and C2 was stimulated by earlier work on the interaction of binding and non-binding nitroxides with CdSe QDs, showing that quenching of QD fluorescence by 4-amino-2,2,6,6-tetramethylpiperidine oxide (4aT) is several orders of magnitude more efficient than quenching by TEMPO itself,[9-11] indicating that amine binding to the QD surface greatly facilitates fluorescence quenching. Several groups have reported on the binding of amines to CdSe QDs[4, 5, 12] but to our knowledge, this is the first in-depth investigation of disulfide interaction with a CdSe QD surface. We have found that binding of disulfide biradical C2 to the QD surface provides a unique perspective of the mechanism by which disulfide binding evolves on the surface. By probing the system with fluorescence and electron paramagnetic resonance (EPR) spectroscopies, we have realized that the disulfide linkage is a useful functionality for the attachment of species to the surface of CdSe QDs leading to robust, strong chemical bonds.[13]

2.2 Results

2.2.1 Fluorescence Quenching

We began this project by looking at the effect of the C2 biradical on the fluorescence of green CdSe QDs (λ_{em} = 515 nm) coated with a layer of trioctylphosphine oxide (TOPO)/trioctylphosphine (TOP) ligands.[14-16] We found that the addition of C2 to the QDs resulted in immediate fluorescence quenching but the fluorescence intensity continued to decrease over many hours (*vide infra*, Figure 2.4). When the decrease in fluorescence stabilized (usually about 18-24 hours), we found that the addition of varying amounts of C2 to green CdSe QDs resulted in dramatic fluorescence quenching at submillimolar concentrations. The Stern-Volmer (SV) analysis of the data (Equation 2.1) shows the effect of C2 concentration (expressed as [C2]×2 to account for the number of radical species) on the observed fluorescence. We were able to determine the initial slope for fluorescence quenching according to:

$$\frac{F_0}{F} = 1 + k_q \tau \times 2 \times [\mathrm{C2}] = 1 + K_{SV} \times 2 \times [\mathrm{C2}] \qquad (2.1)$$

where F_0 and F are the emission intensities in the absence and presence of quencher 24 hours after mixing (*vide infra*), and K_{SV} is the SV constant equal to the slope of the initial fit; k_q is the quenching rate constant and τ is the emission lifetime. The SV plot is non-linear over the full concentration range studied (Figure 2.1); analysis of the steep region yields K_{SV} = 28,500 M^{-1} that, assuming a lifetime of ca. 40 ns based on previous work in the group, corresponds to $k_q \sim 7\text{x}10^{11}$ $M^{-1}s^{-1}$, which would be significantly faster than the diffusion-limited rate constant in toluene. This indicates that fluorescence quenching is occurring through a static mechanism, as was observed in the case of 4aT.[10] As in the case for 4aT, the SV plot shows negative curvature indicating at least two different modes of quenching. We propose that the initial, steeper portion results from binding to unoccupied surface defect sites, such as singly- and doubly-coordinated Cd atoms,[17] while the less-efficient quenching (giving a characteristic slope of 3700 M^{-1}) reflects slow displacement of weakly-bound surface TOPO ligands (see Discussion 2.3).

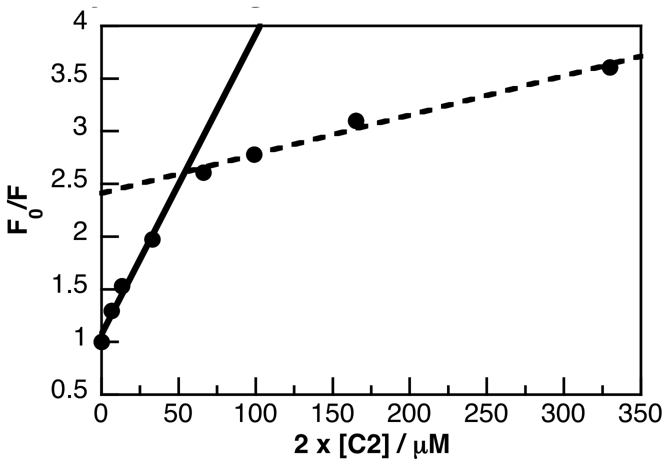

Figure 2.1 Stern Volmer analysis of the luminescence quenching of 5.0 μM QDs in toluene by addition of **C2**. The downward-curving behavior is indicative of multiple modes of quenching.

We wanted to confirm that the quenching phenomenon was in fact due to the presence of the nitroxide moieties of the ligand and not just the disulfide itself. For this reason, C2-cyclohexyl was synthesized. Figure 2.2 shows a comparison of the effect of equimolar C2 and C2-cyclohexyl on QDs after 24 hours. While significant quenching is observed in the case of C2 (*vide supra*), no quenching at all is observed for C2-cyclohexyl. This confirms that the quenching observed for C2 is due to the presence of the nitroxide moieties, as expected from previous studies.[10]

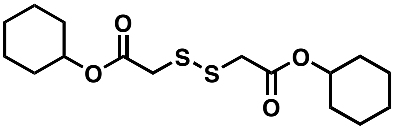

C2-cyclohexyl

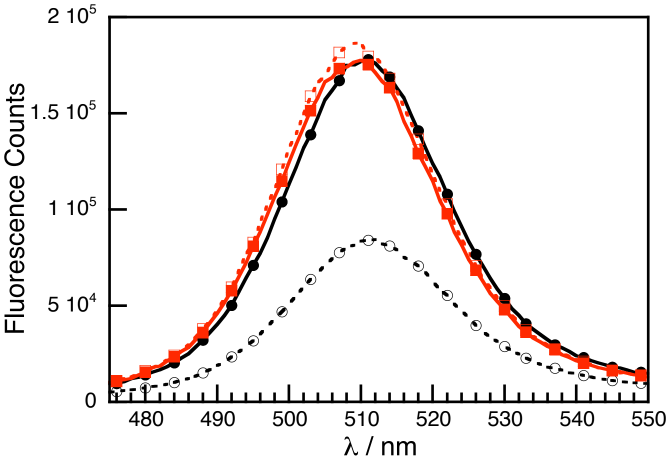

Figure 2.2 Addition of 11.8x excess of C2 (black traces) and C2-cyclohexyl (red traces) to 1.7μM QDs at t = 0 (solid lines) and t = 24 hr (dashed lines).

Addition of amines (cyclohexylamine, hexadecylamine) to QDs whose fluorescence had already been quenched by addition and incubation with C2 did not show any increase in emission intensity, in contrast to the case of 4aT,[10] suggesting stronger binding by C2-derived radicals than in the case of amines. In this system amines are unable to displace thiolate-bound quenchers.

2.2.2 EPR Spectroscopy

EPR spectroscopy provided a convenient tool for studying the dynamics of C2 binding to the QD surface. The C2 biradical gives the characteristic EPR spectrum of Figure 2.3A (initial), where the broad 5-line spectrum is indicative of the two radical centers in each molecule coupling to each other.[18] Upon addition of an excess of QDs (5.0 µM to 1.7 µM C2), the two visible biradical lines gradually disappear after ~24 h to the characteristic 3-line spectrum of simple nitroxides (t = 21hrs).[19] Figure 2.3B shows EPR spectra when QDs are added to a large excess of C2 (8.2 µM QD, 200 µM C2) and 41 h later. Extraction of excess C2 and any free nitroxide (after 41 h) by toluene evaporation followed by methanol washing and resuspension of the QDs leads to the spectrum of bound C2 products. The large excess of C2 is used to maximize the number of radicals bound to the nanoparticles. The disappearance of biradical lines reflects the fact that nitroxide moieties are no longer in proximity to one another once bound to the QD surface, indicative of S-S bond cleavage.

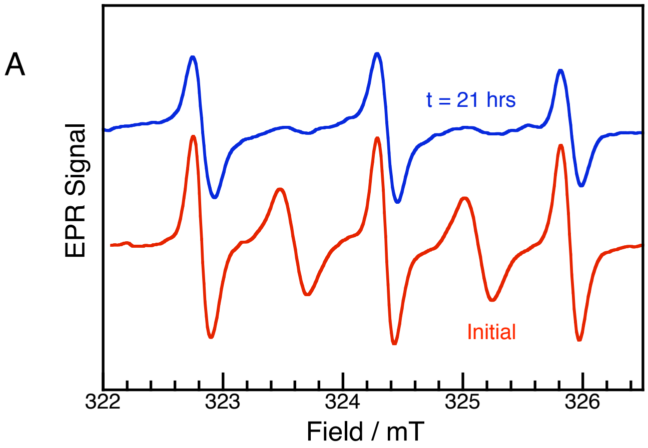

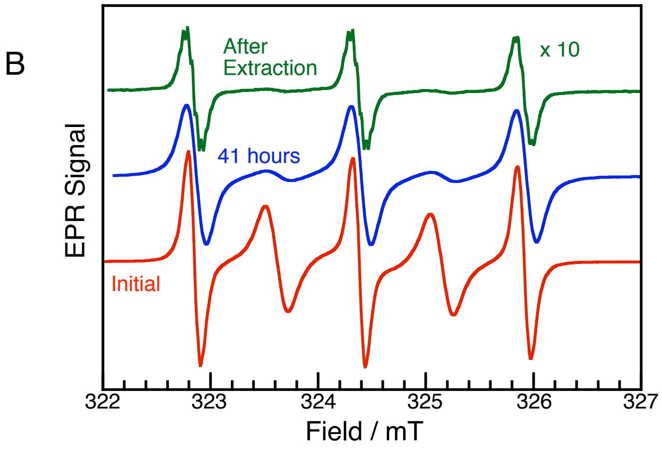

Figure 2.3 A) EPR spectra for 1.7 µM C2 in toluene after addition of 5.0 µM QDs recorded immediately after mixing (red) and 21 h later (blue); B) EPR spectra for 200 µM C2 in toluene after addition of 8.2 µM QDs recorded immediately after mixing (red), 41 h later (blue), and after extraction (green). The extraction process leads to significant sample loss (judged by UV absorbance) and a weaker (but better resolved) spectrum. All microwave parameters are kept constant (modulation width = 0.020mT; time constant = 0.1s; power = 0.2mW).

Previous EPR studies on 4aT and QDs showed that upon binding, hyperfine splitting due to adjacent methyl hydrogens was lost and isotropic behavior observed due to nitroxide rotation restriction by surrounding surface TOPO molecules.[10] In the EPR studies with C2, methyl hydrogen hyperfine splitting only becomes visible following binding to the CdSe surface and loss of the biradical signal. We believe that the alkane and ester spacers in C2 increase the length and flexibility from the binding site (S atom) to TEMPO unit such that the majority of the TEMPO moiety is at or near the edge of the TOPO monolayer, where some rotation is allowed; it is possible that thio-radical head-to-tail trapping (see Discussion 2.3) may also contribute to some rotationally free nitroxide radical and some loss in signal intensity (see 41 h spectrum in Figure 2.3).[20] As the biradical lines fade and monoradical signals appear, we also note some minor broadening of the nitroxide lines (see 41 h spectrum) suggestive of a change from free or loosely bound biradical to bound monoradical.

2.2.3 Binding Dynamics

As described above, both the QD fluorescence quenching and the C2 biradical disappearance took hours to reach a steady state. The time dependence of the two processes is shown in Figure 2.4. Disappearance of the EPR C2 biradical signal followed the same trend as fluorescence decrease, though recorded at different C2 concentrations due to instrumental limitations. This suggests that thiolate-bound nitroxides from disulfide dissociation are the dominant fluorescence quenchers at long times.

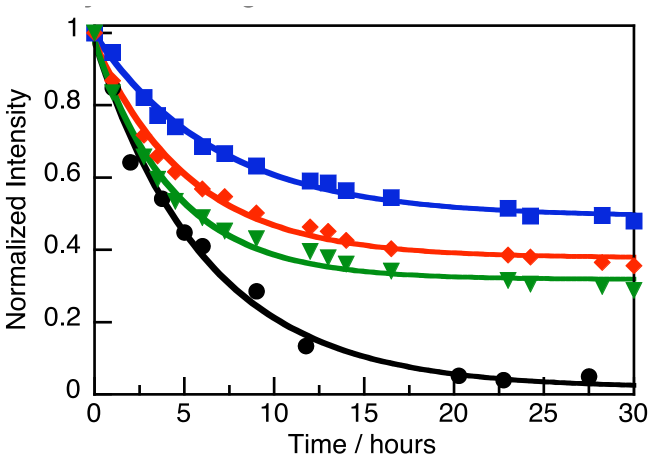

Figure 2.4 Normalized EPR (black) and fluorescence decays in toluene at room temperature under nitrogen. The EPR sample has 2.7 µM QDs and 1.7 µM C2, while the samples for fluorescence have 2.7 µM QDs and 17 (blue), 34 (red) and 85 (green) µM C2. The data were fitted with a monoexponential function for convenience, and the data in the plateau region were used for the SV plot of Figure 2.1. The lifetime derived from EPR is 6.3 h, and from fluorescence are 6.8, 5.3 and 4.4 h for increasing C2 concentrations.

2.3 Discussion

From Figures 2.1 and 2.2, it is clear that C2 efficiently quenches the luminescence of CdSe quantum dots; this was not surprising based on the previous results for nitroxide quenchers with QDs.[9-11] The non-linear, downward-curving SV quenching observed in the present case (Figure 2.1) is the same behaviour observed with 4aT. As described in 2.2.1, we believe that the steep region of the SV plot (Phase 1) reflects binding to surface defects or other non-passivated sites. We see that the K_{SV} value for C2 is much lower than that observed for 4aT,[10] consistent with an activated absorption process (*vide infra*) in the former case.

Interestingly, if we compare the slopes of the high-concentration regions (Phase 2) of the SV plots for 4aT quenching of similarly-sized CdSe[10] and core/shell CdSe/ZnS[21] QDs with that of C2 quenching in the present case, we see that K_{SV} is nearly identical for all three cases (Table 2.1). We hypothesize that this similarity arises due to the displacement of TOPO surface ligands. This implies that the rate-determining step in Phase 2 is the displacement of the TOPO ligands rather than the disulfide bond cleavage (*vide infra*). The negative curvature is not the result of saturation of surface sites as the studies with 4aT have shown that linear quenching continues into the millimolar regime. Scheme 2.1 shows a cartoon depicting the two phases of quenching described above.

Table 2.1 Comparison of the K_{SV} quenching constants in both the high and low concentration regimes for 4aT with CdSe QDs,[10] C2 with CdSe QDs, and 4aT with CdSe/ZnS QDs.[21]

QD	Quencher	K_{SV} / M^{-1} (low [ ])	K_{SV} / M^{-1} (high [ ])
CdSe	4aT	24.3×10^5	4340
CdSe	C2	2.8×10^5	3712
CdSe/ZnS	4aT	2.1×10^5	3640

Scheme 2.1 An illustration of the two proposed modes of binding that contribute to the non-linear nature of the SV plot in Figure 2.1. The steep region, denoted as Phase 1, is likely due to nitroxide binding at surface defects, such as 1- and 2-coordinate Cd ions,[17] and other binding sites where no TOPO (or TOP) is coordinated. The lower SV slope in the high concentration regime is attributed to binding where a TOPO surface ligand must be displaced (Phase 2).

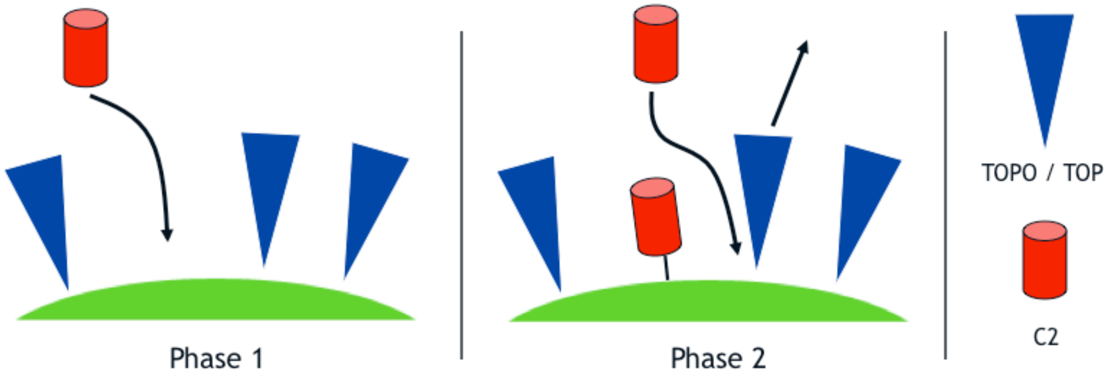

Scheme 2.1 does not address the nature of the binding of C2 to the QD surface. The time-dependent fluorescence quenching plots in Figure 2.4 are all recorded at concentrations that are in Phase 1 of the SV plot or close to the intersection point.

The long incubation times observed suggest an activated adsorption process (Figure 2.5); the exact magnitude of the barrier that leads to S-S dissociation is not known, but the lifetime of this process is about 7 hours (Figure 2.4). If we assume that once the disulfide physisorption equilibrium (A and B in Figure 2.5) is established its dissociation can be treated as a simple unimolecular reaction with a pre-exponential factor of 10^{13} s^{-1}, then the B-C barrier can be estimated as ca. 24 kcal/mol, compared with a typical aliphatic disulfide bond around 70 kcal/mol.[22] Clearly the CdSe surface greatly assists S-S cleavage. Deviations from first-order behaviour and lifetimes which vary with C2 concentration (Figure 2.4) are attributed to the contribution of the two different modes of binding as discussed earlier.

In the EPR studies with C2, minor hyperfine splitting from adjacent CH_2 groups in positions 3 and 5 of the tetramethylpiperidine oxide moieties only become visible following binding to the CdSe surface and loss of the biradical signal (Figure 2.3B). We believe that the alkane and ester spacers in C2 increase the length and flexibility from the binding site (S atom) to the TEMPO unit such that the majority of the TEMPO moiety is at or near the edge of the TOPO monolayer, where some rotation is allowed. It is possible that reaction of C2 with the CdSe surface could lead to one tethered nitroxide moiety binding through a thiolate bond and the release of a sulfur centered radical if vicinal surface sites are not available (Scheme 2.2). Such a radical would almost certainly be trapped by nitroxide moieties, either already bound to a QD or even as free biradical in solution, leading to longer tethers and some loss of nitroxide signal as observed.

Scheme 2.2 The potential "back-biting" reaction that could occur if both nitroxides of the disulfide did not bind directly to the QD upon bond cleavage.

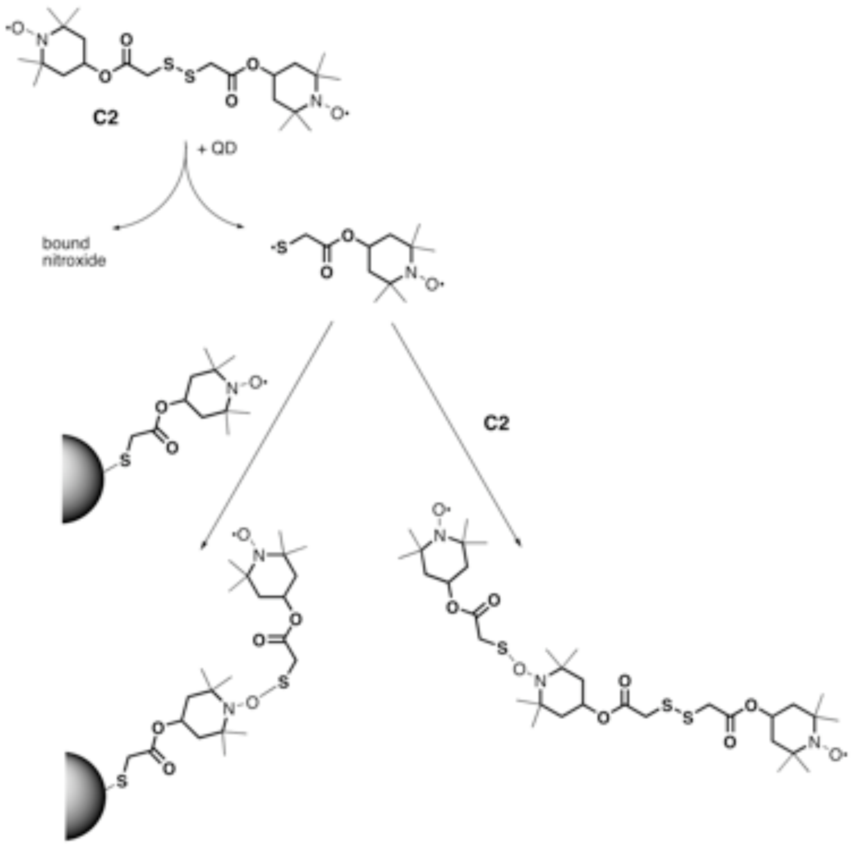

2.4 Summary

Herein we reported a study of the dynamics of interaction between a CdSe TOPO-coated QD surface and a disulfide using biradical signals combined with fluorescence as a reporter of binding events. The time-dependent nature of the binding event and subsequent fluorescence quenching is determined to be largely due to disulfide bond cleavage on the surface of the QD. We found that the CdSe surface seems to catalyze the cleavage of the disulfide linkage, lowering the activation energy for cleavage by almost 50 kcal/mol.

As mentioned in Chapter 1, this project does not lead directly into the work on lithography that will be discussed in subsequent chapters of this thesis. However, it certainly did play an important role in the development of my spectroscopic skill-set and provided me with the background knowledge on nanoparticles that would prove exceptionally useful for the work described in Chapters 6 and 7 of this thesis.

2.5 Experimental

2.5.1 General

All experiments were performed in toluene, unless otherwise stated, and QD solutions under study were deaerated with dry nitrogen prior to spectroscopic measurements. Fluorescence spectra were collected with a luminescence spectrometer from Photon Technology International (Birmingham, NJ). Fluorescence lifetime measurements were obtained using an Easylife LS (Photon Technology International) with excitation at 395 nm using a pulsed LED and emission monitored at 510 nm. EPR measurements were performed using a JEOL FA-100 X-Band EPR spectrometer (JEOL USA, Peabody, MA) equipped with a JEOL ES-UCX2 cylindrical cavity. Samples were deaerated with nitrogen prior to measurements and held in clear-fused silica tubes (5 mm diameter) purchased from Wilmad (Buena, NJ). GC/MS analysis was performed using a GC-MS from Agilent Technologies (6890 GC equipped with a 5973 MSD). HPLC/UV was performed on a Waters 2690 separation module equipped with a Waters 996 photodiode array detector using a reverse phase 4.6 x 250 mm analytical Zorbax SB-C18 column; the mobile phase used was 99:1 acetonitrile:water and the flow rate employed was 1 ml/min. ^{1}H NMR spectra were obtained on a Bruker Avance-400 spectrometer at 400 MHz using DMSO-d6 as a solvent with tetramethylsilane as an internal standard.

2.5.2 Synthesis of QDs

CdSe QDs protected by a layer of trioctylphosphine oxide (TOPO) ligands were synthesized from cadmium oxide and selenium using the procedure reported by Peng and Peng.[15] Typically, selenium (40 mg) was dissolved in trioctylphosphine (2.6 mL) under argon by heating at 60°C for 10 min. Cadmium oxide (51 mg), tetradecylphosphonic acid (223 mg), and TOPO (3.74 g) were heated to 305°C in a 25 mL three-necked round bottom flask equipped with a stir bar and flushed with Ar until the solution turned clear and colourless. This solution was cooled to 270°C, and the TOPSe solution was injected in the flask under strong stirring. Then the QDs grew at 250°C for 2 min to reach the desired size of 2.2-2.3 nm. The reaction was stopped by transferring the reaction mixture from the flask into ice-cold methanol using a gastight syringe. The produced QDs were centrifuged twice in methanol, resuspended in toluene, and stored under nitrogen in a glovebox in amber vials. The lifetime of the QDs was found to be 40ns; this was estimated from the obtained multi-exponential decay as the time it took for the initial fluorescence intensity to decay to 50%.

2.5.3 SV Quenching Experiments

20 mL of an N_2-degassed toluene solution of 5.0 µM QDs was prepared and split into eight optically-matched precision quartz cuvettes under N_2. Added to seven of the cuvettes were varying amounts of either a 9.4 mM or 0.94 mM C2 stock solution and toluene such that the total volume of C2 solution plus solvent added to each

cuvette was 50 µL (concentrations were 3.30×10^{-6} M, 6.6×10^{-6} M, 1.65×10^{-5} M, 3.30×10^{-5} M, 4.95×10^{-5} M, 8.25×10^{-5} M, and 1.65×10^{-4} M); to the eighth cuvette only 50µL toluene was added as a control sample. Each cuvette was sealed with a Teflon cap, which was wrapped in Teflon tape and parafilm to ensure no leakage over the course of the experiment. Fluorescence spectra were recorded for each sample over the course of ~20 h, until the intensity of the signals stabilized. The cuvettes were kept in a dry-box under an N_2 atmosphere in the dark between spectra.

2.5.4 Ligand Synthesis

C2 [bis(2,2,6,6-tetramethyl-1-piperidine oxide) dithiodiglycolate]: 70 mg dithiodiglycolic acid ($C_4H_6O_4S_2$, 0.38 mmol, 1 eq.), 174.4 mg DCC (0.85 mmol, 2.2 eq.), 10 mg DMAP (0.082 mmol, 0.22 eq), and 152 mg 4-hydroxy-TEMPO (0.88 mmol, 2.2 eq.) were dissolved in 50 ml of DCM and refluxed for 3 hours. Solvent was removed by rotary evaporation under vacuum. The crude product was purified by column chromatography using 19:1 hexane:ethyl acetate as the eluting solvent mixture. Obtained 60 mg C2 as an orange powder (0.11 mmol, 30%). HPLC/UV analysis of the sample showed only one major product in >96% yield. Product showed 5-line EPR spectrum characteristic of flexible nitroxide biradicals. MS (electrospray + NH_4): m/z = 492.4, 491.4 (M+), 158.3, 154.2.

C2-cyclohexyl, [bis(cyclohexyl) dithiodiglycolate]: Prepared via the method reported by Mulvaney *et al.*[23] GC/MS analysis following extraction showed product to be >90% pure; no further purification was performed. 1H NMR (DMSO-d6): 1H NMR (400 MHz, DMSO-d6): 4.715 ppm (2H, m, CH), 3.703 (4H, s, -S-CH2-C-), 1.779 (4H, m, ring), 1.679 (4H, m,ring), 1.374 (12H, m, ring); mp – 53-55°C.

2.6 References

1. Alivisatos, A. P., Semiconductor Clusters, Nanocrystals, And Quantum Dots. *Science* **1996,** *271* (5251), 933-937.

2. Bruchez Jr., M.; Moronne, M.; Gin, P.; Weiss, S.; Alivisatos, A. P., Semiconductor Nanocrystals as Fluorescent Biological Labels. *Science* **1998,** *281*, 2013-2016.

3. Heuff, R. F.; Swift, J. L.; Cramb, D. T., Fluorescence Correlation Spectroscopy Using Quantum Dots: Advances, Challenges And Opportunities. *Phys Chem Chem Phys* **2007,** *9*, 1870-1880.

4. Buollen, C.; Mulvaney, P., The Effects of Chemisorption on the Luminescence of CdSe Quantum Dots. *Langmuir* **2006,** *22*, 3007-3013.

5. Kalyuzhny, G.; Murray, R. W., Ligand Effects on Optical Properties of CdSe Nanocrystals. *J Phys Chem B* **2005,** *109*, 7012-7021.

6. Rogach, A. L.; Kornowski, A.; Gao, M.; Eychmuller, A.; Weller, H., Synthesis and Characterization of a Size Series of Extremely Small Thiol-Stabilized CdSe Nanocrystals. *J Phys Chem B* **1999,** *103* (16), 3065-3069.

7. Eychmüller, A.; Rogach, A. L., Chemistry And Photophysics Of Thio-Stabilized II-VI Semiconductor Nanocrystals. *Pure Appl Chem* **2000,** *72* (1-2), 179-188.

8. Dollefeld, H.; Hoppe, K.; Kolny, J.; Schilling, K.; Weller, H.; Eychmuller, A., Investigations On The Stability Of Thiol Stabilized Semiconductor Nanoparticles. *Phys Chem Chem Phys* **2002,** *4*, 4747-4753.

9. Laferriere, M.; Galian, R. E.; Maurel, V.; Scaiano, J. C., Non-Linear Effects In The Quenching Of Fluorescent Quantum Dolts By Nitroxyl Free Radicals. *Chem Comm* **2006,** (3), 257-259.

10. Maurel, V.; Laferriere, M.; Billone, P.; Godin, R.; Scaiano, J. C., Free Radical Sensor Based On CdSe Quantum Dots With Added 4-Amino-2,2,6,6-Tetramethylpiperidine Oxide Functionality. *J Phys Chem B* **2006,** *110* (33), 16353-16358.

11. Scaiano, J. C.; Laferriere, M.; Galian, R. E.; Maurel, V.; Billone, P., Non-Linear Effects In The Quenching Of Fluorescent Semiconductor Nanoparticles By Paramagnetic Species. *Phys Stat Sol A* **2006,** *203* (6), 1337-1343.

12. Wang, M.; Oh, J. K.; Dykstra, T. E.; Lou, X.; Scholes, G. D.; Winnik, M. A., Surface Modification of CdSe and CdSe/ZnS Semiconductor Nanocrystals with Poly(N,N-dimethylaminoethyl methacrylate). *Macromolecules* **2006,** *39* (10), 3664-3672.

13. Billone, P. S.; Maretti, L.; Maurel, V.; Scaiano, J. C., Dynamics of the Dissociation of a Disulfide Biradical on a CdSe Nanoparticle Surface. *J Am Chem Soc* **2007,** *129*, 14150-14151.

14. Peng, X.; Schlamp, M. C.; Kadavanich, A. V.; Alivisatos, A. P., Epitaxial Growth of Highly Luminescent CdSe/CdS Core/Shell Nanocrystals with Photostability and Electronic Accessibility. *J Am Chem Soc* **1997,** *119* (30), 7019-7029.

15. Peng, Z. A.; Peng, X., Formation of High-Quality CdTe, CdSe, and CdS Nanocrystals Using CdO as Precursor. *J Am Chem Soc* **2001,** *123*, 183-184.

16. Qu, L.; Peng, A.; Peng, X., Alternative Routes toward High Quality CdSe Nanocrystals. *Nano Lett* **2001,** *1* (6), 333-337.

17. Ratcliffe, C. L.; Yu, K.; Ripmeester, J. A.; Badruz Zaman, M.; Badarau, C.; Singh, S., Solid State NMR Studies Of Photoluminescent Cadmium Chalcogenide Nanoparticles. *Phys Chem Chem Phys* **2006,** *8*, 3510-3519.

18. Chechik, V.; Wellsted, H. J.; Korte, A.; Gilbert, B. C.; Caldararu, H.; Ionita, P.; Caragheorgheopol, A., Spin-labelled Au nanoparticles. *Faraday Disc* **2004,** *125*, 279-291.

19. Brustolon, M.; Maniero, A. L.; Ottaviani, M. F.; Romanelli, M.; Segre, U., Proton Hyperfine Tensors In Nitroxide Radicals. *J Phys Chem* **1990,** *94* (17), 6589-6594.

20. Skene, W. G.; Scaiano, J. C.; Listigovers, N. A.; Kazmaier, P. M.; Georges, M. K., Rate Constants for the Trapping of Various Carbon-Centered Radicals by Nitroxides: Unimolecular Initiators for Living Free Radical Polymerization. *Macromolecules* **2000,** *33* (14), 5065-5072.

21. Heafey, E.; Laferrière, M.; Scaiano, J. C., Comparative Study Of The Quenching Of Core And Core-Shell CdSe Quantum Dots By Binding And Non-Binding Nitroxides. *Photochem Photobiol Sci* **2007,** *6* (5), 580-584.

22. Franklin, J. L.; Lumpkin, H. E., Some C-S, H-S and S-S Bond Strengths by the Electron Impact Method. *J Am Chem Soc* **1952,** *74* (4), 1023-1026.

23. Mulvaney, J. F.; Murphy, J. G.; Evans, R. L., Esters of Dithiodiglygolic Acid. *J Am Chem Soc* **1948,** *1970*, 1069.

3. Non-reciprocal Acid Generating Schemes Based on Sensitization by Polyaromatic Systems

Table of Contents

Graphical Abstract

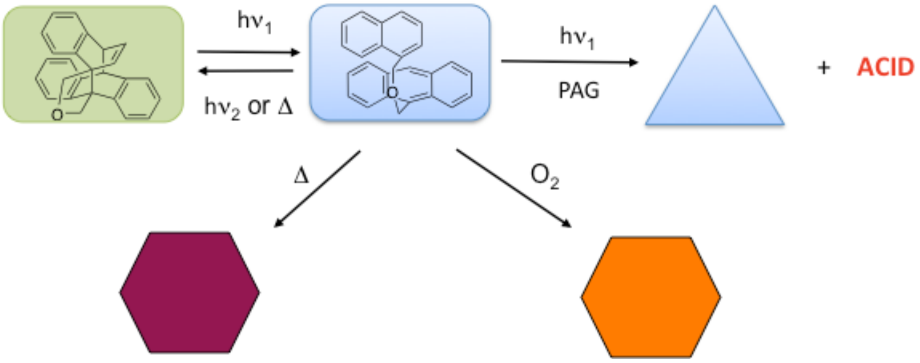

3.1 Introduction

3.1.1 Polyaromatic Sensitizers for Acid Generation in Lithography

The acid-generating ability of sulfonium and iodonium salts has been recognized and utilized in the field of cationic photopolymerization for many decades.[1-5] As briefly described in Chapter 1, CARs rely on photochemical acid production for image formation and these onium salts are prime candidates for this role.[6] However while these PAGs perform very well upon direct irradiation, their sensitivity at wavelengths > 300 nm is low,[4] and since early lithography was performed with long-wavelength Hg-based sources (see Section 1.1) many groups began to study sensitization reactions in order to extend the working wavelength range.[3-5, 7-9] While lithographic technology moved to progressively shorter wavelengths, and thus did not require long wavelength-absorbing sensitizers, there were still numerous advantages to sensitized onium salt-initiated polymerization reactions[10] and therefore it has remained an active field of research.

Particularly well-studied have been the sensitization reactions by anthracene, naphthalene, and their derivatives.[6, 11] While conclusive mechanistic results have not been reported for the sensitization reaction in polymer films, the reaction is believed to proceed by initial electron transfer from the excited sensitizer to the PAG (Scheme 3.1).[6, 7] Cases involving energy transfer sensitization have also been reported[12] but are generally not applicable to long-wavelength irradiation sources since the energy of the excited states are not high enough to effectively participate in energy transfer to the PAGs.[5]

Scheme 3.1 Sensitization of a triphenylsulfonium PAG ($Ph_3S^+X^-$) by naphthalene.

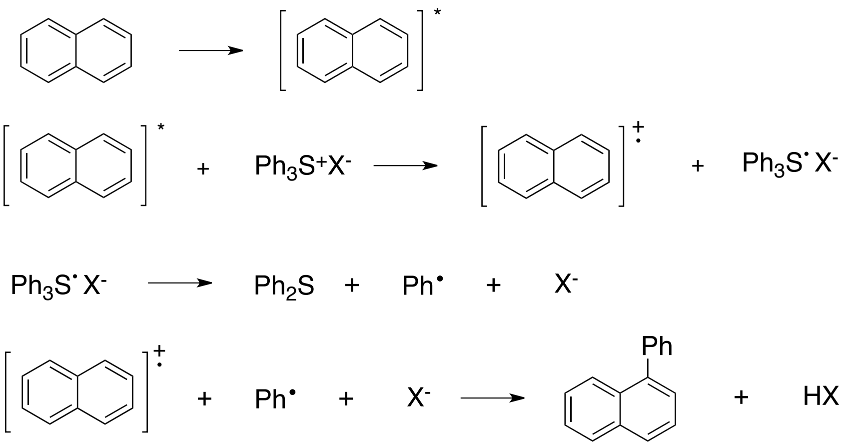

3.1.2 Non-reciprocal Sensitization Schemes Based on 4+4 Cycloaddition and Reversion of Polyaromatics

The primary requirement of a lithographic system to be used in DE lithography is that it have some form of reversibility built in such that if a second photon is not delivered to the previously excited component,[13] it returns to its original state. The first proposal for such a system is illustrated in Scheme 3.2 below. The system receives a photon at 193 nm ($h\nu_1$) to form a ground-state intermediate (blue pentagon), which can then absorb a second 193 nm photon to generate acid either directly (bottom pathway) or by sensitizing an acid generator (top pathway). Reversibility is provided by either a thermal or photochemical reaction (by a different wavelength, $h\nu_2$) from the ground-state intermediate to re-form the starting material.

Scheme 3.2 Non-reciprocal acid-generating system based on the photochemically or thermally reversible conversion between the starting material (green pentagon) and a ground-state intermediate (blue pentagon). Acid is formed when the intermediate receives a second photon of 193 nm irradiation and either sensitizes an acid generator (AG, top pathway) or decomposes intramolecularly (bottom pathway).

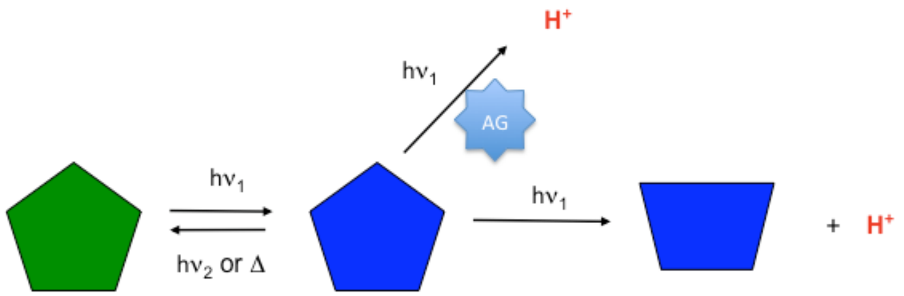

There are several other inherent requirements that must be considered for the system proposed in Scheme 3.2 to be effective. The starting material must be transparent at $h\nu_2$ (if applicable) so that irradiation at that wavelength does not result in the formation of the intermediate species. In addition, the conversion from starting material to intermediate must be efficient in order to compete with other potentially interfering photochemical processes.

Sensitizing systems based on 4+4 pericyclic cycloaddition/reversion reactions have recently been proposed for DE lithography applications.[14, 15] In particular, those based on anthracene and naphthalene satisfy the requirements outlined in the preceding paragraph; the cyclodimers have relatively strong absorption at 193 nm compared to the open forms and the open forms have absorption spectra extending to much longer wavelengths. The latter property is particularly important as the cycloaddition reaction can be affected by irradiation at these lower energies where the dimers do not absorb. Though much of the original interest in these types of systems was based on reversible Contrast Enhancement Layer (rCEL) technology,[16, 17] the ability of the “monomer” units to sensitize acid formation from PAGs was recognized as a more viable option.[14]

A huge volume of work has been dedicated to studying the cycloaddition/cycloreversion reactions of polyaromatic molecules.[18] By tethering the two aromatic systems together, a great deal of additional information regarding the dynamics of the reactions has been obtained and unique properties are observed.[19-23] The photochemistry of such reactions is quite fascinating, showing significant and sometimes unexpected differences with minor changes in the chromophores.[24-26] This chapter explores the utility of various polyaromatic systems, predominantly based on anthracene and naphthalene chromophores, for non-reciprocal acid generation in lithographic applications. The primary goal of the work carried out was to evaluate whether these systems which had been previously proposed[15] were indeed capable of achieving pitch division through DE lithography and to determine their reaction mechanisms. The results presented herein constitute a piece of a more complete study with contributions from Intel Corp., Columbia University, and the University of Texas at Austin.

3.2 Results

3.2.1 cNAME + TES-6

Our involvement in this project began when our collaborators at Intel Corp. described lithographic patterning results they had obtained with the cyclized naphthalene-anthracene tethered molecule cNAME and triethylsulfonium bis(trifluoromethylsulfonyl)imide (TES-6) (Chart 3.1). Using the CAR polymer DupXX (Chart 3.1), they were able to develop images which showed behaviour indicative of pitch division (Figure 3.1). They proposed that cNAME was opening to give NAME upon absorption of the first 193 nm photon, while a second 193 nm photon affected the sensitization reaction. Reversibility was provided by 365 nm lamp irradiation, which they proposed causes re-cyclization (Scheme 3.3). Our role was to evaluate the nature of the non-reciprocal response and try to understand how the system was functioning.

Chart 3.1. Structures of cNAME, TES-6, and the block units of the DupXX polymer.

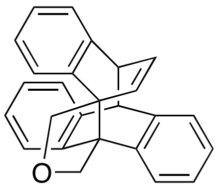

cNAME

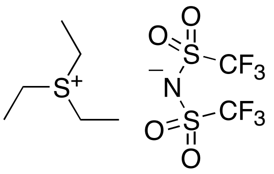

TES-6

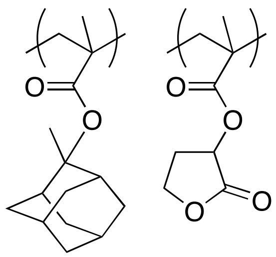

DupXX

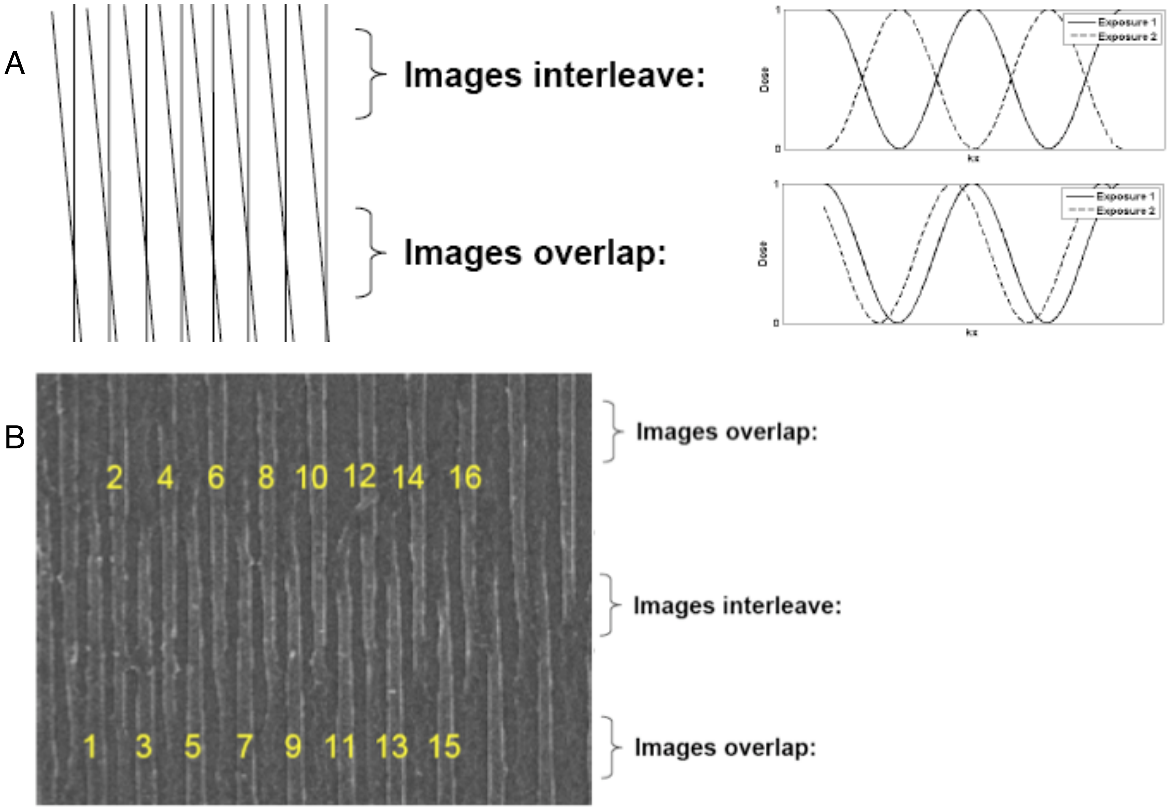

Figure 3.1 A) Diagram showing the exposure pattern and expected image results. A repeating linear pattern mask was used and the film exposed to a 193 nm dose (Exposure 1); the entire film was then exposed to 365 nm light without a mask, the film was rotated 5°, and irradiated with 193 nm through the mask again (Exposure 2). In the areas where the patterns overlap, no pitch division would be expected, while in the areas where the images are interleaved, pitch division is expected (see Chapter 1.1); B) SEM image of a DupXX film containing a 2:1 molar ratio of TES-6:cNAME exposed as described in A) and developed. The numbering is used to help the eye follow the path of each line. The pitch of the mask lines is 180 μm. Modified from Ref. 34.

Scheme 3.3 The initial proposal for acid generation and reversibility for the cNAME/TES-6 system. cNAME absorbs the initial 193 nm photon and opens to yield NAME, which either sensitizes acid formation from TES-6 upon absorbing a second 193 nm photon or re-cyclizes upon absorbing a 365 nm photon.

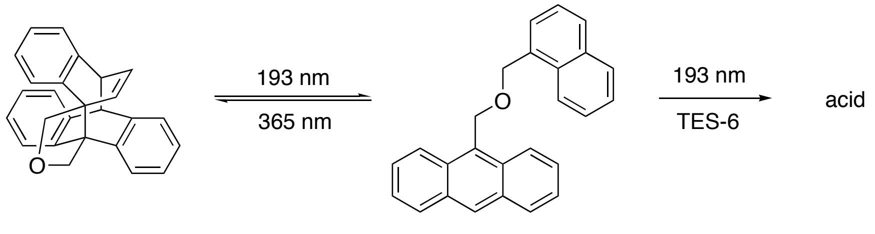

cNAME NAME

Using the C6-based monitoring technique (Section 1.4.1), we wanted to see whether we saw evidence for non-reciprocal behaviour when we exposed films to similar irradiation conditions as in Figure 3.1. As the method precludes the use of a mask, we developed three different exposure sequences to emulate the three different regions in Figure 3.1B; an illustration of the three different simulated exposure areas is given in Figure 3.2A. The exposure sequences are meant to emulate three points along the interleaved exposure pattern of Figure 3.1A, referred to as Point 1 (P1), Mid-Point (MP), and Point 2 (P2). P1 was emulated by a full 193 nm dose followed by a 365 nm dose, P2 was emulated by a 365 nm dose followed by a full 193 nm dose, and MP was emulated by a half of the 193 nm dose followed by a 365 nm dose and then the remainder of the 193 nm dose, such that all three films were exposed to equal total doses of 193 nm and 365 nm irradiation. If the exposed system were exhibiting non-reciprocal behaviour, we would expect to see less acid generated at the emulated MP than at either P1 or P2.

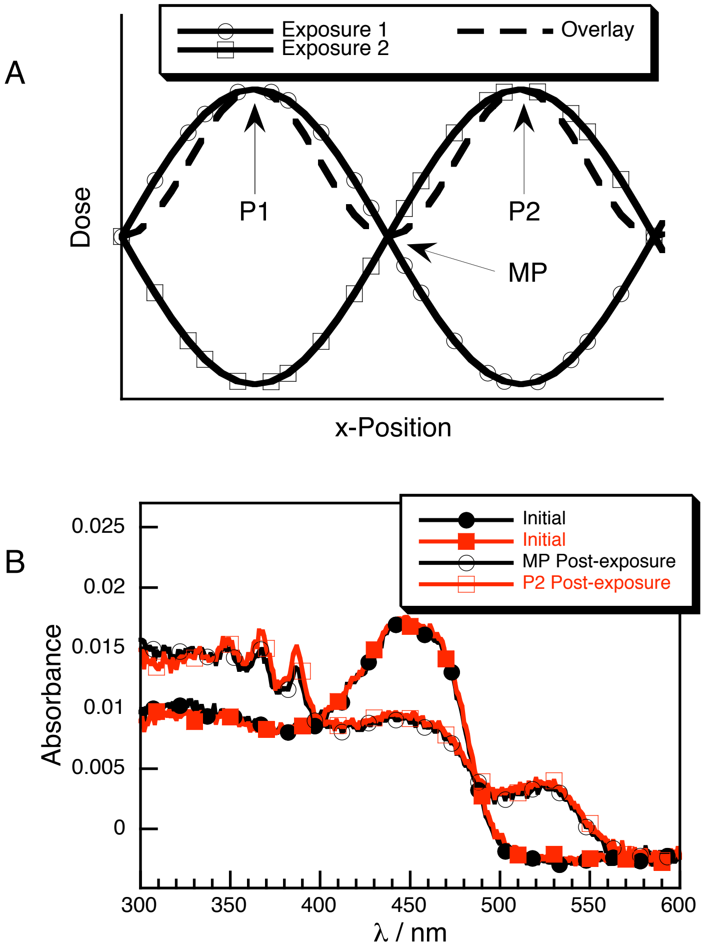

Figure 3.2 A) Diagram showing the expected image intensity (overlay) for two exposures shifted ½ pitch from one another. To test for this behaviour without using a mask, three different exposure sequences were utilized: P1 – full dose 193 nm, full dose 365 nm; MP – half dose 193 nm, full dose 365 nm, half dose 193 nm; P2 – full dose 365 nm, full dose 193 nm; B) Partial absorbance spectra of DupXX films containing 1% w/p C6 and 2:1 TES-6:cNAME (5% w/p of cNAME) before (closed symbols) and after (open symbols) exposure under air at MP (●, O) and P2 (■, □);

193 nm laser ~90 mJ/cm^2 total dose at 1.5 mJ/cm^2 per pulse, 365 nm lamp dose ~500 mJ/cm^2.

The experiments performed at Intel (Figure 3.1) were done under an air atmosphere so all of our experiments were also performed under air. For our trials on the cNAME/TES-6 system, only MP and P2 are reported due to unmatched absorbance in P1 (Figure 3.2B). It is clear that there is no difference in the amount of acid generated at MP and P2 in this case; experiments performed at lower total doses suggest that P1 and P2 produce the same amount of acid but are not shown due to lower signal-to-noise ratios. This suggests that under an environment containing O_2, the difference in the amount of acid generated from the cNAME/TES-6 system *as based on the C6 detection method* (vide infra) is negligible between MP and P2. All of the results above were found to be reproducible in PMMA films as well.

We wanted to check whether cNAME itself was sensitizing acid generation since that would be an interfering route to acid generation and would decrease the non-reciprocity of the system. Thus three films were prepared containing equal loadings of TES-6 (5% w/p); one containing 2:1 cNAME:TES-6, one containing 2:1 NAME:TES-6, and the third containing only the TES-6. The films were exposed to 193 nm irradiation only and the amount of acid generated was monitored. It was observed that the film containing cNAME produced significantly more acid than that containing NAME. However the film containing NAME produced very little additional acid when compared to the TES-6 film alone (Figure 3.3). Because the films were matched with respect to TES-6 concentration, the 193 nm absorbances for each film were different; preparing the films by matching 193 nm absorption through changing sensitizer concentrations was attempted but was not successful.

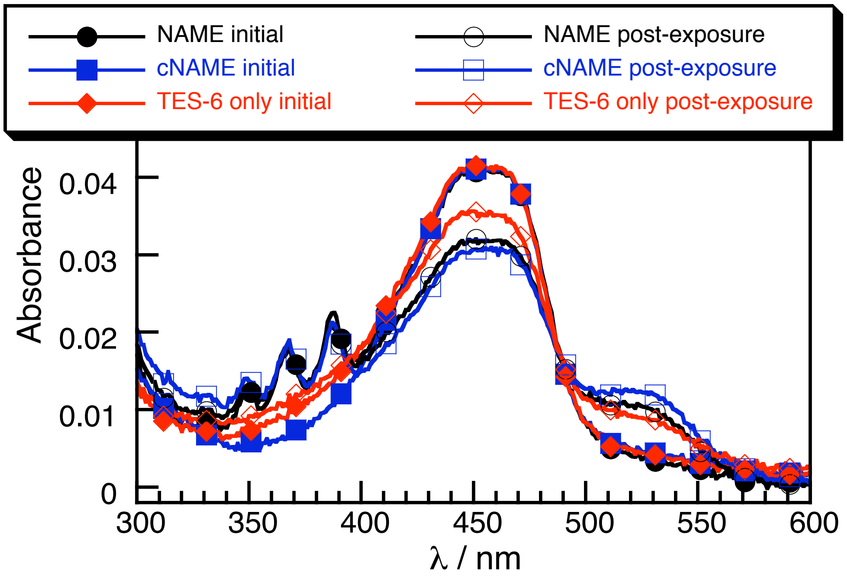

Figure 3.3 Partial absorption spectra of DupXX films containing 1% w/p C6 with 2:1 NAME:TES-6 (black), 2:1 cNAME:TES-6 (blue) and only TES-6 (red) before (closed symbols) and after (open symbols) 42 mJ/cm^2 193 nm irradiation at 1.4 mJ/cm^2 per pulse under air. The films each contain 5% w/p TES-6. The sharp absorption peaks in the 350 – 400 nm region belong to the anthracene units of NAME.

The observation that cNAME appears to be a more efficient sensitizer than NAME was surprising. Even accounting for the higher absorbance of cNAME at 193 nm than NAME, the difference in acid sensitization efficiency seemed to be a real effect. Interestingly, by looking at the anthracene $S_0 \rightarrow S_1$ absorption bands in Figure 3.3

(the sharp peaks in the 350-400 nm region) and comparing the intensities between the NAME and cNAME films, it appears that cNAME quantitatively opens within the dose delivered. This was corroborated by looking at the more intense anthracene absorption band at ~260 nm (data not shown). Thus we decided to monitor the sensitization reaction with cNAME as a function of the number of shots to see how acid formation correlates with the behaviour of the anthracene bands. The corresponding data is shown in Figure 3.4 below. From Figure 3.4B, it is clear that ring-opening, as determined by anthracene absorption, occurs efficiently up to 5 shots (at this laser energy) then decreases with subsequent shots. In contrast, acid generation as monitored by C6 protonation steadily increases with increasing shots.

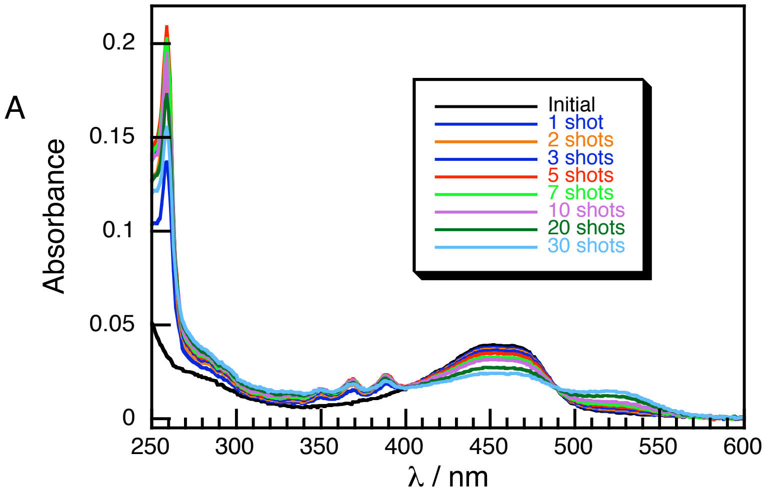

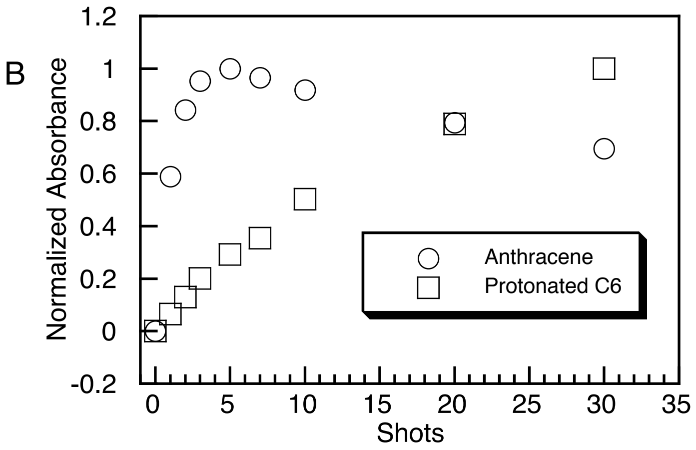

Figure 3.4 A) Absorption spectrum of a DupXX film containing 1% w/p C6 with 2:1 cNAME:TES-6 (5% w/p TES-6) upon irradiation with a 193 nm laser at 4.3 mJ/cm^2 under air; B) Normalized absorbance values for the most intense anthracene absorption (260 nm) and protonated C6 (525 nm) as a function of the number of 193 nm laser pulses.

Considering the above evidence and results from our collaborators, we felt that the promising results obtained by Intel in their lithographic tests (Figure 3.1B) were actually due to secondary species being formed upon reaction with O_2 (see Discussion 3.3). However we still believed that if the system was operating *via* the pathway outlined in Scheme 3.2, the acid generation should show a true energy dependence. Since the reversibility of the cNAME system requires long-wavelength irradiation, experiments were designed such that exposures were done as described in Chapter 1.4.1 but with simultaneous laser and lamp irradiation. Thus, unlike the previous experiments described above, films were exposed to both 193 nm laser irradiation and 365 nm lamp irradiation at the same time. As the 193 nm laser could only be operated at 1 Hz for these experiments, the duration of exposure for the different films was necessarily different, also meaning that the dose of 365 nm light received by each film was not equal. This is likely the origin of the non-linear acid generation observed in Figure 3.5 (*vide infra*). The degree of non-linear acid generation, as determined by the slope of Figure 3.5B, is actually quite significant when compared with true examples of non-reciprocal acid-generating photochemistry (see Chapter 4) and is operative at 193 nm pulse energies in the lithographically relevant range (< 1mJ/cm^2). However, as will be argued in the Discussion section, the mechanism by which this non-linear acid generation is delivered would likely not enable pitch division. Figure 3.6 shows that the non-linear component is indeed a result of the coincident 193 nm and 365 nm irradiation since the same amount of acid is generated for three different films when only exposed to laser irradiation at three different pulse energies (same total dose).

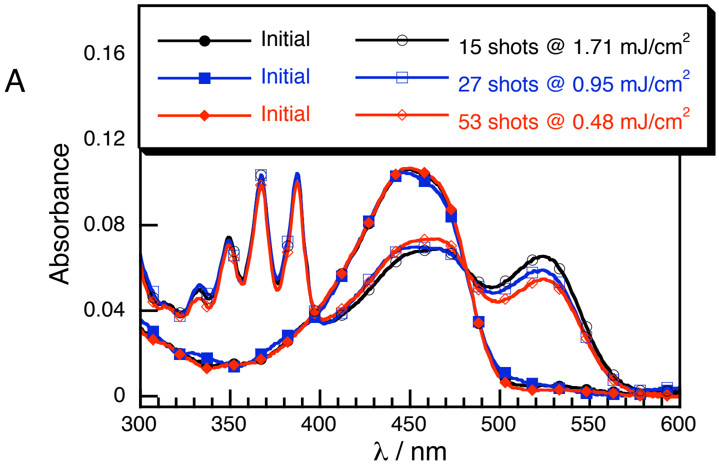

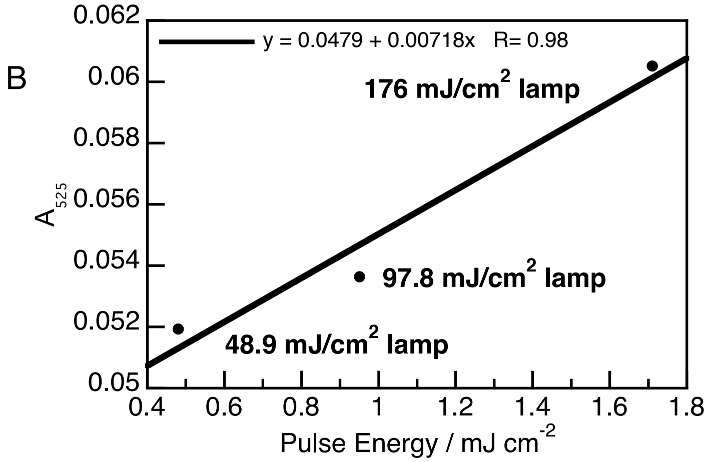

Figure 3.5 A) Partial absorption spectra of PMMA films containing 1% w/p C6 with 2:1 TES-6:cNAME (5% w/p C6) under air before and after 15 shots of 193 nm irradiation at 1.71 mJ/cm^2 per pulse and 15 s of 365 nm lamp irradiation (●, ○), 27 shots of 193 nm irradiation at 0.95 mJ/cm^2 per pulse and 30 s of 365 nm lamp irradiation (■, □), and 53 shots of 193 nm irradiation at 0.48 mJ/cm^2 per pulse and 54 s of 365 nm lamp irradiation (◆,◇). Lamp power was 3.26 mW/cm^2; B) Plot showing the acid yield, as measured by the absorbance signal of protonated C6 at 525 nm, as a function of the 193 nm pulse energy in a). The total incident lamp dose for each film is written beside each point and the data is fit with a linear function; the equation of the fit is also given.

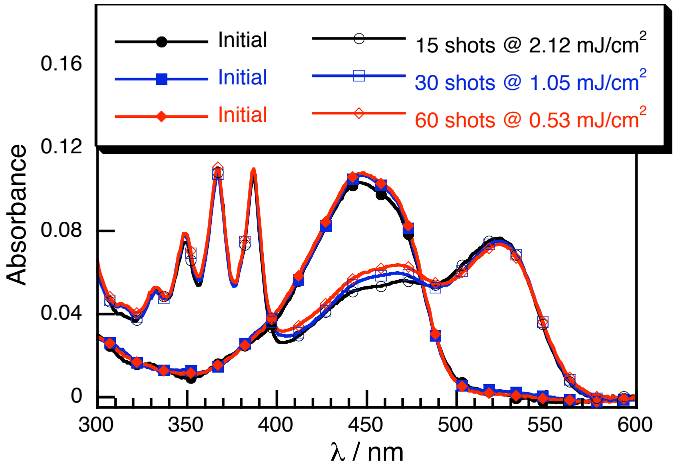

Figure 3.6. Partial absorption spectra of PMMA films containing 1% w/p C6 with 2:1 TES-6:cNAME (5% w/p cNAME) before and after 15 shots of 193 nm irradiation under air at 2.12 mJ/cm^2 per pulse (●, ○), 30 shots of 193 nm irradiation at 1.05 mJ/cm^2 per pulse (■, □), and 60 shots of 193 nm irradiation at 0.53 mJ/cm^2 per pulse (◆,◇).

3.2.2 Anth-PAG, cDAME-PAG, and cNAME-PAG

Referring back to Scheme 3.2, we recognized that an intramolecular acid-generating system (bottom pathway) should be more efficient than one which relies on intermolecular sensitization (top pathway) such as the cNAME/TES-6 system described above. Thus we proposed that tethering a sulfonium PAG to one of the polyaromatic rings in a tethered compound like cNAME would make the system more efficient.

Chart 3.2. Chemical structures of Anth-PAG, cDAME-PAG, and cNAME-PAG

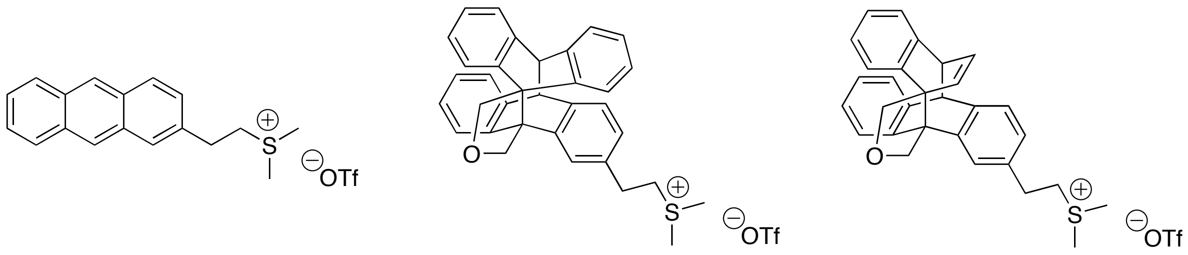

Anth-PAG cDAME-PAG cNAME-PAG

For this purpose, the most logical next step was to investigate the tethered compounds cDAME-PAG and cNAME-PAG. We began by studying cDAME-PAG upon direct 193 nm irradiation. Figure 3.7 shows the results of two separate experiments performed on cDAME-PAG films and it is clear that laser irradiation does not cause any significant acid generation, even at high doses (Figure 3.7B). Like in the cNAME case above (non-tethered), there seems to be a limit of ring-opening in both experiments. In the lower energy experiment (Figure 3.7A) the maximum anthracene level is reached after 10 shots and stays at the same level with an additional 10 shots (20 shots total). Upon 365 nm irradiation, the anthracene peaks decrease consistent with ring closing but with a subsequent 10 shots of 193 nm irradiation, the anthracene peaks reappear. This indicates that the system is reversibly opening and closing but the lower threshold upon further laser irradiation would suggest that there was some decomposition of anthracene moieties upon the UVA irradiation. This was consistent with previous results in the group that had been obtained for the parent molecule DAME.[27] In the higher energy experiment (Figure 3.7B), the anthracene peaks decrease from 5 to 10 shots, indicating decomposition with 193 nm light. UVA irradiation caused further disappearance of the anthracene signals. While there is a small amount of acid generated, it appears that the extent of C6 disappearance does not correspond to the amount of acid generated. Also surprising is the observation that the protonated C6 signal decreases upon UVA irradiation, potentially indicating that UVA irradiation affects the formation of a basic species which competes with C6 for the available protons.

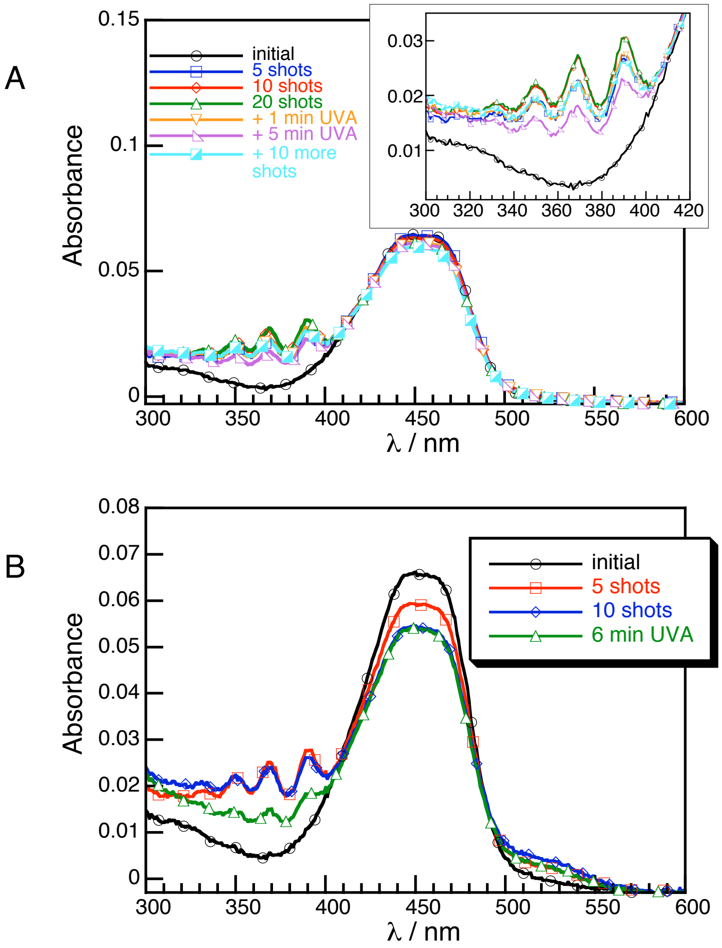

Figure 3.7 A) Partial absorbance spectra of a PMMA film containing 2.5% w/p cDAME-PAG and 1% w/p C6 before and after irradiation under air with a 193 nm laser (2.1 mJ/cm^2 per pulse) and a 365 nm lamp (4.2 mW/cm^2); (inset) An expansion

of the anthracene peaks in the 300-400 nm region of the spectrum; B) Partial absorbance spectra of a PMMA film containing 2.5% w/p cDAME-PAG and 1% w/p C6 before and after irradiation with a 193 nm laser (19.5 mJ/cm^2 per pulse) and a 365 nm lamp (4.2 mW/cm^2).

Since we were unable to generate significant amounts of acid with cDAME-PAG, we chose to move our attention to cNAME-PAG. We expected it to behave very similarly to the cNAME/TES-6 system, so we began by looking at acid generation under the emulated P1, MP, and P2 irradiation conditions. Figure 3.8 shows the results upon irradiating cNAME-PAG films and it appears that P1 generates slightly more acid than MP or P2. For cNAME/TES-6, exposure under air resulted in equal acid yields at P1, MP, and P2. However while cNAME-PAG seemed to show the desired non-reciprocal behaviour according to our detection method, it did not perform well in patterning experiments (done by Intel) and further studies were not performed.

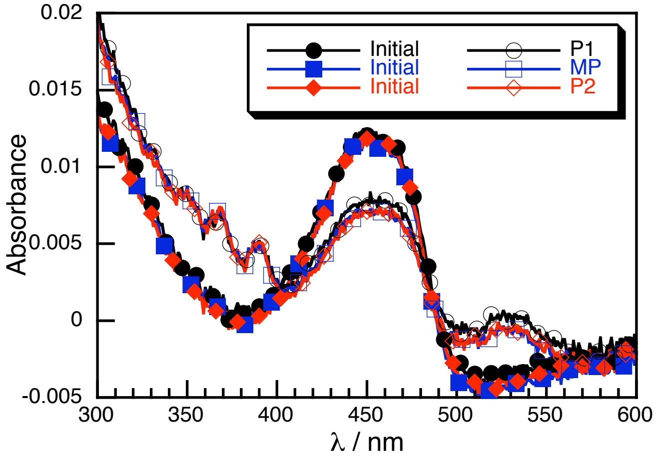

Figure 3.8 Partial absorbance spectra of DupXX films containing 5% w/p cNAME-PAG and 1% w/p C6 before (closed symbols) and after (open symbols) exposure under air at P1 (●, O), MP (■, □) and P2 (◆,◇); 193 nm laser ~50 mJ/cm^2 total dose at 0.7 mJ/cm^2 per pulse, 365 nm lamp dose ~500 mJ/cm^2.

Since the ring-opening/closing scheme did not seem like the ideal candidate for non-reciprocal acid generation, we proposed the mechanism outlined in Scheme 3.4 based on electron transfer. The mechanism is inherently non-linear since it returns to its initial state by back electron transfer if it does not receive a second photon. We decided it would be easiest to test the feasibility of a system such as that in Scheme 3.4 if we had at least two of the three components tethered. Anth-PAG satisfied this latter criteria; it had the potential of acting as the acceptor and PAG tethered together.

Scheme 3.4 Proposed non-reciprocal acid generating scheme based on a triad composed of an electron donor (D), acceptor (A), and PAG. The first photon excites either the acceptor or donor which subsequently undergoes charge separation by electron transfer. A second photon causes electron transfer from the anionic acceptor to the PAG and generates acid. If the second photon is not received, back electron transfer returns the system to the ground-state.

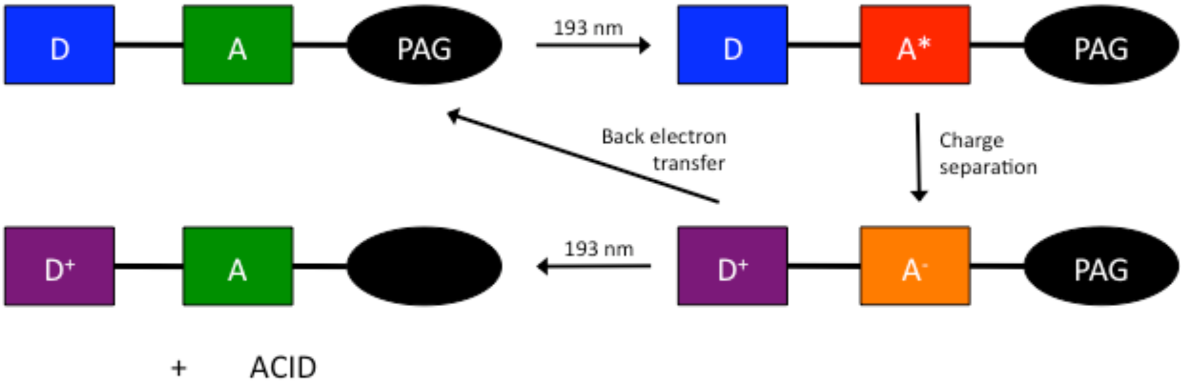

We chose to use *para*-dimethoxybenzene (DMB) as the electron donor with Anth-PAG since it has been shown to efficiently photoionize.[28-30] Figure 3.9 shows the results of an energy dependence experiment on films containing 1.6% w/p of Anth-PAG and a 10:1 molar ration of DMB:Anth-PAG. As expected based on the mechanism of Scheme 3.4, we saw pronounced non-linearity. Unlike Figure 3.5B, no 365 nm light was necessary to affect the non-linear behaviour and we were quite excited about these results.

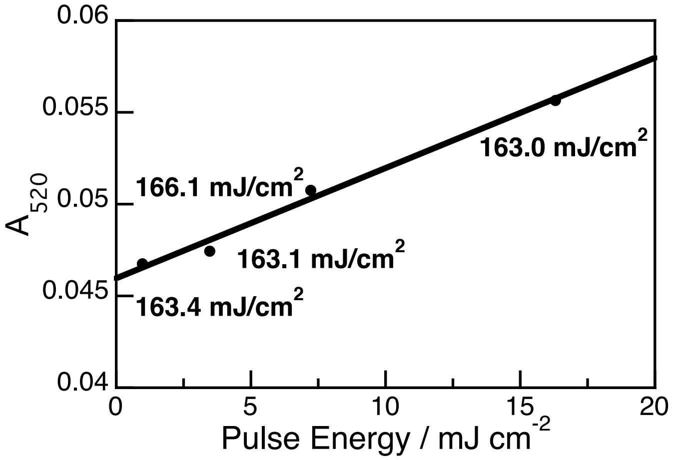

Figure 3.9 Plot of acid yield following 193 nm irradiation, as determined by protonation of C6, as a function of the pulse energy used for exposure under air of PMMA films containing 1.6% w/p Anth-PAG, 5% w/p DMB (~10:1 molar ratio DMB:Anth-PAG), and 0.5% w/p C6. The total doses are given beside the corresponding points.

However we also performed an energy dependence series on films containing only Anth-PAG. Surprisingly, the series also showed significant energy dependence, indicating a non-linear acid-generating process (Figure 3.10B). From the full absorption spectrum in Figure 3.10A, it is evident that while there is decomposition of anthracene upon irradiation, there is no significant difference in the extent of decomposition for the different pulse energies. Since the double electron-transfer mechanism proposed in Scheme 3.4 could presumably not be occurring within Anth-PAG itself, we were confused by the results. We attempted to expose films and monitor the products by NMR but were unsuccessful at detecting any new products in any of the samples.

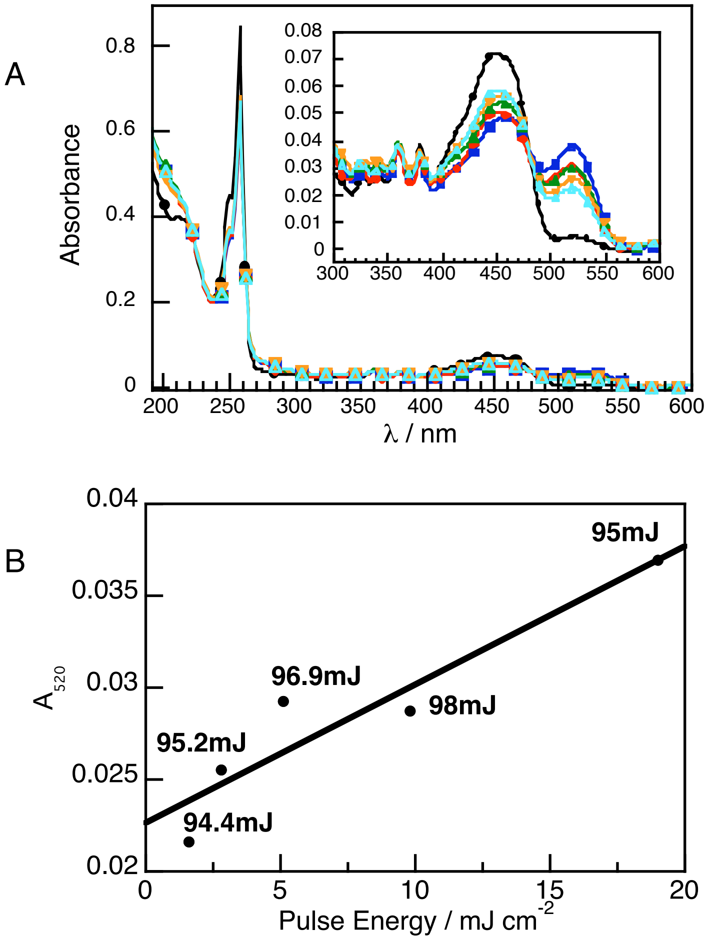

Figure 3.10 A) Absorbance spectra of PMMA films containing 1.6% Anth-PAG and 0.5% C6 exposed under air to 5 shots @ 19 mJ/cm^2 (■), 10 shots @ 9.8 mJ/cm^2 (◆), 19 shots @ 5.1 mJ/cm^2 (▲), 34 shots @ 2.8 mJ/cm^2 (▼), 59 shots @ 1.6 mJ/cm^2 (△); the trace corresponding to the filled circles (●) is a representative initial spectrum before any irradiation; (inset) an expansion of the C6 region of the absorption spectrum; B) Plot of acid yield, as determined by protonation of C6, as a function of the pulse energy used for exposure. The total doses are given beside the corresponding points.

While the total dose was higher in Figure 3.9, the slope of the energy dependence plot is about the same, indicating that the non-linear component of acid generation that is observed probably has the same origin as that in Figure 3.10. The increased y-intercept in Figure 3.10 with respect to Figure 3.9, indicative of a greater one-photon contribution to acid generation, is likely partly due to direct sensitization of the PAG moiety in Anth-PAG by DMB. If we define the efficiency of the two-photon acid generation as the slope of the energy dependence graphs divided by the y-intercepts, we realize that the system is more efficient in the absence of DMB.

We decided to check whether anthracene itself showed non-linear acid generation by sensitizing trialkyl sulfonium PAG. The PAG we used for this trial is shown as an inset in Figure 3.11 and will be referred to as mPAG-2. Figure 3.11 shows the absorption spectra of two films containing anthracene and mPAG-2 exposed to 193 nm irradiation. Unlike Anth-PAG in Figure 3.10, there is no energy dependence in this non-tethered system. In addition, though the yields themselves are not quantitatively comparable due to concentration differences, it is evident that despite approximately equal anthracene loadings there is significantly less acid generated in Figure 3.11, reflecting the increased efficiency of acid generation when the two components are tethered. While difficult to see in Figure 3.11, the anthracene peaks also decrease upon exposure but the extent of decomposition is the same between the two samples. We tried many product studies and thin-film LFP measurements on the Anth-PAG system in an attempt to understand the nature of its non-linear acid generation but we did not find anything conclusive.

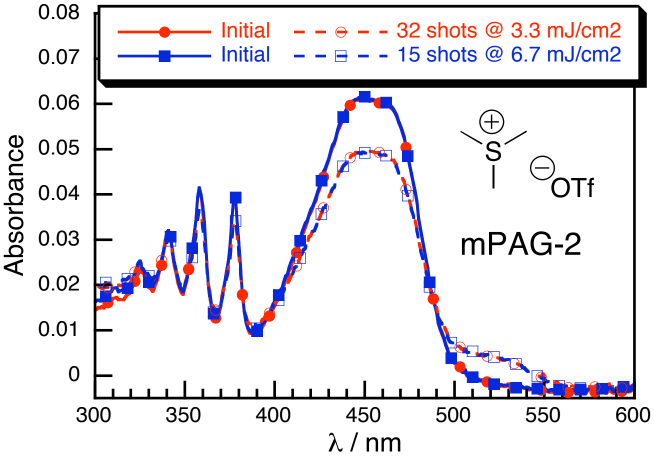

Figure 3.11 Partial absorbance spectra of PMMA films containing 2:1 anthracene:mPAG-2 (2% w/p mPAG-2) and 1% w/p C6 before and after 193 nm laser irradiation under air of 32 shots at 3.3 mJ/cm^2 (●, ○) and 15 shots at 6.7 mJ/cm^2 (■, □). The structure of mPAG-2 is shown in the inset.

3.3 Discussion

The cNAME/TES-6 system that was investigated showed a great deal of initial promise based on the results of our collaborators at Intel on lithographic imaging (Figure 3.1B). However, based on our results presented herein, the performance they observed seems to be at odds with the photochemistry we found. For instance, their lithographic performance was performed under air and showed pitch division behaviour while our experiments under air showed no noticeable differences in acid yield at P1, MP, and P2. However there is a great wealth of information regarding the photochemical reaction of anthracene and oxygen to yield anthracene endoperoxide.[20, 21, 31, 32] Thus if the photolysis is done under air, we expect that the first 193 nm photon would open cNAME while an additional photon (of either 193 nm or 365 nm) could induce endoperoxide formation. While this reaction is not accounted for in Scheme 3.2, it does not preclude the non-reciprocal effect we expected. The requirement in Scheme 3.2 for non-reciprocal photochemistry is that after receiving the first 193 nm photon, the intermediate either sensitizes acid formation upon absorption of a second photon or is deactivated. While the only pathway shown in Scheme 3.2 for deactivation is recyclization, a process that destroys the intermediate irreversibly, such as endoperoxide formation, would yield the same effect.

While our exposure set-up made it impossible in most cases to expose full films and obtain NMR data on the products formed, our collaborators at Intel had set-ups much better suited to these procedures. As a result, they were able to do detailed analysis of the photochemical products in the cNAME/TES-6 system. In addition to the sensitization products expected based on Scheme 3.1, they also observed NAME-endoperoxide (shown in Scheme 3.5) and various other oxygen-containing products from NAME-endoperoxide photolysis.[33] Our results, particularly in Figures 3.3 and 3.4, also clearly indicate that sensitized acid generation was occurring from both cNAME and NAME. With all of the above information in hand, we suggested the reaction pathways shown in Scheme 3.5[34] that are consistent with our observations.

Scheme 3.5 Photochemical reaction pathways of the cNAME/TES-6 system.

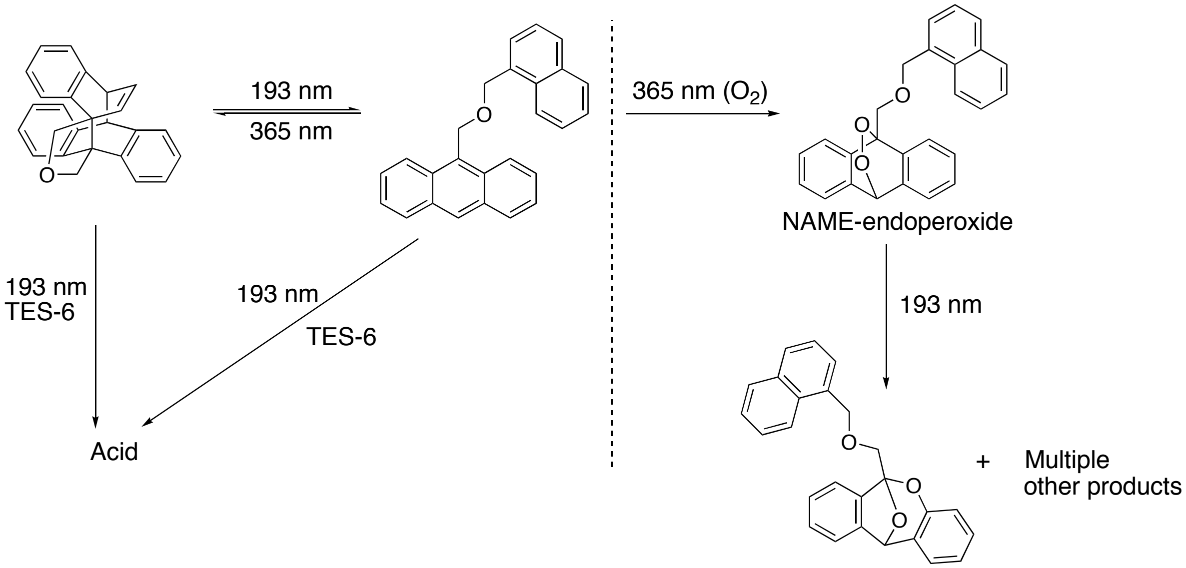

Given the above reaction scheme under air (to the right of the dashed line in Scheme 3.5) and the fact that endoperoxide formation, along with further photolysis products, should still result in non-reciprocal behaviour, the question remained as to why our experiments did not show the response expected. The most reasonable explanation is that our C6 detection method, while extremely well-suited to fast screening of photoacid generation in polymer films,[35-37] is masking the behaviour observed in pure patterning experiments. Our collaborators have proposed that the photolysis products of NAME-endoperoxide are strong enough bases to compete with the basic sites on the adamantyl esters of DupXX.[34, 38] Thus the pitch division in their experiments (Figure 3.1B) is attributed to the fact that at the MP, these basic photoproducts are formed and act as traps for any photogenerated acid, effectively decreasing the amount of available acid for deprotection of the polymer at MP. In our experiments, the C6 dye ($pK_b \sim 9$) is a much stronger base than the expected photoproducts of NAME-endoperoxide, which are likely ethers ($pK_b \sim 18$) or ketones ($pK_b \sim 21$). Thus any mediatory effects of NAME-endoperoxide photolysis products on the amount of free acid at our emulated MP would be hidden by the C6 itself.

While the energy dependence experiments on cNAME/TES-6 also seemed to show non-reciprocal acid generation (Figure 3.5), these experiments were performed under air. Since the power of the lamp irradiation was the same for each film but the energy of the 193 nm laser pulses was different, we propose that in the lower energy exposures there was more of the destructive NAME-endoperoxide photochemistry occurring. This would result in less NAME (or cNAME) available for sensitization of TES-6 and subsequent acid generation. This is supported by the results in Figure 3.6, which show that without lamp irradiation, there is no 193 nm energy dependence.

The yield of acid upon exposure of cDAME-PAG with 193 nm was minimal even at very high energies and doses (see Figure 3.7) while the appearance of anthracene absorption bands was reversible with UVA irradiation. This is consistent with a photochemical reaction scheme where recyclization from DAME-PAG to cDAME-PAG is favoured over sensitization of the sulfonium acid generator upon absorption of a second 193 nm photon (Scheme 3.6).

Scheme 3.6 cDAME-PAG photoreaction upon 193 nm irradiation showing that only recyclization occurs after ring-opening.

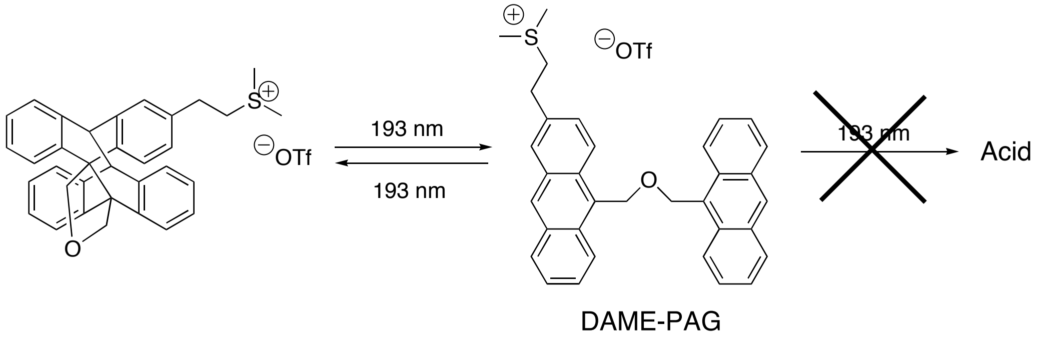

The difference in acid generation between cNAME-PAG and cDAME-PAG is an interesting observation. Unlike cDAME-PAG, cNAME-PAG did generate acid upon photolysis. This behaviour is likely due to the much higher efficiency of ring-closing in the DAME moiety with respect to the NAME moiety and such an assignment is supported by literature examples.[23]

cNAME-PAG did show less acid generation under MP irradiation conditions than at P1 (Figure 3.8), consistent with a non-reciprocal process. The reason for low acid yield at P2, matching that at MP, is unknown. Because the exposures were performed under air, we can expect that different amounts of endoperoxide photolysis products, like in the cNAME case described above, would be formed at P1 and P2. However as argued above, the C6 detection method should hide the decrease of free acid yield that any of these “photobases” would cause. As mentioned in the Results section, we chose not to pursue further mechanistic studies on this compound because lithographic results by our collaborators at Intel were not showing the desired performance.

Contrary to the results for cNAME/TES-6, Anth-PAG did seem to exhibit true non-reciprocal energy dependence under air with only laser and no lamp irradiation, even in the absence of a good electron donor. This was especially surprising given that our attempts with anthracene itself as a sensitizer for acid formation from mPAG-2 showed no energy dependence (Figure 3.11). As described, our attempts to characterize the products of the reaction by NMR were unsuccessful. Although the results were promising as a means of achieving pitch division and indeed was the first indication that we would be able to affect two-photon photochemistry at such low energies, the system we develop in Chapter 4 was more exciting because we were able to achieve better two-photon efficiencies without tethering the components together. Thus we chose to move our focus over to that system.

3.4 Summary

Herein we reported results pertaining to the study of several polyaromatic systems and their sensitization of acid generation from sulfonium PAGs for non-reciprocal acid generation. Working closely with our collaborators at Intel and starting from their lithographic results, we were able to better understand the photochemical reaction mechanism for the cNAME/TES-6 system and how they were able to obtain pitch division. We realized that the pitch division they observed in their imaging experiments was due to the formation of oxygen-centered “photobases” from NAME-endoperoxide which were mediating the effect of photochemically generated acid in the regions where they were formed. Our results also suggested that the system would have been more effective at true pitch division if it were possible to perform the lithographic imaging under an oxygen free environment. The cDAME-PAG and cNAME-PAG molecules, which were meant to operate by the same principals as the cNAME/TES-6 system (Scheme 3.2), did not show the dramatic increases in efficiency we expected based on tethering the components together.

Anth-PAG, originally studied as a model compound, showed promising non-linear acid generating behaviour upon 193 nm exposure alone. While the preliminary experiments performed to evaluate whether the donor-acceptor non-reciprocal scheme would work did not show any additional advantage, the non-reciprocal behaviour observed in the direct exposures was an exciting result. This system gave us our first experience with the type of multi-photon acid generation that is the subject of Chapter 4.

3.5 Experimental

3.5.1 Materials

All chemicals, solvents, and polymers were purchased from Aldrich unless otherwise stated and were of the highest grade available. DupXX polymer was provided by our collaborators at Intel. mPAG-2 was a generous gift from Prof. C.G. Willson's group at The University of Texas at Austin. cNAME, NAME, cDAME-PAG, and cNAME-PAG were all synthesized by Edward Jackson at SAFC Hi-tech (a business unit of Sigma Aldrich) and sent to us as part of our collaboration.

3.5.2 Thin Film Preparation

All thin polymer films for product studies or UV/Vis measurements were spin coated at 2000 rpm for 30 s from 10% w/w solutions of poly(methylmethacrylate) or DupXX in an appropriate solvent onto 1" quartz disks using an Integrated Technologies Inc. P-6000 spin coater and subjected to 60 s post-application bake (PAB) at 105°C directly after coating, unless otherwise stated.

3.5.3 Experiments in Thin Polymer Films

Following PAB, as described above, films were mounted into lens tubes for ease of handling. A Lumonics PM-846 excimer laser was used to generate 193 nm laser pulses (ArF, ~10 ns pulse duration). All films were mounted directly in front of the laser and exposed through a 1 cm x 1 cm mask. Laser energy was attenuated using low-grade quartz blocks ($T193/T_0193 \sim 0.5$ per block) and was measured at precisely the same distance from the laser output as where the samples were mounted using a PM100D Digital Optical Energy Meter with a ES145C broadband pyroelectric energy sensor (ThorLabs). Lamp irradiation at 365 nm was provided by an Oriel 66002 Xe arc lamp with a 325 nm long-pass colour filter and a 280-380 nm band-pass filter. The lamp output was measured with a Luzchem SPR-4001 Spectroradiometer and the output profile is shown in Figure 3.12a. The lamp was positioned such that the sample did not need to be moved between laser and lamp exposures (Figure 3.12b).

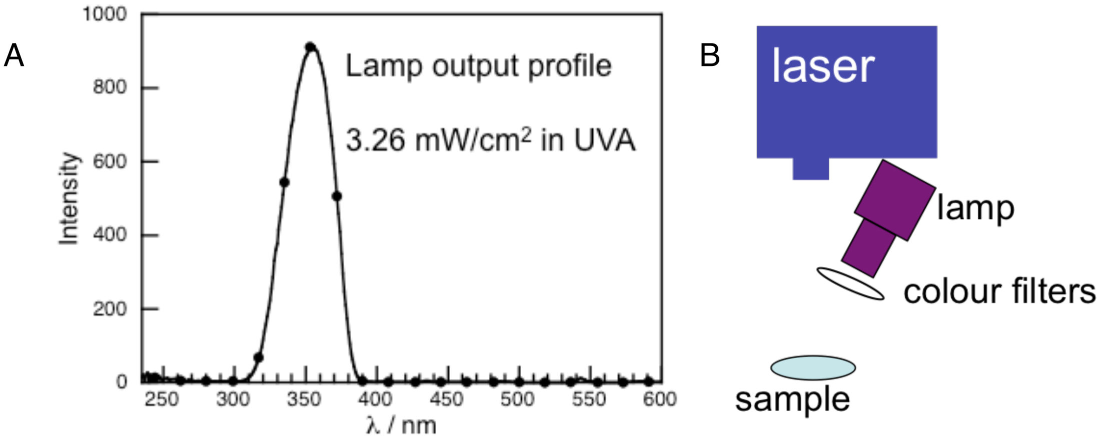

Figure 3.12 A) The output profile of the lamp used for 365 nm irradiation; B) Illustration showing the orientation of the lamp and laser relative to the sample; as described in the text above, long-pass and band-pass colour filters were used to select for UVA irradiation. The output in a) was measured at the position of the sample.

For power-dependence measurements, the energy per pulse was attenuated using the quartz blocks above but the same total dose (in mJ) was delivered to each sample by varying the number of exposures per film. The same sample mount was transferred to a Cary 50 UV/Vis spectrophotometer and each sample was inspected to ensure that the monitoring beam was probing the laser-exposed region. All absorbance spectra were recorded with a baseline of air (A193(air) ~ 0.3 over the pathlength of the instrument) both before and after laser exposure. The absorbance of all thin films prepared was < 1.0 at 193 nm.

Based on our findings in Chapter 4, all absorption spectra were recorded after a 20 min equilibration period to ensure that the yield of protonated C6 was constant.

3.6 References

1. Crivello, J., In *UV Curing: Science and Technology*, Pappas, S., Ed. Technology Marketing Corp.: Norwalk, CT, 1978; pp 23-77.

2. Crivello, J. V.; Lam, J. H. W., Diaryliodoniom Salts - New Class of Photo-Initiators for Cationic Polymerization. *Macromolecules* **1977,** *10* (6), 1307-1315.

3. Kura, H.; Fujihara, K.; Kimura, A.; Ohno, T.; Matsumura, M.; Hirata, Y.; Okada, T., Initial Step Of Anthracene-Sensitized Photoacid Generation From Diphenyliodonium Hexafluorophosphate In An Epoxy Matrix Studied By Steady-State And Laser-Flash Photolyses. *J Polym Sci Pol Phys* **2001,** *39* (23), 2937-2946.

4. Pappas, S. P.; Gatechair, L. R.; Jilek, J. H., Photoinitiation Of Cationic Polymerization. 3. Photosensitization Of Diphenyliodonium And Triphenylsulfonium Salts. *J Polym Sci Pol Chem* **1984,** *22* (1), 77-84.

5. Pappas, S. P.; Tilley, M. G.; Pappas, B. C., Anthracene-Bound Sulfonium Salts: Highly Efficient Photoinitiators For Cationic Polymerization A New Synthesis Of Sulfonium Salts Which Avoids The Use Of Silver Salts. *J Photochem Photobio A* **2003,** *159* (2), 161-171.

6. Wallraff, G. M.; Hinsberg, W. D., Lithographic Imaging Techniques For The Formation Of Nanoscopic Features. *Chem Rev* **1999,** *99* (7), 1801-1821.

7. Devoe, R. J.; Sahyun, M. R. V.; Schmidt, E.; Serpone, N.; Sharma, D. K., Electron-transfer Sensitized Photolysis of Onium Salts. *Can J Chem* **1988,** *66* (2), 319-324.

8. Selvaraju, C.; Sivakumar, A.; Ramamurthy, P., Excited State Reactions Of Acridinedione Dyes With Onium Salts: Mechanistic Details. *J Photochem Photobio A* **2001,** *138* (3), 213-226.

9. Schlegel, L.; Ueno, T.; Shiraishi, H.; Hayashi, N.; Iwayanagi, T., Acid Formation And Deprotection Reaction By Novel Sulfonates In A Chemical Amplification Positive Photoresist. *Chem Mater* **1990,** *2* (3), 299-305.

10. Toba, Y., The Design Of Photoinitiator Systems. *J Photopolym Sci Tec* **2003,** *16* (1), 115-118.

11. Gu, H. Y.; Zhang, W. Q.; Feng, K. S.; Neckers, D. C., Photolysis Of ((3-Trimethylsilyl)Propoxy)Phenyl) Phenyliodonium Salts In The Presence Of 1-Naphthol And 1-Methoxynaphthalene. *J Org Chem* **2000,** *65* (11), 3484-3488.

12. Dektar, J. L.; Hacker, N. P., Photochemistry of Triarylsulfonium Salts. *J Am Chem Soc* **1990,** *112* (16), 6004-6015.

13. This could either refer to ground-state species formed after the absorption of the first photon, as described in this chapter, or species still in their excited states, as presented in Chapter 3.

14. O'Connor, N. A.; Berro, A. J.; Lancaster, J. R.; Gu, X.; Jockusch, S.; Nagai, T.; Ogata, T.; Lee, S.; Zimmerman, P.; Willson, C. G.; Turro, N. J., Toward the Design of a Sequential Two Photon Photoacid Generator for Double Exposure Photolithography. *Chem Mater* **2008,** *20* (24), 7374-7376.

15. Bristol, R.; Shykind, D.; Kim, S.; Borodovsky, Y.; Schwartz, E.; Turner, C.; Masson, G.; Min, K.; Esswein, K.; Blackwell, J. M.; Suetin, N., Double-Exposure Materials for Pitch Division with 193nm Lithography: Requirements, Results. *Proc SPIE* **2009,** *7273*, 727307/1-12.

16. Lee, S.; Jen, K.; Willson, C.; Byers, J.; Zimmerman, P.; Turro, N., Materials Modeling And Development For Use In Double-Exposure Lithography Applications. *J Micro-Nanolith Mem* **2009,** *8* (1), 011011/1-11.

17. Byers, J.; Lee, S.; Jen, K.; Zimmerman, P.; Turro, N. J.; Wilson, G. C., Double Exposure Materials: Simulation Study of Feasibility. *J Photopolym Sci Tec* **2007,** *20*, 707 - 717.

18. McCullough, J. J., Photoadditions of Aromatic Compounds. *Chem Rev* **1987,** *87* (4), 811-860.

19. Bouas-Laurent, H.; Castellan, A.; Desvergne, J., From anthracene photodimerization to jaw photochromic materials and photocrowns. *Pure Appl Chem* **1980,** *52* (12), 2633-2648.

20. Bouas-Laurent, H.; Desvergne, J.; Castellan, A.; Lapouyade, R., Photodimerization of Anthracenes in Fluid Solutions: (Part 2) Mechanistic Aspects of the Photocycloaddition and of the Photochemical and Thermal Cleavage. *Chem Soc Rev* **2001,** *30* (4), 248 - 263.

21. Bouas-Laurent, H.; Desvergne, J.; Castellan, A.; Lapouyade, R., Photodimerization of Anthracenes in Fluid Solution: Structural Aspects. *Chem Soc Rev* **2000,** *29*, 43 - 55.

22. Castellan, A.; Lacoste, J. M.; Bouas-Laurent, H., Study of Non-Conjugated Bichromophoric Systems, The So-Called Jaw Photochromic Materials. 1. Photocyclomerization and Fluorescence of bis-9-anthrylmethyl Ethers. *J Chem Soc, Perkin Trans 2* **1979,** (4), 411-419.

23. Desvergne, J. P.; Bitit, N.; Castellan, A.; Bouas-Laurent, H., Study of Non-Conjugated Bichromophoric Systems. 3. The Photocyclomerization of 9-(2-furylmethoxymethyl)anthracene - Interest of the CH2-O-CH2 Link. *J Chem Soc, Perkin Trans 2* **1983,** (2), 109-114.

24. Noh, T.; Jeon, K.; Jeong, Y.; Jang, S.; Min, K. S., Synthesis Of 9-Cyanophenanthrene-Furan And -Benzene Cyclodimers And Their Reversion. *J Chem Soc, Perkin Trans 2* **1999,** (7), 1299-1303.

25. Noh, T.; Kim, D.; Jang, S., Photoreversion Of Naphthalene-Benzene Cyclodimers And Naphthalenes-Furan Cyclodimers. *B Kor Chem Soc* **1997,** *18* (4), 357-360.

26. Sundaresan, A. K.; Jockusch, S.; Li, Y.; Lancaster, J. R.; Banik, S.; Zimmerman, P.; Blackwell, J. M.; Robert, B.; Turro, N. J., Adiabatic Ring Opening In Tethered Naphthalene And Anthracene Cycloadducts. *Photochem Photobiol S* **2010,** *9*, 1082-1084.

27. Heafey, E. Applications of Spectroscopy to the Creation and Study of Nanostructures. M.Sc. Thesis, University of Ottawa, 2009.

28. Joschek, H. I.; Grossweiner, L., Optical Generation of Hydrated Electrons from Aromatic Compounds. II. *J Am Chem Soc* **1966,** *88* (14), 3261-3268.

29. Bhalerao, U. T.; Sridhar, M., Methoxylated Benzene Sensitized Photoformylation of Aliphatic Primary and Secondary-Amines. *J Chem Soc Chem Comm* **1993,** (2), 115-116.

30. Bhalerao, U. T.; Sridhar, M., Novel Photooxidation of Alkenes Sensitized by p-dimethoxybenzene. *Tetrahedron Lett* **1993,** *34* (27), 4341-4342.

31. Fudickar, W.; Linker, T., Imaging by Sensitized Oxygenations of Photochromic Anthracene Films: Examination of Effects That Improve Performance and Reversibility. *Chem Eur J* **2006,** *12* (36), 9276-9283.

32. Becker, H.; Elebring, T.; Sandros, K., Photochemical Intramolecular 4 pi + 4 pi Cycloaddition of 1, 2-Di (9-anthryl) ethanes. *J Org Chem* **1982,** *47* (6), 1064 - 1068.

33. Corral, I.; González, L.; Lauer, A.; Freyer, W.; Fidder, H., Identifying the Low-lying Electronic States of Anthracene-9,10-endoperoxide. *Chem Phys Lett* **2008,** *452*, 67 - 71.

34. Bristol, R.; Roberts, J.; Shykind, D.; Blackwell, J., Non-reciprocal Double-exposure materials for 193nm pitch division. *Proc SPIE* **2010,** *7639*, 763905-1.

35. Feke, G. D.; Grober, R. D.; Pohlers, G.; Moore, K., On-Wafer Spectrofluorometric Method For Determination Of Relative Quantum Yields Of Photoacid Generation In Chemically Amplified Resists. *Anal Chem* **2001,** *73*, 3472-3480.

36. Billone, P. S.; Park, J. M.; Blackwell, J. M.; Bristol, R.; Scaiano, J. C., Two-Photon Acid Generation in Thin Polymer Films. Photoinduced Electron Transfer As a Promising Tool for Subwavelength Lithography. *Chem Mater* **2010,** *22* (1), 15-17.

37. Scaiano, J. C.; Laferriere, M.; Ivan, M. G.; Taylor, G. N., A Protocol for the Verification of Acid Generation in 157 nm Lithography. *Macromolecules* **2003,** *36* (18), 6692-6694.

38. Shykind, D.; Bristol, R.; Roberts, J.; Blackwell, J.; Borodovsky, Y., Reaction Kinetics of Non-reciprocal Photo-Base Generator (NRPBG) Patterning. *Proc SPIE* **2010,** *7639*, 76391Y-1.

4. Two-Photon Acid Generation by Electron Transfer Sensitization

Table of Contents

Graphical Abstract

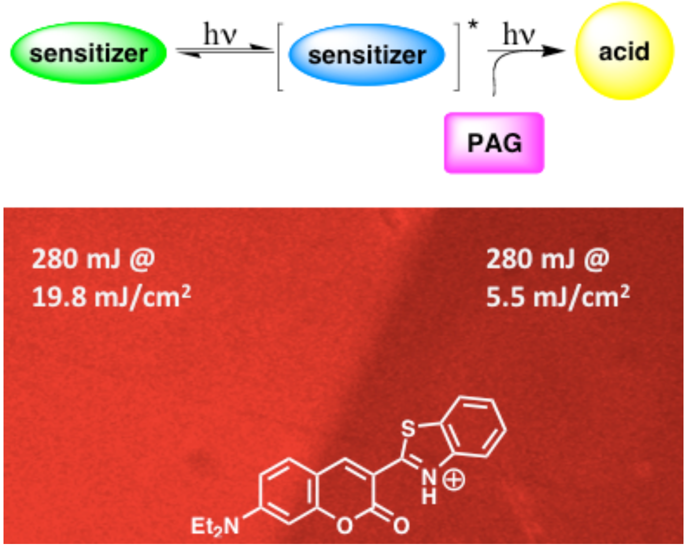

4.1 Introduction

4.1.1 Motivation and Proposed Lithographic System

As described in Chapter 1.1, the viability of double-exposure lithography to extend the lithographic range of 193 nm radiation depends on a reversibility step built in to the lithographic system.[1-3] The model system and strategy proposed in Chapter 3.1 relied on a thermal or photochemical reversibility step. While such an approach may lead to the desired effect, a simpler approach would be one where the reversibility is inherent to the process. In general, excited-state intermediates will return to their corresponding ground-states in the absence of photochemical reaction pathways and thus a reaction scheme which involves an excited-state molecule absorbing a second photon to generate acid would fulfill the requirements for a double-exposure-compatible system. Scheme 3.1 illustrates this pathway in a general way.

Scheme 4.1 Proposed general model for two-photon sensitized acid generation either through an intramolecular process (top) or an intermolecular sensitization process (bottom).

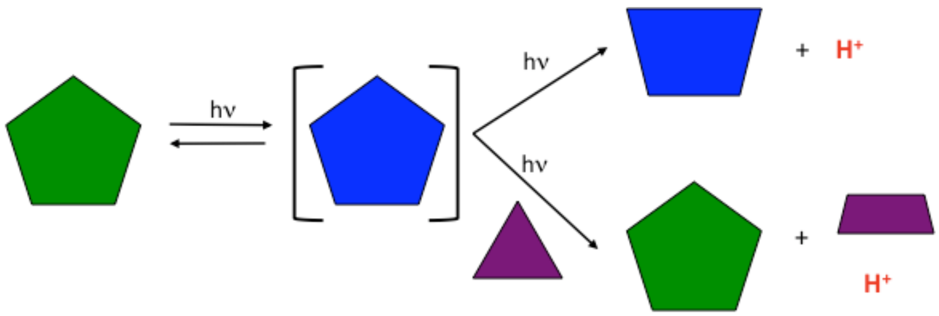

There are two distinct mechanisms of acid generation depicted in Scheme 4.1. The first, illustrated in the top pathway, would be one in which the absorbing molecule, shown as a green pentagon in the ground-state and a blue pentagon in the excited-state, is the same molecule from which the molecule of acid is produced. This is shown as a decomposition of the excited-state to form a molecule of free acid (shown only as H^+ for clarity) and the decomposition product of the absorbing molecule, the blue trapezoid. In the bottom mechanism, the sensitizer molecule absorbs both photons but only produces acid by sensitizing a photoacid generator, shown as the purple triangle. The common motif in both mechanisms is that the chromophore must be able to absorb two photons, preferably sequentially (*vide infra*), without the first photon affecting acid generation.

Two-photon processes are reasonably well understood; in fact, the Scaiano group reviewed the topic more than two decades ago. From a photolithographic point of view, there are two subtly different mechanisms for two-photon processes that could allow for the desired increases in resolution as predicted by LLE technology: 1) the excited state of a molecule is reached by absorption of two photons that combined have enough energy to reach this state, while the light used is such that no one-photon absorption occurs at that wavelength or 2) a one-photon process excites a molecule in a conventional way to yield a reaction intermediate (which could include an excited state) that can absorb a second photon, leading to chemical or spectroscopic consequences sometimes different from those achieved by just one photon. This case is best described as the “photochemistry of reaction intermediates”. Mechanism 1 is ubiquitous in the current lithographic literature, specifically in holographic and 3-D lithographic patterning, and describes the majority of examples in the literature that use the term “2-photon absorption”. However, this mechanism will not be relevant to lithography with 193 nm as it requires very high peak powers, frequently only achievable with picosecond or femtosecond lasers. As the energies delivered per pulse of lithographic laser sources are typically ≤ 1 mJ/cm^2 for pulse durations around 100 ns, the power density would be far too low for mechanism 1. In addition, many of the materials used in lithography readily absorb 193 nm photons. Therefore mechanism 2 is the most promising pathway for two-photon acid production that will be directly relevant to current photolithographic tools. While two-photon acid generating schemes have been proposed before,[4] the non-reciprocity was not inherent in the chemical system; they would require a second wavelength of light to drive the intermediate back to reactants, similar to the systems described in Chapter 3. This additional engineering difficulty is overcome by using unstable intermediates.

4.1.2 Two-Photon Ionization or Electron Transfer

As explained in Chapter 3 (and further discussed in Chapter 5), onium PAGs have been shown to efficiently yield acid upon reduction through electron transfer mechanisms.[5-7] Therefore molecules that are capable of participating in electron transfer reactions with onium PAGs from upper excited states, via either a formal electron transfer reaction or photoionization and electron capture, would satisfy the requirements outlined above. Candidates for study in the present chapter were selected based on literature precedent for two-photon photoionization.

Goez *et al.* have looked extensively at photochemical processes that result in photoionization.[8-11] While many of the systems they have examined photoionize through what they refer to as an absorption/electron transfer/absorption ionization scheme,[11] they have also presented several examples of systems which undergo direct two-photon ionization without the formation of absorbing intermediates.[12, 13] Most interesting was their observation that xanthone itself could undergo photoionization from its first excited triplet state.[12] This type of sequential two-photon photochemistry, distinct from true two-photon absorption, is the behaviour required for the system proposed in Scheme 4.1 to work.[14]

N-methylphenothiazine (mPT, Chart 4.1) has been shown to undergo sequential two-photon ionization when excited with two subsequent laser pulses.[15] This is in contrast with phenothiazine itself, which has been shown to efficiently sensitize acid generation monophotonically by electron transfer.[16, 17] As the pulse width of a typical 193 nm excimer laser is about 10 ns, it was reasoned that the high peak power of such a laser pulse would be enough to cause the same excited-state ionization observed when two laser pulses were used. This chapter presents the results of sensitized acid generation from mPT and a variety of PAGs directly in polymer films, including mechanistic work and attempted product identification.

4.2 Results

4.2.1 Dose Dependence of Acid Generation for mPT + Si3PAG-2

The method outlined in Chapter 1.4.1 was used to evaluate the potential for sensitized non-linear acid generation from mPT. The PAG used in these initial studies is shown in Chart 4.1 and will be referred to as Si3PAG-2. To test whether mPT could sensitize acid generation from a sulfonium PAG, we prepared PMMA films of 4:1 mPT:Si3PAG-2 (with a Si3PAG-2 loading of 4% w/p) containing 1% w/p C6. The spectral results showing changes to the C6 probe for a series of experiments, delivering a total dose of ~175 mJ/cm^2, are shown in Figure 4.1. We were careful to only go to relatively low conversion to avoid any saturation or significant bleaching effects. The absorbance at 193 nm of all films used in Figures 4.1 and 4.2 were equal. It was noted that the absorbance of the protonated form of C6 did increase for about 20 minutes following exposure due to acid diffusion through the film and equilibration. Therefore all results based on C6 protonation in this Chapter are reported following a minimum 20 min equilibration period (see Experimental section 4.5.3).

Chart 4.1. Structures of *N*-methylphenothiazine (mPT), tris(trimethylsilylmethyl)sulfonium triflate (Si3PAG-2), and Coumarin-6 (C6)

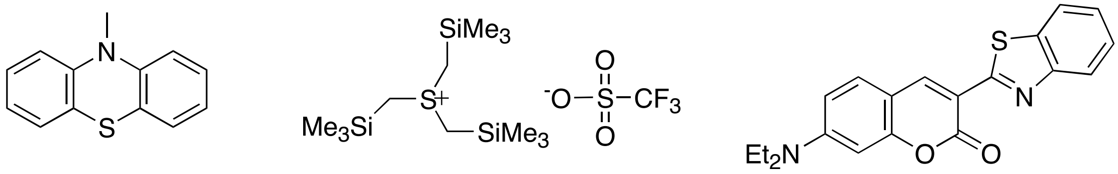

mPT Si3PAG-2 C6

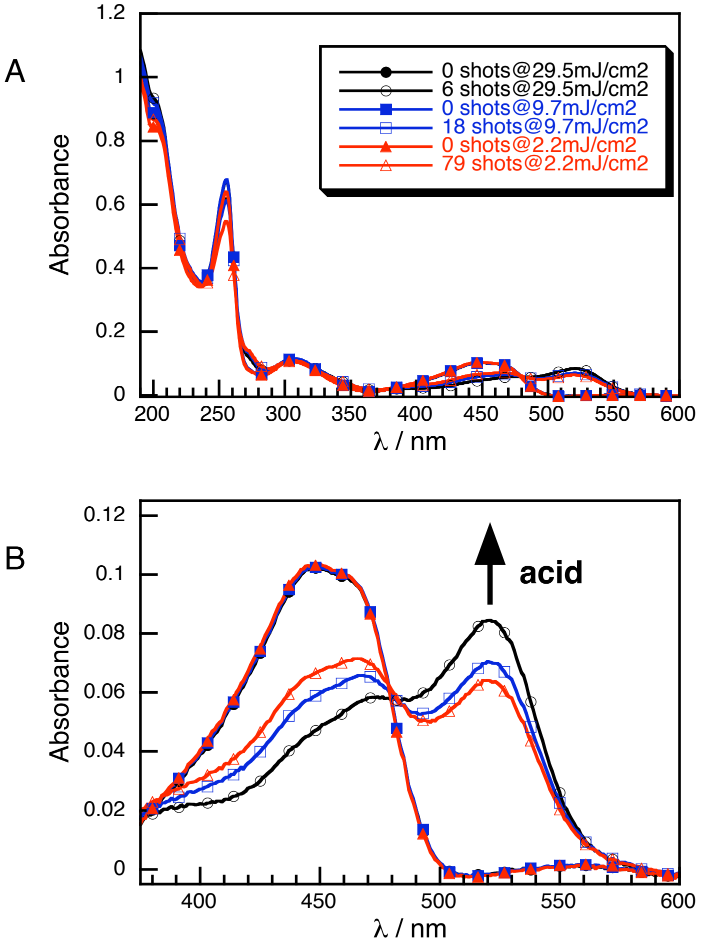

Figure 4.1 A) UV-Vis absorption spectra of a PMMA film containing a 4:1 molar ratio of mPT to PAG (PAG is 4% by weight of polymer) and 1% C6 used as an acid reporter. Spectra are recorded before and after exposure with ~175 mJ/cm^2 of 193

nm total laser irradiation energy delivered by pulses of 29.5 (●, ○), 9.7 (■, □) or 2.2 (▲, △) mJ/cm^2; filled points correspond to the spectra before irradiation and open points to the spectra after irradiation. The appearance of the protonated C6 absorption band at ~520 nm is observed in each sample indicating acid formation; B) An expansion of the C6 region of the spectrum, showing that more acid is formed in samples irradiated with higher pulse energies but the same total energy dose, indicative of a multi-photon acid generating mechanism.

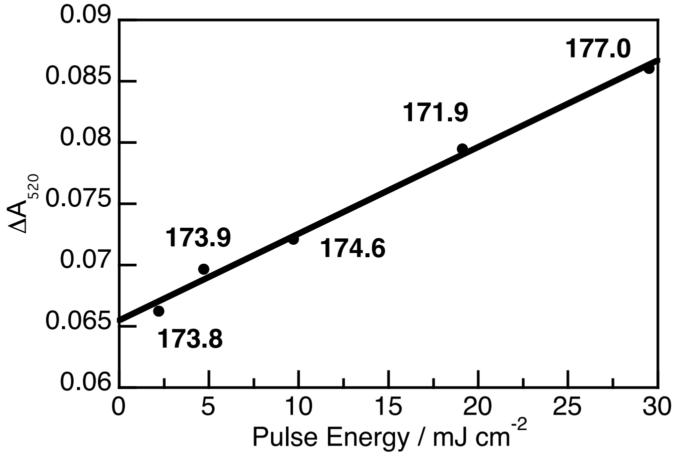

Figure 4.2 Plot showing the yield of protonated C6 in PMMA films prepared as in Figure 4.1 with nearly an equal dose (~175 mJ/cm^2) delivered to each film but with varying energy per pulse. The increasing acid yield with increasing pulse energy is indicative of a multi-photon sensitization mechanism. The values associated with each point indicate the exact dose, in mJ/cm^2, delivered to that film.

Figures 4.1B and 4.2 both demonstrate that there is some non-linear component of acid generation sensitized by mPT. Figure 4.3 shows the results of the same experiment without mPT, verifying that the non-linear component is indeed due to the sensitizing effect of mPT. Comparing Figure 4.3 to Figure 4.1, it is clear that the majority of acid generated is due to direct photolysis of the Si3PAG-2 (or sensitization by C6); the absorbance of protonated C6 for the lowest pulse energy in Figure 4.1B is approximately the same as all samples in Figure 4.3B. This is not surprising as the extinction coefficient of Si3PAG-2 at 193 nm is relatively high and its quantum yield for direct acid generation is moderate (see Chapter 5). This is also evident when looking at the y-intercept of Figure 4.2.

However the most important feature of Figure 4.2 is that there is a significant component of multi-photon acid generation, with about 35% more acid formed at the highest pulse energy tested with respect to the lowest. This is precisely the type of behaviour that would enable DE pitch division (see Figure 1.6). It was found that at more lithographically relevant pulse energies (< 1 mJ/cm^2), the non-linear component of acid generation was not observed. Regardless, this case represents the very first observation of a strongly non-reciprocal acid-generating system in thin polymer films using 193 nm excimer lasers that could be adapted to next-generation lithography.

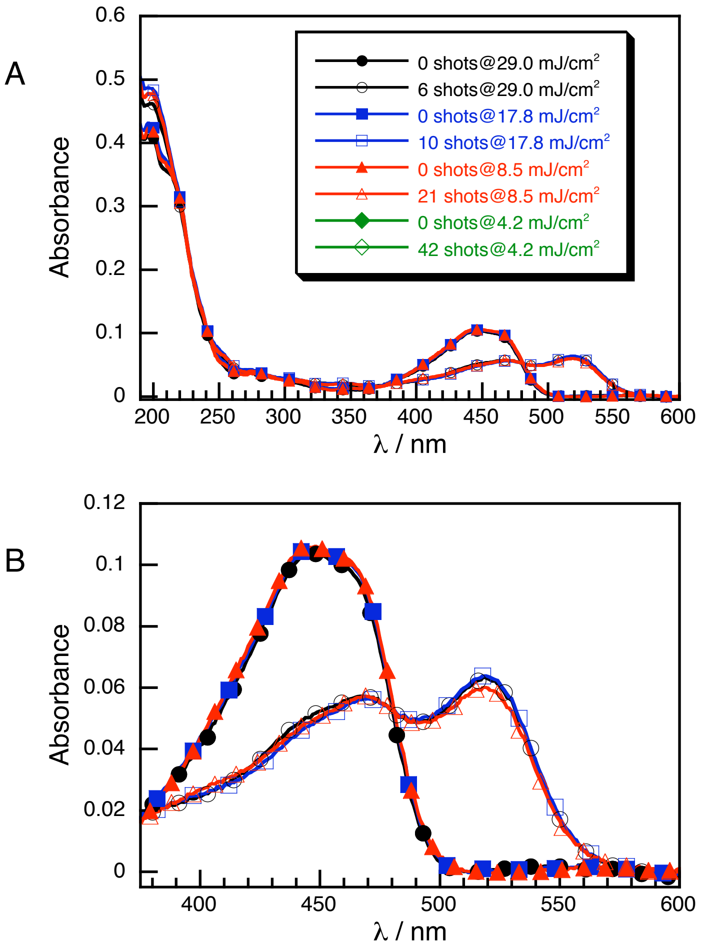

Figure 4.3 A) UV-Vis absorption spectra of a PMMA film containing 4% w/p Si3PAG-2 and 1% C6 used as an acid reporter. Spectra are recorded before and after exposure with ~175 mJ/cm^2 of 193 nm total laser irradiation energy delivered by pulses of 29.0 (●, ○), 17.8 (■, □) 8.5 (▲, △) or 4.2 (◆,◇) mJ/cm^2; filled points correspond to the spectra before irradiation and open points to the spectra after irradiation. The appearance of the protonated C6 absorption band at ~520 nm is observed in each sample indicating acid formation; B) An expansion of the C6 region of the spectrum, showing that the same amount of acid is formed in all samples.

The non-linear nature of acid generation was also observed by fluorescence microscopy (Figure 4.4). Protonation of C6 is accompanied both by the absorbance shift explained earlier (see Chapter 1.4.1) and a corresponding shift in its fluorescence emission wavelength.[18] Using a fluorescence microscope equipped with colour filters to select for only the protonated C6 emission (> 590 nm), it was possible to observe higher fluorescence in an area exposed to high energy pulses versus one exposed to lower energy pulses. Higher total doses were used than in previous experiments to give optimal contrast.

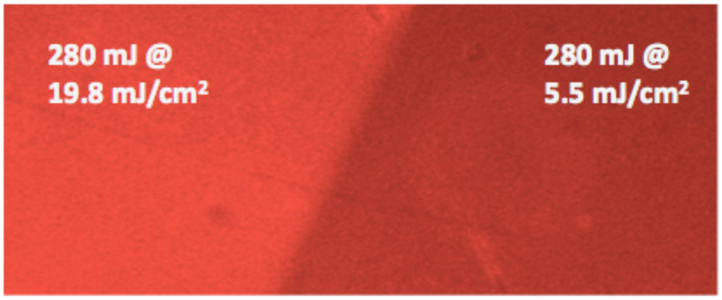

Figure 4.4 Fluorescence microscope colour image ($\lambda_{excitation}$ = 546 nm, $\lambda_{emission}$ > 590 nm) of a film prepared as in Figure 4.1. The left side of the film was exposed to 280 mJ of 193 nm irradiation at 19.8 mJ/cm^2 per pulse and the right exposed to the same total dose at 5.5 mJ/cm^2 per pulse. The brighter red, the result of protonated C6, on the left side of the image as compared to the right indicates that significantly more acid is generated with the higher pulse energy. The imaged area is 18 mm wide.

We also wanted to verify that the growth of the protonated C6 signal was not due to an interaction between excited mPT and C6. Figure 4.5 shows the spectra of three films containing only 10% w/p mPT and 1% w/p of C6 irradiated with ~180 mJ total dose of 193 nm light at three different pulse energies. No significant amount of protonated C6 is generated in any of the three samples, verifying that mPT itself is not responsible for the non-linear acid generation observed above.

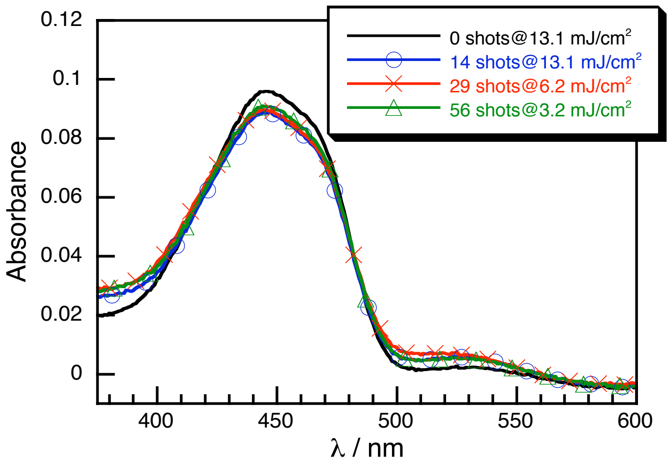

Figure 4.5 UV/Vis absorption spectra of PMMA films containing 10% w/p of mPT and 1% w/p of C6 exposed to 14 shots at 13.1 mJ/cm^2 (183.4 mJ, ○), 29 shots at 6.2 mJ/cm^2 (179.8 mJ, ×) and 56 shots at 3.2 mJ/cm^2 (179.2 mJ, Δ). Comparing with the spectrum of a film before irradiation (–) shows that almost no acid is generated upon photolysis of mPT only, indicating that the presence of the PAG is necessary for the acid generation observed in our experiments.

As mentioned in regards to Figure 4.2, the mPT-Si3PAG-2 system still exhibits a significant amount of single-photon acid generation. One very important consideration is the efficiency of a two-photon (or multi-photon) process as a function of depth from the surface in a polymer film, which would decrease much more rapidly than the efficiency of a one-photon process. Therefore it is possible that while the absorbances of all films used are below 1.0 at 193 nm, the films are simply too thick and the light absorbed is enough that the majority of the film does not actually receive a pulse energy anywhere near that incident on the film surface. As a result, if the thickness of the film was decreased we should see an increase in the proportion of two-photon to one-photon efficiency. Since we were unable to accurately measure film thicknesses on quartz substrates, a limited number of experiments were performed to try and evaluate this effect; Figure 4.6 shows the energy dependence plots for samples all coated from the same stock solution but at different spin-coating speeds.

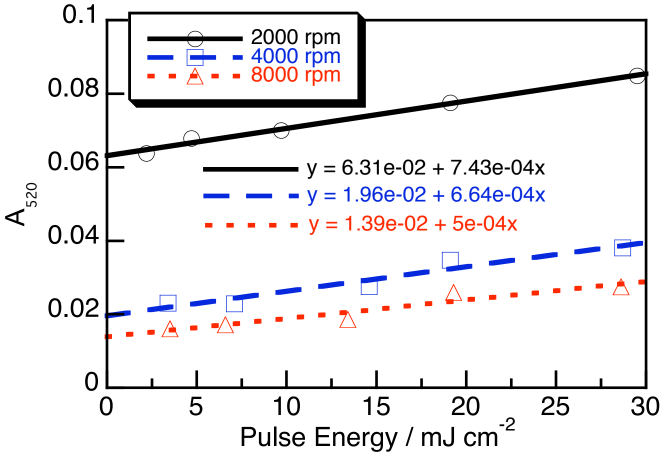

Figure 4.6 Energy dependence plots for 3 sets of PMMA films containing 4:1 mPT:Si3PAG-2 (PAG is 4% w/p) and 1% w/p C6 coated at 2000 rpm (○), 4000 rpm (□), and 8000 rpm (Δ). Each set of data are treated as linear and the equations of best fit are given on the plot. The total dose for each film was ~ 175 mJ/cm^2.

If the slope of the plots in Figure 4.6 is a measure of the non-reciprocity and the y-intercept is a measure of the one-photon contribution, we can use Equation 4.1 to qualitatively describe the efficiency of the multi-photon component with respect to the one-photon component.

$$\text{Efficiency} = \frac{\text{slope}}{\text{intercept}_y} \tag{4.1}$$

Applying Equation 4.1 to the data in Figure 4.6, we obtain efficiency values of 1.18 x 10^{-2}, 3.39 x 10^{-2}, and 3.60 x 10^{-2} for 2000 rpm, 4000 rpm, and 8000 rpm respectively at the given dose. Thus even though the slopes themselves decrease with decreasing film thickness, the efficiency of the multi-photon process seems to increase, as expected.

4.2.2 Mechanistic Investigations of the Sensitization Reaction

None of the experiments performed were able to differentiate between a two-photon or multi-photon (three or more) process but for the remainder of this chapter it will be assumed to be a two-photon process. In an effort to gain some insight into the nature of the sensitization process, we performed an experiment similar to that described for Figure 4.1 but instead of purposefully varying the laser energy, we varied the repetition rate of the laser. Figure 4.7A shows the yield of acid, as measured by protonation of C6, as a function of the repetition rate. Initially it was surprising to see that the higher repetition rate resulted in less acid; of the two potential mechanisms (see Discussion section 4.3), neither was expected to show such a trend. However when we examined the energies of the laser source at the different repetition rates, we noticed that the pulse energy decreased with increasing repetition rates. Plotting the same acid yields from Figure 4.7A in Figure 4.7B but now as a function of the measured pulse energies for each repetition rate, we observed a trend similar to that in Figure 4.2. The high degree of scatter in Figure 4.7B compared to Figure 4.2 is partly due to the fact that each of the five films were exposed to the same number of shots, which necessarily means that each film received different total irradiation doses. For instance, the 90 Hz sample received less than 150 mJ, while the 10Hz sample received over 180 mJ.

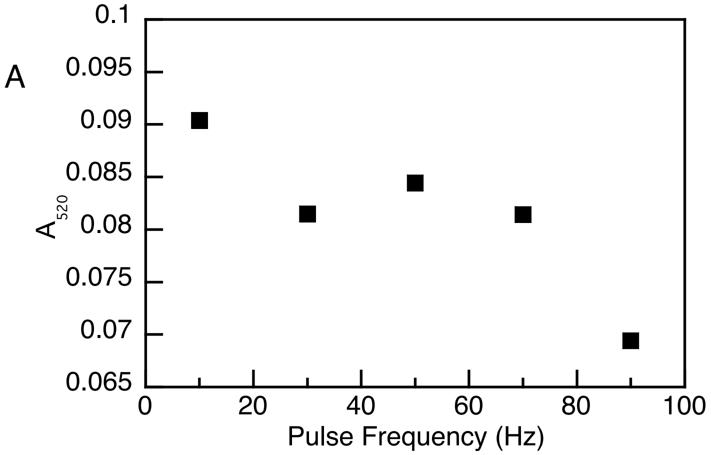

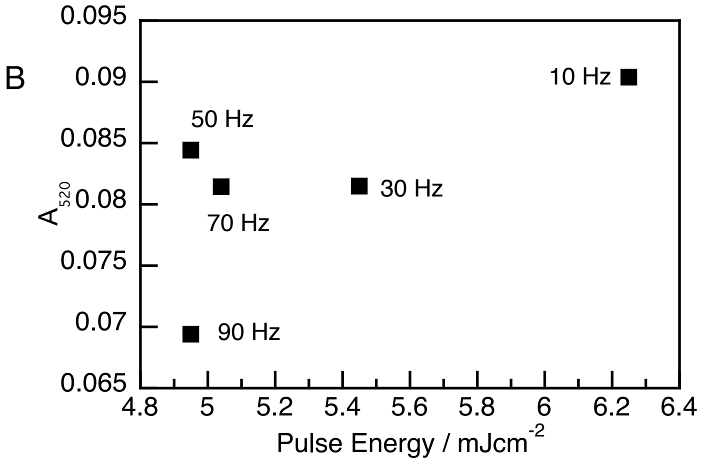

Figure 4.7 A) Five films (prepared as in Figure 4.1) exposed to 193 nm irradiation at varying repetition rates and 30 shots each; B) Replotting the data from a) as a function of the pulse energy at each pulse frequency.

In order to understand the dynamics of the system and potentially observe relevant intermediates in the sensitization reaction, the thin-film LFP technique described in Chapter 1.4.2 was used to probe the excited state of mPT in polymer films upon 193 nm excitation and its potential interaction with Si3PAG-2. Figure 4.8A shows the transient absorption spectrum of mPT in a PMMA film upon 193 nm excitation. The absorption spectrum that we observed in the polymer was almost exactly the same as observed for triplet mPT in solution (Figure 4.8B). The most surprising aspect was the effect of the medium on the lifetime: In PMMA, the mPT triplet lifetime was beyond the timescale of our LFP system (> 1 ms), while in solution the lifetime was less than 5 μs.

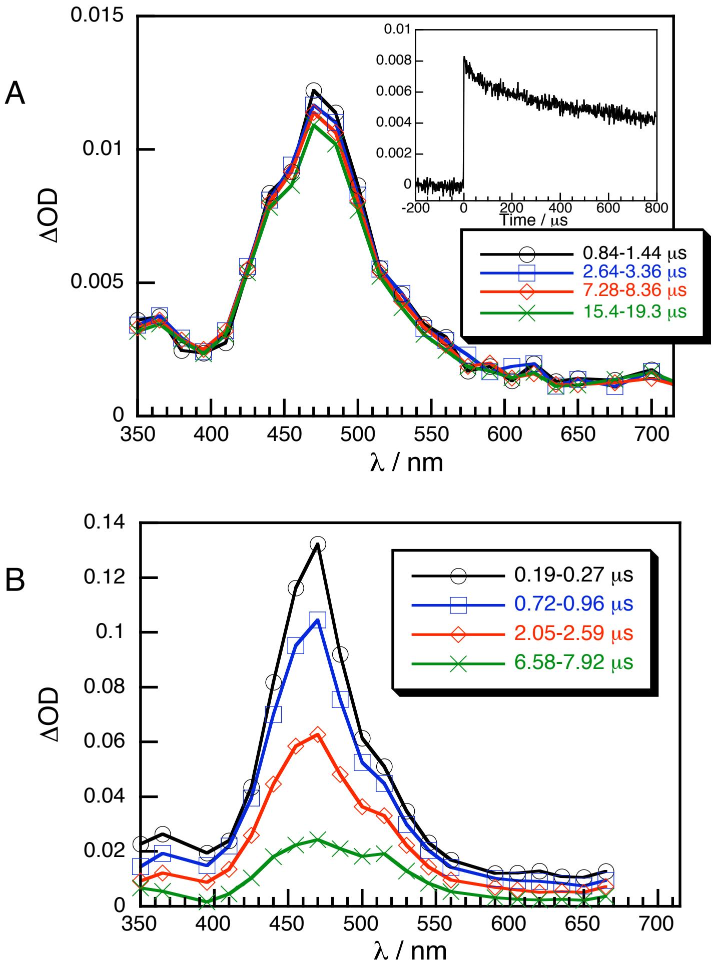

Figure 4.8 A) Transient absorption spectra of 1% mPT w/p in PMMA at various times following 193 nm excitation; the inset shows a kinetic trace recorded at 470 nm over the maximum timescale available; B) Transient absorption spectra of 0.05 mM mPT in MeCN at various times following 193 nm excitation.

We wanted to know whether the presence of Si3PAG-2 had any affect on the lifetime of the mPT triplet and/or whether any new transient absorption signals could be detected that could be attributed to the mPT radical cation. Figure 4.9A shows kinetic decay traces of the mPT triplet, centered at 470 nm, with and without

Si3PAG-2 present in the film as well. There is very little change in the lifetime of the triplet in the presence of the PAG. The difference in the maximum ΔOD between the two traces is likely due to variations in laser power between samples or slightly different film thicknesses. In addition to having no quenching effect on the lifetime of the mPT triplet, there are no new bands observed in the transient absorption spectra recorded over the maximum timescale possible (Figure 4.9B). The shoulder at ~520 nm does not correspond to a distinct transient species; the traverser was paused too late during acquisition of the point at 500 nm and some of the averaged data at that wavelength was collected when the laser and monitoring beam were not hitting the film itself.

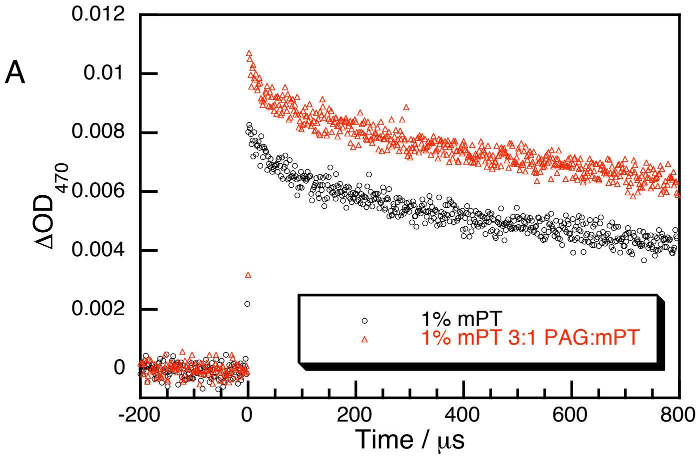

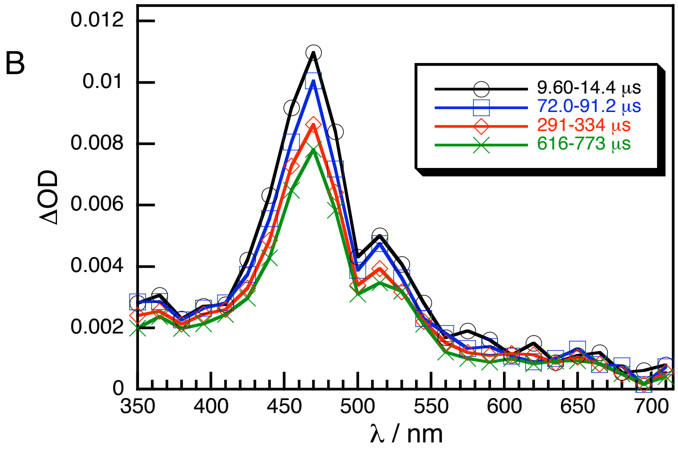

Figure 4.9 A) Kinetic transient absorption traces recorded at 470 nm following 193 nm irradiation of a PMMA film containing only 1% w/p mPT (○) and of a PMMA film containing 1% w/p mPT with a 3:1 molar excess of Si3PAG-2 (Δ); B) Transient absorption spectra of the same a PMMA film containing 1% w/p mPT with a 3:1 molar excess of Si3PAG-2 at various times following 193 nm irradiation.

If the two-photon sensitization observed in previous experiments was resonant absorption through the triplet state of mPT (*vide infra*), we expected to be able to form triplet mPT via one laser pulse and ionize the triplet with a second laser pulse. We used an initial low energy 266 nm laser pulse to initially excite mPT to the triplet state followed by a low energy 193 nm laser pulse. It was important to use relatively low energies in both pulses to avoid any single pulse two-photon photochemistry. Figure 4.10A shows a kinetic trace recorded at the absorption maximum of the mPT triplet after an initial 266 nm laser pulse followed by a 193 nm laser pulse 10 μs later. If photoionization was occurring from the triplet, we expected to see a bleach in the triplet signal with the 193 nm pulse. Instead, only an increase in the triplet signal is observed, even when the energy of both laser pulses were varied (data not shown). Transient absorption spectra were recorded before and after the 193 nm pulse in an attempt to observe signals corresponding to the radical cation of mPT but there were no additional features present (Figure 4.10B). The LFP data, coupled with the repetition rate dependence above, strongly suggest that the nature of the two-photon sensitization arises from resonant two-photon absorption from the first excited state within the same laser pulse.

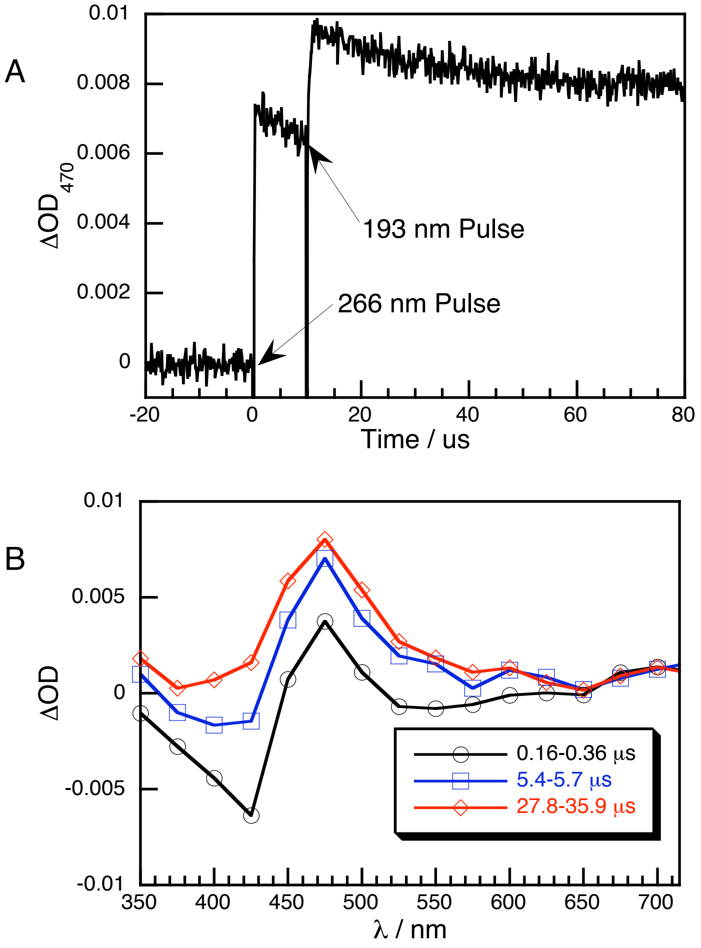

Figure 4.10 A) Two-laser kinetic trace of 0.5% w/p mPT in PMMA film exposed to a 266 nm laser pulse (1 mJ) followed by a 193 nm pulse (0.7 mJ) with a 10 μs delay

between pulses monitored at 470 nm; B) Transient absorption spectra at various times (reported with respect to times after the 266 nm pulse in a)) of the sample in A).

Product studies on reactions directly in polymer films, especially films as thin as those being used in this work, are notoriously difficult to perform.[19] However, since the particular system discussed in this chapter is unlike previous lithographic systems reported, analyzing the products of the sensitization reaction in films had to be attempted. Standard chromatographic techniques were not applicable as we were unable to remove the polymer from solution following dissolution of exposed films (many techniques, including dialysis and thin-layer chromatography, were attempted and were unsuccessful). Therefore we used NMR to try and identify characteristic peaks indicative of photolysis products. Since we were unable to perform any chromatography, the NMR samples are necessarily complicated by the presence of all starting materials and polymer signals. Thus the only area of the NMR spectra that provided useful information was the relatively clear aromatic region. Figure 4.11 shows the ^{1}H aromatic region of four different polymer thin film samples following dissolution in acetone-d_6. The spectra in 4.11A and 4.11B correspond to samples with 10% w/p mPT unexposed and following 468 mJ/cm^2 of 193 nm irradiation, respectively. It is clear that no significant new signals appear upon photolysis of mPT on its own. The spectrum in 4.11C, which includes a 4:1 mPT:Si3PAG-2 ratio, also shows no changes upon photolysis with 462 mJ/cm^2 of

193 nm irradiation at a pulse energy of 7.7 mJ/cm^2; we know from the experiments in Chapter 4.2.1 that a significant amount of acid would be generated at such a dose and pulse energy but the absence of new aromatic peaks seems to preclude a sensitization mechanism involving mPT. Conversely, the sample in Figure 4.11D was prepared from the same stock as that in Figure 4.11C but exposed to only 277 mJ/cm^2 with pulses of 23.1 mJ/cm^2. Even with nearly half the total dose as the previous samples, 4 new signals are evident in the aromatic region (integrating to 1:1:1:1). While the yield of these new products seems to be very low, they seem consistent with the low proportion of 2-photon acid-generating compared to direct photolysis of the Si3PAG-2. The appearance of four new peaks in the mPT region of the spectrum is consistent with substitution on one of the aromatic rings (*vide infra*). None of the internal standards we attempted to use were able to withstand irradiation at 193 nm without decomposition, thus they could not be use to better quantify the differences observed in Figures 4.11B and 4.11D.

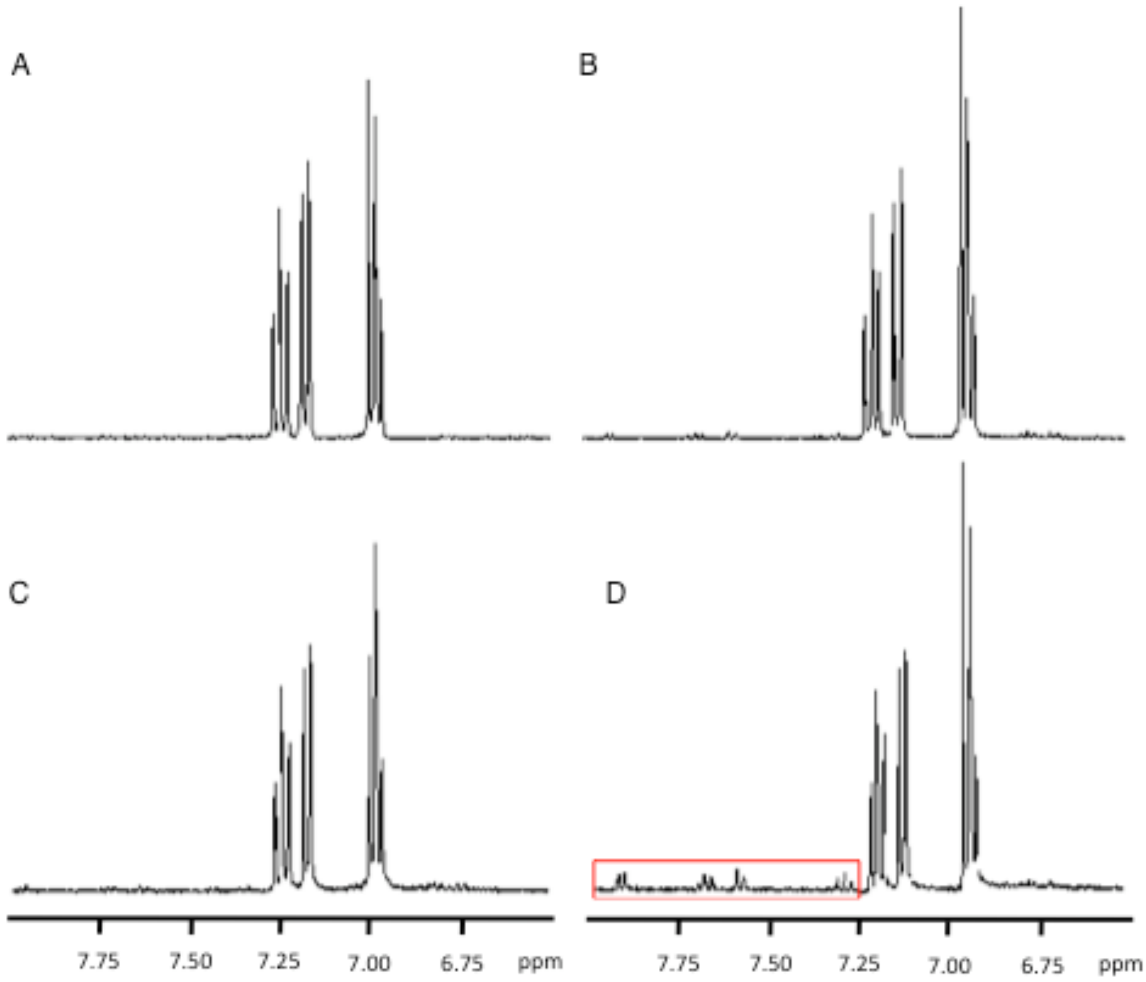

Figure 4.11 ^{1}H-NMR of the aromatic region for 4 different PMMA films following dissolution in acetone-d_6: A) 10% w/p mPT, no exposure; B) 10% w/p mPT, 468 mJ/cm^2 dose @ 7.8 mJ/cm^2 per pulse; C) 4:1 mPT:Si3PAG-2, 10% w/p mPT, 462 mJ/cm^2 dose @ 7.7 mJ/cm^2 per pulse; D) 4:1 mPT:Si3PAG-2, 10% w/p mPT, 288 mJ/cm^2 dose @ 24 mJ/cm^2 per pulse.

We had initially hoped that concentration studies would shed more light on the nature of the sensitization reaction. While the LFP data seemed to indicate that mPT did not photoionize in PMMA, correlating the acid yield with relative concentrations of mPT or Si3PAG-2 could potentially yield a distance-dependence relationship that would distinguish between trivial electron transfer versus an overlap mechanism. Many experiments were performed where the ratios of mPT and Si3PAG-2 relative to one another were varied and the energy dependence was monitored. However these experiments were often irreproducible and did not provide any useful information.

4.2.3 Sensitization of Other Sulfonium PAGs

In the preceding sections, Si3PAG-2 was chosen in the investigation primarily because it was the only “transparent” PAG we had available at the time we started the study. The term “transparent” PAG is a relatively modern concept, referring to PAGs that do not generate acid by direct photolysis at the lithographic wavelength. Instead, they rely on a sensitizer to initiate their decomposition and subsequent acid generation.[19, 20] Based on the data presented above, Si3PAG-2 is not the ideal “transparent” PAG for 193 nm. Near the end of the study with mPT and Si3PAG-3, several new PAGs became available to us (see Experimental section 4.5.1), many of which were significantly more transparent at 193 nm. Since the efficiency of multi-photon acid generation decreases with increasing single-photon contribution (Equation 4.1), these PAGs were expected to show much better performance than Si3PAG-2. The structures of the new PAGs are presented in Chart 4.2. Like Si3PAG-2, both TES-2 and mPAG-2 are expected to yield trifluoromethanesulfonic acid whereas TES-6 is expected to yield bis(trifluoromethylsulfonyl)imide, an organic super-acid of a similar strength as trifluoromethanesulfonic acid.

Chart 4.2. Structures of triethylsulfonium triflate (TES-2), triethylsulfonium bis(trifluoromethylsulfonyl)imide (TES-6), and trimethylsulfonium triflate (mPAG-2).

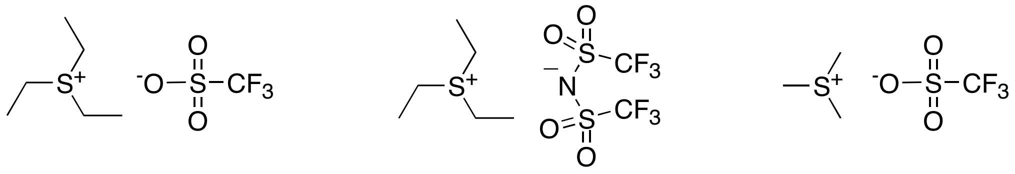

TES-2 TES-6 mPAG-2

We decided to test each of the available PAGs under the same conditions as Si3PAG-2 for energy dependence and the results are presented in Figure 4.12. Figure 4.12A shows energy dependence plots for each mPT-PAG combination, including that for Si3PAG-2. Immediately it is clear that all systems have some component of multi-photon acid generation to them. While the slopes of each plot are quite similar, the y-intercepts are quite different reflecting the fact that while the sensitization efficiency itself is not dramatically different, the overall multi-photon efficiency is significantly varied for the different PAGs. The efficiencies, as calculated by Equation 4.1, are presented in Figure 4.12B for each of the 4 PAGs. Not surprisingly, Si3PAG-2 has the lowest efficiency by a far margin due to its high one-photon contribution. Interestingly TES-2 and TES-6 had nearly identical efficiencies while mPAG-2 was the most efficient. This data suggests that the anion seems to play little role in the efficiency of the sensitization reaction, whereas the identity of the sulfonium plays a major role. This is not surprising when we consider the proposed mechanism of sensitization (see Dicussion 4.3).

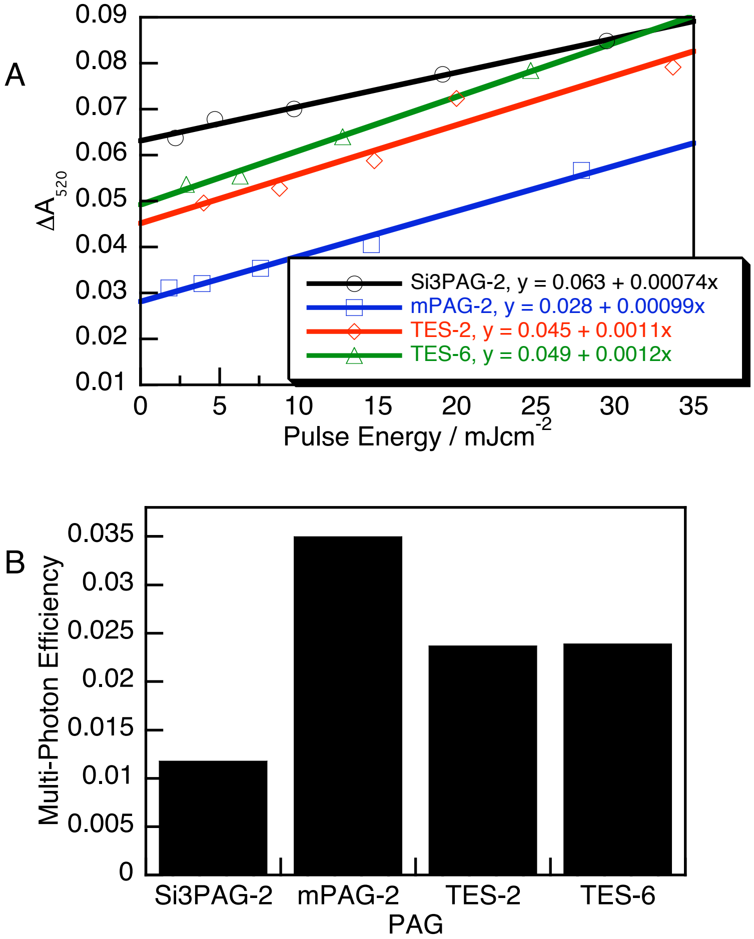

Figure 4.12 A) Energy dependence plots for 4 sets of PMMA films with equal molar concentrations of PAG (based on 2% w/p Si3PAG-2) and a 4:1 molar ratio mPT:PAG; all films were coated using the same conditions; B) Comparison of the multi-photon efficiency, as calculated by Equation 4.1, for each of the 4 PAGs tested.

4.2.4 Tethered mPT-PAG Molecules

Referring back to Scheme 4.1, it is clear that an acid-generating scheme that would proceed *via* the top pathway (intramolecular) would be far more desirable in a lithographic acid generating system since the bottom mechanism requires the close proximity of the sensitizer and the PAG following film casting. Increasing the concentrations of both components is impractical since at high concentrations they will adversely affect the properties of the photoresist, including its coating and dissolution abilities. Therefore we proposed that since the intermolecular multi-photon sensitization between mPT and PAGs was already relatively efficient in polymer matrices, tethering the two components together would drastically improve its performance. Through discussions with our collaborators at Sigma Aldrich Fine Chemicals (SAFC), we decided that tethering at the *meta* position of mPT was the most synthetically accessible route. Scheme 4.2 outlines the general synthesis of a tethered mPT-PAG molecule; mPT-ONf was synthesized by our collaborators at SAFC.

Scheme 4.2 Synthesis of a general mPT-PAG tethered molecule starting from mPT-ONf, where –ONf represents the nonaflate group $-O_3SCF_2CF_2CF_2CF_3$.

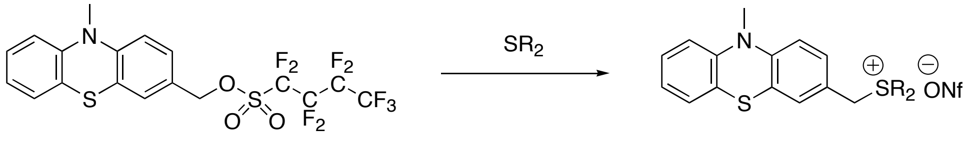

mPT-ONf

Before attempting the synthesis of the tethered compound, we decided to check whether mPT-ONf itself could produce acid photochemically and more importantly, if it did so in a non-linear manner. There are many examples in the literature where photochemical homolytic cleavage of groups pendant to an aromatic ring occurs biphotonically,[15, 21-23] including a recent unpublished example based on 9-bromophenanthrene making HBr from our group that occurs in lithographically relevant polymers. Since the extruded radicals are generally strong H-abstractors, they rapidly form strong acids; if mPT-ONf extruded the nonaflate radical, it would generate nonaflic acid upon H-abstraction. Figure 4.13 shows the absorption spectra of two different polymer films containing mPT-ONf exposed to 193 nm irradiation at two different energies. No signal due to protonated C6 is observed even at the highest doses, though the absorption band at ~250 nm belonging to the mPT moiety decreases with increased irradiation. In Figure 4.13B it is also clear that at higher doses, C6 itself begins to decompose.

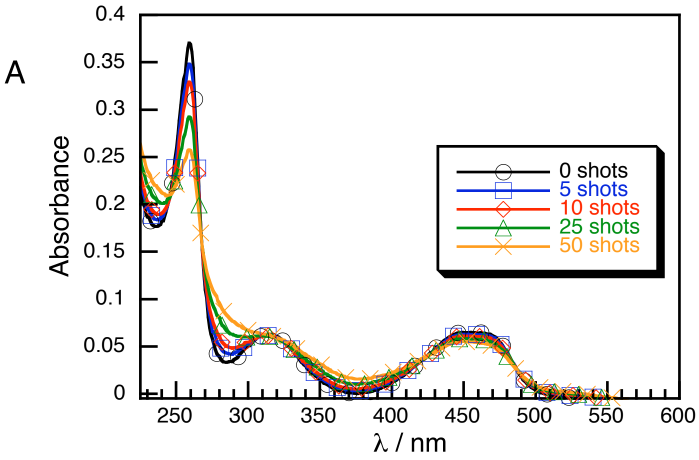

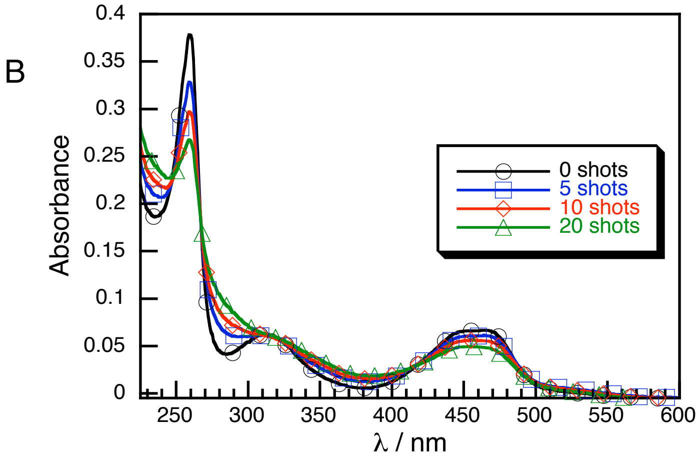

Figure 4.13 A) UV-Vis absorption spectra of a DupXX film containing 2% w/p of mPT-ONf and 1% C6 before and after exposure with 5, 10, 25, and 50 shots of a 193 nm laser at 4.8 mJ/cm^2; B) Film prepared the same as in A) but exposed to 5, 10, and 20 shots at 18 mJ/cm^2. No protonated C6 is observed in either case, though decomposition of the mPT moiety is apparent by the decrease in the band at ~250 nm.

We decided to attempt the synthesis of mPT-PS-3 (Scheme 4.3) as propyl sulfide is relatively easy to work with and is expected to be a good reagent in these sulfonium substitution reactions.[24-26] Three different reactions were attempted (Scheme 4.3) to promote the substitution reaction but all three yielded only starting material (as determined by NMR). Originally we were concerned that self-condensation of a thiazole sulfur on one molecule and the electrophilic center on another would interfere with the desired reaction, but it seems that the mPT-ONf is simply too unreactive for product formation. Extending the tether by one extra methylene likely would have made the carbon center reactive enough but in that case the self-condensation reaction may have also become more significant. Further attempts at making different analogs were not pursued.

Scheme 4.3 Three synthetic routes towards mPT-PS-3 that were attempted; additional details are given in the Experimental section 4.5.

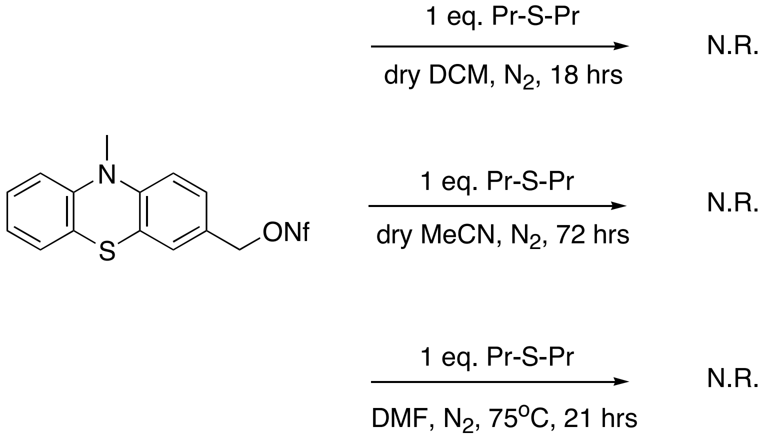

4.3 Discussion

The mPT + Si3PAG-2 system reported here is a very promising technology, but it obviously suffers from severe limitations that would limit its application. It does not seem to perform well at lithographically relevant pulse energies, likely due to a) the significant direct photolysis acid generation from Si3PAG-2 itself and b) the intermolecular nature of the sensitization reaction. With regards to the former problem, the efficiency of the two-photon process significantly increases upon switching the PAG to a more “transparent” one (Figure 4.12). The latter issue, to be addressed by synthesizing a tethered molecule, would have required significant synthetic effort. Since our collaborative funding had moved away from two-photon acid generation for pitch-division, this goal was not purused further than the preliminary attempts described herein.

Our proposed mechanism of sensitization, based on that suggested for the one-photon sensitization of sulfonium PAGs by other polyaromatic compounds,[19] is outlined in Scheme 4.4 below. The scheme does not specify the nature of the first or second excited state of mPT. Based on the thin-film LFP results in Chapter 4.2.2, we favour a singlet-state process. Our reasons for believing that the mechanism proceeds via the singlet state are: a) Monophotonic electron transfer from the parent phenothiazine to PAGs in films occurs from the singlet state in spite of the presence of a long-lived triplet[17] and b) The yield of acid is independent of the repetition rate, even though the mPT triplet looks like it would live close to 1 ms, long enough for a small fraction to persist between 100 Hz pulses. If the triplet was involved one would expect that at higher repetition rates the triplet state would be re-excited by subsequent laser pulses; therefore we presume that both photons of Scheme 4.4 are delivered within the same 10 ns pulse.

Scheme 4.4 Proposed two-photon sensitization mechanism for mPT and Si3PAG-2 to generate triflic acid.

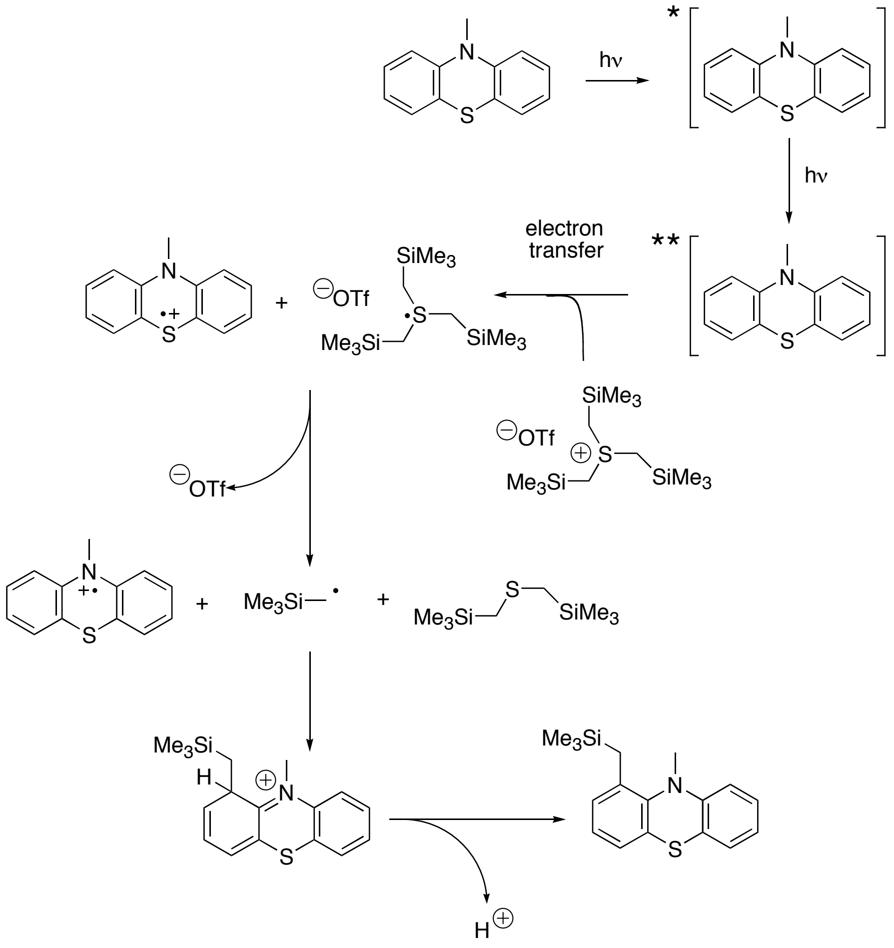

Through the LFP experiments, we were also unable to spectroscopically observe any of the intermediates following the proposed electron transfer. This is not surprising since, unlike in a solution phase reaction, the reagents are unable to diffuse apart and therefore the entire reaction following electron transfer would happen very rapidly. Unfortunately as described in Section 4.2.2, separation and identification of the products following photolysis was not possible. The fact that four new distinct peaks are observed in the aromatic region of the ^{1}H NMR spectrum only in the presence of Si3PAG-2 *and* when exposed to high 193 nm pulse energies supports the proposal that the two-photon sensitization reaction forms a product distinct from the starting materials. The product in Scheme 4.4 is expected to show 7 distinct aromatic proton signals, though it is reasonable to assume that several of those peaks are buried under the aromatic peaks of the starting material. It again must be emphasized that the final coupling product is only a proposed product based on similar types of reactions in the literature and with which our data is consistent.

4.4 Summary

These mPT + PAG systems are the very first reported examples of photochemical systems that would potentially enable DE lithography.[27] By comparing the two-photon sensitization efficiency of mPT with several different PAGs (calculated using Equation 4.1), it was found that the most transparent mPAG-2 had the highest efficiency. Mechanistic investigations on the mPT + Si3PAG-2 lend strong evidence to the proposal that the sensitization mechanism takes place from the singlet manifold and that both photons are absorbed by mPT during a single laser pulse. Product studies were inconclusive but based on previous one-photon sensitization mechanisms, we propose a process that proceeds by electron transfer followed by radical generation and recombination.

We proposed that a tethered mPT-PAG system would dramatically increase the efficiency of two-photon acid generation but were unable to synthesize a simple tethered molecule. While several other routes to tethered molecules were discussed, time and availability of materials did not permit us to pursue their syntheses.

Despite the inefficiencies of the mPT-based lithographic system, it must be emphasized that these results are the very first examples that would potentially enable pitch division. The work done on this system has formed the foundation for almost all of our group's current work on non-linear processes in lithographically relelvant systems.

4.5 Experimental

4.5.1 Materials

All chemicals, solvents, and polymers were purchased from Aldrich unless otherwise stated and were of the highest grade available. PMMA was purchased from Aldrich and had M_w ~ 100,000 Da with unspecififed PDI. DupXX polymer was previously described in Chapter 3 and was provided by our collaborators at Intel. Si3PAG-2 and TES-2 PAGs were prepared by our collaborators at Intel; mPAG-2 was a generous gift from Prof. C.G. Willson's group at The University of Texas at Austin. mPT-ONf was synthesized by Dr. Ed Jackson at SAFC as part of our collaborative project.

4.5.2 Thin Film Preparation

All thin polymer films for product studies or UV/Vis measurements were spin coated at 2000 rpm for 30 s from 10% w/w solutions of poly(methylmethacrylate) in 2-heptanone onto 1" quartz disks using an Integrated Technologies Inc. P-6000 spin coater and subjected to 60 s post-application bake (PAB) at 105°C directly after coating, unless otherwise stated. While thickness measurements were unreliable for the films coated on quartz slides due to the minimal differences in refractive index, we estimate the thickness of films prepared in the above manner to be about 400 nm thick.

All polymer films used for LFP measurements were prepared on 3” x 1” quartz microscope slides using laboratory metering rods purchased from Diversified Enterprises. These rods enabled the preparation of thicker films (~10 μm wet thickness) from the same solutions used to spin-coat other samples. The films were subjected to the same PAB as above.

4.5.3 Experiments in Thin Polymer Films

Following PAB, as described above, films were mounted into lens tubes for ease of handling. A Lumonics PM-846 excimer laser was used to generate 193 nm laser pulses (ArF, ~10 ns pulse duration). All films were mounted directly in front of the laser and exposed through a 1 cm x 1 cm mask. Laser energy was attenuated using low-grade quartz blocks (T^{193}/T_0^{193} ~ 0.5 per block) and was measured at precisely the same distance from the laser output as where the samples were mounted using a PM100D Digital Optical Energy Meter with a ES145C broadband pyroelectric energy sensor (ThorLabs). For power-dependence measurements, the energy per pulse was attenuated using the quartz blocks above but the same total dose (in mJ) was delivered to each sample by varying the number of exposures per film. The same sample mount was transferred to a Cary 50 UV/Vis spectrophotometer and each sample was inspected to ensure that the monitoring beam was probing the laser-exposed region. All absorbance spectra were recorded with a baseline of air (A_{193}(air) ~ 0.3 over the pathlength of the instrument) both before and after laser exposure. The absorbance of all thin films prepared was < 1.0 at 193 nm.

As mentioned in section 4.2.1, all measurements on films containing C6 were measured after a minimum 20 min wait period. Figure 4.14A shows the evolution of protonated C6 signal as a function of time after irradiation for a sample containing 4:1 mPT:Si3PAG and 1% w/p Si3PAG. We see that the absorbance doesn't come to a stable value until about 15 min after exposure. Initially we thought that this was due to the time required for acid diffusion through the polymer matrix. However Figure 4.14B presents the results for a film containing the same molar ratio of mPT and Si3PAG but a 4% w/p loading of Si3PAG, which shows a much longer growth. Therefore we attribute the growth to the time required for equilibrium to be established between protonation of mPT (or the products derived from it) and the protonation of C6; while C6 is a stronger base than mPT (pK_b ~ 13), the concentration of mPT is significantly higher.

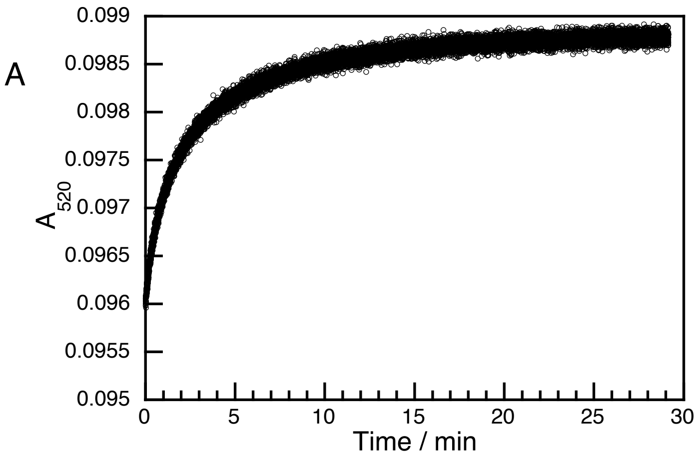

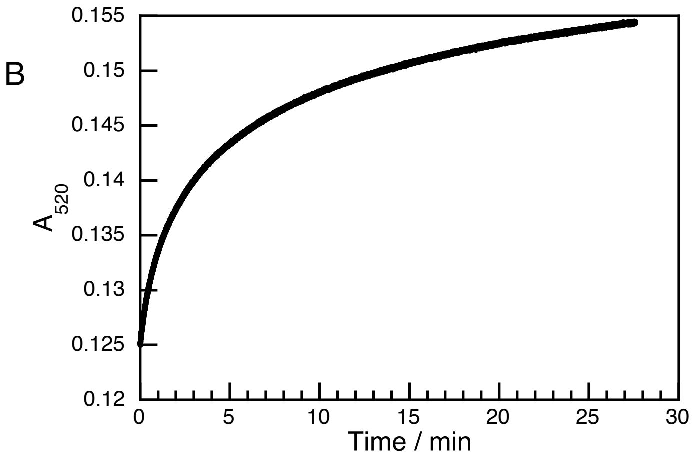

Figure 4.14 A) Absorbance at 520 nm as a function of time for a PMMA film containing a 4:1 molar ratio of mPT:Si3PAG with 1% w/p Si3PAG following exposure to 72 shots at 2.4 mJ/cm^2; B) Absorbance at 520 nm as a function of time for a PMMA film containing a 4:1 molar ratio of mPT:Si3PAG with 4% w/p Si3PAG following exposure to 72 shots at 2.4 mJ/cm^2.

4.5.4 Attempted Synthesis of mPT-PS-3

Attempt #1: Added 5.3 mg (4.48 x 10^{-5} mol) propyl sulfide to 0.5 mL dry DCM under N_2 with stirring in a round bottom flask equipped with a condenser. 23.5 mg (4.47 x 10^{-5} mol) mPT-ONf was dissolved in 0.5 mL DCM and added slowly to the sulfide solution by syringe over 1 min. The reaction was allowed to stir overnight (18 hrs). The entire solution was rotovapped to yield a clear, yellow oil. To this was added 1 mL *n*-hexane; upon addition, a white solid precipitated. The hexane was decanted off and 1 mL of MeCN was added; the solid remained insoluble, so the MeCN was decanted off and the washed solid was dried on the rotovap to yield 18.6

mg of off-white solid. ^{1}H NMR in acetone-d_6 confirmed that only starting material was present.

Attempt #2: Added 5.8 mg (4.91 x 10^{-5} mol) propyl sulfide to 0.35 mL dry MeCN under N_2 with stirring in a round bottom flask equipped with a condenser. Added 25.8 mg (4.91 x 10^{-5} mol) mPT-ONf to 1 mL MeCN to form an insoluble suspension. The suspension was added to the sulfide solution by pipette and the heterogeneous reaction was allowed to stir for 72 hrs. To the final suspension was added 2 mL *n*-hexane and stirred vigorously for 30 s. The hexane layer was removed and the suspension was filtered through a Buchner funnel to yield 3.1 mg of white solid. ^{1}H NMR in acetone-d_6 confirmed that only starting material was present.

Attempt #3: Added 4.8 mg (4.06 x 10^{-5} mol) propyl sulfide to 0.5 mL DMF under N_2 with stirring in a round bottom flask equipped with a condenser. 20.3 mg (3.86 x 10^{-5} mol) mPT-ONf was dissolved in 0.5 mL DMF and added dropwise to the sulfide solution over a minute. The reaction was heated to 75°C with an oil bath and left stirring overnight. After 21 hrs, the heat was removed and once the solution was cool, 1 mL *n*-hexane was added and stirred for 2 min; the hexane was then removed. The DMF solution was rotovapped with heat to near dryness to yield a yellow concentrated solution. ^{1}H NMR in acetone-d_6 confirmed that only starting material, in addition to DMF, was present.

4.6 References

1. Bristol, R.; Shykind, D.; Kim, S.; Borodovsky, Y.; Schwartz, E.; Turner, C.; Masson, G.; Min, K.; Esswein, K.; Blackwell, J. M.; Suetin, N., Double-Exposure Materials For Pitch Division With 193nm Lithography: Requirements, Results. *Advances in Resist Materials and Processing Technology XXVI* **2009,** *7273*, 727307-12.

2. Byers, J.; Lee, S.; Jeri, K.; Zimmerman, P.; Turro, N. J.; Willson, C. G., Double Exposure Materials: Simulation Study of Feasibility. *J Photopolym Sci Tec* **2007,** *20* (5), 707-717.

3. Finders, J.; Dusa, M.; Vleeming, B.; Hepp, B.; Maenhoudt, M.; Cheng, S.; Vandeweyer, T., Double Patterning Lithography For 32 nm: Critical Dimensions Uniformity And Overlay Control Considerations. *J Micro-Nanolith Mem* **2009,** *8* (1), 011002.

4. O'Connor, N. A.; Berro, A. J.; Lancaster, J. R.; Gu, X.; Jockusch, S.; Nagai, T.; Ogata, T.; Lee, S.; Zimmerman, P.; Willson, C. G.; Turro, N. J., Toward the Design of a Sequential Two Photon Photoacid Generator for Double Exposure Photolithography. *Chem Mater* **2008,** *20* (24), 7374-7376.

5. Crivello, J. V.; Jang, M., Anthracene Electron-Transfer Photosensitizers For Onium Salt Induced Cationic Photopolymerizations. *J Photochem Photobio A* **2003,** *159* (2), 173-188.

6. Iwaki, J.; Suzuki, S.; Park, C.; Miyagawa, N.; Takahara, S.; Yamaoka, T., Sensitization Mechanism Of The Anthracene Derivatives/Photoacid Generator Photoinitiating System. *J Photopolym Sci Tec* **2004,** *17* (1), 123-124.

7. Narewska, J.; Strzelczyk, R.; Podsiadly, R., Fluoflavin Dyes As Electron Transfer Photosensitizers For Onium Salt Induced Cationic Photopolymerization. *J Photochem Photobio A* **2010,** *212* (1), 68-74.

8. Goez, M.; Zubarev, V., Two-Photon Ionization Of 1,5-Anthraquinonedisulfonate Via Photoinduced Electron Transfer. *J Phys Chem A* **1999,** *103* (48), 9605-9613.

9. Goez, M.; Zubarev, V., Light Intensity Dependence Of A Two-Photon Catalytic Cycle: Photoionization Via Absorption-Electron Transfer-Absorption. *Chem Phys* **2000,** *256* (1), 107-116.

10. Goez, M.; Zubarev, V.; Eckert, G., Photoionization Via Absorption Electron Transfer Absorption Studied By Two-Pulse Two-Color Laser Flash Photolysis. *J Am Chem Soc* **1998,** *120* (21), 5347-5348.

11. Zubarev, V.; Goez, M., Absorption Electron Transfer Absorption - An Efficient Pathway To Hydrated Electrons In Laser Flash Photolysis. *Angew Chem Int Ed* **1997,** *36* (23), 2664-2666.

12. Goez, M.; Hussein, B., Photoionization Of Xanthone Via Its Triplet State Or Via Its Radical Anion. *Phys Chem Chem Phys* **2004,** *6*, 5490-5497.

13. Goez, M.; Zubarev, V., Efficient Photoionization of a Norrish II Diradical. *Angew Chem Int Ed* **2006,** *45* (13), 2135-2138.

14. I attempted experiments using both xanthone and propiophenone with different PAGs in the manner described later in the chapter and neither system showed any two-photon acid-generating behaviour, likely due to unfavourable energetics (in the case of xanthone) or the inability of our laser pulses to affect ionization (in the case of propiophenone).

15. Smith, G. A.; McGimpsey, W. G., Two-Laser Photochemistry of Phenothiazine in Solution: Ionization and Bond Cleavage from Upper States. *J Phys Chem* **1994,** *98* (11), 2923-2929.

16. Barra, M.; Calabrese, G. S.; Allen, M. T.; Redmond, R. W.; Sinta, R.; Lamola, A. A.; Small, R. D.; Scaiano, J. C., Photophysical And Photochemical Studies Of Phenothiazine And Some Derivatives - Exploratory Studies Of Novel Photosensitizers For Photoresist Technology. *Chem Mater* **1991,** *3* (4), 610-616.

17. Barra, M.; Redmond, R. W.; Allen, M. T.; Calabrese, G. S.; Sinta, R.; Scaiano, J. C., Photochemistry Of Phenothiazine Sensitizers In Poly (Methyl Methacrylate) Films. *Macromolecules* **1991,** *24*, 4972-4977.

18. Scaiano, J. C.; Laferriere, M.; Ivan, M. G.; Taylor, G. N., A Protocol for the Verification of Acid Generation in 157 nm Lithography. *Macromolecules* **2003,** *36*, 6692-6694.

19. Wallraff, G. M.; Hinsberg, W. D., Lithographic Imaging Techniques For The Formation Of Nanoscopic Features. *Chem Rev* **1999,** *99* (7), 1801-1821.

20. Sanders, D. P., Advances in Patterning Materials for 193 nm Immersion Lithography. *Chem Rev* **2010,** *110* (1), 321-360.

21. McGimpsey, W.; Scaiano, J., Photochemistry And Photophysics From Upper Triplet Levels Of 9,10-Dibromoanthracene. *J Am Chem Soc* **1989,** *111* (1), 335-340.

22. Scaiano, J. C.; Arnold, B. R.; McGimpsey, W. G., 2-Laser, 2-Color Photochemistry from Upper Triplet-States of 2-Bromonaphthalene and 9-Bromophenanthrene in Benzene. *J Phys Chem* **1994,** *98* (21), 5431-5434.

23. Scaiano, J. C.; Johnston, L. J.; McGimpsey, W. G.; Weir, D., Photochemistry Of Organic Reaction Intermediates: Novel Reaction Paths Induced By Two-Photon Laser Excitation. *Acc Chem Res* **1988,** *21*, 22-29.

24. Sokka, I.; Fischer, A.; Kloo, L., Optimization Of The Synthesis Of Non-Symmetrical Alkyl Dimethyl Sulfonium Halides. *Polyhedron* **2007,** *26* (17), 4893-4898.

25. Aggarwal, V. K.; Thompson, A.; Jones, R. V. H., Synthesis of Sulfonium Salts by Sulfide Alkylation; an Alternative Approach. *Tetrahedron Lett* **1994,** *35* (46), 8659-8660.

26. Pappas, S. P.; Tilley, M. G.; Pappas, B. C., Anthracene-Bound Sulfonium Salts: Highly Efficient Photoinitiators For Cationic Polymerization A New Synthesis Of Sulfonium Salts Which Avoids The Use Of Silver Salts. *J Photochem Photobio A* **2003,** *159* (2), 161-171.

27. Billone, P. S.; Park, J. M.; Blackwell, J. M.; Bristol, R.; Scaiano, J. C., Two-Photon Acid Generation in Thin Polymer Films. Photoinduced Electron Transfer As a Promising Tool for Subwavelength Lithography. *Chem Mater* **2010,** *22* (1), 15-17.

5. “Transparent” Photoacid Generators: Performance Evaluation and Mechanistic Investigation

Table of Contents

Graphical Abstract

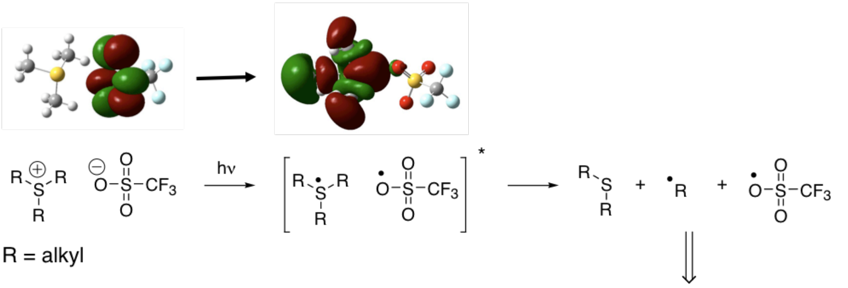

PAG	ε_{193} / cm^{-1}M^{-1}
TES-2	104.54
TES-3	56.14
TES-6	22.95
Si3PAG-2	1007.1
mPAG-2	7.01

5.1 Introduction

5.1.1 Sulfonium Photoacid Generators (PAGs)

As described in Chapter 1.2, photolabile ionic salts are the most widely used PAGs in CAR lithography and have been since the original development of the technology.[1-5] In particular, sulfonium salts have been shown to generate strong acids with high quantum yields and to efficiently catalyze cationic polymerizations and CAR deprotection. Scheme 5.1 illustrates a general acid-producing reaction for a sulfonium PAG with counterion X upon photolysis; the acid generated is HX and therefore the strength of the acid is entirely dependent on the identity of X. While heterolytic mechanisms for photocleavage of sulfonium salts have been observed and discussed as potential acid-generating pathways,[6, 7] the systems most applicable to lithography proceed primarily through homolytic cleavage mechanisms.[3, 5, 7, 8] The direct photolysis cleavage mechanism, as shown in Scheme 5.1, is very similar in nature to the sensitized mechanism discussed in Chapter 3.1 (and illustrated in Scheme 3.1 for naphthalene sensitization) in that they both involve radical intermediates. Although both of these mechanisms are largely agreed upon, there is little more than product studies to support the mechanisms.

Scheme 5.1 Homolytic acid generation from a general sulfonium PAG upon direct photolysis. R’ is formed from proton abstraction by the conjugate base of HX.

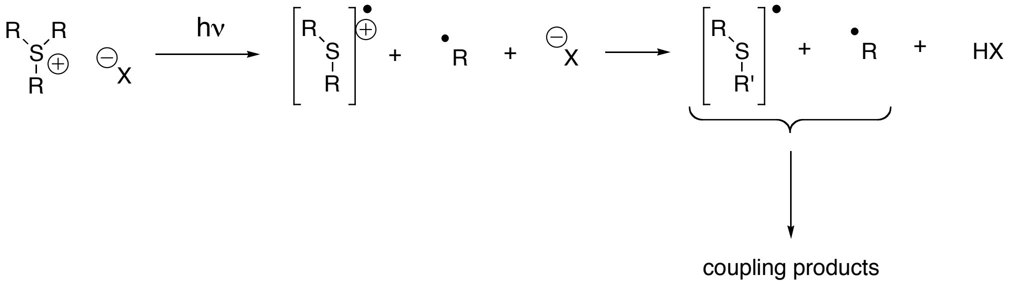

The most widely-used PAGs for lithographic applications, all the way down to the 193 nm technology node, have been those based on triphenylsulfonium (TPS). TPS PAGs have been shown to have excellent quantum yields of acid generation and exceptional lithographic performance.[9] However many of the current technologies and those proposed for next-generation lithography (see Chapters 3 and 4, for example) require the development of “transparent” PAGs. As described in Chapter 4, the main source of inefficiency in the two-photon performance of the mPT-based lithographic system was direct photolysis and acid generation from the PAG itself. That example highlights the importance of designing and synthesizing PAGs that are weakly absorbing at 193 nm. The transparency requirement has been recognized as a major issue in developing new lithographic materials.[10, 11] The general technique to increase transparency at 193 nm has been naturally to decrease the absorbance of the substituents on the sulfonium center; replacing the phenyl groups in TPS with alkyl groups is expected to decrease the absorbance significantly. Unfortunately these changes are also expected to decrease the acid generating ability of the

PAGs dramatically.[12, 13] However this argument assumes that excitation in the sulfonium PAGs is $\pi \rightarrow \pi^*$ and the effect of conjugated substituents is to lower the energy of the π^* excited state such that it efficiently overlaps with the σ^* of the S-C bond (see Scheme 5.1). The results presented herein suggest that this is not a valid assumption.

Most of the attention in developing new PAGs has been directed towards the cationic onium species; sulfonate counterions make Brønsted superacids upon acid extrusion (Scheme 5.1) and are generally transparent at 193 nm. In addition, since the PAGs are salts, metathesis reactions make it simple to vary the sulfonate counterions in order to tailor the properties of the resulting acid.[3, 14-16] Some researchers have looked at the possibility of using specifically-tailored anions to function as the primary absorption units[17, 18] but there are only isolated examples where the effect of the anion on the lithographic performance of the PAGs is evaluated.[19] Even in these cases, little attention is paid to the role of the anion in the actual photochemistry of the PAGs. Since many initial trials are done using simple counterions (e.g., triflate) with the intention of using more relevant counterions for applications once a proof of concept has been shown, it is very important to understand the effects that the anions have on the photochemistry.

5.1.2 Density Functional Theory (DFT) Calculations on PAGs

Despite the enormous industrial impact of lithographic technology and the underlying chemistry, there are still many chemical processes which are not well understood. As mentioned above, the mechanistic state of sensitization reactions is mostly defined by product studies.[3] It is therefore surprising how limited computational studies on lithographically relevant chemistry are; most of the literature examples are focused solely on using time-dependent DFT (TD-DFT) to calculate the absorption spectra of materials meant for use with 157 nm lithography.[20, 21] One group used *ab initio* methods in an attempt to discriminate between the factors which favour homolytic versus heterolytic cleavage of sulfonium salts but their computational methods are low-level and fail to consider many of the complexities of the photochemical reactions studied, including vertical transitions and internal conversion processes.[8] However with recent advances in computational capabilities, DFT calculations could provide useful information regarding electronic transitions, cleavage efficiencies, and sensitization mechanisms that would prove invaluable to future development of lithographic materials.

5.2 Results

5.2.1 Absorption Properties of PAGs at 193 nm

Considering the importance of making PAGs "transparent" for applications at 193 nm, we wanted to systematically look at a series of related trialkyl sulfonium PAGs to understand the nature of their absorption. The five PAGs studied throughout this chapter are shown in Chart 5.1 along with their trivial names. The particular set of PAGs was chosen because it gave the opportunity to study the effect of varying only the anion, in the sub-series of TES-2, TES-3, and TES-6, and the effect of varying the alkyl components of the sulfonium cation, in the sub-series of TES-2, Si3PAG-2, and mPAG-2. The triflate (TES-2, Si3PAG-2, and mPAG-2), nonaflate (TES-3), and triflimide (TES-6) anions are all conjugate bases of organic superacids that are expected to form upon photolysis of their corresponding salts, according to Scheme 5.1.

Chart 5.1 Chemical structures of TES-2, TES-3, TES-6, Si3PAG-2, and mPAG-2.

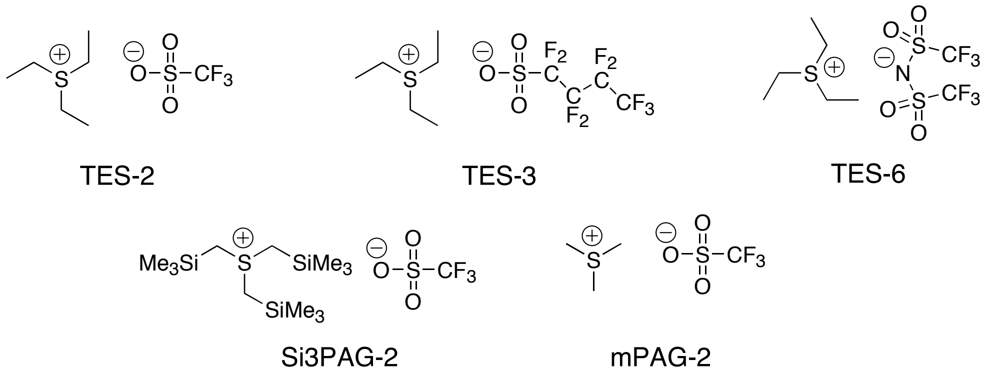
TES-2

TES-3

TES-6

Si3PAG-2

mPAG-2

To evaluate transparency, we felt it most pertinent to measure the absorption coefficients of each of the PAGs at 193 nm. Most of the studies in this chapter are done in solution because it is too difficult to accurately determine concentrations in thin films due to aggregation and preferential adhesion effects.[19] Table 5.1 presents the absorption coefficients of the five PAGs in Chart 5.1 and the concentration range over which they were measured. The absorption coefficients were determined by measuring the absorbance of various concentrations of each PAG and fitting the data to Beer's law:

$$A_{193} = \varepsilon_{193} l C \tag{5.1}$$

where A_{193} is the absorbance at 193 nm, ε_{193} is the absorption coefficient at 193 nm, l is the path length of the cuvette, which is 1 cm in all cases, and C is the concentration of the salt.

Table 5.1 Absorption coefficients of TES-2, TES-3, TES-6, Si3PAG-2, and mPAG-2 in MeCN.

PAG	ε_{193} / cm^{-1}M^{-1}	[ ] Range / mM (n)[a]
TES-2	105	3.2 – 12.5 (4)
TES-3	56.1	2.5 – 15 (6)
TES-6	23.0	3 – 22 (8)
Si3PAG-2	1010	0.5 – 1.6 (3)
mPAG-2	7.01	3 – 22 (8)

[a] The number of points measured in the given concentration range.

From Table 5.1, we can see that Si3PAG-2 is the most strongly-absorbing of all five PAGs at 193 nm, while mPAG-2 is the most transparent. This result was in line with what we expected since the sheer number of molecular orbitals on the cation of

Si3PAG-2 is much greater than in mPAG-2, with the triethylsulfonium cations being in between the two. Interestingly there is a significant difference between the absorption coefficients of the three triethylsulfonium PAGs TES-2, TES-3, and TES-6. This was rather surprising as the absorption properties of sulfonium PAGs have generally only been related to electronic transitions occurring on the sulfonium cation.[8, 18]

To help explain the absorption properties of the PAGs in Chart 5.1, we carried out TD-DFT calculations on them (full computational details are given in the Experimental section 5.5.3). We hoped that these calculations would: a) give a good indication as to how accurate DFT calculations are at predicting the absorption spectra of simple sulfonium PAGs and, b) elucidate the transitions that are contributing to the absorption spectra so that the structures could eventually be tuned accordingly. Figure 5.1 presents the experimental and computational absorption spectra for TES-2, TES-6, Si3PAG-2, and mPAG-2; TES-3 is omitted due to problems with convergence of the TD-DFT calculations. An important issue is that the relative intensities of the computational spectra do not match the experimental observations. While the spectra in Figure 5.1A are not all taken at the same PAG concentrations, the values in Table 5.1 can be compared with the computational results in Figure 5.1B. The computational results suggest that TES-6 has the strongest 193 nm absorption, while TES-2 and Si3PAG-2 have close to identical absorptions.

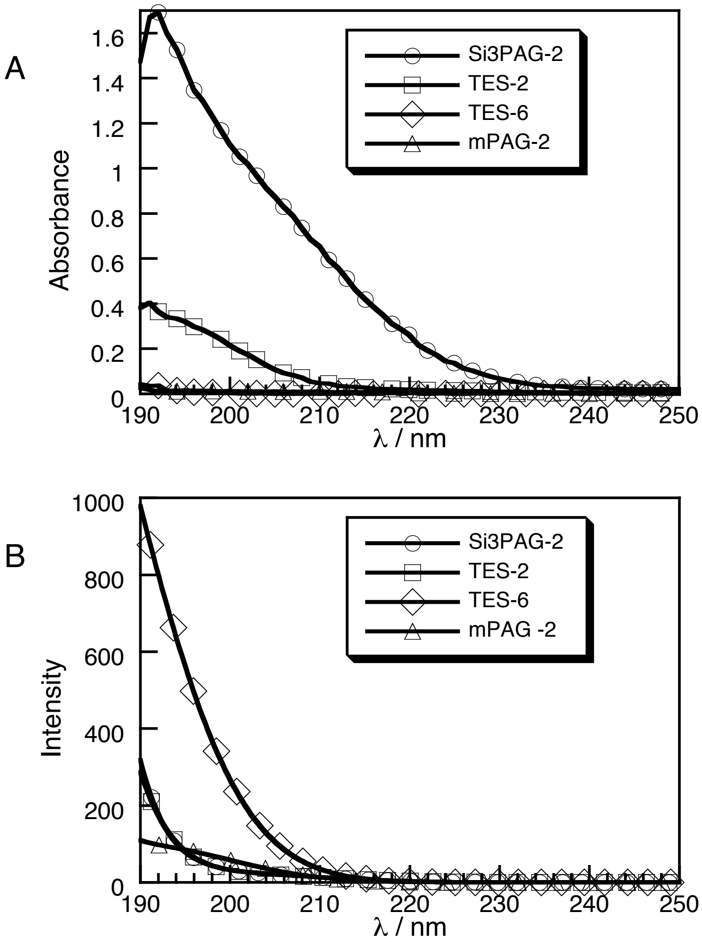

Figure 5.1 A) Experimental UV-Vis absorption spectra of Si3PAG-2 (0.5 mM), TES-2 (3.2 mM), TES-6 (3.0 mM) and mPAG-2 (3.0 mM) in MeCN; B) Electronic absorption spectra of Si3PAG-2, TES-2, TES-6, and mPAG-2 as calculated using TD-DFT.

A possible reason for the discrepancy is evident when looking at the calculated orbitals involved in the transitions contributing most significantly to the 193 nm transitions for each of the PAGs (Figure 5.2). Every transition identified occurs from an occupied orbital predominantly on the anion to an orbital on the cation, for both the triflate and the triflimide salts. Intuitively, this is a logical conclusion as the non-bonding lone-pair orbitals on the anions are expected to be much higher in energy than any of the occupied orbitals centered on the cations; unfortunately this fact has been ignored in developing the mechanisms of Scheme 5.1 and the development of sulfonium PAGs in general. Equilibrium between conformational isomers in solution would affect the oscillator strength of each transition, due to angular momentum constraints on vertical excitation,[22] and therefore change the aggregate oscillator strength of the solution-phase experimental spectrum at each wavelength from those predicted by our calculations (see Discussion 5.3). Despite this shortcoming, the computational results do highlight the fact that the 193 nm transitions identified populate S-C σ^*-antibonding orbitals (Figure 5.2 shows molecular orbital diagrams for mPAG-2), consistent with the homolytic cleavage in the first step of Scheme 5.1, and that the main contributing transitions all occur from the anion to the cation.

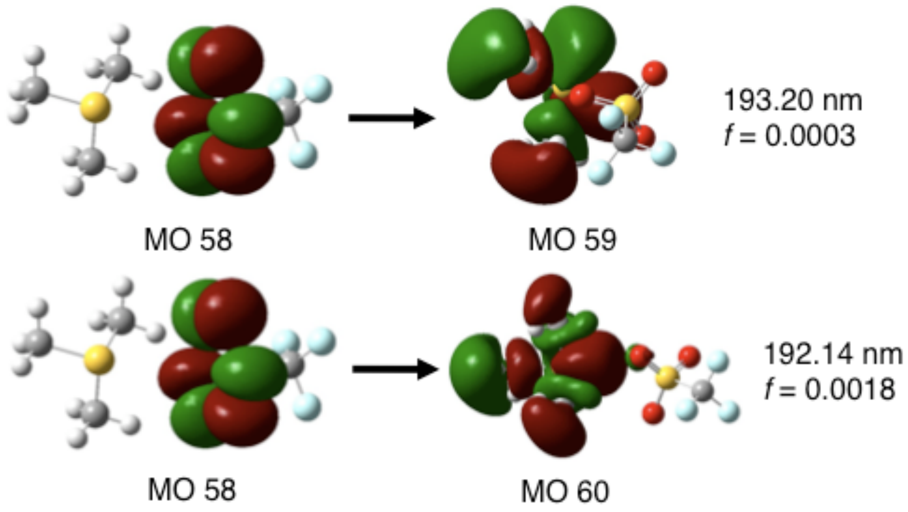

Figure 5.2 Orbitals involved in the transitions contributing most strongly to the 193 nm absorption for mPAG-2 in Figure 4.1B, as identified by TD-DFT. The wavelength

and the oscillator strength (*f*) for each transition are given to the right of each transition. All other PAGs also showed only transitions occurring from anion to cation.

5.2.2 Quantum Yields of Acid Generation from Direct Photolysis

As described in 5.1.1, it is important that a PAG not only be relatively transparent at 193 nm but also have a sufficiently low quantum yield of direct, monophotonic acid generation. While many protocols for measuring acid generation quantum yields have been reported,[9, 10, 13, 23] we did our measurements in solution because our 193 nm exposure set-up is not ideal for large area film irradiations. We also chose to use potentiometric monitoring of the titrations for increased sensitivity and to avoid possible complications from using colourimetric dyes.[24] We chose to use the decarbonylation of diphenylcyclopropenone (DPCP, Scheme 4.2, $\Phi \sim 1$) as our actinometer as it has been shown to work well for reactions at 193 nm.[25] Full experimental details are provided in section 5.5.4 for the trials included in this section. We measured the quantum yield of Si3PAG-2 against the actinometer DPCP and proceeded to use Si3PAG-2 as a secondary actinometer for all of the other PAGs. Unfortunately we were unable to measure the Φ for mPAG-2 because we did not have enough compound to make solutions with $A_{193} > 3$. Plots corresponding to the determination of Φ for Si3PAG-2 are included in Figure 5.3 while Figure 5.4 presents the data for the remaining PAGs measured with respect to Si3PAG-2.

Scheme 5.2 Photodecarbonylation of DPCP.

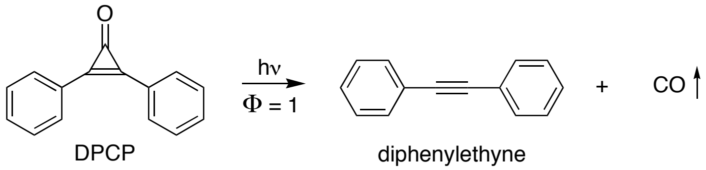

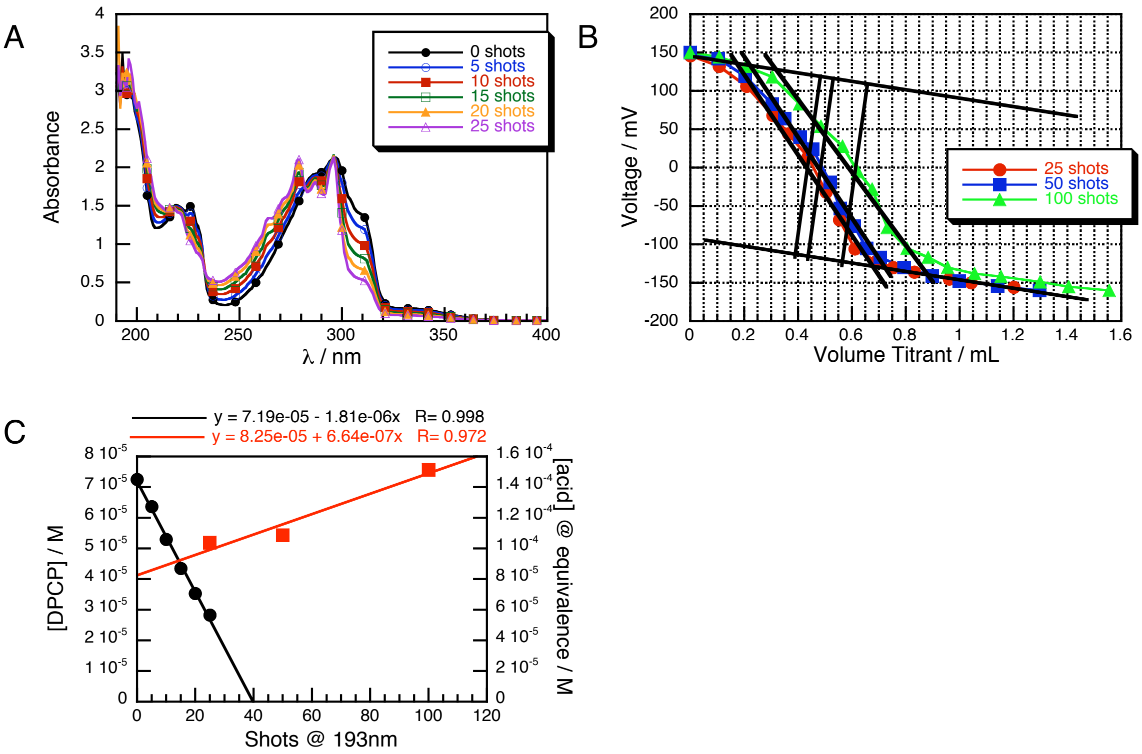

Figure 5.3 A) Absorption spectrum of a MeCN solution of ~0.1 mM DPCP upon exposure to 193 nm laser pulses of 9.3 mJ/pulse; B) Potentiometric titration curves for three samples of 3.7 mM Si3PAG-2 ($A_{193} > 3$) after 25, 50, and 100 shots of 193 nm laser irradiation at 9.3 mJ/pulse; the black lines used to fit the titration data are shown. The titrant was a standardized 2.465 mM NaOH solution; C) Comparison of the disappearance of DPCP and the yield of acid from Si3PAG-2 as a function of 193 nm laser pulses.

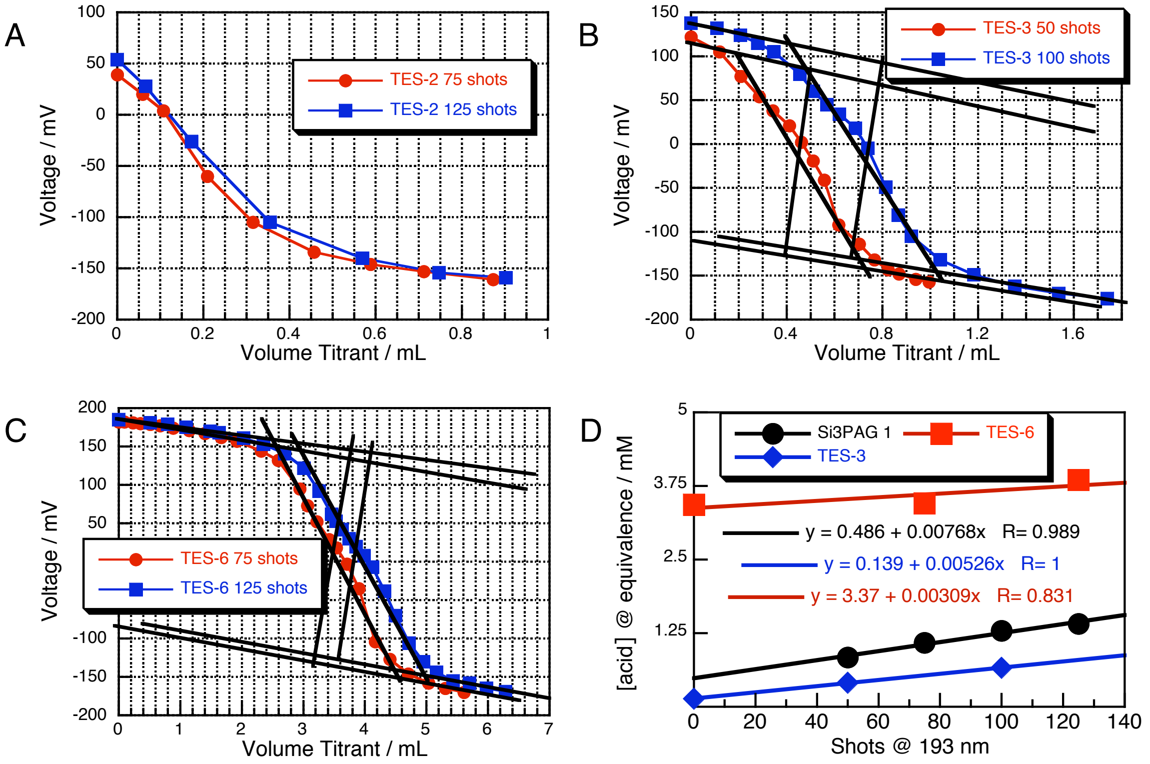

Figure 5.4 A) Potentiometric titration curves for two samples of ~50 mM TES-2 solutions following 75 and 125 shots of 193 nm laser irradiation at 31 mJ/laser pulse; B) Potentiometric titration curves for two samples of ~65 mM TES-3 solutions following 50 and 100 shots of 193 nm laser irradiation at 31 mJ/laser pulse; C) Potentiometric titration curves for two samples of ~200 mM TES-6 solutions following 75 and 125 shots of 193 nm laser irradiation at 31 mJ/laser pulse; D) Comparison of the yield of acid at equivalence for Si3PAG-2, TES-3, and TES-6 as a function of the number of laser shots; no significant acid yield was observed for TES-2 upon irradiation. Titrant was a standardized solution of 2.267 mM NaOH for all points other than the zero points. Zero points for TES-3 and TES-6 were also

determined from the same stock solutions but using a more dilute titrant (standardized 0.349 mM NaOH solution), thus the titration curves are not shown.

Comparing the slope of the acid yield for Si3PAG-2 with the slope of the disappearance of DPCP as a function of laser pulses (Figure 5.3C) we are able to determine a quantum yield of 0.37 for Si3PAG-2. Using that value, we were able to determine quantum yields for TES-3 and TES-6 from the plots in Figure 5.4D; Table 5.2 presents the quantum yield of acid generation values, Φ_{acid}. Note that TES-2 (Figure 5.4A) shows no acid generation upon irradiation beyond the limit of detection for the titration method. Also surprising was the amount of acid present in the PAGs, especially TES-6, with no irradiation. Because the starting materials are expected to be quite pure (i.e., TES-6 was purchased from Aldrich as > 99.0% purity and a new bottle was used for these experiments), the initial acid may be due to hydrolysis of the sulfonium salts upon dilution in the aqueous media used for the titrations.[26] Since photolyses were done before dilution in water and conversions were quite low, we should not expect that the hydrolysis reactions had any impact on the quantum yield measurements.

Table 5.2 Quantum yields of acid generation by direct photolysis of TES-2, TES-3, TES-6, and Si3PAG-2.

PAG	Φ_{acid}
TES-2	~0
TES-3	0.25 ± 0.03
TES-6	0.15 ± 0.10
Si3PAG-2	0.37 ± 0.09

Looking at Table 5.2 it is clear that with the exception of TES-2, the PAGs tested have quite significant acid quantum yields. Without a value for mPAG-2, it is impossible to comment on the influence of the alkyl substituents in the quantum yield. The series of triethylsulfonium PAGs is very informative. As with the absorption properties (5.2.1), the identity of the anion significantly affects the photochemistry of the PAGs. However the trend is not mirrored as one may expect; TES-2, which had the highest ε_{193} value, has the lowest Φ_{acid} of the three. Even more unexpected is that the difference between the triflate and nonaflate anions, in TES-2 and TES-3 respectively, is so pronounced. A plausible explanation for this behaviour is provided in the Discussion section.

5.2.3 PAG Reactivity With $^1O_2$

We had concerns that in the presence of oxygen, some of the molecules proposed as sensitizers for acid generation could also sensitize singlet oxygen ($^1O_2$) formation.[27-30] We wanted to check whether our PAGs react with $^1O_2$, which could adversely affect the performance of sensitizing systems like those in Chapter 3 and

4. Thus we used $^1O_2$ phosphorescence to directly monitor the kinetics of $^1O_2$ disappearance, which has a lifetime of ~80 μs in MeCN.[31, 32] We chose to use methylene blue (MB, Chart 5.2, $\Phi_{1O2} = 0.52$ in MeCN) to sensitize $^1O_2$ formation, then observe the effect on $^1O_2$ lifetime of added PAGs. However we found that with sulfonium triflate salts, there was some sort of reaction to form a new, long-wavelength absorbing species. Thus we used phenalenone (PH, Chart 5.2, Φ_{1O2} = 0.98 in MeCN)

Chart 5.2 Structures of methylene blue (MB) and phenalenone (PH).

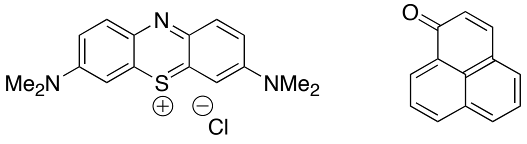

MB PH

Addition of TES-2 had no effect on the lifetime of $^1O_2$ generated from PH sensitization (Figure 5.5) and confirmed that the sulfonium PAGs do not react appreciably with $^1O_2$. This was verified by ^1H and ^{19}F NMR experiments, which both showed no new products upon extended UVA irradiation (30 min) of MeCN-d_3 solutions containing PH and TES-2, TES-6, or Si3PAG-2.

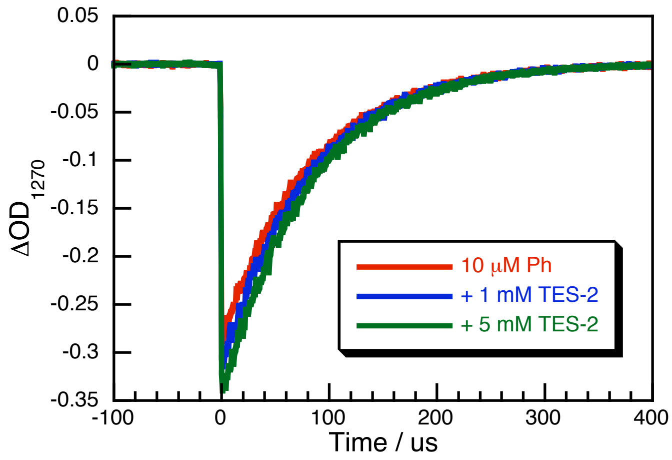

Figure 5.5 The phosphorescence decay of $^1O_2$, measured at 1270 nm, following 355 nm irradiation of a 10 μm solution of PH in MeCN with the addition of increasing concentrations of TES-2. Decay traces measured by LFP are frequently shown "inverted" reflecting the sign of photomultiplier output.

5.3 Discussion

In our evaluation of the absorption properties of the PAGs, we were surprised to find that the role of the anion in sulfonium PAGs had such an influence on the 193 nm absorption coefficients. However, the results are not unexpected: The onset of absorption for all five of the PAGs studied in this chapter is ≤ 230 nm, indicating that the transitions at 193 nm are among their lowest-energy transitions. Intuitively, the highest energy occupied orbitals of each PAG, including the HOMO, would be largely composed of the non-bonding lone pair orbitals of the anions. This was confirmed by our calculations. Therefore the lowest energy transitions likely involve orbitals centered on the anions. As mentioned earlier, this is not unheard of in sulfonium-based PAGs,[17, 18] but in the previously reported cases, the anions were tailored to contain highly conjugated moieties. The involvement of anion orbitals in the absorption properties of PAGs at the 248 nm and 193 nm technology nodes has largely been ignored.[19] The results presented in Table 5.1 are convincing proof that the identity of the anion must be explicitly considered when trying to design “transparent” PAGs for 193 nm lithography. When looking only at the triethylsulfonium series, the triflimide anion would be the most sterically bulky, followed by the nonaflate and then the triflate. The absorptivity increases with the same trend, suggesting that the more sterically hindered the anion is, the greater the inter-ion distances are and therefore the less efficient the electronic transitions would be.

The fact that the 193 nm transitions in these "transparent" PAGs are occurring from the anion to the cation also has very important implications for the mechanism of photoinduced decomposition of sulfonium PAGs. The excited states of the PAGs following the transitions in Figure 5.2 are effectively charge-transfer states and would resemble neutral biradical pairs (Scheme 5.3) which could still generate acid, as shown. Thus the mechanism of acid generation by direct photolysis of trialkyl sulfonium PAGs is likely different than that for triarylsulfonium PAGs (Scheme 5.1). This new mechanism (Scheme 5.3) would be very difficult to verify by experiment: The expected products would still be formed by radical coupling, as in Scheme 5.1. The oxygen-centered triflate radical would readily abstract a hydrogen atom from one of the R-groups on the thioether or from the surrounding polymer to generate the acid molecule.[33] One would assume that similar chemistry occurs when the triflimide counterion is used.

Scheme 5.3 Proposed mechanism for photoinduced cleavage of trialkylsulfonium PAGs; triflate is shown as the anion in this case, but the mechanism is likely the same for nonaflate and triflimide.

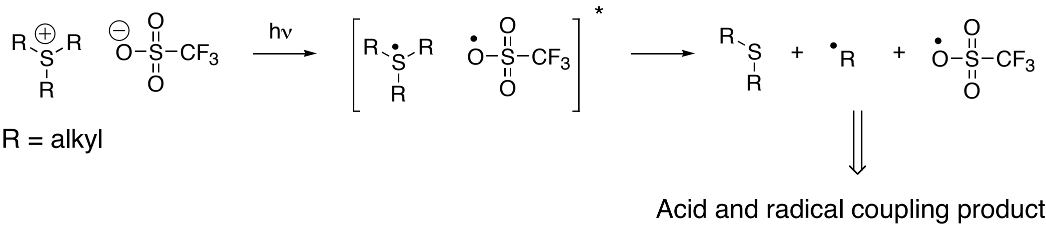

We had hoped that our TD-DFT calculations would help screen for PAG transparency without having to synthesize all potential PAG candidates. However, as evident from a comparison of the results in Table 5.1 with the relative absorbances of the spectra in Figure 5.1B, it appears that current methods, which have proven to be quite robust and useful in the calculation of electronic absorption spectra,[34-37] perform poorly on our sulfonium PAG systems. The reason for this is likely the nature of the inter-ion transitions described above. While the calculations are performed with a solvent correction included, they would not account for the mobility of the two ions with respect to one another. Thus while a sub-population of the salts may adopt the low-energy conformation identified in the calculations, it is reasonable to assume that there are many other orientations in equilibrium due to solubilization of the two ions. This type of effect has been reported for the Raman spectra of other ionic species.[38, 39] One could expect that the absorption properties of the PAGs in restricted, condensed phases such as solids and polymer thin films would match those predicted by our current TD-DFT calculations due to the loss of conformational freedom. All attempts to measure relative absorption coefficients of the PAGs in thin films were unsuccessful due to their low absorptivities, in addition to the issues of aggregation and adhesion[19] mentioned in section 5.2.1.

Referring to Table 5.2, the identity of the anion also has a large effect on the acid quantum yields for sulfonium PAGs when considering the triethylsulfonium PAGs. Previous reports have only considered the role of the sulfonium cations in the acid-generating photochemistry of such PAGs[8, 9, 14, 40] or have found that there *is no effect* of anion identity,[13] though in the latter case the cation also possessed non-bonding orbitals. One other literature case was found where sulfonyl radicals were responsible for acid generation by hydrogen abstraction,[33] as in Scheme 5.3. In that case, the authors also found a difference in quantum yields between triflate and triflimide. However their acid-generating molecules contained covalent bonds between the oxygen of the sulfonyl radicals and a nitrogen on the main chromophore. The photochemical mechanism involved cleavage of that bond and therefore the differences in quantum yields were attributed to the difference in the BDEs, which is not valid in the present case. One possible explanation for the results in Table 5.2 is that the anion, upon absorption and charge-transfer, affects the rate of intersystem crossing (ISC) from the singlet to the triplet state. If ISC is very fast, back electron transfer, which would return the system to its ground state, would be slow and therefore the decomposition of the sulfonyl radical (Scheme 5.3) would occur eventually resulting in acid formation. However if ISC were slow, back electron transfer would compete with the cleavage reaction and the formation of acid would be less likely.

Of the three anions tested, triflate would be expected to be slightly less effective at accelerating ISC than nonaflate, consistent with TES-3 having a higher quantum yield of acid generation than TES-2, despite being more "transparent" at 193 nm. Steric effects are likely the main contribution to the difference in acid quantum yields between the two, however. While we would not expect there to be any significant difference in sterics between triflate and nonaflate if they were coordinating end-on to the sulfonium, our DFT calculations indicate that in all of the PAGs, the S-C bond vector in the triflate is not collinear with the S-S interion bond vector. Since we do not expect a difference in the nature of binding between triflate and nonaflate, the perfluorinated butyl chain of the nonaflate is expected to have more steric repulsion with the ethyl groups of the sulfonium, increasing the interion distance. This is expected to result in both decreased absorptivity and increased ISC rates due to slower back electron transfer (BET), consistent with the higher quantum yield of acid generation.

Concerning the triflimide anion, the ISC rate is expected to be greatly accelerated with respect to sulfonate anions due to the nitrogen having two sulfur atoms attached directly to it. However, the stability of the nitrogen-centered triflimide radical would be significantly different than the oxygen centered triflate and nonaflate radicals, though its relative reactivity would be dependent on its specific electronic configuration.[41] Since we have no information regarding the relative radical reactivity and the quantum yield of acid generation based on the mechanism of Scheme 5.3 would depend not only on the excited state dynamics and radical separation but also on the ability of the formed radicals to abstract a H-atom from the surrounding medium, we are unable to conclusively rationalize the difference between TES-6 and the sulfonate-based PAGs.

The higher Φ_{acid} for Si3PAG-2 compared to the TES series PAGs can be rationalized on the basis of the stability of the alkyl radical formed upon decomposition. As carbon-centered radicals are electron-deficient species, pendant electron-donating groups stabilize them.[42] The trimethylsilyl groups of Si3PAG-2 are better electron-donating groups than the methyl groups in the TES cations and therefore would stabilize the generating radicals and accelerate the rate of cleavage. Considering the combined lack of stabilizing groups and the triflate counterion, we would expect mPAG-2 to have a very low Φ_{acid}, probably close to 0 like TES-2.

Finally, given the reactivity of $^1O_2$ with organic sulfides,[43] it was surprising that there was no reaction of any of the PAGs with $^1O_2$. However, as shown in Schemes 5.1 and 5.3, sulfides are the expected decomposition products of the PAGs and therefore we could expect that upon acid generation from sensitizing systems, the potential formation of singlet oxygen could result in unwanted side-reactions. The interaction between the triflate-containing PAGs and MB, and the quenching of $^1O_2$ generated, was unexpected. The results are included to serve as a caution for future work, but the nature of the interaction and quenching is interesting, nonetheless.

5.4 Summary

The information compiled in this chapter for our limited subset of model "transparent" sulfonium PAGs will remain useful for the lifetime of 193 nm photolithographic technology. Particularly, we have shown that the role of the counterion cannot be ignored while designing a PAG for a specific application. This is especially relevant when a model compound with a triflate counterion is used to model the behaviour of a more lithographically relevant counterion, such as nonaflate. Not only does the anion affect the absorption coefficient, and thus the transparency, and the quantum yields of direct photolysis acid generation, it likely does so as a result of being an integral part of the excited state process. Unlike in Scheme 5.1, where the anion is essentially a spectator, these trialkylsulfonium PAGs likely involve charge-transfer excited states that decompose via radical mediated processes, including H-atom abstraction by the radical of the anion (Scheme 5.3). We have also shown that the sulfonium PAGs are unreactive towards $^1O_2$, a reactive species that could be formed during aerobic lithography with certain sensitizers.

5.5 Experimental

5.5.1 General

All chemicals, solvents, and polymers were purchased from Aldrich unless otherwise stated and were of the highest grade available; the PMMA used had $M_W \sim$ 100,000. Si3PAG-2 and TES-2 PAGs were prepared by our collaborators at Intel; mPAG-2 was a generous gift from Prof. C.G. Willson’s group at The University of Texas at Austin; NMR analysis of all materials indicated that they had not decomposed over the time of storage.

Absorption spectra were measured using a Cary 50 UV-Vis Spectrophotometer from Varian, Inc.

5.5.2 Absorption Coefficient Measurements

All PAG absorption coefficients were measured using the same procedure; a representative example for TES-6 is given. A stock solution of TES-6 was prepared by adding 72.6 mg TES-6 to 500 μL MeCN (0.364 M). Two 1x1 cm quartz precision cuvettes were filled with 2.5 mL MeCN and the absorption spectrum of each was recorded to ensure they were identical. Then 20 μL of the TES-6 stock solution was added to one cuvette and 20 μL MeCN was added to the second; the second cuvette was used as the baseline for the TES-6 measurement. This process was repeated eight times.

5.5.3 DFT Calculations

All calculations were carried out using the Gaussian 03 package.[44] DFT calculations utilized the B3LYP[45-47] exchange correlation functional with the TZVP[48] basis set for all atoms. Tight SCF convergence criteria (10^{-8} au) were used and the converged wavefunctions were tested to ensure that there were no negative vibrational frequencies. The PCM model[49] was employed for solvent corrections in all calculations, with MeCN selected as the solvent. The anion and cation were first constructed and optimized separately, then they were combined and re-optimized. The composition and population of molecular orbitals was determined using the AOMix program.[34] The energies and intensities of the lowest 50-75 (depending on the PAG) singlet-singlet transitions were calculated using TD-DFT. Absorption profiles were calculated from the TD-DFT bands using the reported method,[50] assuming a bandwidth at half-height of 3000 cm^{-1} for all transitions. Pseudo-Voigt functions with 50% weights for contributing Gaussian and Lorentzian functions were used to simulate the absorption bands.

5.5.4 Quantum Yield Measurements

An accumet® single junction, Ag/AgCl glass electrode from Fisher Scientific and a portable pH meter were used for all potentiometric measurements. A description of the experiment to determine the Φ_{acid} of Si3PAG-2 versus DPCP is given below; the Φ_{acid} values for all other PAGs were determined using the same titration technique but were calculated versus the value determined for Si3PAG-2.

The NaOH titrant first had to be calibrated (this was done directly before every titration). 86.8 mg of NaOH was dissolved in 100 mL of H_2O; 10 mL of this solution was removed and diluted to 100 mL with H_2O to make up the titrant solution. Potassium hydrogen phthalate (KHPh) was used as an organic acid standard: 21.6 mg of KHPh was dissolved in 100 mL H_2O (1.06 mM). 10 mL of the KHPh standard solution was added to a beaker with rapid stirring by a magnetic stir bar and diluted to ~30 mL. The titrant was added in small increments from a burette and the potential of the solution (in mV) was measured at each point. This standardization procedure was done twice for every experiment and the average value of the two endpoints was used to calculate the calibrated concentration of the NaOH titrant. An example of the calibration titrations is shown in Figure 5.6.

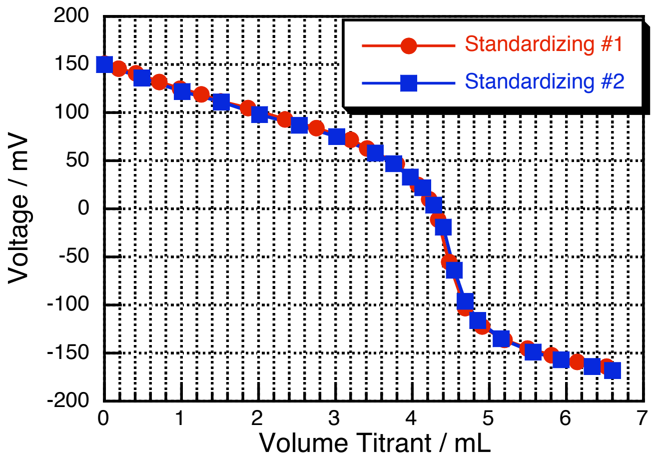

Figure 5.6 Two standardization titrations of the NaOH titrant by titrating 1.06×10^{-5} M KHPh in aqueous solution.

A solution of DPCP was prepared by dissolving ~1 mg of DPCP in 2.5 mL MeCN; the solution was diluted directly in a quartz cuvette, by removing solution and adding

MeCN, until the absorption of the long-wavelength bands at ~300 nm was <2 but $A_{193} > 3$ (~0.1 mM based on its extinction coefficient[25]). The cuvette was sealed and purged with N_2 for 30 min, then exposed to 193 nm laser irradiation; lenses were used to ensure that the entirety of the beams energy was entering the cuvette. The cuvette was shaken after each shot and the absorption spectrum was measured periodically (Figure 5.3A).

A solution of Si3PAG-2 was prepared by dissolving 16.2 mg Si3PAG-2 in 10 mL MeCN (3.66 mM) and 2.5 mL of this solution was put into 3 precision quartz cuvettes; each cuvette was sealed and purged with N_2 for 30 min. The three cuvettes were then exposed to 25, 50, and 100 shots of 193 nm laser irradiation, respectively, at the same energy as the DPCP samples; each cuvette was shaken after every 5 shots. Following exposure, the samples were each transferred quantitatively to a beaker containing ~30 mL of H_2O with rapid stirring by a magnetic stir bar and immediately titrated with the calibrated NaOH titrant, as described above.

The disappearance of the DPCP absorption band at 310 nm and the yield of acid at the endpoint for each Si3PAG-2 titration were plotted against the number of shots absorbed (Figure 5.3C). By taking the absolute value of the slope of DPCP disappearance as 1.0, we were able to calculate the Φ_{acid} for Si3PAG-2.

5.5.5 PAG Reactivity with $^1O_2$

The singlet oxygen phosphorescence time profiles were registered at 1270 nm after excitation of 10 μM sensitizer solutions in MeCN with 355 nm laser irradiation using a Surelite II (Continuum) Nd-YAG laser operating at 355 nm using a Peltier-cooled (–62.8 °C) Hamamatsu NIR detector operating at –700 V, coupled to a computer-controlled grating monochromator. Primary data were acquired and analyzed with a customized Luzchem Research LFP-112 system.

An example will be given for the experiment in Figure 5.7, with phenalenone (PH) and TES-2; all other experiments were performed in the same manner. 3.7 mg of PH was dissolved in 100 mL MeCN (200 μM) and 31.4 mg TES-2 was dissolved in 11.6 mL MeCN (10 mM)). Three cuvettes were prepared: 1) 150 μL PH solution and 2.85 mL MeCN, 2) 150 μL PH solution, 300 μL TES-2 solution and 2.55 mL MeCN, and 3) 150 μL PH solution, 1500 μL TES-2 solution and 1.35 mL MeCN. Each cuvette was purged with O_2 for 15 min. The singlet oxygen phosphorescence time profiles were then measured as described above, with averaging over 10 shots per cuvette.

5.6 References

1. Ito, H.; Willson, C. G.; Frechet, J. M. J. Positive- And Negative-Working Resist Compositions With Acid Generating Photoinitiator And Polymer With Acid Labile Groups Pendant From Polymer Backbone. U.S. Patent # 4,491,628, 1985.

2. Ito, H., Chemical Amplification Resists For Microlithography. *Adv Polym Sci* **2005,** *172*, 37-245.

3. Wallraff, G. M.; Hinsberg, W. D., Lithographic Imaging Techniques For The Formation Of Nanoscopic Features. *Chem Rev* **1999,** *99* (7), 1801-1821.

4. Crivello, J. V., Design And Synthesis Of Photoacid Generating Systems. *J Photopolym Sci Tec* **2008,** *21* (4), 493-497.

5. Sanders, D. P., Advances in Patterning Materials for 193 nm Immersion Lithography. *Chem Rev* **2010,** *110* (1), 321-360.

6. Davidson, R. S.; Goodin, J. W., Some Studies On The Photoinitiated Cationic Polymerization Of Epoxides. *Eur Polym J* **1982,** *18* (7), 589-595.

7. Hoefer, M.; Liska, R., Photochemistry and Initiation Behavior of Phenylethynyl Onium Salts as Cationic Photoinitiators. *J Polym Sci Pol Chem* **2009,** *47* (13), 3419-3430.

8. Ohmori, N.; Nakazono, Y.; Hata, M.; Hoshino, T.; Tsuda, M., Ab Initio Study Of The Photochemical Decomposition Mechanism Of Sulfonium Compounds, A Photoacid Generator. *J Phys Chem B* **1998,** *102* (6), 927-930.

9. Brainard, R.; Higgins, C.; Hassanein, E.; Matyi, R.; Wuest, A., Film Quantum Yields of Ultrahigh PAG EUV Photoresists. *J Photopolym Sci Tec* **2008,** *21* (3), 457-464.

10. Cameron, J. F.; Pohlers, G.; Suzuki, Y.; Chan, N., Transparency Versus Efficiency: Important Considerations In The Design Of Photoacid Generators For ArF Lithography. *J Photopolym Sci Tec* **2002,** *15* (3), 453-464.

11. Nishimae, Y.; Yamato, H.; Asakura, T.; Ohwa, M., Chromophore Effect Of Non-Ionic Photoacid Generators On Resist Performances. *J Photopolym Sci Tec* **2008,** *21* (3), 377-381.

12. Saeva, F. D.; Breslin, D. T.; Martic, P. A., The Effect Of The Nature Of The Lowest Unoccupied Molecular-Orbital (LUMO) Of Some Arylmethylsulfonium Salt Derivatives On Photochemical And Redox Behavior. *J Am Chem Soc* **1989,** *111* (4), 1328-1330.

13. Zhou, W. H.; Kuebler, S. M.; Carrig, D.; Perry, J. W.; Marder, S. R., Efficient Photoacids Based Upon Triarylamine Dialkylsulfonium Salts. *J Am Chem Soc* **2002,** *124* (9), 1897-1901.

14. Dektar, J. L.; Hacker, N. P., Photochemistry Of Triarylsulfonium Salts. *J Am Chem Soc* **1990,** *112* (16), 6004-6015.

15. Ayothi, R.; Yi, Y.; Cao, H. B.; Yueh, W.; Putna, S.; Ober, C. K., Arylonium Photoacid Generators Containing Environmentally Compatible Aryloxyperfluoroalkanesulfonate Groups. *Chem Mater* **2007,** *19* (6), 1434-1444.

16. Crivello, J. V., Applications For Photoacid Generation In Photoimaging And Nanotechnology. *J Photopolym Sci Tec* **2007,** *20* (4), 599-603.

17. Naitoh, K.; Ishii, K.; Yamaoka, T.; Omote, T., Photoreactive Fluorinated Polyimide Protected by Tetrahydropyranyl (THP) Group Based on Chemical Amplification: Acid Generation in Polyimide Film and Lithographic Properties. *Polym Advan Technol* **1993,** *4*, 294-301.

18. Toba, Y., The Design Of Photoinitiator Systems. *J Photopolym Sci Tec* **2003,** *16* (1), 115-118.

19. Lawson, R. A.; Lee, C.; Tolbert, L. M.; Henderson, C. L., Effect Of Acid Anion On The Behavior Of Single Component Molecular Resists Incorporating Ionic Photoacid Generators. *Microelectron Eng* **2009,** *86* (4-6), 738-740.

20. Dixon, D. A.; Matsuzawa, N. N.; Ishitani, A.; Uda, T., Time-Dependent Density Functional Theory Calculations Of Photoabsorption Of Fluorinated Cyclic Molecules In The Vacuum Ultraviolet Region. *Phys Status Solidi B* **2001,** *226* (1), 69-77.

21. Ando, S.; Fujigaya, T.; Ueda, M., Density Functional Theory Calculations Of Photoabsorption Spectra Of Organic Molecules In The Vacuum Ultraviolet Region. *Jpn J Appl Phys 2* **2002,** *41* (2A), L105-L108.

22. Turro, N. J.; Ramamurthy, V.; Scaiano, J. C., *Principles of Molecular Photochemistry. An Introduction.* University Science Books: Sausalito, Calif, 2009.

23. Frechet, J. M. J., The Photogeneration Of Acid And Base Within Polymer-Coatings - Approaches To Polymer Curing And Imaging. *Pure Appl Chem* **1992,** *64* (9), 1239-1248.

24. Sanrame, C. N.; Brandao, M. S. B.; Coenjarts, C.; Scaiano, J. C.; Pohlers, G.; Suzuki, Y.; Cameron, J. F., Mechanism Of Photoacid Generation For An Arylcycloalkylsulfonium Salt By Ring Opening And Aryl Cleavage. *Photochem Photobiol Sci* **2004,** *3* (11-12), 1052-1057.

25. Heafey, E. Applications of Spectroscopy to the Creation and Study of Nanostructures. M.Sc. Thesis, University of Ottawa, 2009.

26. Szabo, D.; Varga, J.; Csampai, A.; Kapovits, I., Optically Active Cyclic Diaryl(Alkoxy)Sulfonium Salts With Intramolecular S•••O Interaction: Synthesis, Absolute Configuration And Stereoselective Hydrolysis. *Tetrahedron-Asymmetry* **2000,** *11* (6), 1303-1312.

27. Baciocchi, E.; Del Giacco, T.; Lanzalunga, O.; Lapi, A.; Raponi, D., The Singlet Oxygen Oxidation Of Chlorpromazine And Some Phenothiazine Derivatives. Products And Reaction Mechanisms. *J Org Chem* **2007,** *72* (15), 5912-5915.

28. Chin, K. K.; Trevithick-Sutton, C. C.; McCallum, J.; Jockusch, S.; Turro, N. J.; Scaiano, J. C.; Foote, C. S.; Garcia-Garibay, M. A., Quantitative Determination Of Singlet Oxygen Generated By Excited State Aromatic Amino Acids, Proteins, And Immunoglobulins. *J Am Chem Soc* **2008,** *130* (22), 6912-6913.

29. Fidder, H.; Lauer, A.; Freyer, W.; Koeppe, B.; Heyne, K., Photochemistry of Anthracene-9,10-endoperoxide. *J Phys Chem A* **2009,** *113* (22), 6289-6296.

30. Tung, C. H.; Wu, L. Z.; Zhang, L. P.; Chen, B., Supramolecular Systems As Microreactors: Control Of Product Selectivity In Organic Phototransformation. *Acc Chem Res* **2003,** *36* (1), 39-47.

31. Schweitzer, C.; Schmidt, R., Physical Mechanisms Of Generation And Deactivation Of Singlet Oxygen. *Chem Rev* **2003,** *103* (5), 1685-1757.

32. Baciocchi, E.; Del Giacco, T.; Lanzalunga, O.; Lapim, A., Singlet Oxygen Promoted Carbon-Heteroatom Bond Cleavage In Dibenzyl Sulfides And Tertiary Dibenzylamines. Structural Effects And The Role Of Exciplexes. *J Org Chem* **2007,** *72* (25), 9582-9589.

33. Malval, J.; Suzuki, S.; Morlet-Savary, F.; Allonas, X.; Fouassier, J.; Takahara, S.; Yamaoka, T., Photochemistry Of Naphthalimide Photoacid Generators. *J Phys Chem A* **2008,** *112* (17), 3879-3885.

34. Gorelsky, S. I. *AOMix: Program for Molecular Orbital Analysis*, 6.42; University of Ottawa: Ottawa, Canada, 2009.

35. Kotyk, M. W.; Gorelsky, S. I.; Conrad, J. C.; Carra, C.; Fogg, D. E., Geometric and Electronic Structure of a C-1-Symmetric Ruthenium-Aryloxide Metathesis Catalyst: An Experimental and Computational Study. *Organometallics* **2009,** *28* (18), 5424-5431.

36. Sarangi, R.; Gorelsky, S. I.; Basumallick, L.; Hwang, H. J.; Pratt, R. C.; Stack, T. D. P.; Lu, Y.; Hodgson, K. O.; Hedman, B.; Solomon, E. I., Spectroscopic And

Density Functional Theory Studies Of The Blue-Copper Site In M121SeM And C112SeC Azurin: Cu-Se Versus Cu-S Bonding. *J Am Chem Soc* **2008,** *130* (12), 3866-3877.

37. Xie, X. J.; Gorelsky, S. I.; Sarangi, R.; Garner, D. K.; Hwang, H. J.; Hodgsont, K. O.; Hedman, B.; Lu, Y.; Solornon, E. I., Perturbations To The Geometric And Electronic Structure Of The CuA Site: Factors That Influence Delocalization And Their Contributions To Electron Transfer. *J Am Chem Soc* **2008,** *130* (15), 5194-5205.

38. Lassegues, J. C.; Grondin, J.; Holomb, R.; Johansson, P., Raman And Ab Initio Study Of The Conformational Isomerism In The 1-Ethyl-3-Methyl-Imidazolium Bis(Trifluoromethanesulfonyl)Imide Ionic Liquid. *J Raman Spectrosc* **2007,** *38* (5), 551-558.

39. Umebayashi, Y.; Mitsugi, T.; Fujii, K.; Seki, S.; Chiba, K.; Yamamoto, H.; Lopes, J. N. C.; Padua, A. A. H.; Takeuchi, M.; Kanzaki, R.; Ishiguro, S., Raman Spectroscopic Study, DFT Calculations and MD Simulations on the Conformational Isomerism of N-Alkyl-N-methylpyrrolidinium Bis-(trifluoromethanesulfonyl) Amide Ionic Liquids. *J Phys Chem B* **2009,** *113* (13), 4338-4346.

40. Pause, L.; Robert, M.; Saveant, J. M., Stepwise And Concerted Pathways In Photoinduced And Thermal Electron-Transfer/Bond-Breaking Reactions. Experimental Illustration Of Similarities And Contrasts. *J Am Chem Soc* **2001,** *123* (21), 4886-4895.

41. Hedaya, E.; Hinman, R. L.; Schomaker, V.; Theodoro, S.; Kyle, L. M., Succinimidyl Radical Problem . Ease Of Formation Of Nitrogen And Oxygen Pi And Sigma Free Radicals. *J Am Chem Soc* **1967,** *89* (19), 4875-&.

42. Anslyn, E. V.; Dougherty, D. A., *Modern Physical Organic Chemistry*. University Science Books: Sausilito, 2004.

43. Clennan, E. L., Persulfoxide: Key Intermediate In Reactions Of Singlet Oxygen With Sulfides. *Acc Chem Res* **2001,** *34* (11), 875-884.

44. Frisch, M. J. T., G. W.; Schlegel, H. B.; Scuseria, G. E.; Robb, M. A.; Cheeseman, J. R.; Montgomery, Jr., J. A.; Vreven, T.; Kudin, K. N.; Burant, J. C.; Millam, J. M.; Iyengar, S. S.; Tomasi, J.; Barone, V.; Mennucci, B.; Cossi, M.; Scalmani, G.; Rega, N.; Petersson, G. A.; Nakatsuji, H.; Hada, M.; Ehara, M.; Toyota, K.; Fukuda, R.; Hasegawa, J.; Ishida, M.; Nakajima, T.; Honda, Y.; Kitao, O.; Nakai, H.; Klene, M.; Li, X.; Knox, J. E.; Hratchian, H. P.; Cross, J. B.; Bakken, V.; Adamo, C.; Jaramillo, J.; Gomperts, R.; Stratmann, R. E.; Yazyev, O.; Austin, A. J.; Cammi, R.; Pomelli, C.; Ochterski, J. W.; Ayala, P. Y.; Morokuma, K.; Voth, G. A.; Salvador, P.; Dannenberg, J. J.; Zakrzewski, V. G.; Dapprich, S.; Daniels, A. D.;

Strain, M. C.; Farkas, O.; Malick, D. K.; Rabuck, A. D.; Raghavachari, K.; Foresman, J. B.; Ortiz, J. V.; Cui, Q.; Baboul, A. G.; Clifford, S.; Cioslowski, J.; Stefanov, B. B.; Liu, G.; Liashenko, A.; Piskorz, P.; Komaromi, I.; Martin, R. L.; Fox, D. J.; Keith, T.; Al-Laham, M. A.; Peng, C. Y.; Nanayakkara, A.; Challacombe, M.; Gill, P. M. W.; Johnson, B.; Chen, W.; Wong, M. W.; Gonzalez, C.; and Pople, J. A. *Gaussian 03*, D.01; Gaussian, Inc.: Wallingford, CT, 2003.

45. Becke, A. D., Density-Functional Thermochemistry .3. The Role Of Exact Exchange. *J Chem Phys* **1993,** *98* (7), 5648-5652.

46. Miehlich, B.; Savin, A.; Stoll, H.; Preuss, H., Results Obtained With The Correlation-Energy Density Functionals Of Becke And Lee, Yang And Parr. *Chem Phys Lett* **1989,** *157* (3), 200-206.

47. Lee, C. T.; Yang, W. T.; Parr, R. G., Development Of The Colle-Salvetti Correlation-Energy Formula Into A Functional Of The Electron-Density. *Phys Rev B* **1988,** *37* (2), 785-789.

48. Schafer, A.; Huber, C.; Ahlrichs, R., Fully Optimized Contracted Gaussian-Basis Sets Of Triple Zeta Valence Quality For Atoms Li To Kr. *J Chem Phys* **1994,** *100* (8), 5829-5835.

49. Miertus, S.; Scrocco, E.; Tomasi, J., Electrostatic Interaction Of A Solute With A Continuum - A Direct Utilization Of Abinitio Molecular Potentials For The Prevision Of Solvent Effects. *Chem Phys* **1981,** *55* (1), 117-129.

50. Gorelsky, S. I.; Lever, A. B. P., Electronic Structure And Spectra Of Ruthenium Diimine Complexes By Density Functional Theory And INDO/S. Comparison Of The Two Methods. *J Organomet Chem* **2001,** *635* (1-2), 187-196.

6. Synthesis and Characterization of Fluorescent Silver Nanoparticles

Table of Contents

Graphical Abstract

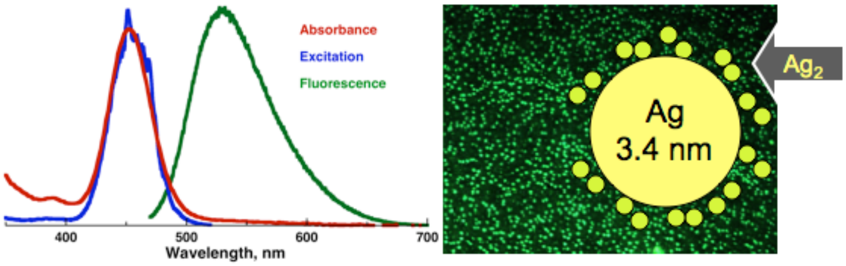

6.1 Introduction

All of the lithography discussed in previous chapters has been concerned with photoinduced acid-catalysed chemical amplification that causes a solubility change in the photoresist formulation being irradiated. As described in Section 1.1, the image formed is one of bare substrate and remaining photoresist; the substrate is subsequently functionalized and forms the basis of the working device. This type of positive-tone photolithography is used to produce almost all of the world's microchips and integrated circuits.[1, 2] However this is but one of a multitude of photolithographic strategies for making functional micro- and nanomaterials.

One of the most active fields of current photolithographic research involves patterning of functionality directly into the photoresist.[3] Because the desired properties do not arise from patterning a rigid substrate such as silicon, these functional polymers can be used to form flexible electronics for applications such as flexible display development and flexible electronic devices.

Polymers functionalized with fluorescent patterns are especially appealing for digital optical data storage devices, among other applications.[4, 5] Specifically, photolithographic fluorescence patterning provides a convenient route to holographic 3-D images which are important in high-density data storage devices; holographic patterning has been proposed as a potential candidate for next generation storage devices due to its ability to store information in 3-D arrays as opposed to the 2-D data architecture of traditional lithographic techniques.[6] While significant advances have been made in holographic imaging for optical data storage and many materials have been developed, most of them are based on organic fluorophores or fluoropolymers.[7-12] While many of these materials exhibit the desired spectral properties or are easily patterned, the fact that they are all based on organic emitters leaves them prone to device degradation, especially in a device where reading must be done with an optical source.[7]

Among many other desirable properties, fluorescent semiconductor nanomaterials are traditionally characterized by moderate-to-high quantum yields[8-13] and perhaps more importantly for device applications, great chemical and photochemical robustness.[14] While these exceptional properties have garnered these materials a lot of attention for sensing[14-18] and tracking[19] applications, they are synthesized using solution processes[8-10] and therefore are not suitable for photolithographic fluorescence patterning. In addition, semiconductor quantum dots (Chapter 2) frequently present problems related to the intrinsic blinking of their luminescence, and to toxicity issues that limit their applications in the health sciences,[20] where lithography remains relevant for applications in assay production and microfluidics.[21] Further, while a shell makes them more robust and perhaps more amenable to biological applications, it also limits their use in some sensing applications, since the same shell that brings these benefits also reduces their sensitivity to potential solution analytes.[18, 22] Thus it is desirable to be able to photochemically synthesize fluorescent nanomaterials that retain the desirable photophysical and photochemical properties of QDs but at the same time possess more well-characterized emission behaviour and be more chemically inert.

Metal nanoparticles, particularly those from coin metals, are expected to have lower toxicity than semiconductor QDs. Particles of a few nanometers in diameter frequently display a plasmon absorption that in the case of gold and silver is readily detectable in the visible spectral region.[23-25] This absorbance is due to the collective oscillation of the electrons in the conduction band and is not associated with any significant emission, although other chromophores near the surface can undergo enhanced transitions, sometimes resulting in increased luminescence.[26, 27] The vast majority of reductive processes leading to metal nanoparticles rely on the use of thermal methods, such as citrate or borohydride reduction.[28, 29] However, some applications make use of photochemical methods that offer temporal and spatial control (as needed for imaging applications) and where the rate of reduction can be readily controlled by adjusting the incident light intensity.[30, 31] Thus while metallic nanoparticles are easily synthesized using photochemical means, as desired for lithographic applications, they lack the corresponding emission which makes semiconductor QDs so appealing in the applications discussed above.

In contrast with metal nanoparticles in the nanometer scale, very small clusters can show remarkably strong emission.[38-56] In the case of silver, clusters such as Ag_2, Ag_3 and Ag_4 have well characterized fluorescence.[32-35] This emission has molecular-type properties, and can have relatively long lifetimes and good, mirror image relationship between absorption and emission. However, these aggregates by themselves are effectively too small and unstable for many practical applications, and it is desirable to stabilize or encapsulate them with other materials, suitable for applications in sensing, chemical biology or advanced materials.[36] Thus we hoped to use a photochemical synthesis to generate small silver clusters along with silver nanoparticles and couple their desirable emission properties to the fluorescence enhancement capabilities of the silver nanoparticles. This chapter describes the facile photochemical synthesis of highly fluorescent functional silver nanoparticles both in solution and polymer films. These particles are very stable and can be reliably and reproducibly synthesized. While the observable silver fluorescent nanoparticles (AgFNP) are of nanometer dimensions, we believe that the emission arises from nanoparticle-supported small metal clusters, a conclusion based on their spectroscopic properties and fluorescence microscope images of the polymer-embedded particles. Luminescence from small clusters on particle surfaces is rare but not unprecedented.[37]

6.2 Results

6.2.1 Photochemical Synthesis and UV-Vis Spectroscopy

Ketyl radicals are known to be strong reducing agents, suitable for metal ion reduction.[38-41] In our case we chose I-2959 as our source of ketyl radicals; the choice reflects the excellent absorption properties of I-2959 in the UVA region, the high quantum yield of radical generation, as well as the fact that the short triplet lifetime of I-2959 reduces the likelihood of excited state quenching by other solution components,[42] notably amines[43] and silver ions.[30] Scheme 6.1 shows the proposed mechanism for the formation of silver nanoparticles.

Scheme 6.1 Overview of the proposed mechanism for the formation of stabilized silver fluorescent nanoparticles (AgFNP).

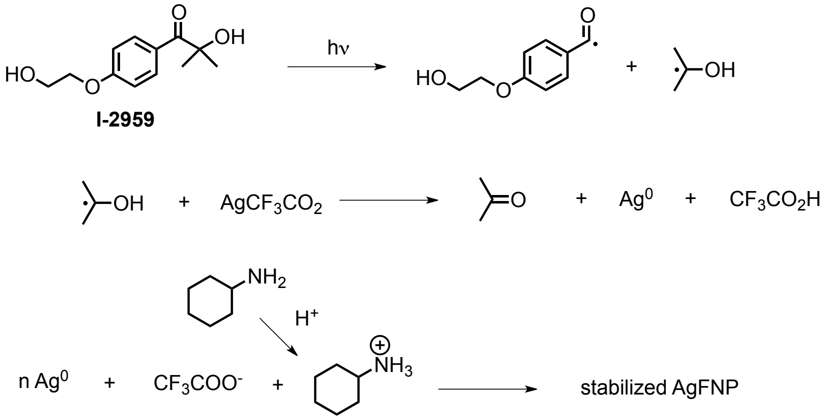

The spectral changes observed upon irradiation (4 UVA lamps) of a quartz cuvette containing 2 mM each of $AgCF_3COO$, I-2959 and cyclohexylamine are shown in Figure 6.1. Approximately 80% of the maximum achievable absorption is reached within three minutes of exposure. The maximum is initially at 447 nm and gradually shifts to 449 nm; it is likely that this shift simply reflects an underlying increase in light scattering, or the formation of plasmon absorbance due to nanoparticles (*vide infra*). The particles produced in this manner were stable for at least several months, even in the presence of air and without protection from ambient light, as determined by their UV-Vis spectra.

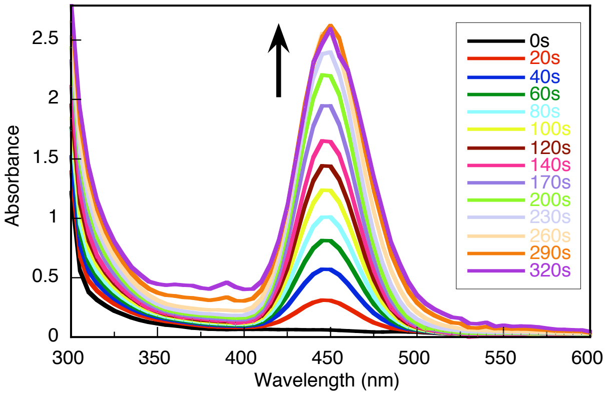

Figure 6.1 UV-Vis absorption spectra following irradiation (350 nm, 4 lamps) of a toluene solution containing 2 mM silver trifluoroacetate, 2 mM I-2959, 2 mM cyclohexylamine. Reaction performed and monitored directly in a 0.7x0.3 cm quartz cuvette.

While cyclohexylamine proved to be effective in the formation and stabilization of these particles, other amines were also found to work. While our search was not exhaustive, for example, hexadecylamine (HDA) also gave excellent results. Many other amines, including triethylamine and butylamine, were tested and did not yield fluorescent particles, resulting sometimes in cloudy orange/brown suspension, suggestive of extensive nanoparticle aggregation. Absorbance spectra of samples prepared with triethylamine and in the absence of amine are presented in Figure 6.2. With triethylamine, a weak absorption band is visible at 415-420 nm, with no associated fluorescence, and there is significant optical scattering at longer irradiation times, indicative of the formation of large aggregates of Ag nanoparticles or bulk silver.

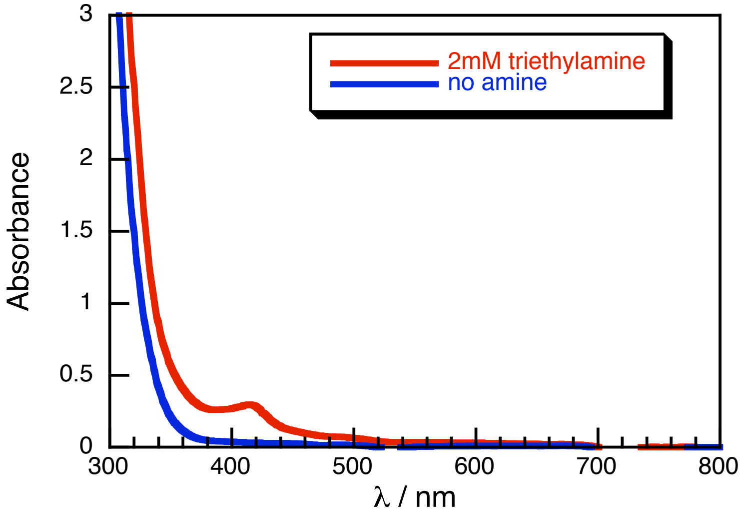

Figure 6.2 Absorbance spectra of 2 mM silver trifluoroacetate, 2 mM I-2959, and 2 mM triethylamine (**red**), and 2 mM silver trifluoroacetate, and 2 mM I-2959, with no amine (**blue**), in THF following 10 min irradiation (4 lamps, 350 nm) in 1×1 quartz cuvettes.

The growth plot for hexadecylamine also shows a maximum at 449 nm, and is slightly lower than that for cyclohexylamine. The two growth plots are compared in Figure 6.3. Interestingly, with hexadecylamine at irradiation times longer than 300 seconds we observe a small band at 552 nm, possibly due to larger aggregates (*vide infra*).

While toluene proved an excellent solvent for AgFNP synthesis, a few other solvents were tested. Among these THF proved to be a convenient one.

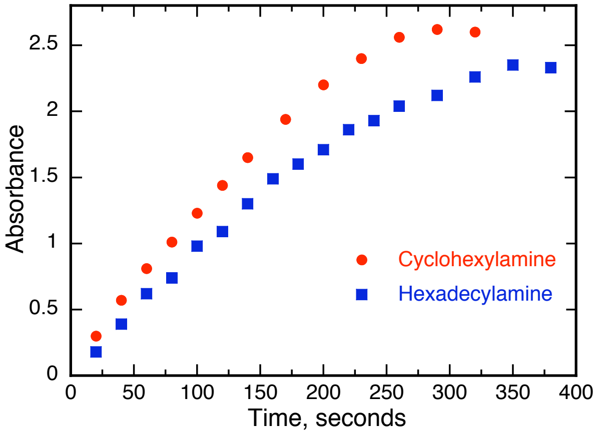

Figure 6.3 Growth of the 450 nm absorption band upon irradiation (350 nm, 4 lamps) in toluene. Initial concentrations: 2 mM silver trifluoroacetate, 2 mM I-2959, 2 mM amine. Reaction performed in 0.7x0.3 cm quartz cuvette.

In a typical experiment, a nitrogen saturated THF solution of 5.0 mM $AgCF_3COO$, 5.0 mM cyclohexylamine, and 5.0 mM I-2959 was irradiated with UVA light. Upon irradiation we observe the growth of a sharp absorption band centered at 438 nm with a smaller peak at 390 nm (Figure 6.4 and below in Figure 6.7). Control reactions were performed in the absence of the photoinitiator at the same working concentrations and no absorption was observed. The concentration of starting reagents was also varied from 2 – 30 mM for each component. When the concentrations were kept equimolar and below 10 mM, an absorption band centered at 438 nm was observed to grow upon photolysis in THF as solvent. The most significant difference between these experiments was that the value at which the absorption band was found to plateau increased with increasing concentrations. However, the decay of the absorption band (*vide infra*) was also accelerated at higher concentrations; thus, 5 mM was adopted as the optimal compromise for signal intensity and stability. Figure 6.5 shows the spectra of reaction mixtures performed at various concentrations. One can see by comparison between Figures 6.4 and 6.5 that there does seem to be an optimal concentration ratio of 1:1:1 between the three components where formation of the absorbing species is maximized; the absorptions at 438 nm of the traces in Figure 6.5 represented by ◇ and × are more than three times lower than the corresponding 2 min trace in Figure 6.4. At higher concentrations than those shown in Figure 6.5 (30 mM of each), a thermal reaction occurred over several hours and similar absorption and emission peaks were observed. This thermal reaction was extremely sensitive to the age and quality of both reagents and solvent and was of limited use because of its irreproducibility. The use of amines as reducing agents had previously been reported as a route to metallic nanoparticles.[44]

The effect of oxygen on the synthesis of AgFNP was also examined in THF. The only significant effect observed in aerated solutions was an approximately 2 minute induction period, which we attribute to the sacrificial use of some of the initially photogenerated radicals to consume the dissolved oxygen; we note that since the samples are not stirred and the irradiation times are quite short, oxygen is unlikely to be significantly replenished from the gas phase. Interestingly, the reaction of ketyl radicals with oxygen yields superoxide radicals (or $HO_2\bullet$ in non-polar solvents).[45, 46] It would seem that under our experimental conditions $HO_2\bullet$ does not reduce Ag^+ to Ag^0. The maximum under these conditions was at about 438 nm, slightly blue shifted with respect to that observed in toluene.

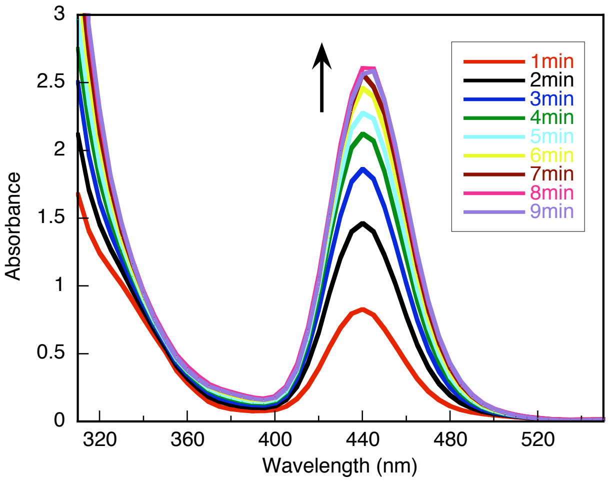

Figure 6.4 UV/VIS absorption spectra at various time intervals during irradiation (350 nm, 4 lamps) directly in THF. Initial concentrations: 5 mM silver trifluoroacetate, 5 mM I-2959, 5 mM cyclohexylamine. Reaction performed in 1x1 cm quartz cell.

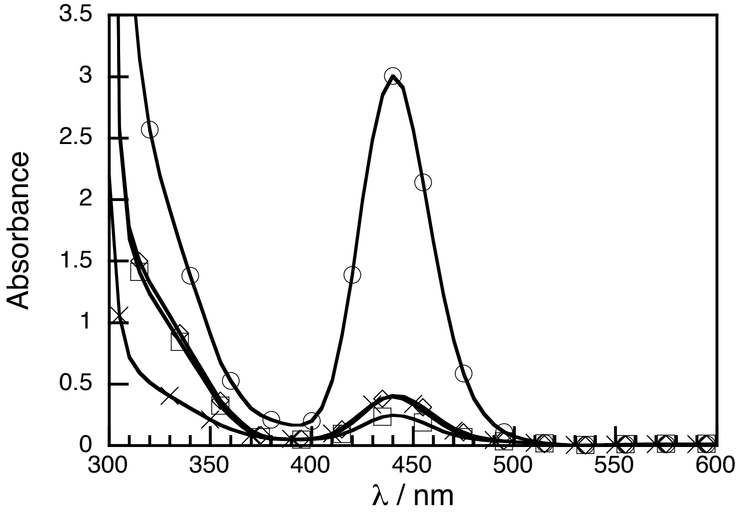

Figure 6.5 Absorbance spectra of 10 mM silver trifluoroacetate, 10 mM I-2959, and 10 mM cyclohexylamine (○), 2 mM silver trifluoroacetate, 2 mM I-2959, and 5 mM cyclohexylamine (□), 5 mM silver trifluoroacetate, 5 mM I-2959, and 2 mM cyclohexylamine (◇), and 5 mM silver trifluoroacetate, 2 mM I-2959, and 5 mM cyclohexylamine (×), all in THF following 2min irradiation (4 lamps, 350 nm) in 1×1 quartz cuvettes.

In contrast to the case of toluene where particles are stable for months, this is not the case in THF, where particles decay over a few hours, as shown in Figure 6.6. The thermal decay of the absorbance in THF follows a first-order monoexponential decay with a lifetime of 154 minutes.

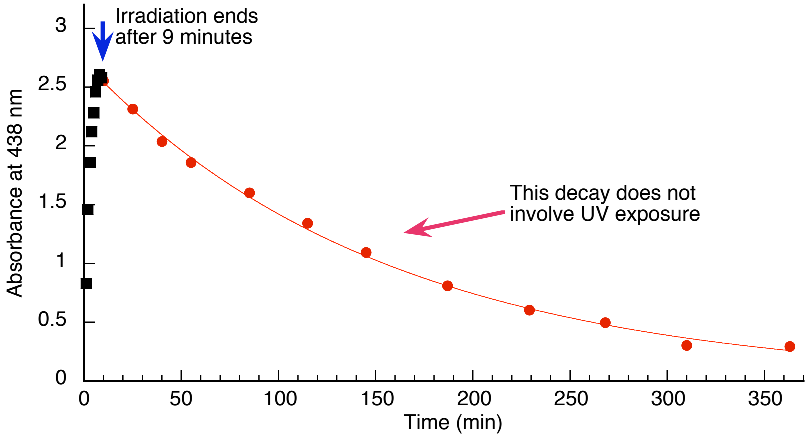

Figure 6.6 Growth and decay of the absorbance at 438 nm following 9 min UVA exposure under the same conditions as in Figure 6.4.

We believe that the instability in THF is due to dissolution of the ammonium trifluoroacetate salt which forms a major part of the stabilizing layer on the particles, as indicated by NMR results (*vide infra*). Given the lack of long-term stability shown in Figure 6.6, one could assume that synthesis in THF solvent was simply not practical. However, imaging data (*vide infra*) suggests that use of THF for nanoparticle synthesis leads to narrower polydispersity than in the case of toluene. This led us to explore ways of purifying particles originally made in THF to enhance their long-term stability. Transfer to toluene was an obvious choice, given the recorded stability in this solvent. After THF evaporation we added toluene to yield a bright yellow solution and a white precipitate which was filtered and characterized by NMR as 4-ethanoloxybenzoic acid (**6.1**; an oxidation product of the benzoyl radical of Scheme 6.1). We found that upon redispersion in toluene, the particles were stable for several weeks when stored at –5°C. Upon standing at -5°C, a white precipitate is formed and characterized as excess cyclohexylammonium salt **6.2** present in the reaction mixture. The preceding procedure, including evaporation of THF overnight under high-vacuum, redispersion in toluene, gravity filtering of insoluble **6.1**, storage at -5 °C overnight, and gravity filtering of any insoluble salts, will be referred to as the cool/filtration purification process for the remainder of this chapter. Sometimes after removal of the sample from the fridge and re-equilibration to room temperature the particles decomposed quickly giving a brown solution. We believe the stability following removal to room temperature is an indication of how much salt **6.2** had precipitated from solution; when too much **6.2** was precipitated due to extended storage at -5°C, the particles decomposed quickly upon warming to room temperature. In addition we observed shifts in the absorption and emission bands to ~450 nm and 530 nm, respectively (*vide infra*). This change may be due to the difference in dielectric constants of the two solvents[47] as well as to the degree of surface coverage by the quaternary ammonium salt.

Chart 6.1 Structure of 4-(2-ethanoloxy)benzoic acid, **6.1**, and cyclohexylammonium trifluoroacetate, **6.2**.

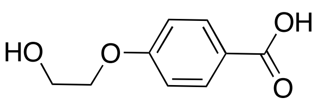

6.1

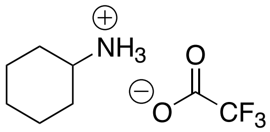

6.2

It was interesting to note that in addition to the strong absorption band (at 452 nm after toluene resuspension), we also observed a weak but characteristic peak at approximately 390 nm, as shown in the inset in Figure 6.7. We do not believe that the bands around 450 nm are due to the plasmon band of Ag NPs, but it is likely that the absorbance at 390 nm (with no associated emission) is due to plasmon transitions.

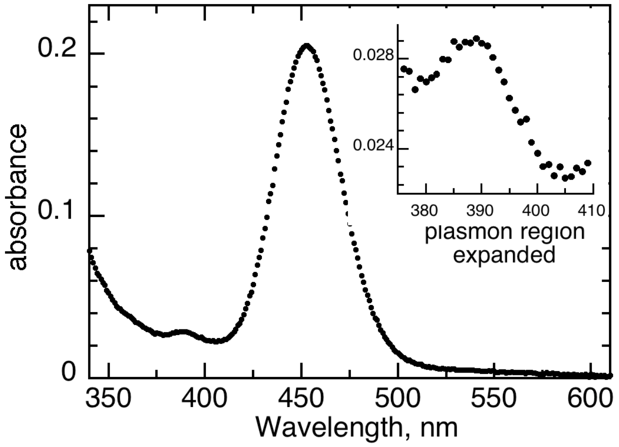

Figure 6.7 UV/Vis absorption spectrum of Ag particles in toluene prepared using the same procedure as in Figure 6.4 followed by transfer to toluene. The inset shows the band we believe to be due to plasmon absorption.

6.2.2 Fluorescence Spectroscopy

The nanoparticles described in the preceding section showed strong luminescence in the visible region. Figure 6.8 shows the emission, excitation and absorbance spectra from a sample irradiated for four minutes under the conditions described above in Figure 6.4. A comparison between the emission and excitation spectra in THF and toluene is included in Figure 6.9. Interestingly, in THF the emission was quite red shifted (λ_{max} 580 nm) with respect to the maximum at 528 nm observed in toluene. The sample yielding the fluorescence spectra in THF solution contains silver nanoparticles, but also the photoproducts originated from the photodecomposition of I-2959 (these products emit weakly at 465 nm). Instead, the fluorescence spectra obtained in toluene solutions and originally prepared in THF reflect AgFNP that have been purified by the cooling/filtration process.

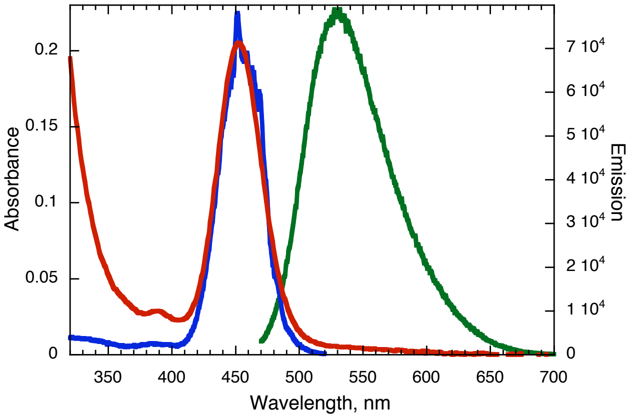

Figure 6.8 Absorption (red), emission (green) and excitation (blue) spectra of Ag particles after 4 minutes of irradiation in THF under the conditions of Figure 6.4 and re-suspension in toluene.

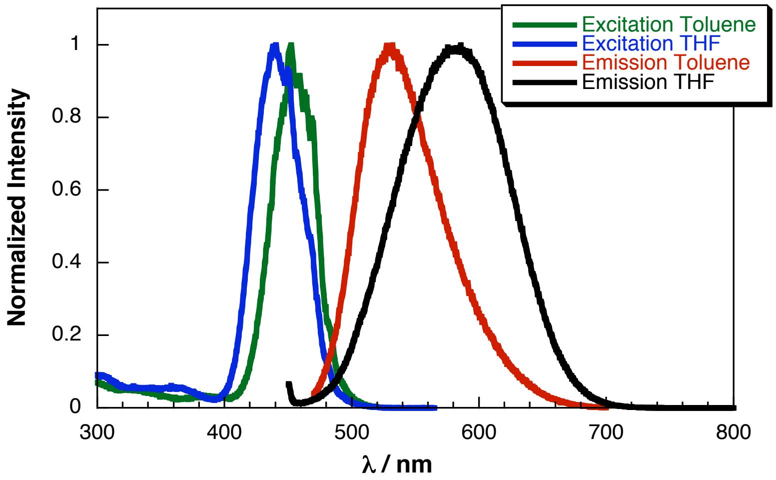

Figure 6.9 Normalized Excitation and Emission spectra for AgFNPs in both toluene and THF synthesized from 2 mM silver trifluoroacetate, 2 mM I-2959, and 2 mM cyclohexylamine. The spectra in THF were recorded immediately after 9 min irradiation (350 nm, 4 lamps), while the spectra in toluene were recorded following the cool/filtration purification process (described in Section 6.2.1) on particles initially synthesized in THF under the same irradiation conditions as the THF sample.

The determination of quantum yields was carried out using fluorescein as an emission standard. It is important to select a reference compound with an adequate spectral overlap with the material under study.[18] Relevant spectra are shown in Figure 6.10. Equation 6.1 shows the expression used for the case of toluene, and includes an appropriate refractive index correction.

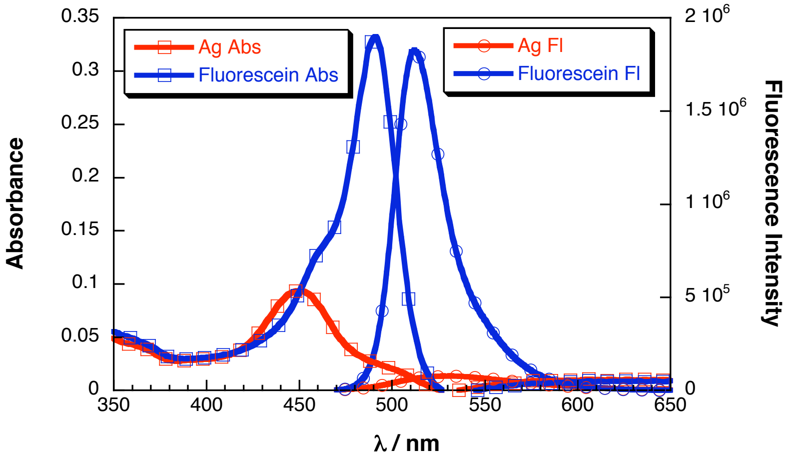

Figure 6.10 Absorbance (□) and fluorescence (○) spectra of fluorescein in aqueous 0.1 M NaOH (–**)** and cyclohexylamine-AgFNPs in toluene (–) used to determine the quantum yield of fluorescence of the AgFNPs. The AgFNPs in this spectrum were synthesized in THF and purified by the cooling/filtration procedure explained in the text. The quantum yield of fluorescein in aqueous 0.1 M NaOH is known to be 0.925.[48] Excitation wavelength used was 450 nm. All other quantum yields were obtained using the same fluorescein solution and optical matching at 450 nm.

$$\Phi_{\text{sample}} = \Phi_{\text{ref}} \cdot \frac{I_{\text{sample}}}{I_{\text{ref}}} \cdot \frac{A_{\text{ref}}}{A_{\text{sample}}} \cdot \frac{\eta^2_{\text{sample}}}{\eta^2_{\text{ref}}} \qquad (6.1)$$

where Φ_{ref} is the known quantum yield of the reference compound, I_{sample} and I_{ref} are the integrated fluorescence intensities of the sample and reference, respectively, A_{ref} and A_{sample} are the absorbance of the reference and the sample at the excitation wavelength, and η_{sample} and η_{ref} are the refractive index of the sample solvent and reference solvent, respectively.

The fluorescence quantum yields obtained are summarized in Table 6.1, and are based on the integrated fluorescence between 470 nm and 700 nm. The absorbance of each sample and the fluorescein reference at 450 nm (excitation wavelength) was 0.090 (Figure 6.10).

Table 6.1 Fluorescence quantum yields in toluene for various AgFNP determined using fluorescein as a reference standard, and for different synthesis solvents.

Solvent	Synthesis amine	Φ_{F1}[†] (±10%)
Toluene	Hexadecylamine	0.11
Toluene	Cyclohexylamine	0.15
THF	Cyclohexylamine	0.11

[†] Fluorescein standard. Excitation wavelength 450 nm.

The fluorescence quantum yields obtained are quite high making their emission readily observable under weak irradiation conditions, such as those available from laboratory TLC lamps. An example of the observed emission is presented as part of the graphical abstract for this chapter.

6.2.3 Fluorescence Lifetimes

Unlike semiconductor QDs, where fluorescence decay is typically an aggregate of multiple lifetimes and requires multi-exponential analysis, these AgFNPs fit exceptionally well to a monoexponential lifetime expression according to Equation 6.2. In the case of toluene the decay was fit to a monoexponential function with a lifetime of 2.6 ± 0.1 ns and a goodness of fit χ^2=1.46. The corresponding decay, fit and instrument functions are shown in Figure 6.11. Similar lifetimes have been recorded in DNA encapsulated systems,[36] while in argon matrices the lifetime of Ag_2 clusters has been reported as 4.6 ns.[49]

$$I_t = \alpha \cdot e^{\frac{-t}{\tau}} \Rightarrow \ln I_t = \ln \alpha - \frac{t}{\tau} \tag{6.2}$$

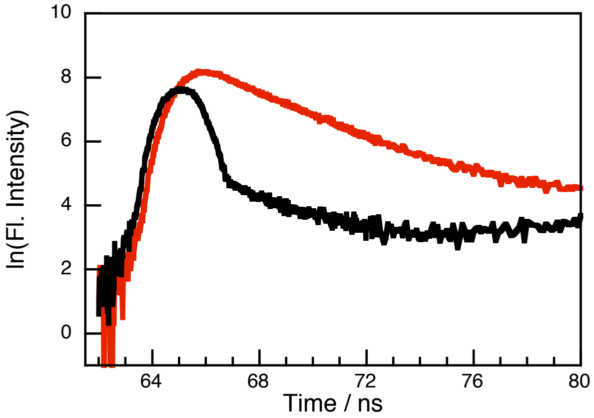

Figure 6.11 Fluorescence lifetime of Ag particles in toluene, as prepared in Figure 6.1 and diluted to an appropriate concentration, with excitation at 440 nm and detection at 550 nm (red). The instrument response function (black) is also included.

6.2.4 NMR Spectroscopy

Our synthesis experiments showed unequivocally that the presence of trifluoroacetate anions was critical for the preparation of highly fluorescent AgFNP. That is, while the reduction of Ag^+ by I-2959 would occur regardless of the presence of this anion, the particles would not normally fluoresce. For example, silver nitrate is readily reduced in the presence of photochemically generated ketyl radicals but the product is not fluorescent.

^{19}F-NMR is a sensitive technique offering excellent diagnostics for the environment of ^{19}F atoms. The ^{19}F-NMR data for AgFNP prepared in toluene with hexadecylamine are shown in Figure 6.12. Spectrum C shows a reference spectrum from hexadecylammonium trifluoroacetate. Spectrum A clearly shows that the ^{19}F peak is considerably shifted to -73.76 ppm (compared to -76.71 ppm for the reference). As the sample is diluted (spectrum B) the relative importance of the reference peak also increases. In both spectrum A and spectrum B, a significant broadening of the peak centered at -73.76 is observed.

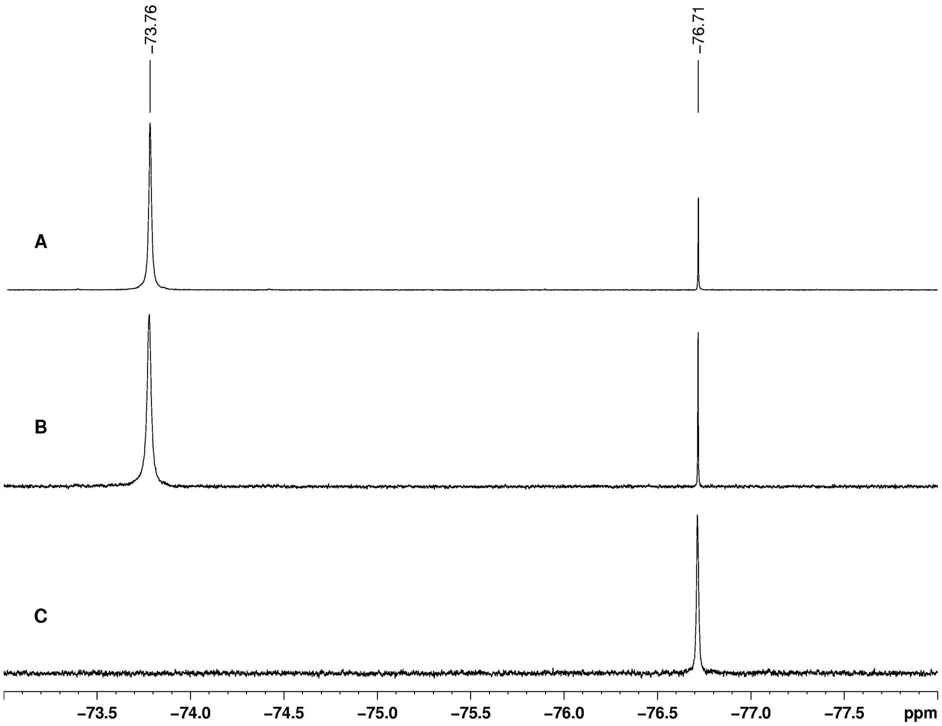

Figure 6.12 ^{19}F NMR spectra of concentrated (A) and dilute (B) hexadecylamine-Ag particles following the cooling/filtration procedure described in the text. Spectrum C is the independently prepared hexadecylammonium trifluoroacetate salt. All samples

were prepared in toluene-d_8 and additional details are included in the Experimental Section.

A number of important conclusions can be drawn from the NMR spectra of Figure 6.12. First, the trifluoroacetate anion is in a different environment when the AgFNP are present, as would be expected if they form part of a nanoparticle stabilizing layer. Second, the increased peak width is consistent with restricted mobility and an exchange time similar to or longer than the timescale of the experiment. Third, the fact that the proportion of free anion increases upon dilution is a clear indication of a dynamic equilibrium between associated and free ions. Our experiments do not show if all, or only part, of the stabilizing anions are exchangeable.

NMR experiments were also performed when the stabilizing salt was based on cyclohexylamine, though they were far less conclusive. Briefly, similar trends are observed in all systems examined, but for cyclohexylamine the ^{19}F peak is broader and shows some shifts with concentration (Figure 6.13), suggesting that more than one site may be available to the trifluoroacetate anion. The fact that the behavior depends on the counterion (i.e., the protonated amine) suggests that the ammonium ion must also be part of the stabilizing layer, as suggested in Scheme 6.1. In both the concentrated and dilute AgFNP spectra, a residual peak of the free salt is observed, consistent with an equilibrium between bound and free forms of the salt. The increased broadness of the bound salt peak in the concentrated sample, with respect to the dilute sample, is consistent with a higher concentration of the bound species on the surface, which would result in signal broadening. The difference in chemical shifts of the bound species (-75.61 ppm for concentrated AgFNPs, -75.07 ppm for dilute AgFNPs) is small but may be attributed to occupation of different binding sites depending on concentration and an exchange between the sites faster than the timescale of the experiment.

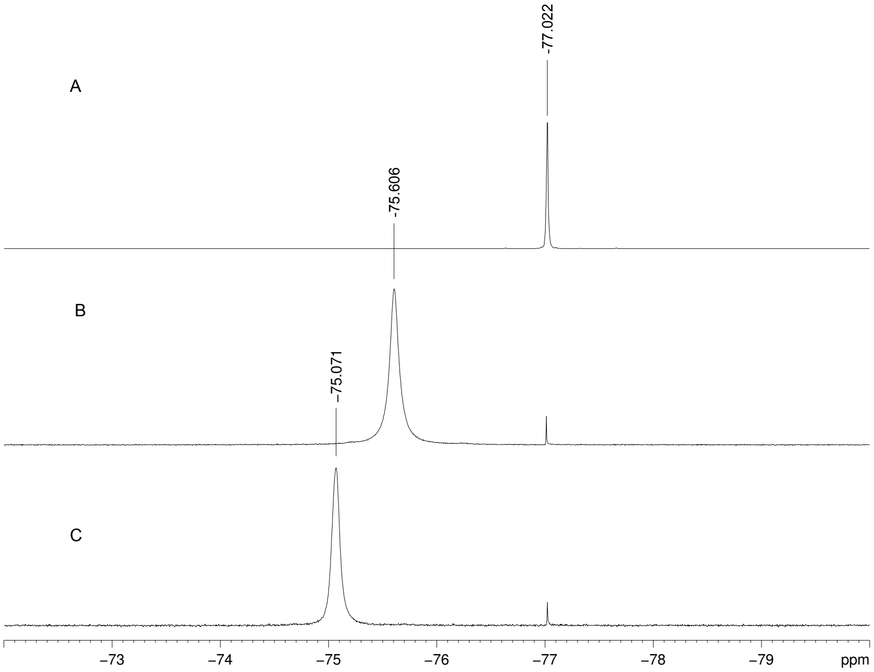

Figure 6.13 ^{19}F NMR spectra of cyclohexylammonium trifluoroacetate (A) and two concentrations of cyclohexylamine-AgFNPs recorded in toluene-d_8: A concentrated sample (B) and a diluted sample (C).

Attempts to monitor ^{1}H – NMR for the amine were inconclusive, although it is clear that the presence of AgFNP influenced the spectrum (Figure 6.14), also consistent with the amine or the ammonium salt forming part of the particle stabilizing layer.

There are literature reports indicating that base sites may contribute to AgFNP stabilization.[50] Although there are significant differences in the spectrum of the free salt Reference spectrum (Figure 6.14A) and both spectra containing AgFNPs (Figure 6.14B and 6.14C), the complicated spectral patterns and severe overlap made it impossible to rationalize the changes based on surface binding.

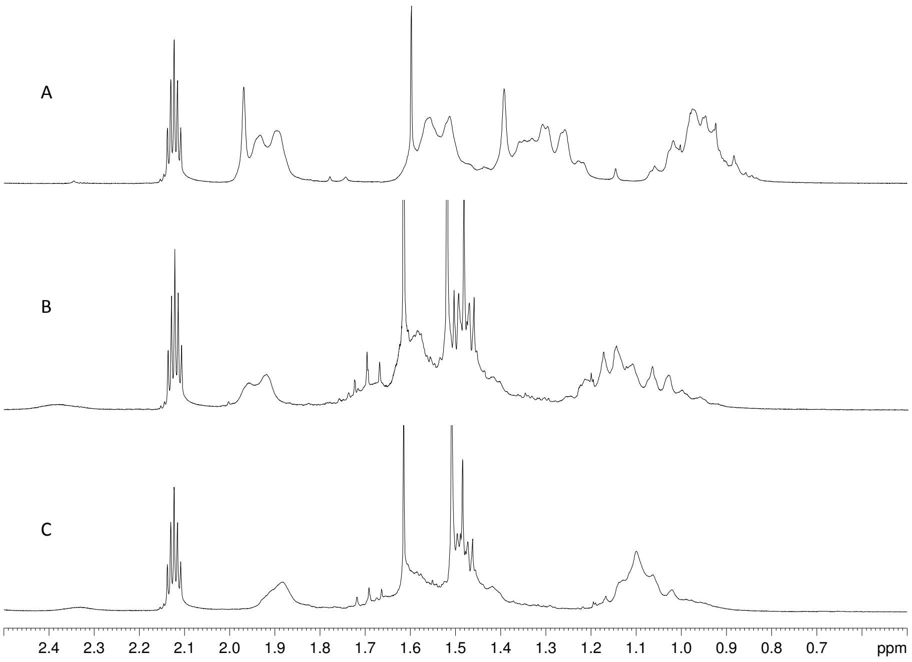

Figure 6.14 Expanded low-field region of ^{1}H NMR of the same samples as in Figure 6.13.

6.2.5 Nanoparticle TEM Imaging

TEM imaging experiments were performed on samples dispersed in toluene, using both solutions obtained directly in this solvent, as well as particles originally made in THF and then resuspended in toluene, as described in the AgFNP synthesis section.

This purification procedure was found to minimize the presence of organic crystals in the image.

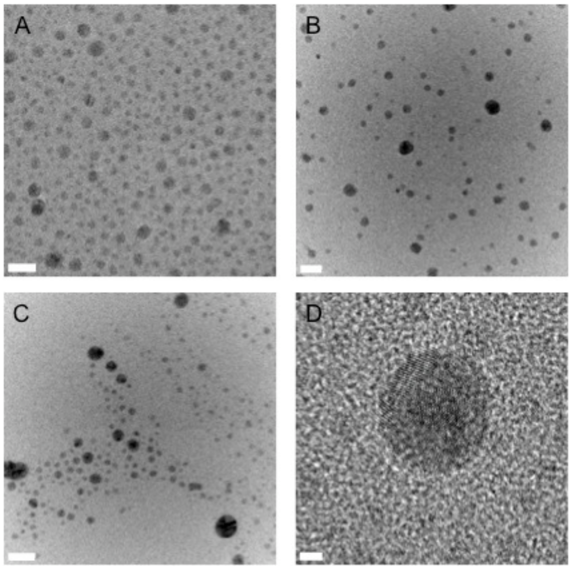

Figure 6.15 TEM images of AgFNPs prepared using different procedures: A) Particles synthesized in THF with cyclohexylamine, redispersed in toluene, and dropcast from toluene; B) Particles synthesized in toluene with cyclohexylamine, purified as discussed in the text, and dropcast from toluene; C) Particles synthesized in toluene with hexadecylamine, purified as discussed in the text, and dropcast from toluene; D) HR-TEM image of a large particle in sample A). Scale bars are 10 nm, 20 nm, 20 nm and 2 nm for A) to D) respectively.

Measurement of a range of particles prepared in THF (Figure 6.15A) leads to an average size of (3.4 ± 0.7) nm for the AgFNP; a histogram of the size analysis is given in Figure 6.16.

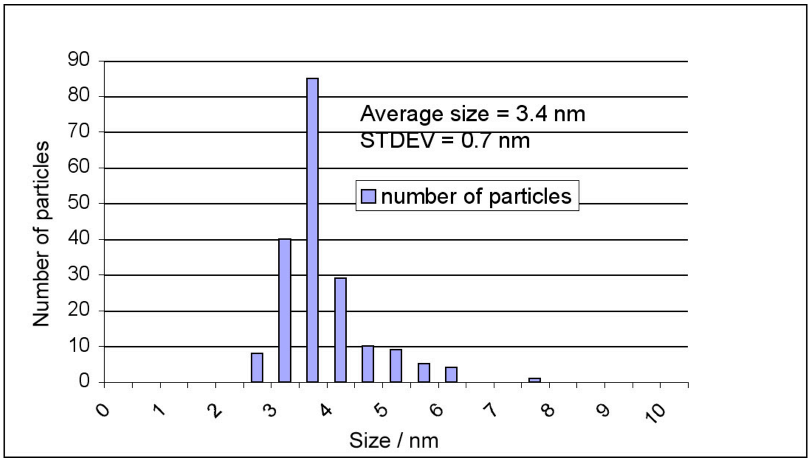

Figure 6.16 Histogram showing the distribution of particle sizes from TEM images of cyclohexylamine-AgFNPs prepared in THF, purified by the cooling/filtration process, redispersed in toluene, and dropcast on copper TEM grid from toluene, as in Figure 6.15A. The histogram represents the sizes of 200 counted particles.

Analysis of the crystal lattice spacing clearly shows Ag(1,1,1) with its characteristic 0.236 nm spacing (Figure 6.15D). We note that while some single crystal particles are detected, the majority proved polycrystalline. Energy dispersive spectroscopy (EDS) characterization of the particles showed that they are composed of metallic silver (Figure 6.17), as expected. X-ray photoelectron spectroscopy (XPS) measurements were attempted on the same samples used for TEM microscopy but only confirmed the presence of Ag^0 and Ag^{1+}, the latter likely from residual unreacted silver trifluoroacetate.

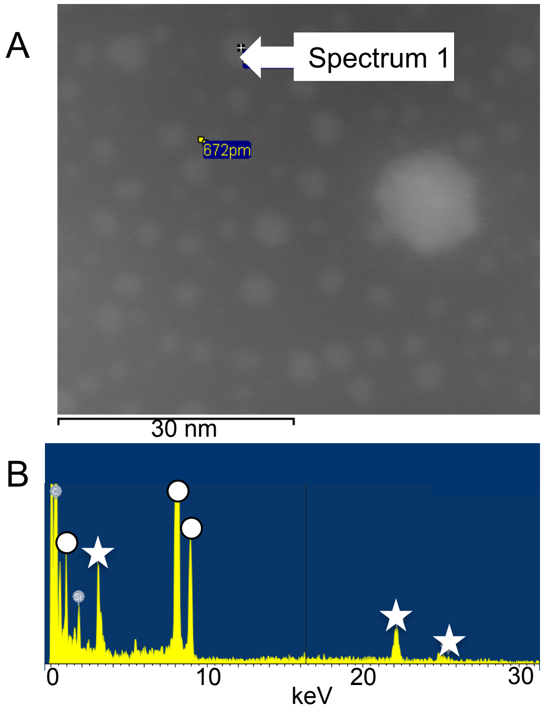

Figure 6.17 EDS analysis of AgNP sample from Figure 6.15a; A) TEM image showing particle being sampled; B) EDS spectrum of the indicated spot. Peaks indicative of Ag(0) (☆) are indicated; peaks marked by ○ are due to the Cu grid.

6.2.6 Fluorescence Quenching Studies

Our recent studies of CdSe quantum dots[21, 28, 69, 70] (Chapter 2) have led us to the conclusion that nitroxides are excellent quenchers of nanoparticle fluorescence, and that these studies can yield information on the form of quenching, the nature of binding interactions, the ligand environment at the nanoparticle surface, and the dynamics of quencher-surface interactions. Among the nitroxides tested, 4-amino-TEMPO (4aT) proved very convenient, with excellent surface binding properties.[15, 22] Amines are known to bind well to noble metal particles.[25]

Chart 6.2 Structures of the two nitroxide quenchers used in this study, 2,2,6,6-tetramethylpiperidine-N-oxide (TEMPO) and 4-amino-2,2,6,6-tetramethylpiperidine-N-oxide (4aT).

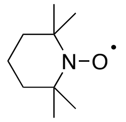

TEMPO

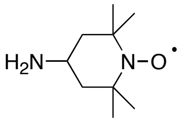

4aT

Stern-Volmer analysis is a common technique used to acquire information regarding fluorescence quenching mechanisms[51, 52] and has proven useful in the interpretation of the quenching experiments with CdSe quantum dots.[15, 17, 53, 54] Briefly, when the mechanism for deactivation of an excited state, fluorescent in the present case, is a simple competition between first order processes that determine the excited state lifetime, τ (fluorescence, intersystem crossing, thermal deactivation) and a bimolecular quenching process by some quencher Q with rate constant k_q; the fluorescence intensity in the absence of quencher, F_0, and in the presence of quencher, F, can be related by Equation 6.3, where $k_q\tau = K_{SV}$.[52]

$$\frac{F_0}{F} = 1 + k_q\tau\;[\mathrm{Q}] = 1 + K_{SV}[\mathrm{Q}] \tag{6.3}$$

Quenching experiments with both TEMPO and 4aT were performed in toluene with AgFNP prepared directly in this solvent. The corresponding Stern-Volmer quenching plot for 4aT is shown in Figure 6.18, and also includes a 4aT quenching plot recorded in the presence of 40 μM cyclohexylamine. The fact that cyclohexylamine attenuates the quenching by 4aT is a clear indication that the amine groups in 4aT and cyclohexylamine compete for binding sites at the AgFNP surface. The data has been fit with a parabola for convenience; the linear coefficient of the fit corresponds to the initial slope (i.e., *lim*[4aT] → 0), yielding values of 44,200 M^{-1} and 30,100 M^{-1} in the absence and presence of 40 μM cyclohexylamine, respectively.

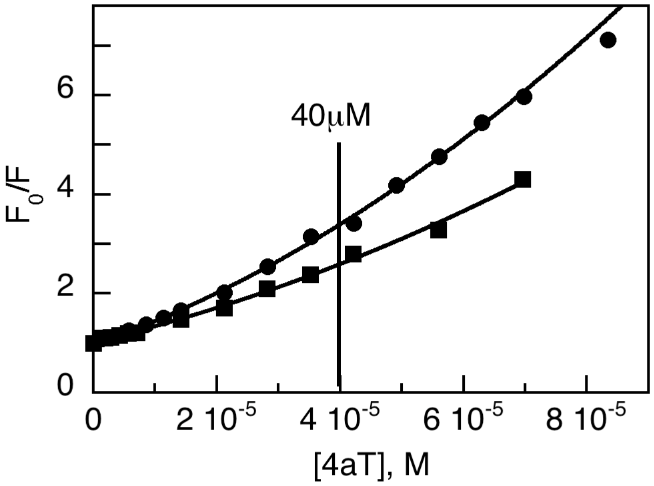

Figure 6.18 Stern-Volmer plot of fluorescence quenching of AgFNPs with 4aT in toluene. When analyzed using Equation 6.3, the quenching rate constants obtained at low 4aT concentrations are above the diffusion-controlled rates, indicating a static quenching mechanism involving binding to the particle surface. The efficiency of quenching is significantly higher in the absence of cyclohexylamine (•) than in the presence of 40 μM cyclohexylamine (■) which implies a competition for surface sites between 4aT and cyclohexylamine.

It is important to note that both primary amine and free radical functionalities are essential for quenching where the amine group provides only a binding interaction as cyclohexylamine addition by itself has almost no effect on fluorescence. On the other hand TEMPO itself is a poor quencher, and 15 mM TEMPO leads to a quenching ratio F_0/F of 2.6 (Figure 6.19); the same value can be achieved with ~30 μM 4aT (see Figure 6.18). Thus, 4aT is approximately 400 times more efficient than TEMPO as a quencher.

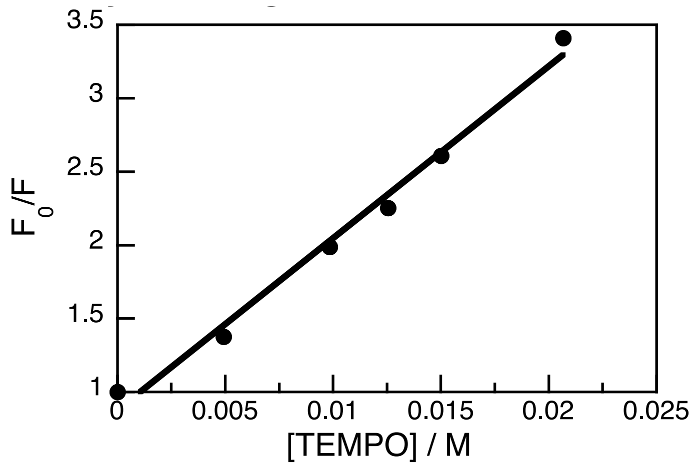

Figure 6.19 Stern-Volmer plot of AgFNP fluorescence quenching by TEMPO.

Given $K_{sv} = k_q\tau$, where k_q is the bimolecular rate constant for excited state quenching and τ the excited state lifetime, then it is possible to extract k_q for both quenchers, given the knowledge of τ from fluorescence studies (τ ~ 2.6 ns in toluene). This analysis yields a value of $k_q = 1.7\text{x}10^{13}$ $M^{-1}s^{-1}$ (from the initial slope in Figure 6.18). This number is three orders of magnitude larger than that for a diffusion-controlled process in toluene.[51] This type of behavior is normally referred to as "static quenching", that is, diffusion is not required for quenching to occur, with the quencher already bound to the fluorophore before excitation takes place. In our system this requires 4aT to bind strongly to the AgFNP, in a similar fashion that 4aT binds to quantum dots.[22, 55] Figure 6.20 shows fluorescence lifetime measurements in the absence of 4aT and in the presence of 17 μM 4aT, corresponding to the F_0/F value of 2.1 in Figure 6.18. The fact that the fluorescence lifetime remains unchanged, while the maximum intensity decreases, is also indicative of a static quenching mechanism. The reasons for the upward curvature at moderately high 4aT concentrations in Figure 6.18 are analyzed in the Discussion section. In the case of TEMPO, both the high concentrations required for significant quenching and low slope of the linear fit suggest a dynamic quenching mechanism and no surface binding. These observations are in contrast to what is observed in the case of 4aT, which must quench AgFNP fluorescence through a static mechanism facilitated by its primary amine binding site.

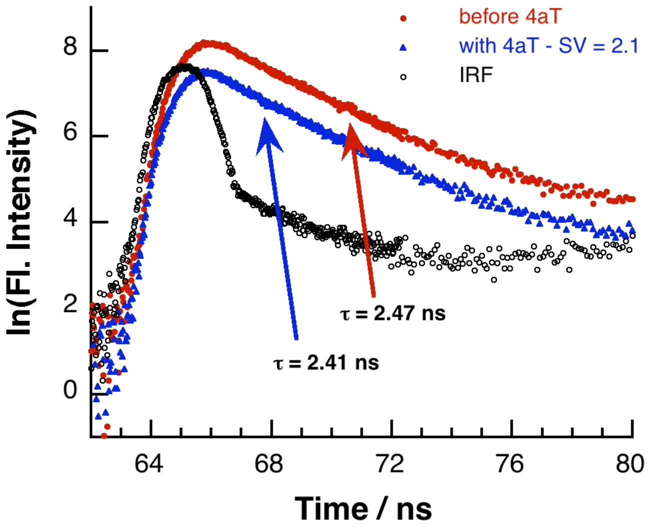

Figure 6.20 Fluorescence lifetime measurements, run under the same conditions as Figure 6.11, in the absence of 4-amino-TEMPO (red) and after the addition (blue)

of 17 μM of 4-amino-TEMPO, corresponding to a value of F_0/F of 2.1 in the Stern-Volmer quenching plot Figure 6.18. The black curve shows the instrument response function.

6.2.7 EPR Studies

EPR experiments were performed to observe if binding to the surface of the Ag particles showed the same type of anisotropic line broadening observed in the case of 4aT bound to CdSe quantum dots.[15] As seen in Figure 6.21, there is no broadening of the low and mid-field nitroxide peaks upon addition of concentrated Ag particle solution. However, there is a relative decrease in the peak-to-peak height of the high-field line, which was reproducible with many different batches of particles. Control experiments were performed by addition of synthetically prepared cyclohexylammonium trifluoroacetate and no effects on the isotropic 4aT spectrum were observed. Therefore we conclude that the small degree of anisotropy observed in Figure 6.21b is a result of 4aT binding to the surface of the Ag particles.[56, 57] The absence of broadening on the two low-field features suggests that the local environment of the bound nitroxide is close to that of free nitroxide where its axial degrees of rotational freedom are not hindered by a closely-packed ligand environment.[58]

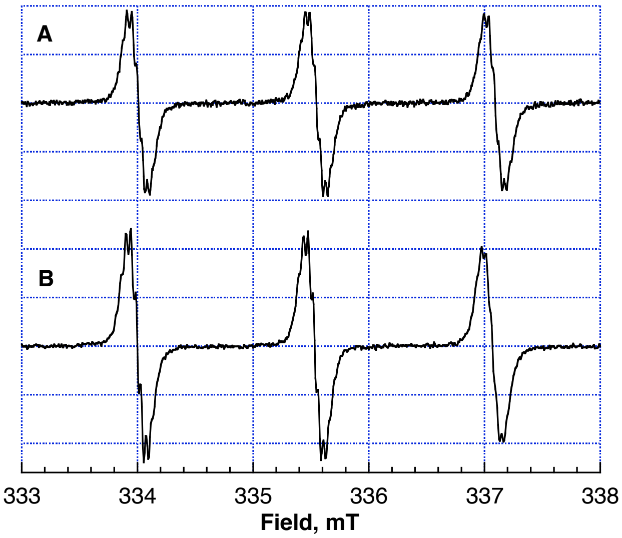

Figure 6.21 (A) EPR spectra of 18.0μM 4aT in deaerated toluene; (B) deaerated toluene solution of concentrated AgFNPs (A_{448}=1.3) and 18.0μM 4aT. A decrease in the relative intensity of the high-field feature of 4aT in the presence of AgFNPs is observed. All EPR parameters for both spectra are included in the Experimental Details.

6.2.8 Synthesis and Fluorescence Microscopy in Polymer Films

Having synthesized and characterized highly fluorescent nanomaterials in solution using photochemistry, the goal became to extend this type of methodology to a process more amenable to lithography; namely direct synthesis of the fluorescent clusters in polymer films. For this purpose solutions of similar composition as those described above, but containing polystyrene, were spin coated on fused silica disks and exposed to UVA light. Figure 6.22 shows an image obtained in this manner.

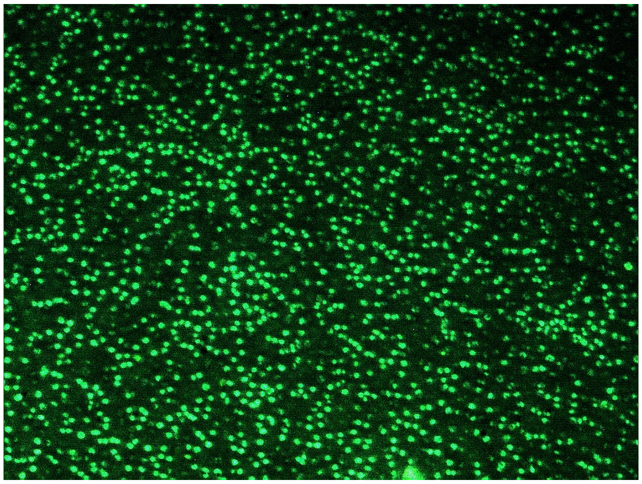

Figure 6.22 Fluorescence microscopy image (100x) of a polystyrene (PS) film containing hexadecylamine-AgFNPs with (microscope) excitation at 436 nm and broadband detection at $\lambda > 470$ nm. The sample was prepared by UVA photolysis of a spin-coated PS film containing 20 mM silver trifluoroacetate, 20 mM I-2959, and hexadecylamine for 20 minutes. Spot size is diffraction limited (>300 nm) and shows correctly particle location but not dimensions.

Figure 6.22 demonstrates unequivocally that the emission arises from discrete particles and thus Ag emissive clusters must be located at or near the AgNP surface. The fact that small (predominantly Ag_2) fluorescent clusters are associated with larger nanoparticles is also consistent with the fluorescence quenching studies above. While our data are consistent with the absorption, emission spectra and fluorescence lifetime for Ag_2, we cannot rule out possible involvement of species such as Ag_3 and Ag_4. A fluorescence spectrum of a single fluorescing particle as observed in Figure 6.22 is included in Figure 6.23. The emission maximum in the polystyrene matrix matches exceptionally well with that observed in toluene solution (Figure 6.8).

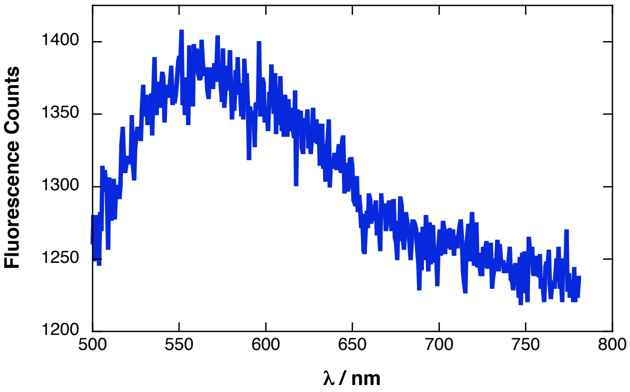

Figure 6.23 A fluorescence spectrum of a single particle as observed in Figure 6.22. Experimental details are given in Section 6.5.

Once it had been demonstrated that synthesis of these fluorescent nanoparticles is possible in polystyrene, the next task was to test the lithographic potential. More specifically, could the photochemical synthesis of AgFNPs be used to pattern fluorescent images in thin polymer films? Figure 6.24 shows the fluorescence microscope images of two different patterned polymer thin films: Polystyrene (PS) and Polymethylmethacrylate (PMMA). While the magnification of the images is such that individual fluorescing particles are not visible (as in Figure 6.22), the periodic line pattern, a result of fluorescent particle generation matching the aerial image, is clear in both polymers (Figure 6.24). The large bright spots in the PMMA image (6.24B) are due to the poor solubility of the reagents in the polymer film; these spots are visible in the film before exposure by optical microscopy but are not fluorescent.

It is believed that they are undissolved crystals of silver trifluoroacetate and that their enhanced brightness in the fluorescence image is due to interfacial reduction.

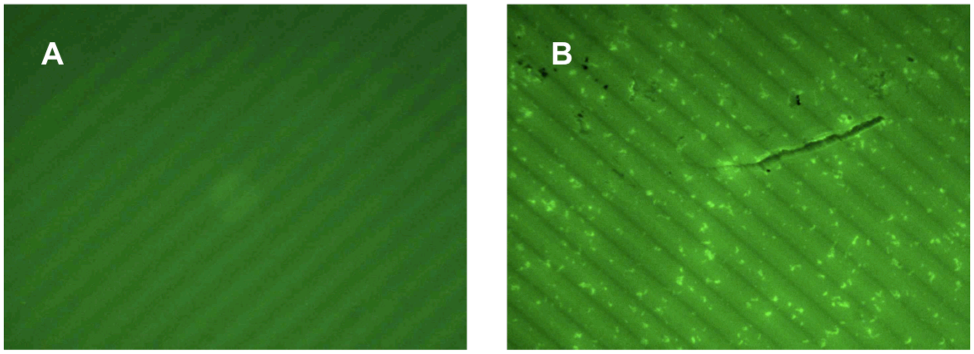

Figure 6.24 Fluorescence microscope image (5x) of 5% w/p silver trifluoroacetate and 1:1:1 molar ratio of Ag^+:I-2959:HDA in A) PS and B) PMMA following irradiation (8 lamps, UVA) through a 55 μm mask. Microscope excitation was at 436 nm and broadband detection at $\lambda > 470$ nm.

6.3 Discussion

Numerous methods are available for the reliable synthesis of metal nanoparticles, including silver. [23, 59] Most of these methods employ reductants such as borohydride and stabilize the particles in solution with a variety of coatings to avoid or minimize precipitation.[29, 60] Some of these protected layers can have biological functions incorporated. Typically silver nanoparticles show a distinct plasmon band which is traditionally between 390 and 420 nm.[25, 30] We were initially surprised when the absorption band obtained was closer to 450 nm (see Figure 6.1). We now believe that this absorbance is not due to the silver plasmon band, but rather to the presence of small silver clusters. Previous studies have identified absorbance bands at 385, 410 and 442 nm, depending on their local geometries, as belonging to Ag dimers in Ar matrices,[61] the latter which corresponds well to the absorption we observe in the present case around 450 nm. As evident from the TEM images (Figure 6.15) and the observed weak absorption band at 390 nm in certain samples, large (3.4 nm) particles are formed in the photoreaction. We have been unable to determine the chemical yield of the small silver clusters versus the yield of larger nanoparticles. While the spectroscopic data for the particles are well documented,[62] (and gives about 0.5 nM particles) that for the clusters is not; further, it is unclear if surface enhancement effects may influence the cluster optical properties. Gel permeation chromatography (GPC) was used in an attempt to verify that the fluorescence of the samples was associated with species attached to the larger nanoparticles but the fluorescence was unstable under these conditions, possibly due to on-column interactions.

While photochemical methods have been used to synthesize silver nanoparticles before, the choice of chromophore and wavelength are frequently not optimized; the rationale for making suitable choices was discussed in a recent contribution.[39] The current approach has been to generate well-established reductive species, such as ketyl radicals, under conditions where the precursor (I-2959 in our case)[31, 39] has strong absorptions, and where radicals are produced in fast processes that minimize or preclude quenching events. For example, although Ag^+ is an excellent excited state quencher,[30, 40] it is unable to quench significantly the triplet state of I-2959, which has a lifetime of just a few nanoseconds.[42] In addition, photoinduced intramolecular cleavage to generate the reducing ketyl radical lends itself exceptionally well to the lithographic application desired.

The transmission electron microscopy measurements reveal particles about 3.4 mm in diameter, somewhat more polydisperse when they are prepared directly in toluene compared with those synthesized in THF and then transferred into toluene. As a functional material, the description as 3.4 nm fluorescent silver nanoparticles is accurate but somewhat misleading. Metal nanoparticles of this size are not expected to fluoresce, and plasmon absorptions do not have a corresponding emission band. For this reason, emissions are attributed to small silver clusters, predominantly Ag_2 supported by the readily detectable nanoparticles and stabilized by the presence of protonated amines and trifluoroacetate anions. Further support for the presence of small fluorescent clusters comes from the remarkably clean monoexponential decay of the fluorescence, resembling that of simple molecules and a characteristic that is not usually observed with fluorescent nanoparticles. Other researchers have detected fluorescence in the 2–3 ns range and attributed it to Ag_2 clusters.[32, 36, 63] We have verified that any Ag^+ complexes that may form with either the starting reagents or any of the photoproducts are non-fluorescent, precluding the possibility of silver complexes contributing to the observed emission. We have also observed that the organic photoproducts **6.1** and **6.2**, which have been isolated, are not fluorescent at the wavelengths observed in the present case.

Small clusters are known to have a tendency for agglomeration. These aggregates of clusters still retain the key emissive properties of the individual clusters, although not surprisingly the solution behaviors lack the sharp excitation and emission profiles[32] that characterize small clusters in matrices at cryogenic temperatures. The fact that these clusters, most likely Ag_2, survive on the nanoparticle surface may reflect the intrinsic bond strength of 160 kcal/mol in diatomic silver and further stabilization due to the amine and trifluoroacetate moieties.

A few studies have also noted that an excess of positive charges tends to facilitate particle or cluster stabilization.[41, 64, 65] In our case NMR provides unequivocal evidence that trifluoracetate ions are part of the surface coverage and perhaps a few ions are needed to neutralize excess Ag^+ charges. However, ammonium ions derived from the amine are clearly also on the surface. Most likely it is these hydrophobic groups (e.g. from hexadecylamine) that ultimately provide the compatibility with a very non-polar solvent such as toluene. Small amines appear to fail to provide equivalent stabilization.

Once the particles have been purified and the excess salt (such as cyclohexylammonium trifluoroacetate) separated, the material retains some affinity for free amines. In the case of nitroxide free radicals, for instance, we see much higher quenching efficiency with 4aT than with TEMPO, which lacks the primary amine functionality. The quenching by 4aT is remarkably efficient, even when compared with the quenching of quantum dot emission by the same quencher.[15, 22] These results can only be explained by invoking static quenching in which 4aT is strongly bound to the AgFNP surfaces, which appears to provide excellent access to the fluorescent clusters these particles support. The upward curvature (Figure 6.18), while small, is rather intriguing. In the case of quantum dots, quenching plots by 4aT leads to negative (downward) curvature, attributed to the replacement of TOPO (trioctylphosphine oxide) at high concentration, while in the low concentration regime 4aT binds to available sites.[21, 28, 73] Using a similar rationale for AgFNP, one would conclude that the more difficult sites to access (i.e., at higher concentrations) are also the ones in closest proximity to the emissive clusters supported by the nanoparticles, thus leading to more efficient quenching (upward curvature). In any event the effect is small and quenching remarkably effective, even more so when the short excited state lifetime (~2.6 ns) is taken into account.

One may ask if small silver clusters, specially Ag_2, are free in solution, or associated with AgNP such as imaged by TEM and shown in Figure 6.15; as already indicated, we favor the latter explanation. The data in Figures 5.18 and 5.22 provide support for this interpretation. Quenching data support that 4aT binds strongly to the luminescent species (i.e., quenches efficiently), and earlier work shows strong binding to nanoparticles.[21, 28, 31, 70, 82] Thus, when we add 40 μM cyclohexylamine, as it binds to the nanoparticle surface we would expect more 4aT to become available in the solution and less at the particle surface. Thus, if the emissive Ag_2 was located in the solution, addition of cyclohexyl amine would lead to enhanced quenching by 4aT, since displacement of 4aT from the nanoparticle surface would make more available for quenching in the solution. In contrast we observe reduced quenching, consistent with the fact that cyclohexylamine displacement of 4aT from the surface also reduces abundance of quenchers in the proximity of the fluorescent clusters. Further, it would be hard to see how Ag_2 free in solution could lead to curved Stern-Volmer plots, since Ag_2 should show molecular-type quenching behavior.

Fluorescence microscopy images in polystyrene films (a polymer structurally similar to the toluene solvent used here) demonstrate unequivocally that the emission arises from discrete particles, thus also supporting the conclusion that the emissive clusters are located at or near the AgNP surface. That fact that the observed fluorescence spectrum of a single particle in a PS film (Figure 6.23) correlates so well with the fluorescence spectrum observed in toluene solution (Figure 6.8) is an excellent indication that the fluorescing componenets in solution are the same as the discrete AgFNPs observed in the polymer matrix. This is an important observation because without taking it in to consideration, one could argue that the discrete fluorescing clusters in the PS film may simply be due to some form of aggregates. However, aggregation would be expected to shift the fluorescence spectrum significantly, which is not the case.

In the last few years a number of contributions have reported on the bright emission from small silver clusters;[66] their properties are such that aqueous systems are interesting from a biological perspective and have already been examined in DNA and in cells.[36, 50, 67-69] On the other hand AgFNP soluble in non-polar organic media may have applications in polymeric functional materials; further, photochemical synthesis provides a route for imaging and the efficient fluorescence a mechanism for mapping material distribution.

6.4 Summary

In conclusion, we recently pointed out that ketones are good sensitizers for nanoparticle synthesis not because of the energy they can deliver, but rather because of the free radicals they can generate.[39] The synthesis and characterization of AgFNP show the generality of these concepts and the fact that ketyl radicals are excellent tools for nanoparticle synthesis. In the example reported here, nanoparticles synthesized are around 3 nm in diameter but their fluorescent properties are derived from small silver clusters, predominantly Ag_2, that are believed to be located at the nanoparticle surface or stabilization layer. It is possible that interactions with the surface contribute to the high emission quantum yield observed (0.11-0.15). The new AgNFP are interesting functional materials with potential applications in imaging and nanophotonics. Their excellent long-term stability and excellent solubility in organic solvents may prove key to future applications.

6.5 Experimental Section

Unless otherwise indicated, solvents and reagents were purchased from Aldrich and used as received. Irgacure-2959™(I-2959, 1-[4-(2-hydroxyethoxy)phenyl]-2-hydroxy-2-methyl-1-propane-1-one) was a generous gift from Ciba Specialty Chemicals. I-2959 is an efficient source of ketyl radicals.[39, 42]

The size of the nanoparticles was determined by transmission electron microscopy (TEM), while the crystalline structures of the nanoparticles were characterized by high-resolution transmission electron microscope (HRTEM). Both TEM and HRTEM studies were performed using a JEOL JEM-2100F field emission transmission electron microscope equipped with an ultra high resolution pole-piece operating at 200 kV. An Oxford energy dispersive X-ray spectrometer (EDS) attached to the JEM-2100F microscope was used to determine the elemental composition of the nanoparticles. TEM specimens were prepared by placing microdrops of nanoparticle solution directly onto a copper grid coated with carbon film (300 mesh, EMS).

All the steady state emission spectra were recorded using a Photon Technology International spectrofluorimeter. Fluorescence lifetime measurements were performed on an Easylife LS (Photon Technology International). The excitation was performed with a 440 nm pulsed LED and the broadband emission was measured using a 10 nm bandpass filter centered at 540 nm.

All absorption spectra were recorded on a Varian CARY-50 UV-vis spectrophotometer. All samples were placed in UV quality quartz cuvettes, 1 cm path length unless otherwise noted. The resolution of our measurements was set to 1 nm. Some experiments required the use of cuvettes with a 3 mm path length, since otherwise the absorbance exceeded 3.0 and was beyond the reliable dynamic range of the spectrometer.

The samples were exposed to ultraviolet light in a Luzchem photoreactor equipped with UVA lamps. Typically the unit was operated with 4 lamps, corresponding to about 26 Watt/m^2 with approximately 4% spectral contamination, mostly visible and UVB light.

^{19}F NMR measurements were performed on a Bruker AVANCE 300 NMR spectrometer. The solvent used in all cases was toluene-d_8. ^{19}F spectra were recorded using a 2.59 s acquisition time with 0.3 Hz of line broadening, proton decoupling and 12626 Hz spectral width. An external chemical shift standard of 0.05% trifluorotoluene (-63.72 ppm) was used to calibrate ^{19}F chemical shift values.

EPR measurements were performed using a JEOL FA-100 X-Band EPR spectrometer equipped with a JEOL ES-UCX2 cylindrical cavity. Samples were deaerated with nitrogen prior to measurements and held in clear-fused silica tubes (5 mm diameter) purchased from Wilmad. All spectra were recorded over 2 min at 0.1 mW power, modulation width of 0.01 mT, time constant of 0.03 s, and a sweep width of 5 mT.

Fluorescence microscopy studies employed a Leica DMLS optical microscope, with a 50 W mercury lamp which provided the excitation lamp, and a Leica DFC 300

FX camera. Solutions were spin coated on one inch diameter fused silica discs at 2000 rpm for 20 s, using a spin coater from Specialty Coatings, Inc. The solution was prepared by dissolving 200 mg of polystyrene in 5 ml of toluene and then adding appropriate amounts of silver trifluoroacetate, I-2959 and hexadecylamine. Solutions were used on the same day in which they were prepared. Films were exposed to UVA light at approximately 13 W m^{-2}.

The fluorescence emission spectrum in Figure 6.23 was measured using an Olympus IX-71 inverted microscope operated in a confocal form and provided with a closed-loop sample scanning stage (Nano LP100, Mad City Labs, Madison, WI) used for imaging and sample positioning. Samples were excited continuously employing 488 nm (1000 W/cm2) output from an Ar+ laser The circularly polarized laser beam was introduced via a single mode fiber optic and directed by a dichroic beamsplitter (z514-633rdc or z488rdc DCLP, Chroma, Rockingham, VT) to the sample via a high numerical aperture (N.A. = 1.40) oil immersion objective (Olympus U PLAN SAPO 100X). Fluorescence emission was collected through the same objective and then transmitted or reflected by a beam splitter (640DCXR Chroma, Rockingham, VT) to two avalanche photodiode detectors (Perkin Elmer Optoelectronics SPCM-AQR-14, Vaudreuil, Quebec, Canada). The emission was cleaned from any residual laser excitation by a HQ500LP (from Chroma, Rockingham, VT) filter when using 488 nm as the excitation wavelength.[70] This work was done at McGill University with the help of Mr. Pierre Karam and Dr. Gonzalo Cosa.

6.6 References

1. Wallraff, G. M.; Hinsberg, W. D., Lithographic Imaging Techniques For The Formation Of Nanoscopic Features. *Chem Rev* **1999,** *99* (7), 1801-1821.

2. Sanders, D. P., Advances in Patterning Materials for 193 nm Immersion Lithography. *Chem Rev* **2010,** *110* (1), 321-360.

3. Vekselman, A. M.; Zhang, C. H.; Darling, G. D., Functional Imaging With Chemically Amplified Resists And Organic Molecules. *Chem Mater* **1997,** *9* (9), 1942-1948.

4. Irie, M.; Fukaminato, T.; Sasaki, T.; Tamai, N.; Kawai, T., Organic Chemistry: A Digital Fluorescent Molecular Photoswitch. *Nature* **2002,** *420* (6917), 759-760.

5. Kim, J., The "Precursor Approach" To Patterned Fluorescence Images In Polymer Films. *Macromol Rapid Comm* **2007,** *28* (11), 1191-1212.

6. Leong, T. G.; Zarafshar, A. M.; Gracias, D. H., Three-Dimensional Fabrication at Small Size Scales. *Small* **2010,** *6* (7), 792-806.

7. Kocher, C.; Montali, A.; Smith, P.; Weder, C., Patterning Of Oriented Photofunctional Polymer Systems Through Selective Photobleaching. *Adv Funct Mater* **2001,** *11* (1), 31-35.

8. Peng, X.; Schlamp, M. C.; Kadavanich, A. V.; Alivisatos, A. P., Epitaxial Growth of Highly Luminescent CdSe/CdS Core/Shell Nanocrystals with Photostability and Electronic Accessibility. *J Am Chem Soc* **1997,** *119* (30), 7019-7029.

9. Peng, Z. A. P., X., Formation of High-Quality CdTe, CdSe, and CdS Nanocrystals Using CdO as Precursor. *J Am Chem Soc* **2001,** *123*, 183-184.

10. Qu, L. P., A.; Peng, X., Alternative Routes toward High Quality CdSe Nanocrystals. *Nano Lett* **2001,** *1* (6), 333-337.

11. Yu, W. W. Q., L.; Guo, Q.; Peng, X., Experimental Determination of the Extinction Coefficient of CdTe, CdSe, and CdS Nanocrystals. *Chem Mater* **2003,** *15*, 2854-2860.

12. Alivisatos, A. P., Semiconductor Clusters, Nanocrystals, And Quantum Dots. *Science* **1996,** *271* (5251), 933-937.

13. Bruchez Jr., M., Moronne, M., Gin, P., Weiss, S., Alivisatos, A.P., Semiconductor Nanocrystals as Fluorescent Biological Labels. *Science* **1998,** *281*, 2013-2016.

14. Sapsford, K. E.; Pons, T.; Medintz, I. L.; Mattoussi, H., Biosensing With Luminescent Semiconductor Quantum Dots. *Sensors-Basel* **2006,** *6* (8), 925-953.

15. Maurel, V.; Laferriere, M.; Billone, P.; Godin, R.; Scaiano, J. C., Free Radical Sensor Based On CdSe Quantum Dots With Added 4-Amino-2,2,6,6-Tetramethylpiperidine Oxide Functionality. *J Phys Chem B* **2006,** *110* (33), 16353-16358.

16. Tomasulo, M.; Yildiz, I.; Raymo, F. M., pH-Sensitive Quantum Dots. *J Phys Chem B* **2006,** *110* (9), 3853-3855.

17. Jin, W. J.; Fernandez-Arguelles, M. T.; Costa-Fernandez, J. M.; Pereiro, R.; Sanz-Medel, A., Photoactivated Luminescent CdSe Quantum Dots as Sensitive Cyanide Probes in Aqueous Solution. *Chem Commun* **2005**, 883-885.

18. Rene-Boisneuf, L.; Scaiano, J. C., Sensitivity versus Stability: Making Quantum Dots More Luminescent by Sulfur Photocuring without Compromising Sensor Response. *Chem Mater* **2008,** *20* (21), 6638-6642.

19. Mulder, W. J. M.; Koole, R.; Brandwijk, R. J.; Storm, G.; Chin, P. T. K.; Strijkers, G. J.; Donega, C. D.; Nicolay, K.; Griffioen, A. W., Quantum Dots With A Paramagnetic Coating As A Bimodal Molecular Imaging Probe. *Nano Lett* **2006,** *6* (1), 1-6.

20. Medintz, I.; Mattoussi, H.; Clapp, A., Potential Clinical Applications of Quantum Dots. *Int J Nanomed* **2008,** *3* (2), 151-167.

21. Klostranec, J. M.; Xiang, Q.; Farcas, G. A.; Lee, J. A.; Rhee, A.; Lafferty, E. I.; Perrault, S. D.; Kain, K. C.; Chan, W. C. W., Convergence Of Quantum Dot Barcodes With Microfluidics And Signal Processing For Multiplexed High-Throughput Infectious Disease Diagnostics. *Nano Lett* **2007,** *7* (9), 2812-2818.

22. Heafey, E.; Laferrière, M.; Scaiano, J. C., Comparative Study Of The Quenching Of Core And Core-Shell CdSe Quantum Dots By Binding And Non-Binding Nitroxides. *Photochem Photobiol Sci* **2007,** *6* (5), 580-584.

23. Burda, C.; Chen, X.; Narayanan, R.; El-Sayed, M. A., Chemistry and Properties of Nanocrystals of Different Shapes. *Chem Rev* **2005,** *105* (4), 1025-1102.

24. Henglein, A., Small-Particle Research: Physicochemical Properties Of Extremely Small Colloidal Metal And Semiconductor Particles. *Chem Rev* **1989,** *89* (8), 1861-1873.

25. Kamat, V. K., Photophysical, Photochemical and Photocatalytic Aspects of Metal Nanoparticles. *J Phys Chem B* **2002,** *106* (32), 7729-7744.

26. Lakowicz, J. R., Radiative Decay Engineering 5: Metal-Enhanced Fluorescence And Plasmon Emission. *Anal Biochem* **2005,** *337*, 171-194.

27. Tam, F.; Goodrich, G. P.; Johnson, B. R.; Halas, N. J., Plasmonic Enhancement of Molecular Fluorescence. *Nano Lett* **2007,** *7* (2), 496-501.

28. Turkevich, J., Stevenson, P.C., Hiller, J., A Study of the Nucleation and Growth Processes in the Synthesis of Colloidal Gold. *Discuss Faraday Soc* **1951,** *11*, 55-75.

29. Brust, M.; Walker, M.; Bethell, D.; Schiffrin, D. J.; Whyman, R., Synthesis of Thiol-derivatized Gold Nanoparticles in a Two-Phase Liquid-Liquid System. *J Chem Soc Chem Comm* **1994**, 801-802.

30. Scaiano, J. C.; Aliaga, C.; Maguire, S.; Wang, D., Magnetic Field Control of Photoinduced Silver Nanoparticle Formation. *J Phys Chem B* **2006,** *110* (26), 12856-12859.

31. McGilvray, K. L.; Decan, M. R.; Wang, D.; Scaiano, J. C., Facile Photochemical Synthesis of Unprotected Aqueous Gold Nanoparticles. *J Am Chem Soc* **2006,** *128* (50), 15980-15981.

32. Rabin, I.; Schulze, W.; Ertl, G., Light Emission During The Agglomeration Of Silver Clusters In Noble Gas Matrices. *J Chem Phys* **1998,** *108* (12), 5137-5142.

33. Rabin, I.; Schulze, W.; Ertl, G.; Felix, C.; Sieber, C.; Harbich, W.; Buttet, J., Absorption And Fluorescence Spectra Of Ar-Matrix-Isolated Ag3 Clusters. *Chem Phys Lett* **2000,** *320* (1), 59-64.

34. Felix, C.; Sieber, C.; Harbich, W.; Buttet, J.; Rabin, I.; Schulze, W.; Ertl, G., Fluorescence And Excitation Spectra Of Ag4 In An Argon Matrix. *Chem Phys Lett* **1999,** *313*, 105-109.

35. Fedrigo, S.; Harbich, W.; Buttet, J., Optical Response of Ag2, Ag3, Ag4 and Au3 in Argon Matrices. *J Chem Phys* **1993,** *99* (8), 5712-5717.

36. Vosch, T.; Antoku, Y.; Hsiang, J.-C.; Richards, C. I.; Gonzalez, J. I.; Dickson, R. M., Strongly Emissive Individual DNA-Encapsulated Ag Nanoclusters As Single-Molecule Fluorophores. *P Natl Acad Sci USA* **2007,** *104* (31), 12616-12621.

37. Treguer, M.; Rocco, F.; Lelong, G.; Le Nestour, A.; Cardinal, T.; Maali, A.; Lounis, B., Fluorescent Silver Oligomeric Clusters And Colloidal Particles. *Solid State Sci* **2005,** *7*, 812-818.

38. Hada, H.; Yonezawa, Y.; Akio, Y.; Kurakake, A., Photoreduction Of Silver Ion In Aqueous And Alcoholic Solutions. *J Phys Chem* **1976,** *80* (25), 2728-2731.

39. Marin, M. L.; McGilvray, K. L.; Scaiano, J. C., Photochemical Strategies for the Synthesis of Gold Nanoparticles from Au(III) and Au(I) Using Photoinduced Free Radical Generation. *J Am Chem Soc* **2008,** *130* (49), 16572-16584.

40. Kometani, N. D., H.; Asami, K.; Yonezawa, Y., Laser Flash Photolysis Study Of The Photochemical Formation Of Colloidal Ag Nanoparticles In The Presence Of Benzophenone. *Phys Chem Chem Phys* **2002,** *4*, 5142-5247.

41. Henglein, A.; Tausch-Treml, R., Optical Absorption and Catalytic Activity of Subcolloidal and Colloidal Silver in Aqueous Solution: A Pulse Radiolysis Study. *J Coll Interf Sci* **1981,** *80* (1), 84-93.

42. Jockusch, S.; Landis, M. S.; Freiermuth, B.; Turro, N. J., Photochemistry and Photophysics of α-Hydroxy Ketones. *Macromolecules* **2001,** *34* (6), 1619-1626.

43. Cohen, S. G.; Parola, A.; Parsons, G., Photoreduction by Amines. *Chem Rev* **1973,** *73*, 141-161.

44. Newman, J. D. S. B., G.J., Formation of Gold Nanoparticles Using Amine Reducing Agents. *Langmuir* **2006,** *22*, 5882-5887.

45. Maillard, B.; Ingold, K. U.; Scaiano, J. C., Rate Constants for the Reactions of Free Radicals with Oxygen in Solution. *J Am Chem Soc* **1983,** *105* (15), 5095-5099.

46. Ingold, K. U.; Paul, T.; Young, M. J.; Doiron, L., Invention of the First Azo Compound To Serve as a Superoxide Thermal Source under Physiological Conditions: Concept, Synthesis, and Chemical Properties. *J Am Chem Soc* **1997,** *119* (50), 12364-12365.

47. Link, S.; El-Sayed, M. A., Spectral Properties and Relaxation Dynamics of Surface Plasmon Electronic Oscillations in Gold and Silver Nanodots and Nanorods. *J Phys Chem B* **1999,** *103* (40), 8410-8426.

48. Martin, M. M., Hydrogen-Bond Effects On Radiationless Electronic-Transitions In Xanthene Dyes. *Chem Phys Lett* **1975,** *35* (1), 105-111.

49. Konig, L.; Rabin, I.; Schulze, W.; Ertl, G., Chemiluminescence in the Agglomeration of Metal Clusters. *Science* **1996,** *274*, 1353-1355.

50. Sengupta, B.; Ritchie, C. M.; Buckman, J. G.; Johnsen, K. R.; Goodwin, P. M.; Petty, J. T., Base-Directed Formation of Fluorescent Silver Clusters. *J Phys Chem C* **2008,** *112* (48), 18776-18782.

51. Turro, N. J.; Ramamurthy, V.; Scaiano, J. C., *Principles of Molecular Photochemistry: An Introduction*. University Science Publishers: New York, N.Y., 2008; p 493.

52. Turro, N. J., *Modern Molecular Photochemistry*. Benjamin/Cummings Publishing Co.: Menlo Park, 1978; p 628.

53. Scaiano, J. C.; Laferriere, M.; Galian, R. E.; Maurel, V.; Billone, P., Non-Linear Effects In The Quenching Of Fluorescent Semiconductor Nanoparticles By Paramagnetic Species. *Phys Stat Sol A* **2006,** *203* (6), 1337-1343.

54. Billone, P. S.; Maretti, L.; Maurel, V.; Scaiano, J. C., Dynamics of the Dissociation of a Disulfide Biradical on a CdSe Nanoparticle Surface. *J Am Chem Soc* **2007,** *129*, 14150-14151.

55. Laferriere, M.; Galian, R. E.; Maurel, V.; Scaiano, J. C., Non-Linear Effects In The Quenching Of Fluorescent Quantum Dolts By Nitroxyl Free Radicals. *Chem Commun* **2006,** (3), 257-259.

56. Wertz, J. E.; Bolton, J. R., *Electron Spin Resonance. Elementary Theory and Practical Applications*. McGraw-Hill: Toronto, 1972.

57. Weil, J. A.; Bolton, J. R., *Electron Paramagnetic Resonance: Elementary Theory and Practical Applications*. 2nd ed.; Wiley-Interscience: New Jersey, 2007.

58. Chechik, V.; Wellsted, H. J.; Korte, A.; Gilbert, B. C.; Caldararu, H.; Ionita, P.; Caragheorgheopol, A., Spin-labelled Au Nanoparticles. *Faraday Discuss* **2004,** *125*, 279-291.

59. Eustis, S.; El-Sayed, M. A., Why Gold Nanoparticles Are More Precious Than Pretty Gold: Noble Metal Surface Plasmon Resonance And Its Enhancement Of The Radiative And Nonradiative Properties Of Nanocrystals Of Different Shapes. *Chem Soc Rev* **2006,** *35* (3), 209-217.

60. Mirkhalaf, F.; Paprotny, J.; Schiffrin, D. J., Synthesis of Metal Nanoparticles Stabilized by Metal-Carbon Bonds. *J Am Chem Soc* **2006,** *128* (23), 7400-7401.

61. Rabin, I.; Schulze, W.; Ertl, G., Absorption Spectra Of Small Silver Clusters Ag N≥3. *Chem Phys Lett* **1999,** *312*, 394-398.

62. Link, S.; Wang, Z. L.; El-Sayed, M. A., Alloy Formation of Gold-Silver Nanoparticles and the Dependence of the Plasmon Absorption on Their Composition. *J Phys Chem B* **1999,** *103* (18), 3529-3533.

63. Fedrigo, S.; Harbich, W.; Duttet, J., Optical Responses of Ag2, Ag3, Au2 and Au3 in Argon Matrices. *J Chem Phys* **1991,** *99a*, 5712.

64. Zhang, J.; Xu, S.; Kumacheva, E., Photogeneration of Fluorescent Silver nanoclusters ib Polymer microgels. *Adv Mater* **2005,** *17*, 2336-2340.

65. Messere, A. G., A.; Garella, I.; Temussi, F.; Di Blasio, B.; Fiorentino, A., Nitration of Cinnamic Acids Using Cerium (IV) Ammonium Nitrate Immobilized on Silica. *Synth Comm* **2004,** *34* (18), 3317-3324.

66. Zheng, J.; Nicovich, P. R.; Dickson, R. M., Highly Fluorescent Noble-Metal Quantum Dots. *Annu Rev Phys Chem* **2007,** *58*, 409-431.

67. Ritchie, C. M.; Johnsen, K. R.; Kiser, J. R.; Antoku, Y.; Dickson, R. M.; Petty, J. T., Ag Nanocluster Formation Using A Cytosine Oligonucleotide Template. *J Phys Chem C* **2007,** *111* (1), 175-181.

68. Makarava, N.; Parfenov, A.; Baskakov, I. V., Water-Soluble Hybrid Nanoclusters with Extra Bright and Photostable Emissions: A New Tool for Biological Imaging. *Biophys J* **2005,** *89*, 572-580.

69. Richards, C. I.; Choi, S.; Hsiang, J. C.; Antoku, Y.; Vosch, T.; Bongiorno, A.; Tzeng, Y. L.; Dickson, R. M., Oligonucleotide-stabilized Ag Nanocluster Fluorophores. *J Am Chem Soc* **2008,** *130* (15), 5038-5039.

70. Karam, P.; Ngo, A. T.; Rouiller, I.; Cosa, G., Unraveling Electronic Energy Transfer In Single Conjugated Polyelectrolytes Encapsulated In Lipid Vesicles. *P Natl Acad Sci Usa* **2010,** *107* (41), 17480-17485.

7. Future Directions and Final Comments

Table of Contents

Graphical Abstract

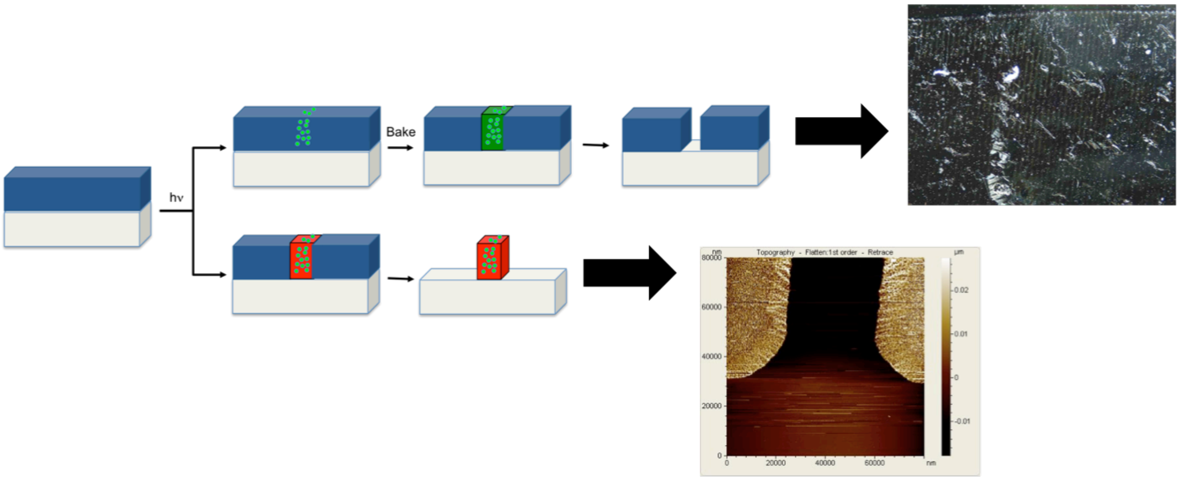

7.1 Future Directions

Based on the trends in semiconductor IC development, there is little doubt that computing power will continue to increase at a rate close to that predicted by Moore's Law.[1] While Chapters 3-5 present strategies which have the promise and potential to extend 193 nm lithography to the next generations of chip development, it is clear that as EUV and other high resolution imaging techniques become more accessible in the future they will be the basis for semiconductor ICs.[2-5] Despite this, the role of existing 193 nm lithographic technology will not be eliminated from IC production in the foreseeable future; with the exception of the smallest features in an IC chip (those in the FEOL of Figure 7.1), the patterned features are not generally at or near the resolution limit. Therefore it will remain more economically practical to continue using 193 nm technology to image those features in the BEOL layers (Figure 7.1). The mPT-sensitized non-linear acid generating systems we developed in Chapter 4 remain the only published examples which show the photochemical response required for pitch division and generate technologically-relevant sulfonic acids.[6] Continued efforts should be made to synthesize a tethered mPT-PAG system as proposed in Chapter 4.2.4. If these tethered molecules increase the efficiency of the non-linear acid generating process significantly, they are poised to make 22 nm lithography with 193 nm irradiation a reality.

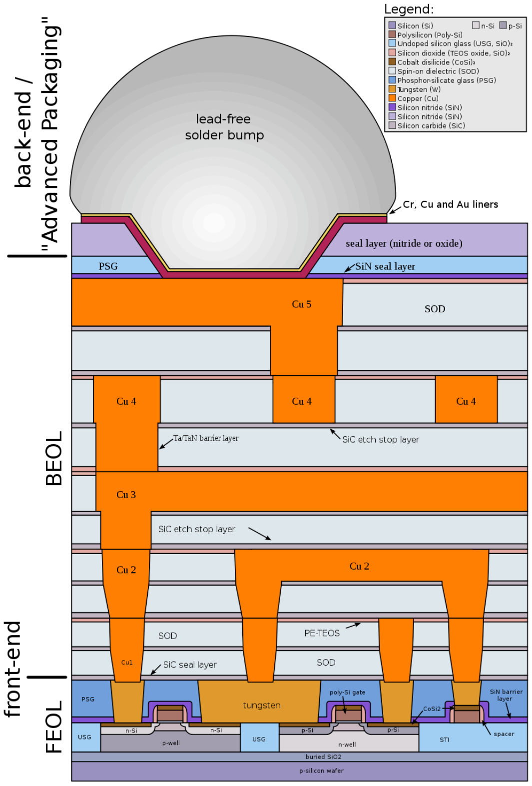

Figure 7.1 A schematic diagram showing a general profile view of the cross-section of a CMOS IC.[7] The components in the Front End of the Line (FEOL) are the only features that are generally at or near the resolution limit of the imaging technology. The features in the Back End of the Line (BEOL) require lower resolution and thus can be patterned using technology from previous generation lithography to minimize cost.

Functional nanoscale devices do not need to push the resolution limits of technology to be useful, however. Advanced nano-scale materials based on lithographically-patterned structures were briefly discussed in Chapter 6. In particular, the idea of patterning images using photochemically-robust polymer-embedded fluorescent nanoparticles was explored and examples showing that the synthesis of these particles directly in polymer matrices were presented (e.g. – Figure 6.24). We feel that combining lithographic polymer patterning with nanoparticle synthesis will be a fast and simple way to construct hybrid nanomaterials, a technology that is already rapidly developing.[8-12] In the following sections, we describe our approach to making these materials and some of the preliminary results we have obtained thus far. The two different approaches we propose are illustrated in Figure 7.2. The first relies on acid-mediated CAR lithography combined with polymer-based nanoparticle lithography (see Section 6.2.8), while the second is based on negative-tone imaging.

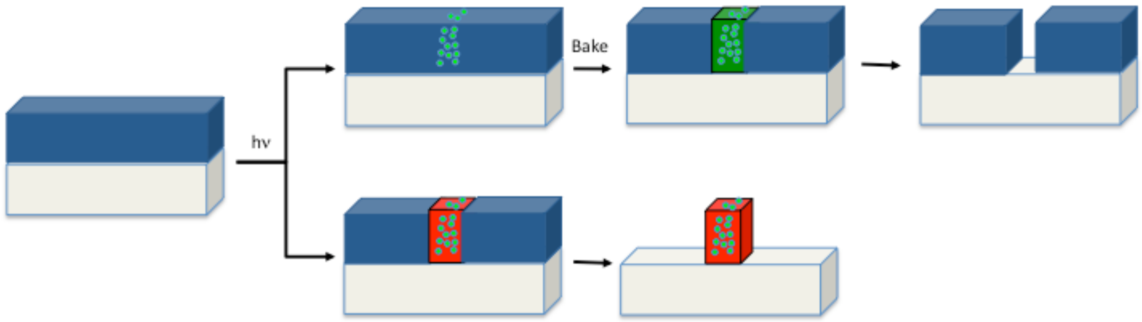

Figure 7.2 Two approaches to nanoparticle mediated lithography. Top – Upon patterned exposure, nanoparticles are formed in the irradiated regions along with strong acid. Baking the film causes deprotection in the exposed areas and subsequent development leaves a positive-tone image (see 7.1.1). Bottom – Patterned exposure forms nanoparticles in the irradiated regions at the same time as the resist is cross-linked. Development leaves a negative-tone image, where the remaining polymer areas also contain nanoparticles (see 7.1.2).

7.1.1 Nanoparticle Synthesis and CAR Lithography

The photochemical method to synthesize metallic nanoparticles that the Scaiano group has developed[13-15] necessarily generates one mole of acid for each mole of metal reduced (see Chapter 6.2.1). We realized that the identity of the acid produced would depend on the counter-ion of the original metal salt (Scheme 7.1) and that by changing the salt, we could tune the strength of the generated acid. As described in Chapter 1, sulfonic superacids are generally required to perform the deprotections so we reasoned that using traditional photoresists, we would only be able to develop patterns when a metal sulfonate salt was used. While this technique initially seems counter-productive in that the nanoparticles being formed would be removed during the development, we envision that a CAR system relying on acid generation according to Scheme 7.1 would be accompanied by fluorescent image patterning (Section 6.2.8). Therefore the fluorescence could be used as a map for the regions where acid has been generated, allowing the user to confirm that their intended pattern has been transferred to an aerial image before development.

Scheme 7.1 Tailoring the strength of a photogenerated acid molecule as a byproduct of Ag^{1+} reduction, where X is the counterion in the silver salt and HX is the resulting acid.

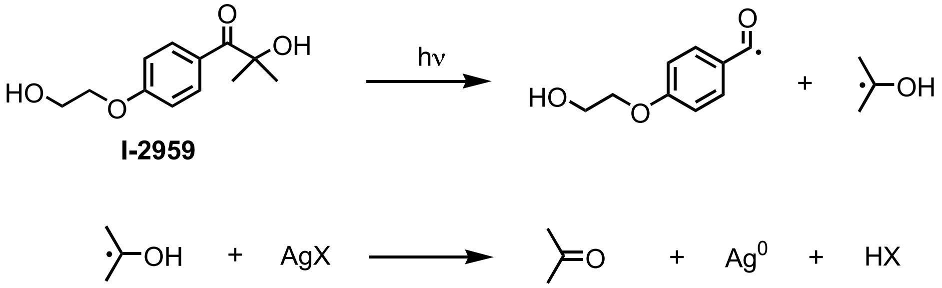

Polymer dissolution issues, likely resulting from the high loadings used, have plagued our initial experiments on this system. We were unable to get clean development of the entire exposed area in any of our experiments and we had difficulty with reproducible development conditions. However we did see promising results in many cases. For instance, Figure 7.3 shows an optical microscope image of a DupXX film containing 1:1 I-2959:AgOTf following patterned exposure and development with a 2.38% TMAH developer solution. While lines are visible, it is clear that development was not clean. We were also able to obtain AFM images of films prepared in nearly the same manner (Figure 7.4). The development in Figure 7.4 is very uneven; the developed lines are actually made up of locally-developed “holes”. These “holes” suggest that instead of a bulk change in the polymer being responsible for the solubility switch, there are microdomains that are acting as dissolution nucleation sites. While we could optimistically consider these sites to be spots where nanoparticles were formed, there is no way to confirm this. Also concerning is that development was only possible with H_2O alone; when basic developer was used, the entire film would dissolve almost immediately. As mentioned above, this was likely due to the very high loadings used (total ~30% of the film weight was non-polymer).

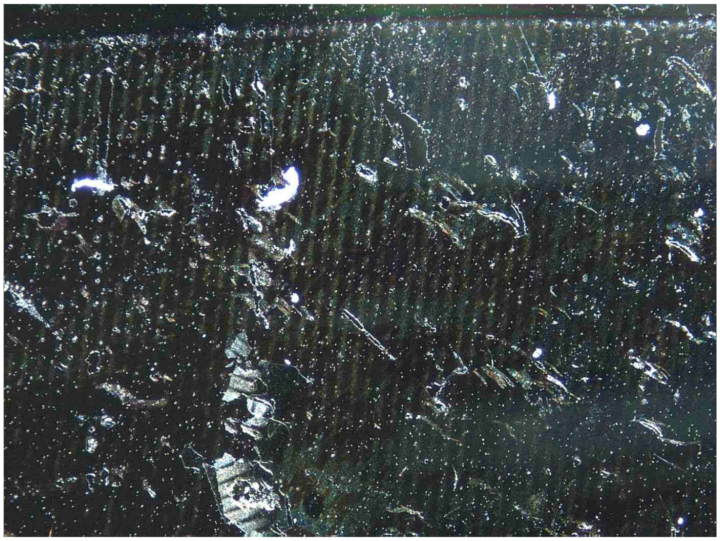

Figure 7.3 Optical microscope image of a DupXX film spin-coated from a 10% cyclohexanone solution onto a Si wafer, containing 1:1 AgOTf:I-2959 (10% w/p I-2959), exposed to 60 min irradiation (UVA, 6 lamps) through an 18 μm linear pattern mask followed by 30 min PEB @ 100°C and 7 min development in basic developer solution.

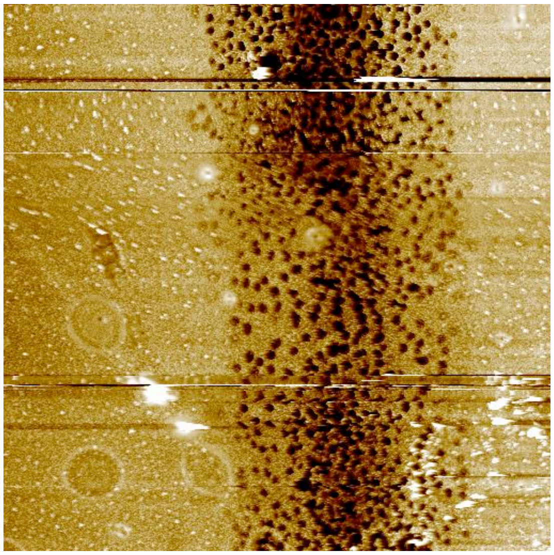

Figure 7.4 AFM image of a DupXX film on a Si substrate, containing 1:1 AgOTf:I-2959 (15% w/p I-2959), exposed to 60 min UVA irradiation (UVA, 6 lamps) through a 55 μm mask followed by 15 min PEB @ 100°C and 10 s development in H_2O.

Despite the uneven development, we were able to confirm that exposure was generating silver nanoparticles. Figure 7.5 shows UV-Vis spectra of films prepared in the same manner as in Figure 7.3 but casted onto quartz discs in order to directly measure the absorbance spectra. We show that upon irradiation, the absorbance which we attribute to the SPB of Ag nanoparticles grows in at ~400 nm. Upon subsequent PEB a new peak is observed at ~350 nm but the original absorption is unchanged. Baking an unexposed film does not result in any significant spectral changes, suggesting that the peak at ~350 nm in the exposed + baked sample is due to a heat-induced change in the NP SPB absorption. This may be consistent with a surface reconstruction of some population of the nanoparticles, although most SPB modes of Ag NPs are at > 405 nm.[16]

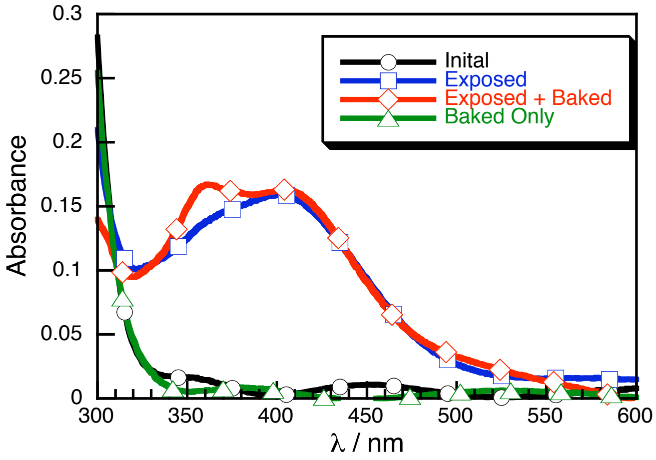

Figure 7.5 UV-Vis absorption spectra of DupXX films containing 1:1 AgOTf:I-2959 (10% w/p I-2959) on quartz discs. ○ - Film with no irradiation or PEB; ☐ - Film with 60 min irradiation (UVA, 6 lamps) only; ◇ - Film with 60 min irradiation (UVA, 6 lamps) followed by 30 min PEB @ 105°C; △ - Film with no irradiation but baked 30 min @ 105°C.

We then used the developer solution to strip the films in Figure 7.5 (the unexposed, baked sample was not soluble in the developer) and centrifuged the resulting yellow solutions at 10,000 rpm. While the supernatant solution remained clear yellow, a small amount of dark orange precipitate was separated and re-dispersed in H_2O then drop cast onto a TEM grid for SEM measurements. Upon SEM imaging, we confirmed the presence of small, polydisperse, spherical nanoparticles in the 5-20 nm size regime (Figure 7.6A). These particles are consistent with the absorption spectrum we obtained for the developer solution after stripping the films, before centrifugation (Figure 7.6B).

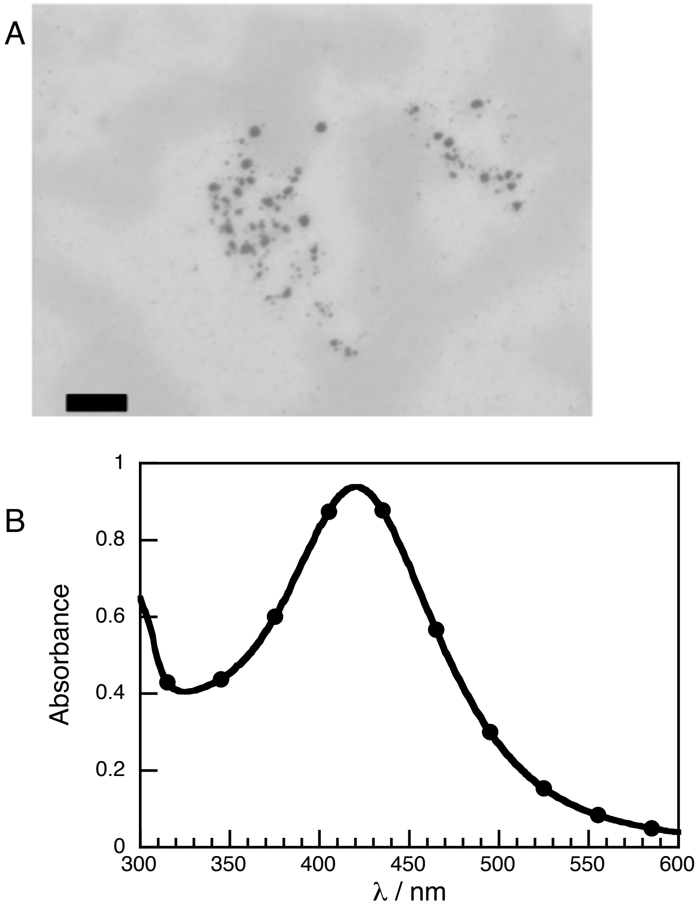

Figure 7.6 A) SEM image of nanoparticles from the exposed + baked film in Figure 7.5 following development, centrifugation, and resuspension as described in the text. The scale bar is 100 nm; B) UV-Vis absorption spectrum of the aqueous developing solution after stripping the exposed + baked film from Figure 7.5 but before centrifugation.

Unfortunately, none of the films patterned using AgOTf as a silver source yielded fluorescence even when an amine was added, unlike $AgCF_3CO_2$ in Chapter 6. We did find, however, that when films were irradiated as in Figure 7.3 but using $AgCF_3CO_2$ in place of AgOTf, we were unable to develop patterned lines. This is consistent with our proposal that the carboxylic acid formed upon reduction of $AgCF_3CO_2$ by a ketyl radical according to Scheme 7.1 would be unable to deprotect an ester-protected photoresist such as DupXX, while reduction of AgOTf does allow for development. This precludes the use of the AgOTf-based lithographic system as a fluorescent reporter of areas that have been exposed to lithographic photons before development but it does provide an indication that we are able to control the strength of acid by varying the silver salt used in Scheme 7.1. Attempts to perform similar experiments with silver methanesulfonate, expected to form a weaker acid than AgOTf but a slightly stronger acid than $AgCF_3CO_2$, were unsuccessful due to non-solubility of the methanesulfonate salt in any of the casting solvents compatible with DupXX.

While these preliminary results demonstrate the feasibility of our approach, there is plenty of room for further development. First, the formulations and conditions of the above systems must be optimized if they are to be more practical. In addition, efforts must be made to find a system which generates both a strong enough acid to effect polymer deprotection and fluorescent particles if the fluorescent imaging technology described above is to be realized.

The apparent disadvantage of the system described above, and outlined in the top pathway of Figure 7.2, is that the polymer containing the nanoparticles after patterning is washed away. A far more useful functional material would be one where the remaining patterned polymer contains embedded nanoparticles. While the lower pathway in Figure 7.2 presents one approach to achieving this goal, and some preliminary results are given in Section 7.1.2, another method would be to simply use a secondary process, either thermal or photochemical, to form nanoparticles in the remaining polymer following development according to the top pathway in Figure 7.2. Since the entire resist would contain the nanoparticle precursors (AgOTf and I-2959 in the examples discussed above), flood irradiation of the remaining film after development would also generate polymer-embedded nanoparticles. Such a system is desirable as it doesn't require any additional coating or manipulation between the two steps.

7.1.2 Negative-Tone Imaging

The preceding section presented a method for positive-tone photolithography operating according to the upper pathway of Figure 7.2. From a functional device perspective, the lower pathway in Figure 7.2 would be far more desirable. While there are many examples of polymer-embedded nanoparticle imaging techniques,[9, 10, 12] most of them suffer the same drawbacks as next-generation lithographic sources (see Chapter 1): They are generally costly and time-intensive. Thus methods based on UV irradiation would be beneficial. Some examples of polymer embedded nanomaterials patterned using photolithographic patterning have been reported[8] but require prior preparation and functionalization of the nanoparticles before patterning.

Our preliminary results presented in this section were initially not intended to yield negative-tone images. We were using the polymer TER-70, shown below, as a positive-tone photoresist to perform the same types of experiments in Section 7.1.1. However we found that upon patterned exposure, films of TER-70 containing AgOTf and I-2959 became less soluble in the exposed regions. Figure 7.7 presents an AFM image following UVB irradiation and developing with a 2.4% tetramethylammonium hydroxide solution. The dark regions were not exposed and are fully developed down to the bare Si substrate; the light regions are the exposed areas and were not dissolved by the developer. The height different between the developed and undeveloped regions is about 40 nm, consistent with the original thickness of the film.

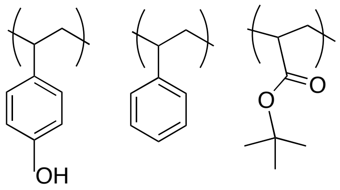

TER-70

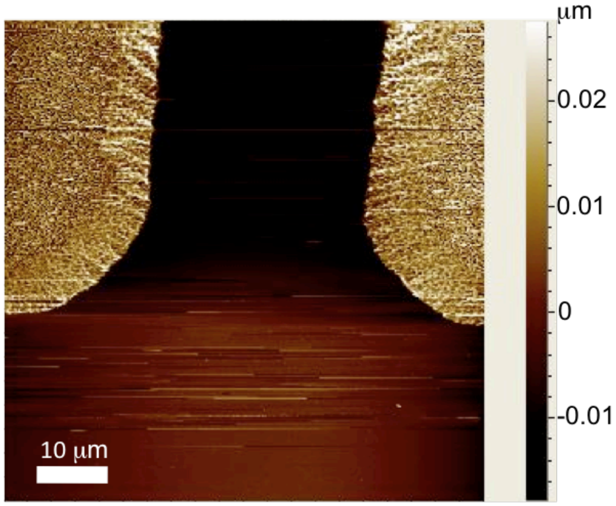

Figure 7.7 AFM topography image of a TER-70 film, casted from a 2-heptanone solution of 0.25 M I-2959 and 0.05 M AgOTf that was about 1% w/w of TER-70, following 30 min patterned exposure (UVB, 6 lamps) and 30 s developing with basic developer solution.

We believe that the negative-tone images are formed due to free-radical-induced cross-linking of the phenolic units of the TER-70 polymer. Traditional negative-tone photoresists operating through a very different mechanism[17-20] but free-radical cross-linking of phenols is well known in the chemical literature.[21] We found that the irradiated film in Figure 7.7 were even relatively resistant to dissolution by organic solvents, consistent with a significant degree of cross-linking throughout the polymer. Surprisingly, films exposed containing only I-2959 were totally insoluble, including areas that had not been irradiated during patterning experiments; no lines were visible by optical microscopy or AFM following development as in Figure 7.7. To help understand what was happening in the films, we performed some dissolution measurements (Figure 7.8). Consistent with the patterning experiments, we observed a dramatic increase in the dissolution time between an unexposed film (Figure 7.8A) and an exposed film (Figure 7.8B). We did the same experiment on films prepared from the same stock solution but without any AgOTf; in that case, the decreased rate of development for the exposed film (Figure 7.8C) was even more evident when compared to the unexposed film (Figure 7.8D). These results provide important insight into the imaging results: They suggest that in the absence of

AgOTf, polymer cross-linking is initiated by irradiation of I-2959 in the exposed regions but subsequently propagates throughout the film due to phenoxyl or similar phenol-derived radicals.[21] However, the presence of the AgOTf quenches both the initiation reaction (presumably through the reduction reaction of Scheme 7.1), indicated by the faster dissolution in Figure 7.8B than Figure 7.8C, and the propagation reaction. While extensive additional mechanistic work and characterization need to be done on this system to confirm the explanation, the results thus far are quite promising.

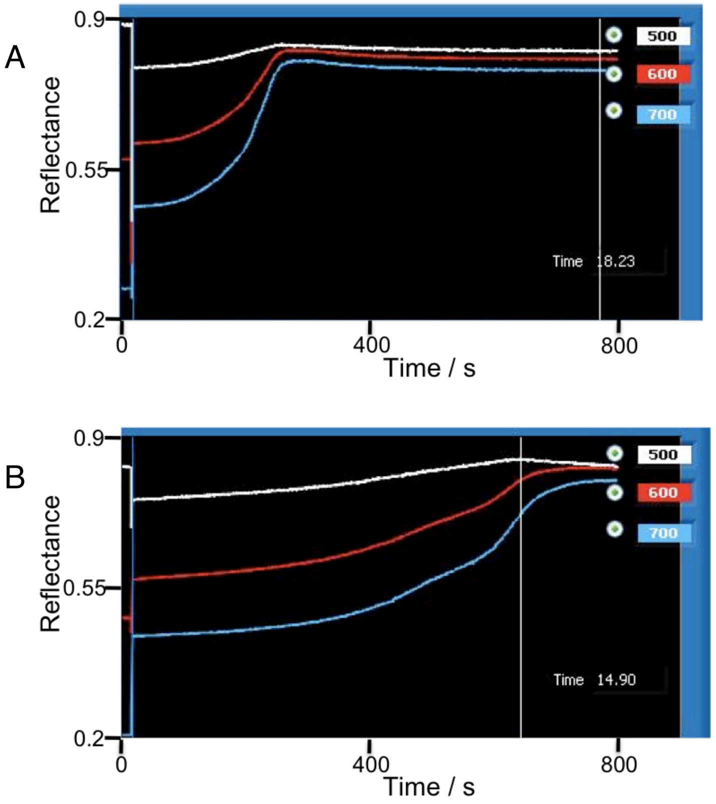

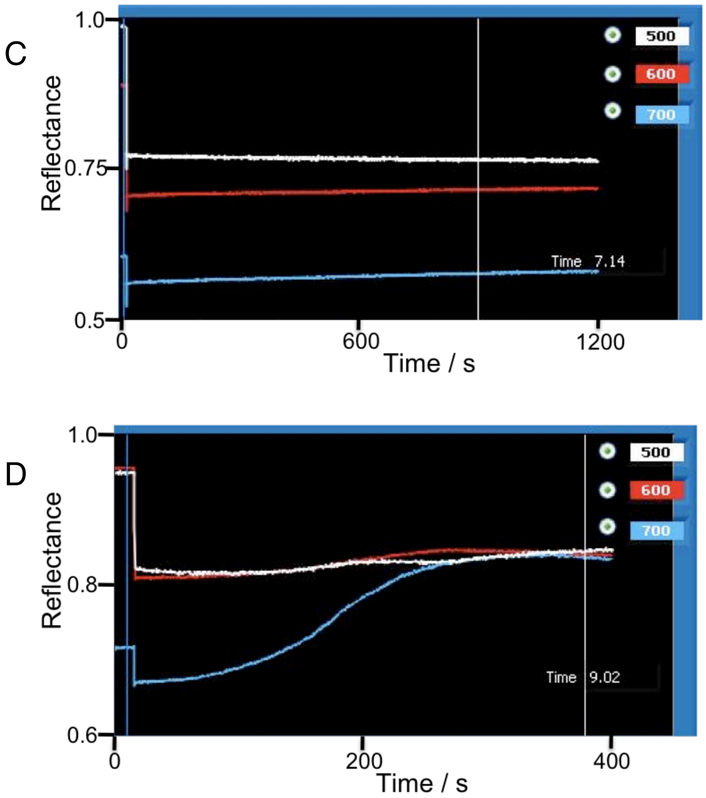

Figure 7.8 Dissolution of TER-70 films with commercial basic developer solution as measured by time-resolved interferometry. While the films were too thin to obtain proper interferograms (~40 nm, less than the instrumental limit of ~90 nm), an increase in reflectance intensity is qualitatively indicative of dissolution. A) Unexposed film containing both I-2959 and AgOTf; B) Exposed film containing both I-2959 and AgOTf; C) Exposed film containing only I-2959; D) Unexposed film containing only I-2959. Films A) and B) were cast from TER-70 solution containing 0.25 M I-2959 and 0.05 M AgOTf; Films C) and D) case from TER-70 solution containing only 0.25 M I-2959. All films were spin-coated at 2000 rpm for 30 s followed by 1 min PAB @ 105°C. Films B) and C) were exposed to 30 min irradiation (UVB, 6 lamps) and *all* films were then baked again for 1 min 105°C.

7.2 Final Comments

The results presented in this thesis address a broad range of lithographically relevant chemistry, with the exception of the CdSe QD results in Chapter 2. Through our collaborative research project with Intel Corporation, we proposed and investigated several potential methods for achieving pitch division in double exposure lithography. Specifically, our lithographic system based on mPT and sulfonium PAGs represents the first and only published example of two-photon lithography to produce acid with energies close to the industry standard. We also delved deeper into the properties of sulfonium PAGs themselves, exploring their photochemical and electrochemical properties in relation to 193 nm lithography. From there, we turned our attention to nanoparticle lithography for both fluorescent pattern development and for methods akin to traditional resist development lithography. The research program has therefore demonstrated our mechanistic but creative approaches to performing lithographic imaging for functional material development.

The results we obtained for disulfide binding on CdSe quantums dots in Chapter 2 provided significant insight into the process. Since disulfides are common ligands for building nanoparticle composites, it was useful to learn the mechanism by which they attached to the surface. In addition, we found that the CdSe surface seems to catalyze the disulfide cleavage reaction, lowering the E_A of the reaction by nearly 50 kcal/mol. The techniques used and the experience working with nanomaterials was invaluable for my future studies.

While the results presented in Chapter 3 on polyaromatic sensitizers did not yield any truly exceptional results as they may pertain to lithographic processes, the work played an important role in the evolution of our lithographic research program. Many of the specialized techniques we developed, including thin-film LFP, were initially designed to help evaluate the dynamics of the ring-opening/-closing reactions. In addition, the work gave us a general idea on how to monitor the acid-producing photoreactions explored in that chapter and those that followed. Our mechanistic investigation of the cNAME/TES-6 system, in conjunction with results from our collaborators' groups, provided crucial insight into why patterning experiments were showing behaviour consistent with a non-reciprocal process while acid generation itself did not show non-reciprocal behaviour. We also discovered that the photochemical ring-closing of two anthracene units outcompetes intramolecular electron transfer sensitization to a sulfonium PAG, while sensitization was relatively efficient from the system containing tethered anthracene/naphthalene units.

The mPT-based system developed and explored in Chapter 4 is the first example of a successful two-photon acid-generating system under lithographically relevant conditions. The properties of this system largely satisfied the requirements originally outlined by Intel Corp. when they approached us with the challenge of developing such a lithographic system. The two biggest limitations are its inability to maintain non-reciprocity at pulse energies < 1 mJ/cm^2 and the significant yield of one-photon acid generated. The two issues are likely related to one another since the breakdown in non-reciprocity at low energies is probably a result of direct acid generation from irradiation of the PAG. While we proposed that tethering the mPT and PAG together would increase the efficiency of the two-photon process, we were unable to synthesize the tethered system within the timeline of the project. Nevertheless the mPT results indicate that a true two-photon photochemical reaction can be performed at low energy densities and within a polymer matrix.

The investigation of sulfonium PAG properties in Chapter 5 was meant to provide instructive information for the future development of “transparent” PAGs. Our discovery that the photochemistry and electrochemistry of the sulfonium PAGs studied are significantly affected by the identity of the anion is something that had long been ignored by the semiconductor industry. It was generally assumed by the semiconductor industry that initial tests could be done on PAGs with simple anions, such as triflate, as models for those with larger, more lithographically applicable ones; our work emphasizes the importance for studying each candidate PAG individually. Based on our findings, we also proposed a new mechanism for photolytic cleavage of the sulfonium PAG molecules to generate acid based on a charge-transfer excited state. While this discovery will not have a significant effect on the lithographic behaviour of these compounds, it is interesting from a mechanistic point of view.

While the synthesis of fluorescent Ag NPs in Chapter 6 was not immediately applicable to lithography, our discovery that the synthesis could be performed directly in polymer films made us realize that functional fluorescent patterning could be achieved. The fluorescent particles, which are postulated to actually be Ag_2 stabilized on the surface of larger Ag NPs, have high quantum yields of fluorescence and provide a robust alternative to organic fluorophores for fluorescent patterning. The film-based synthesis of these nanoparticles provides routes to novel types of functional materials through lithographic patterning, as described in Section 7.1. Our preliminary experiments demonstrate the feasibility of our approach.

This body of work presents significant developments in both lithographic systems themselves and the tools used to characterize and evaluate them. While the Scaiano group continues collaborating with Intel Corp. for the development of next-generation 193 nm lithographic systems, the techniques developed for this work will prove invaluable. In addition, the concept of combining nanoparticle patterning with traditional negative- and positive-tone photoresist lithography provides facile access to a class of desirable functional materials. We emphasize the importance of mechanistic understanding in developing next-generation lithography and promote the development of hybrid chemical approaches as unique and effective ways to access novel materials.

7.3 Claims to Original Research

1. C2 bound to CdSe QD surfaces via an activated absorption process involving disulfide bond cleavage. The QD surface significantly lowers the activation energy of the disulfide cleavage reaction.
2. The cNAME/TES-6 system achieves pitch-division lithography under DE conditions due to the reaction of NAME with O_2; the reaction yields ether-containing products which act as basic sites. This non-reciprocity is not observable using the C6-based acid detection technique because C6 is a stronger base than the O-centered bases generated.
3. Anth-PAG is found to generate acid with a slight energy dependence upon irradiation with 193 nm light only. Irradiation of a sulfonium PAG in the presence of non-tethered anthracene, as a mimic for Anth-PAG, does not show the same energy dependence. The efficiency of the non-linear process does not increase when irradiated in the presence of a good photolytic electron donor.
4. mPT was shown to sensitize acid generation from sulfonium PAGs via a two-photon process in thin polymer films upon exposure with 193 nm irradiation. Single-photon acid generation from direct photolysis of the PAGs interfered with the two-photon. We found that we could increase efficiency of the two-photon process by decreasing film thickness. While products were not unequivocally identified, NMR studies suggest that different products are

formed upon irradiation with different energy laser pulses, although dose was matched. NMR is also consistent with radical addition to the aromatic ring of the mPT corresponding to a mechanism involving electron transfer from mPT to the PAG, followed by decomposition of the PAG yielding acid and radical species.

5. Extinction coefficients and quantum yields of acid generation were determined for TES-2, TES-3, TES-6, mPAG-2, and Si3PAG-2. TD-DFT calculations at the B3LYP/TZVP level were unable to predict relative absorption intensities. However results indicate that the anion of the trialkylsulfonium salts is involved in the photochemistry of the molecules. The PAGs were found to be unreactive towards $^1O_2$.
6. Fluorescent Ag NPs were generated using a photochemical method. Fluorescence was attributed to Ag_2 clusters supported on the surface of larger Ag NPs (average size ~3.4 nm). The particles had significant fluorescent quantum yields. The fluorescent Ag NPs were synthesized directly in polymer films. Irradiation through masks resulted in patterned fluorescence across the polymer film.
7. Irradiation of I-2959 and AgOTf in DupXX, followed by development, resulted in positive-tone images. Exposed areas were found to contain Ag NPs. Irradiation with $AgCF_3CO_2$ did not cause a solubility change in exposed areas. Irradiation of I-2959 and AgOTf in TER-70 phenol-based polymer, followed by

development, resulted in negative-tone images likely due to free radical-induced cross-linking of the polymer.

7.4 Publications

7.4.1 Results Presented in This Thesis

Billone, P.S., Park, J.M., Blackwell, J.M., Bristol, R., Scaiano, J.C. “Two-photon acid generation in thin polymer films. Photoinduced electron transfer as a promising tool for subwavelength lithography”, *Chem. Mater.* **2010**, *22*, 15-17.

Maretti, L., **Billone, P.**, Liu, Y., Scaiano, J.C. “Facile photochemical synthesis and characterization of highly fluorescent silver nanoparticles”, *J. Am. Chem. Soc.* **2009**, *131(39)*, 13972-13980.

Scaiano, J.C., **Billone, P.**, Gonzalez, C.M., Maretti, L., Marin, M.L., McGilvray, K.L., Yuan, N. “Photochemical routes to silver and gold nanoparticles”, *Pure Appl. Chem.* **2009**, 635-647.

Billone, P.S., Maretti, L., Maurel, V., Scaiano, J.C. “Dynamics of the Dissociation of a Disulfide Biradical on a CdSe Nanoparticle Surface”, *J. Am. Chem. Soc.* **2007**, *129(46)*, 14150-14151.

7.4.2 Results Not Contained in This Thesis

Billone, P.S., Johnson, P, Lin, S., Scaiano, J.C., DiLabio, G.A., Ingold, K.U. “Accurate O-H Bond Dissociation Energies of Hydroxylamines Determined by EPR Spectroscopy: Insight Into the Effect of Stereoelectronics on BDEs and Spectroscopic Properties”, *J. Org. Chem. (in press, jo-2010-021794).*

Korobkov, I., Vidjayacoumar, B., Gorelsky, S.I., **Billone, P.S.**, Gambarotta, S. “Attempting to Reduce the Irreducible: Preparation of a Rare Paramagnetic Thorium Species”, *Organometallics*, **2010**, *29*, 692-702.

Fußß, W., Schmid, W.E., Trushin, S.A., **Billone, P.S.**, Leigh, W.J. “Forward and backward pericyclic photochemical reactions have intermediates in common, yet cyclobutenes break the rules”, *ChemPhysChem* **2007**, *8(4)*, 592-596.

Maurel, V., Laferriere, M., **Billone, P.**, Godin, R., Scaiano, J.C. “Free radical sensor based on CdSe quantum dots with added 4-amino-2,2,6,6-tetramethylpiperidine oxide functionality”, *J. Phys. Chem. B* **2006**, *110(33)*, 16353-16358.

Scaiano, J.C., Laferriere, M., Gallian, R.E., Maurel, V., **Billone, P.** “Non-linear effects in the quenching of fluorescent semiconductor nanoparticles by paramagnetic species”, *Phys. Stat. Sol. A* **2006**, *203(6),* 1337-1343.

7.4.3 In Preparation

Billone, P.S., Park, J.M., Scaiano, J.C. “Photochemical reduction of silver ions as a route to lithographic patterning”, In preparation.

Billone, P.S., Huck, L.A., Beleznay, K.M., Harrington, C.R., Leigh, W.J. “The Photochemistry of a Potential Precursor to Dihydrogermylene, GeH2, and Tetrahydrodigermene, Ge2H4, in Solution”, In preparation.

Billone, P.S., Liras, M., Heafey, E., Bristol, R., Blackwell, J.M., Esswein, K., Scaiano, J.C. “Study of the Photoreversible Cycloaddition of a Tethered Anthracene as a Tool for Advanced Photolithography”, In preparation.

7.5 References

1. Moore, G., Progress in Digital Integrated Electronics. *IEDM Technical Digest* **1975,** *21*, 11-13.

2. Lin, B. J., The Ending Of Optical Lithography And The Prospects Of Its Successors. *Microelectron Eng* **2006,** *83* (4-9), 604-613.

3. Lin, B. J., Successors of ArF Water-Immersion Lithography: EUV Lithography, Multi-E-Beam Maskless Lithography, or Nanoimprint? *J Micro-Nanolith Mem* **2008,** *7* (4), 040101.

4. Lin, B. J., New Prospect of Successors to ArF Water-Immersion Lithography. *J Micro-Nanolith Mem* **2010,** *9* (2), 020101.

5. Wua, B.; Kumar, A., Extreme Ultraviolet Lithography: A Review. *J Vac Sci Technol B* **2007,** *25* (6), 1743-1761.

6. Billone, P. S.; Park, J. M.; Blackwell, J. M.; Bristol, R.; Scaiano, J. C., Two-Photon Acid Generation in Thin Polymer Films. Photoinduced Electron Transfer As a Promising Tool for Subwavelength Lithography. *Chem Mater* **2010,** *22* (1), 15-17.

7. Schumacher, H. CMOS-chip structure in 2000s. http://commons.wikimedia.org/wiki/File:Cmos-chip_structure_in_2000s_(en).svg (accessed 15.11.2010).

8. Huh, S.; Kim, S. B., Fabrication of Conducting Polymer Films Containing Gold Nanoparticles with Photo-Induced Patterning. *J Phys Chem C* **2010,** *114* (7), 2880-2885.

9. Marques-Hueso, J.; Abargues, R.; Canet-Ferrer, J.; Agouram, S.; Luis Valdes, J.; Martinez-Pastor, J. P., Au-PVA Nanocomposite Negative Resist for One-Step Three-Dimensional e-Beam Lithography. *Langmuir* **2010,** *26* (4), 2825-2830.

10. Pang, J.; Xiong, S.; Jaeckel, F.; Sun, Z.; Dunphy, D.; Brinker, C. J., Free-Standing, Patternable Nanoparticle/Polymer Monolayer Arrays Formed By Evaporation Induced Self-Assembly At A Fluid Interface. *J Am Chem Soc* **2008,** *130* (11), 3284-3285.

11. Shankar, S. S.; Rizzello, L.; Cingolani, R.; Rinaldi, R.; Pompa, P. P., Micro/Nanoscale Patterning of Nanostructured Metal Substrates for Plasmonic Applications. *ACS Nano* **2009,** *3* (4), 893-900.

12. Westerlund, F.; Bjornholm, T., Directed Assembly Of Gold Nanoparticles. *Curr Opin Colloid In* **2009,** *14* (2), 126-134.

13. Maretti, L.; Billone, P. S.; Liu, Y.; Scaiano, J. C., Facile Photochemical Synthesis and Characterization of Highly Fluorescent Silver Nanoparticles. *J Am Chem Soc* **2009,** *131* (39), 13972-13980.

14. McGilvray, K. L.; Decan, M. R.; Wang, D.; Scaiano, J. C., Facile Photochemical Synthesis Of Unprotected Aqueous Gold Nanoparticles. *J Am Chem Soc* **2006,** *128* (50), 15980-15981.

15. Scaiano, J. C.; Billone, P.; Gonzalez, C. M.; Maretti, L.; Marin, M. L.; McGilvray, K. L.; Yuan, N., Photochemical Routes To Silver And Gold Nanoparticles. *Pure Appl Chem* **2009,** *81* (4), 635-647.

16. Stamplecoskie, K. G.; Scaiano, J. C., Light Emitting Diode Irradiation Can Control the Morphology and Optical Properties of Silver Nanoparticles. *J Am Chem Soc* **2010,** *132* (6), 1825-1827.

17. Frechet, J. M. J., The Photogeneration Of Acid And Base Within Polymer-Coatings - Approaches To Polymer Curing And Imaging. *Pure Appl Chem* **1992,** *64* (9), 1239-1248.

18. Ito, H., Chemical Amplification Resists: Inception, Implementation In Device Manufacture, And New Developments. *J Polym Sci Pol Chem* **2003,** *41* (24), 3863-3870.

19. Ito, H., Chemical Amplification Resists For Microlithography. *Adv Polym Sci* **2005,** *172*, 37-245.

20. Wu, H. P.; Gonsalves, K. E., A Novel Single-Component Negative Resist For DUV And Electron Beam Lithography. *Adv Mater* **2001,** *13* (3), 195-197.

21. Matasovic, B.; Bonifacic, M., Reductive Halogen Elimination From Phenols By Organic Radicals In Aqueous Solutions; Chain Reaction Induced By Proton-Coupled Electron Transfer. *J Phys Chem A* **2007,** *111* (35), 8622-8628.